UNIVERSITY OF SOUTHAMPTON

Faculty of Science

Department of Oceanography

A geophysical Study of the Salt Tectonics of the Sabratah Basin NW-offshore Libya

by

MOHAMED IBRAHIM ABUHAJAR

B.Sc.

A Doctoral Thesis submitted in partial fulfilment of the requirements for the award of Doctor of Philosophy of the University of Southampton

June, 1991

This thesis is dedicated to

My mother, late father,
my wife and children.

UNIVERSITY OF SOUTHAMPTON

ABSTRACT

FACULTY OF SCIENCE
DEPARTMENT OF OCEANOGRAPHY

Doctor of Philosophy

A GEOPHYSICAL STUDY OF THE SALT TECTONICS OF THE SABRATAH BASIN, NW-OFFSHORE LIBYA

by MOHAMED IBRAHIM ABUHAJAR

Geophysical studies (using the *seismic, gravity and magnetic methods*) have been carried out with the principal aim to investigate the nature and extent of salt tectonics in the Sabratah Basin, NW-offshore Libya. The Sabratah Basin is located within a large intracratonic basin situated on the passive continental margin of the African plate. Diapiric phenomena related to Triassic salt movement have affected the study area. Sedimentary units in the Basin were deformed as a result of halotectonic and halokinetic movements during Upper Cretaceous time.

The seismic reflection investigation and its interpretation shows the extent of diapiric phenomena and salt structure configuration and its influence on sediment sequence development. The study area was divided into three structural domains: the *Salt Domain*, the *Continental Shelf Domain*, and the *Thick Sediment Domain*. The salt structures have been classified into three types: *salt walls, salt diapirs, and salt pillows*. The Continental Shelf Domain has been affected by extensional faults related to cratonic rifting, and is characterized by considerable subsidence and volcanic activity (*intrasedimentary volcanic units*). The sediment thickness of the Thick Sediment Domain has been estimated to be greater than 9 km. The dominant tectonic trends in the Basin are: (i) a NW-SE *Sirtic* tectonic trend. (ii) a W-E *Jeffara* tectonic trend, and (iii) a W-E *Salt* tectonic trend. The geological evolution model for the Libyan Continental Shelf Domain has shown the development of this domain, from Late Triassic/Early Jurasic time to the present time.

Gravity and magnetic investigations and their interpretations involved analysis of the gravity and magnetic anomaly maps, using the methods of trend surface analysis, second derivative, upward continuation, power spectrum, and wavenumber filtering. Quantitative interpretation of selected gravity and magnetic profiles was carried out, using two-dimensional models. The broad aim was produce a geological interpretation of the gravity and magnetic data, delineating the deep, intermediate and shallow structures, and to improve the geological interpretation of the seismic data.

The combination of several geophysical methods, has proved particularly useful in identifying the cause of various anomalies and delineating regional and local structures in the Sabratah Basin. It is clear that uncertainties in interpretation from any one method are reduced by this combined approach. The gravity and magnetic maps exhibit a strong correlation with the regional geological controls and seismic interpretation. These maps support the existence of the salt/thick sedimentary basin and intrasedimentary volcanic units, which can be correlated with the main sources of the negative and positive potential field anomalies, respectively. Basement depth estimation is 6 km in the Continental Shelf Domain, greater than 9 km in the Thick Sediment Domain. No depth estimate was possible in the Salt Domain.

ACKNOWLEDGEMENTS

All gratitude is going to ALLAH for guiding and aiding me to bring forth this thesis to light.

I would like to express my sincere gratitude to my supervisors Dr. E. Hailwood (*Oceanography department*) and Prof. N. Hamilton (*Geology department*) for their continuous encouragement and support.

I would like also to thank Dr. A. Mouzughi (NOC), and Dr. R. Blow, for their encouragement and for helpful discussions on the subject of research.

I am grateful to all the colleagues and staff in the Exploration Department of the National Oil Corporation of Libya, who have provided me with the essential data for my research. In particular, thanks are due to the Exploration Manager Mr. I. Al Baggar.

My thanks are also extended to the staff of the Exploration Department of the Sirte Oil Company, with special thanks to the Exploration Manager Mr. T. Taleb, and to Mr. A. Amoura (*Weybridge office*).

I would like also to thank my friends and colleagues, particular thanks to Dr. R. Salami, Miss. K. Saull, and Mr. P. Riddy.

I am deeply indebted to Mr. A. Rabae (Bristol University) for his help on the gravity and magnetic computing. I have greatly benefited from his experience on gravity and magnetic programing.

My warmest thanks go to my wife and children for their continuous encouragement and care. I would like to express my deepest gratitude and indebtedness for my mother's continuous moral support throughout my life.

Finally, I wish to thank the Libyan Society for their financial support which made my stay in Britain possible.

TABLE OF CONTENTS

LIST OF FIGURES

LIST OF TABLES

Note: The SI unit for intensity of magnetization quoted in this thesis is A/m. The susceptibility in SI system is dimensionless.

LIST OF ABBREVIATIONS

NOC	:	National Oil Corporation of Libya.
SOC	:	Sirte Oil Company.
WT-84	:	Rosa project seismic lines.
A75	:	Agip Company seismic lines.
C9-83	:	Mobil Company seismic lines.
ZA, ZB	:	Elf-Aquitaine Company seismic lines.
TWT	:	Two-way time.
IGRF	:	International Geomgnetic Reference Field.
NRM	:	Natural Remanent Magnetization.
FFT	:	Fast Fourier Transformation.

Chapter 1

Introduction

1.1 General introduction and aims of this research

Libya, situated on the Mediterranean foreland of the African shield, extends over a platform of cratonic basins which are part of the stable Saharan platform. These basins were active in late Tertiary and Holocene times (Goudarzi, 1980). Libya encompasses several sedimentary and structural basins as shown in Figure 1.1. The region around the Sabratah Basin (northern offshore Libya) was affected by extensional tectonics related to cratonic rifting. Various phases marked its development; these were characterized by considerable subsidence and volcanic activity (Finetti, 1982). The region (including the study area) has been framed into the plate tectonic model through the work of many authors, including Pitman and Talwani (1972), Dewey et al (1973), Biju-Duval et al (1977), Pitman et al (1981), and Finetti (1982).

The study area location, off the north-west coast of Libya, is bounded geographically by the Tunisian offshore border to the west, the Tripolitanian coast to the south, the Gulf of Sirte to the east, and extends into the Mediterranean Sea to the north, between longitudes 12° E and 13° E and latitudes 33° N and 34° N, as shown in Figure 1.1.

The Sabratah Basin, within which the study area lies, is located within a large

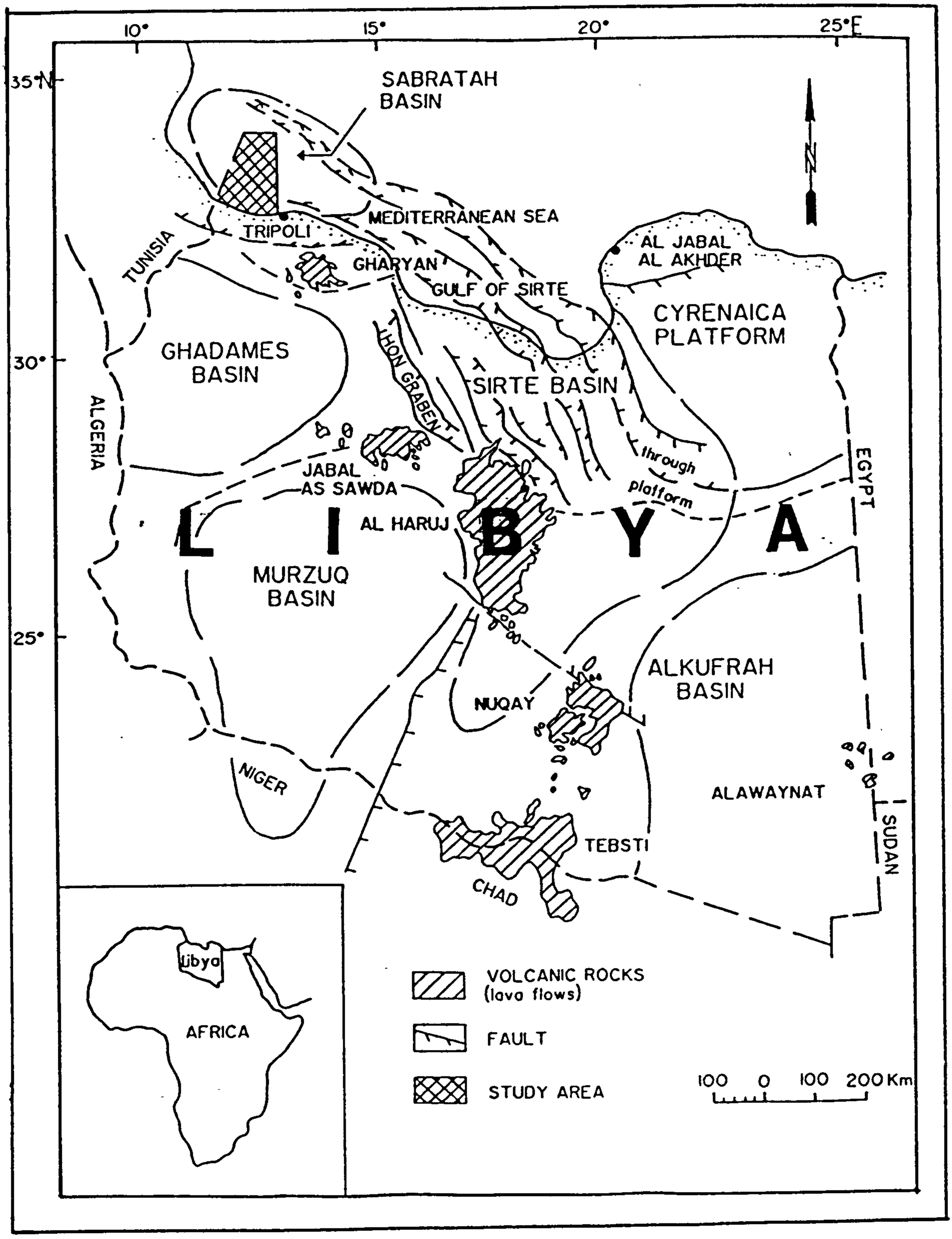

Figure 1.1: Location map of the study area.

intracratonic basin situated on the passive continental margin of the African plate. The formation of this basin was related to events in Upper Triassic to Middle-Upper Jurassic times and is connected to the opening of the Tethyan ocean basin and the evolution of the north (central) Atlantic ocean basin.

Diapiric phenomena related to Triassic salt movement affected the western part of the study area. The salt basin was deformed as a result of halotectonism (compressive tectonic forces) related to the E-W Sirte shearing movements (in Upper Cretaceous time), and also halokinesis (autonomous, isostatic salt movement) during the mobilization of Triassic salt in Cenomanian/Turonian times. Salt structures generally exhibit three stages of growth: pillow, diapir, and salt wall. The alignments of these principal salt structures are parallel with major tectonic features (the Jeffara and coastal fault systems). Genetic connections between individual salt diapirs are recognizable, and the characteristic part of a salt stock family is observed in the study area. The form of the salt diapirs is characterized by elliptical to sub-circular structures, whereas salt walls are generally cylindrical. The majority of salt structure trends have distinct W-E or WNW-ESE alignments.

Several commercial companies have worked in the area, e.g Elf- Aquitaine Libya, on concession 137; Agip Libya, on concession NC-41; Mobil Oil Company, in concession 9; and the Sirte Oil Company, (Rosa project). The Rosa project was authorized by the National Oil Corporation of Libya (NOC), and undertaken by the Sirte Oil Company. This project involved a geophysical survey which covered most of offshore Libya, including the present study area, using seismic, gravity and magnetic techniques. Little information has been published regarding the salt structures and only a small part of the exploration activity concerns the origin and development of salt basin diapirs. An understanding of salt tectonics in NW-offshore Libya requires an integration of various geophysical and geological data. All the available data for this study have been provided by the National Oil Corporation of Libya.

The principal aim of the study is to integrate information from the geophysical data (seismic, gravity, and magnetic) and well log controls, in order (i) to investigate the extent of salt tectonics in the area and its influence on sediment sequence development, (ii)

to establish the tectonic framework of the Sabratah Basin, including an investigation of the deeper structural controls, by using various filtering and analytical techniques for the gravity and magnetic data, and (iii) to establish a basic methodology for two dimensional gravity and magnetic modelling of the geological structures in this region.

The bathymetric map of Figure 1.2, was obtained from a regional map provided by the Sirte Oil Company (1989). Generally, the bathymetry is shallow on the Pelagian platform (particularly in the study area), the continental shelf is relatively wide and the continental slope descends gradually away from the coast of Tripoli to a depth of 300 m

1.2 Outline of thesis chapters

As regards the overall plan of the thesis, the initial Chapters are essentially reviews of basic aspects of the study area. Chapter 2, discusses the geologic and tectonic history of the (Central) Mediterranean region, based on the plate tectonic model, which was largely controlled by the relative motions between Africa and Europe. Knowledge of the geologic and tectonic structure and history of the Sabratah Basin is based largely on the results of seismic survey and exploratory wells. The latter provide a description of the stratigraphy and sedimentary history of the study area. Chapter 3 focuses on a review of ideas concerning the origin and structure of evaporite basins and the physical properties of the salt. In particular, the distribution and development (age, movement, form, tectonic, structure,.. etc) of the salt structures.

Chapter 4 presents results of detailed seismic investigations and gives an interpretation of several key seismic lines which are tied to available borehole data. This interpretation demonstrated the presence of diapiric structures, and provided information on the extent and configuration of such salt structures and their influence on sediment sequence development. Two-way time structure contour maps of two horizons have been constructed: the shallow horizon (Horizon A) representing the Salambo/Cherahile Formation interface (base of the Oligocene), and the deep horizon (Horizon B) representing the top of the Zebbag Formation (Upper Cretaceous). These maps delineate the regional

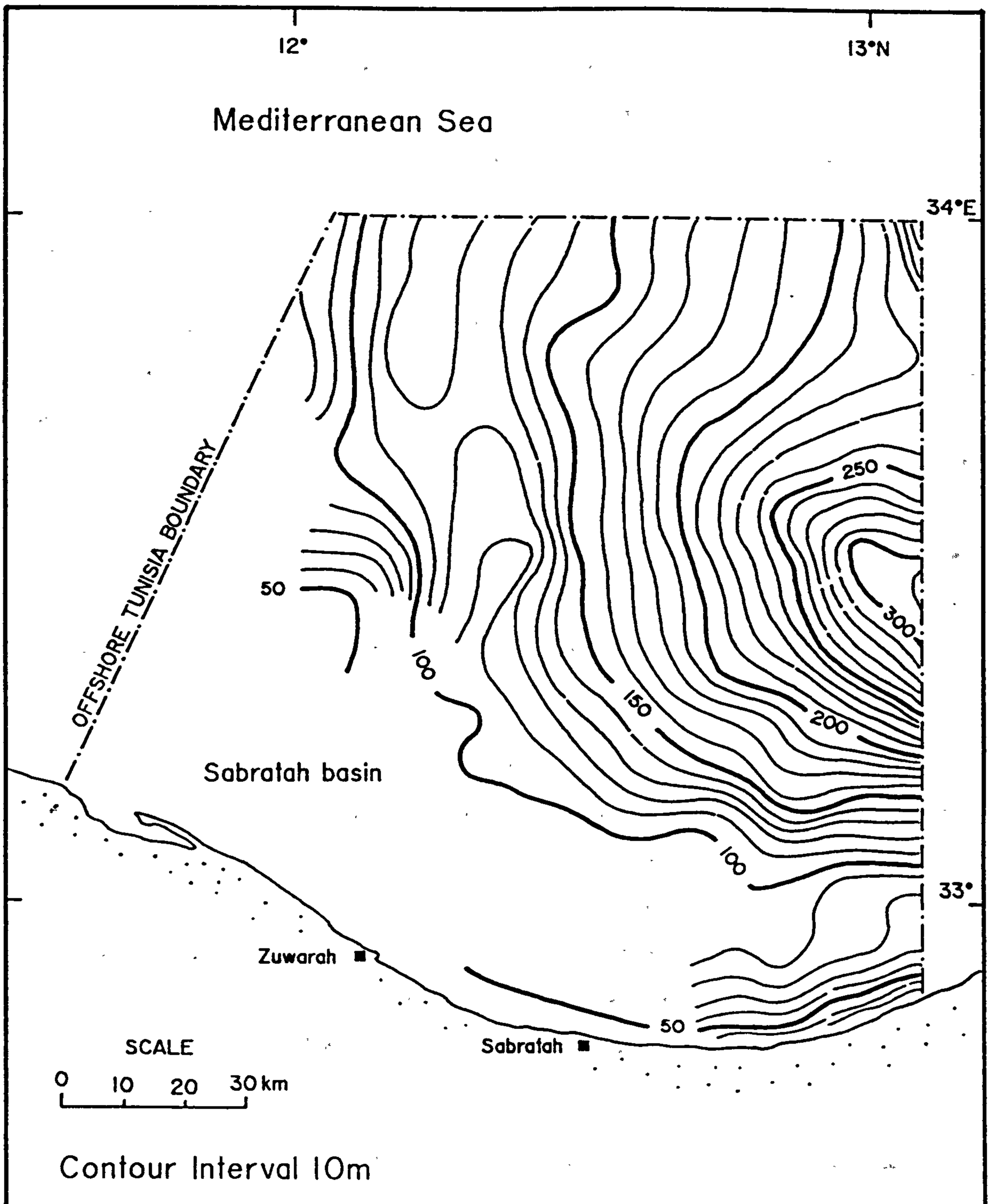

Figure 1.2: Bathymetry map of the study area. After Sirte Oil Co. (1989).

geological structure which can be subdivided into three parts: (i) an area of Salt Tectonics (in the west), (ii) a Thick Sediment Basin (in the center and north), and (iii) the Continental Shelf (in the south). Several seismic profiles which illustrate good examples of salt structures (***salt pillows, diapirs and walls***), and indicate several key features related to the salt tectonics; are shown.

Since the different geophysical methods are used in combination at the interpretation stages, ambiguity arising from results of the seismic survey may be reduced by consideration of the results from other survey methods (such as gravity or magnetic). Chapter 5 describes the processing and interpretive techniques used for the gravity and magnetic data. These include various analytical methods such as polynomial surface-fitting, second-derivative calculation, upward continuation, power spectral analysis, and two dimensional modeling. A detailed magnetic anomaly map (based on a 55x55 dataset) has been used for 2-D interpretation of the intrasedimentary volcanic units and uplift structure anomaly.

Chapter 6 is directed towards the interpretation of the gravity and magnetic anomalies, in particular a negative gravity anomaly and a low amplitude magnetic anomaly associated with the Salt/Thick Sediment Domains (in the west and central parts of the study area). A positive gravity anomaly and high amplitude magnetic anomalies are associated with the uplift structure and intrasedimentary volcanic units (southern part). The application of the interpretive techniques used for the Bouguer and total field magnetic intensity maps and their derived maps, and the estimated depths of the different groups of sources, are illustrated in this chapter.

Chapter 7 includes a combination of the analytical interpretive techniques used for the gravity and magnetic data with geological and seismic considerations. These comparisons are most successful and delineate individual anomalies, which provide a good agreement for depth estimations. The thesis ends with a discussion of the results and conclusions from this study together with recommendation for future work in this area.

Chapter 2

Geological setting of the study area

2.1 Introduction

The Mediterranean Sea has been divided into several physiographic provinces and sedimentary basins, which have been described in detail by many investigators, such as Ryan et al (1969), Biju-Duval et al (1974), Hammuda et al (1980), and Finetti (1982). These physiographic provinces are shown in Figure 2.1. From west to east they are:

1. *The Western Mediterranean.*

   This includes the following basins:

   - The North Balearic Basin.
   - The South Balearic Basin.
   - The Tyrrhenian Basin.

2. *The Central Mediterranean.*

   This includes the following basins:

   - The Ionian Basin.

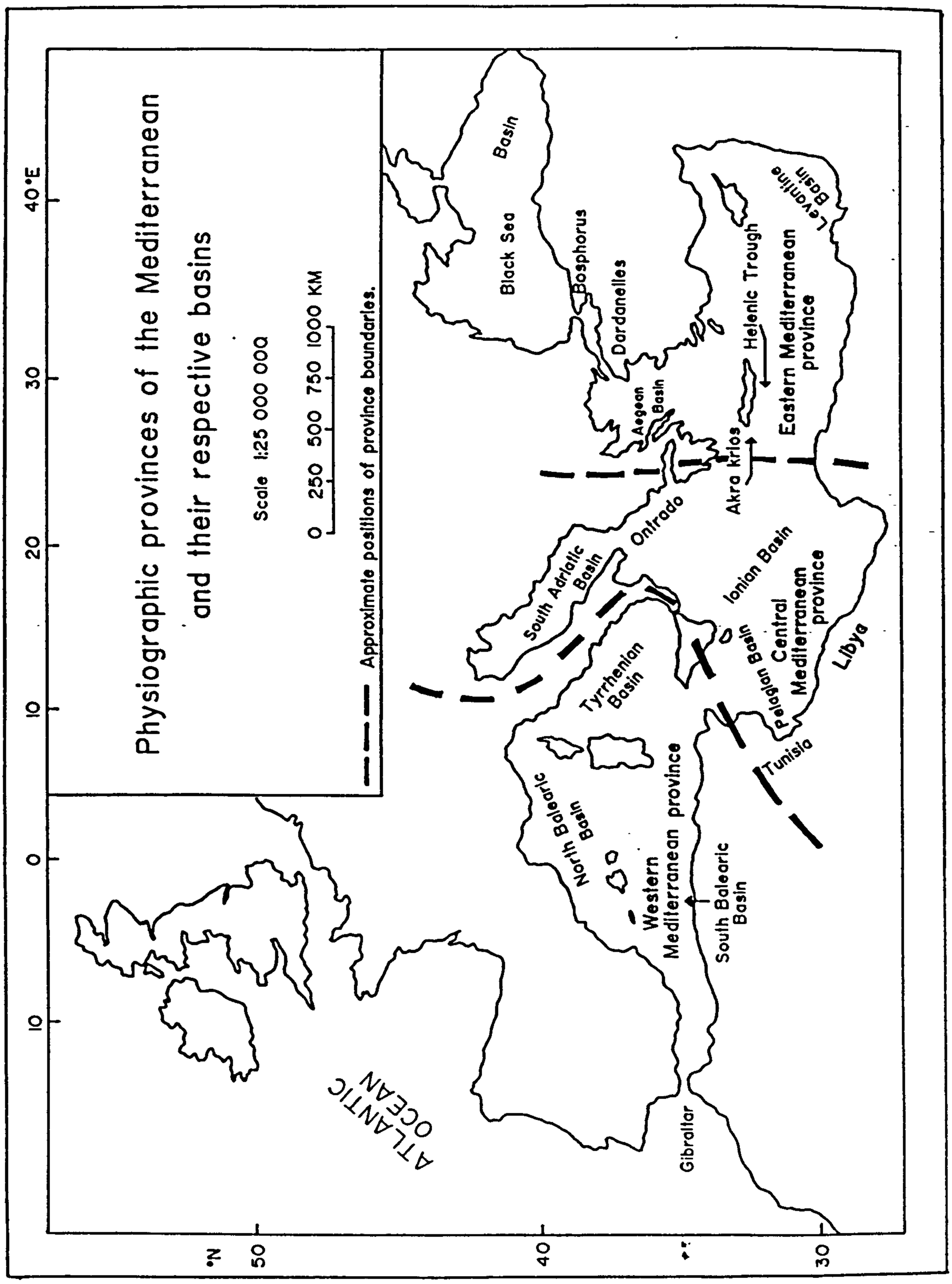

Figure 2.1: Physiographic provinces of the Mediterranean and their respective basins.

- The South Adriatic Basin.
- The Pelagian Basin.

3. *The Eastern Mediterranean.*

This includes the following basins and Seas:

- The Aegean Sea and its related basins.
- The Levantine Basin.
- The Cyprus Basin.

Biju-Duval et al (1974), subdivided the basins of the Mediterranean into two types, which have a different age, structure and genesis. These are:

- *Cenozoic basins*, which are located mostly in the western Mediterranean (including the Tyrrhenian Basin), but also in the eastern Mediterranean (including the Aegean and North Cyprus basins). These were tectonized during the Mesozoic and bear a close relationship to the Alpine fold belts.

- *Mesozoic-Cenozoic basins*, which are mostly located in the central and eastern Mediterranean, and have been affected only slightly, or not at all, by Alpine folding. They form the northern prolongation of the African continent.

The Pelagian Basin, within which the study area of this thesis is situated, is located in the Central Mediterranean near to the African coast, in the offshore region of NW-Libya. The geological sequences in this area are known from drilling to range in age from Mesozoic to Recent.

The specific study area, the Sabratah Basin, forms part of a large intracratonic basin situated on the passive continental margin of the African plate. It lies at the southern margin of the Pelagian Basin.

2.2 Regional geology

2.2.1 Geological history of the Central Mediterranean (Pelagian Basin)

The geological history of the Central Mediterranean based on the plate tectonics model, has been described by Pitman and Talwani (1972), Dewey (1973), Biju-Duval et al (1977), Pitman et al (1981) and Finetti (1982). The tectonic evolution of this region has been controlled directly or indirectly by the relative motions between the African and European plates. Three distinct phases of relative motion between Africa and Europe have been identified (Dercourt, 1970; Smith, 1971; Dewey et al 1973; Biju-Duval et al 1977). In the first phase of Jurassic to early Cretaceous age, the Central Atlantic between Africa and North America was opening and movement of Africa relative to Europe was eastward. In the second phase, of latest Cretaceous to early Cenozoic age, the North Atlantic began to open between North America and Europe, and the motion of Africa relative of Europe was westward. In the third phase Africa moved northward. These motions are illustrated by Smith (1971), Dewey et al (1973); Biju-Duval et al (1977); and Dewey et al (1989).

Finetti (1982) has subdivided the Central Mediterranean into seven geological provinces, as follows: The Pelagian Sea, Sirte Rise, Ionian Abyssal Basin, Apulian Platform, Southern Adriatic Basin, Calabrian Arc, and Hellenic Arc. The study area of this thesis is located in the Pelagian Basin province, which lies between Sicily, Tunisia, the Tripolitania Coast, the Sicily-Malta escarpment, and the Medina bank (Figure 2.6). The shallow Pelagian platform is bounded to the west by Tunisia, to the south by the Libyan coast, and to the north by the Kerkennah high and the Graben fault zone . To the east, it is bordered by a major fault zone *the Medina escarpment* corresponding with the easterly deepening of the Ionian Sea. This fault is linked to that forming the eastern coast of Sicily (the Malta-Sicily escarpment) and to the Misurata fault of NW-Libya. It is marked by recent volcanic activity, including that of Etna in Sicily, and Gharyan , and Jebel es soda, in the northern and central parts of Libya, respectively. The possibility of the fault pattern extending to Tibesti in the southern part of Libya, has been suggested by Burollet (1969).

The geological history of the Pelagian basin has been described by Finetti (1982) and is summarized in Figure 2.2. Four main phases of geodynamic evolution have been identified, ranging in age from the Middle-Upper Triassic to the Quaternary; these are briefly summarized below:

1. In the Middle to Upper Triassic an extensional phase occurred, represented by extensive rifting and the development of a carbonate platform.

2. In the Middle Jurassic a second extensional phase occurred, as indicated by abundant volcanic activity of this age. The maximum opening of the Tethyan Ocean took place in this period with the fragmentation of the carbonate platform formed during the Triassic.

3. In the Upper Cretaceous the widespread Cenomanian marine transgression affected much of North Africa. This was accompanied by new rifting in the Pelagian Basin, reactivation of pre-existing faults and subsidence. Basaltic and pyroclastic magmatic activity occured in several parts of the Central Mediterranean, particularly in the Sirte basin. Subsequently, throughout the Tertiary, strong subsidence took place, and the African plate began to underthrust the European plate giving rise to the Alpine arc. In the Lower to Middle Miocene the Calabrian arc overthrust the paleo-oceanic crust of the Ionian Abyssal basin, which continued to be subducted.

4. The fourth extensional phase was active from the Middle-Upper Miocene through to the Quaternary. It led to the forming of an intracratonic basin, due to rifting of the Sicily Channel in the Pantelleria, Linosa and Malta areas.

The present day situation of the African continental margin is delineated in the seismic sections crossing the Libyan continental margin shown in Figures 4.18 and 4.21, (Chapter 4).

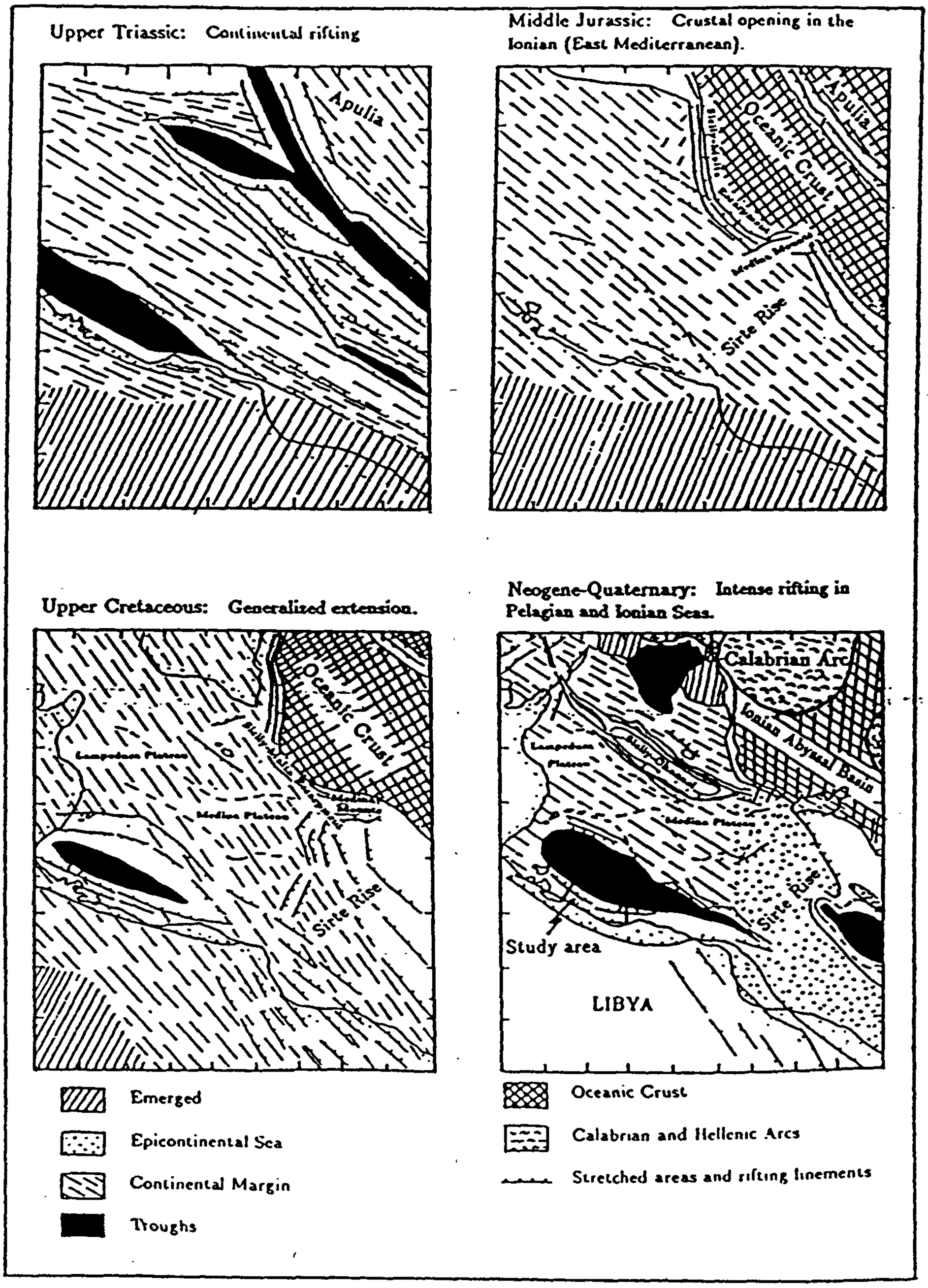

Figure 2.2: The geodynamic evolution of the Pelagian Basin and Ionian Seas. *After Finetti (1982).*

2.2.2 Geology of the Sabratah Basin (study area)

The Sabratah Basin of the southern Pelagian Sea, has been referred to by several other names, including the Gabes-Tripoli-Misurata Basin (Finetti, 1982 and Agip Co., 1985), Gabes-Tarabulus basin (Hammuda et al, 1985), and Sabratah Basin (Sirte Co., 1989). In this particular study the term *Sabratah Basin* is used for the geological unit which extends from the Gabes Basin to offshore Misurata (Figure 2.6). It is limited to the south by the Gafsa-Jeffara fault system and to the north by the Melita-Medina platform. Southern Tunisia and Tripolitania (including the Sabratah Basin) form part of the Saharan platform, which received an epicontinental sequence of Cambrian to Mississippian rocks (Burollet et al, 1978). These rocks were gently folded during the Carboniferous and subsequently eroded, so that the oldest strata occur in the north, in the Jeffara area. Step faulting during the Permian caused the area north of Jeffara to subside and a marine invasion resulted in the local deposition of great thicknesses of sediment. This subsidence of the Jeffara region was the first step in the development of the Tethys trough.

The geological history of the study area is based on interpretation of the seismic reflection profiles and the exploratory wells shown in Figure 4.1. These profiles across the Libyan continental margin, show that the Sabratah basin was formed largely during the late Triassic to late Jurassic by normal faulting to the north along an east-west trending hinge zone (Figures 4.17, 4.18, and 4.21, Chapter 4). The area seaward (north) of the hinge zone has continued to subside since this time, receiving a total of more than 5 km of sediment. This change in depth towards the Mediterranean Sea is seen in the correlation of wells in Figures 2.3 and 2.4. For instance, the top of the Abu-Shaybah Formation at a depth of 1175 m in well A1-38 *(onshore area)*, lies at a depth of 3780 m near the base of well L1-137 *(offshore area)* (Figure 2.4). Step faulting with an overall throw of some 2600 m during Permian time, caused deposition of the great thickness of sediments in the offshore area.

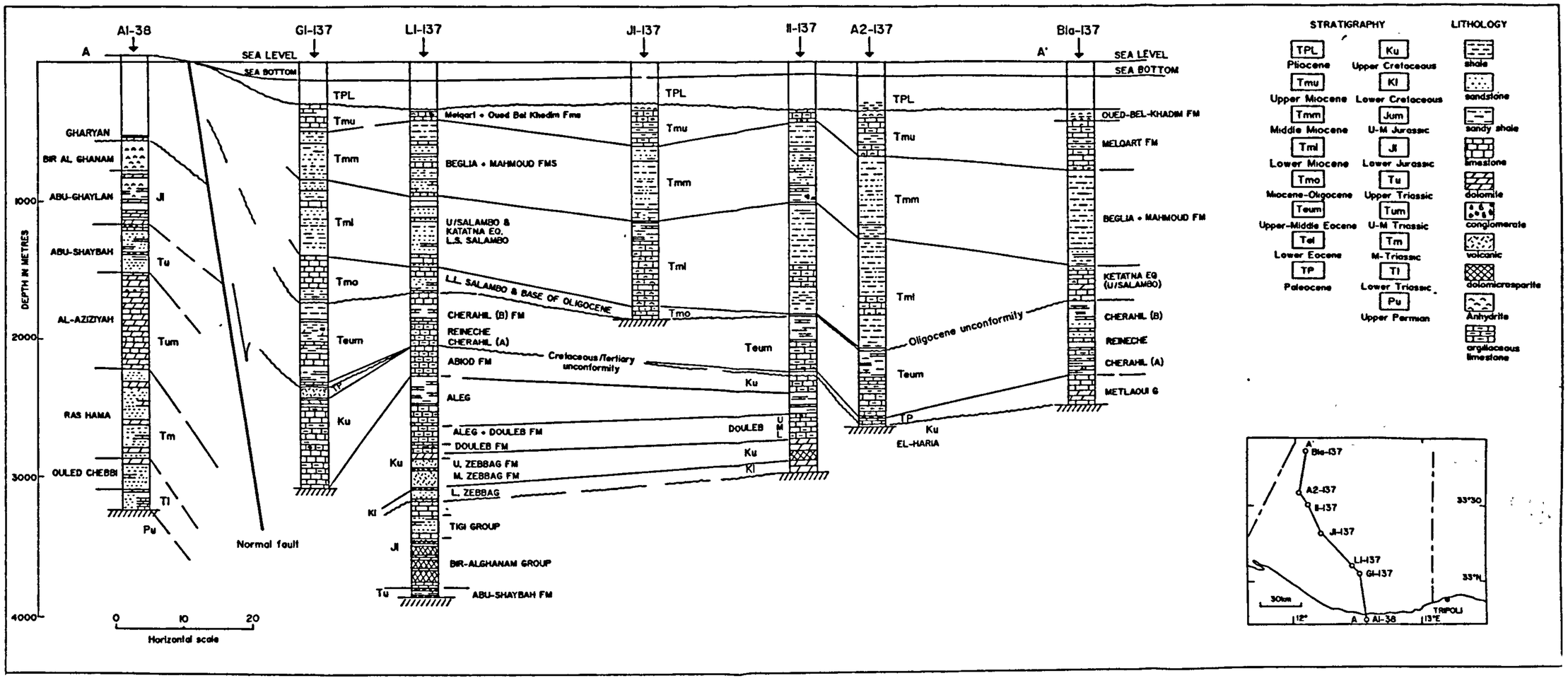

Figure 2.3: Diagrammatic section AA′ showing stratigraphy and lithology along profile AA′ in the study area, Sabratah Basin NW-offshore Libya.

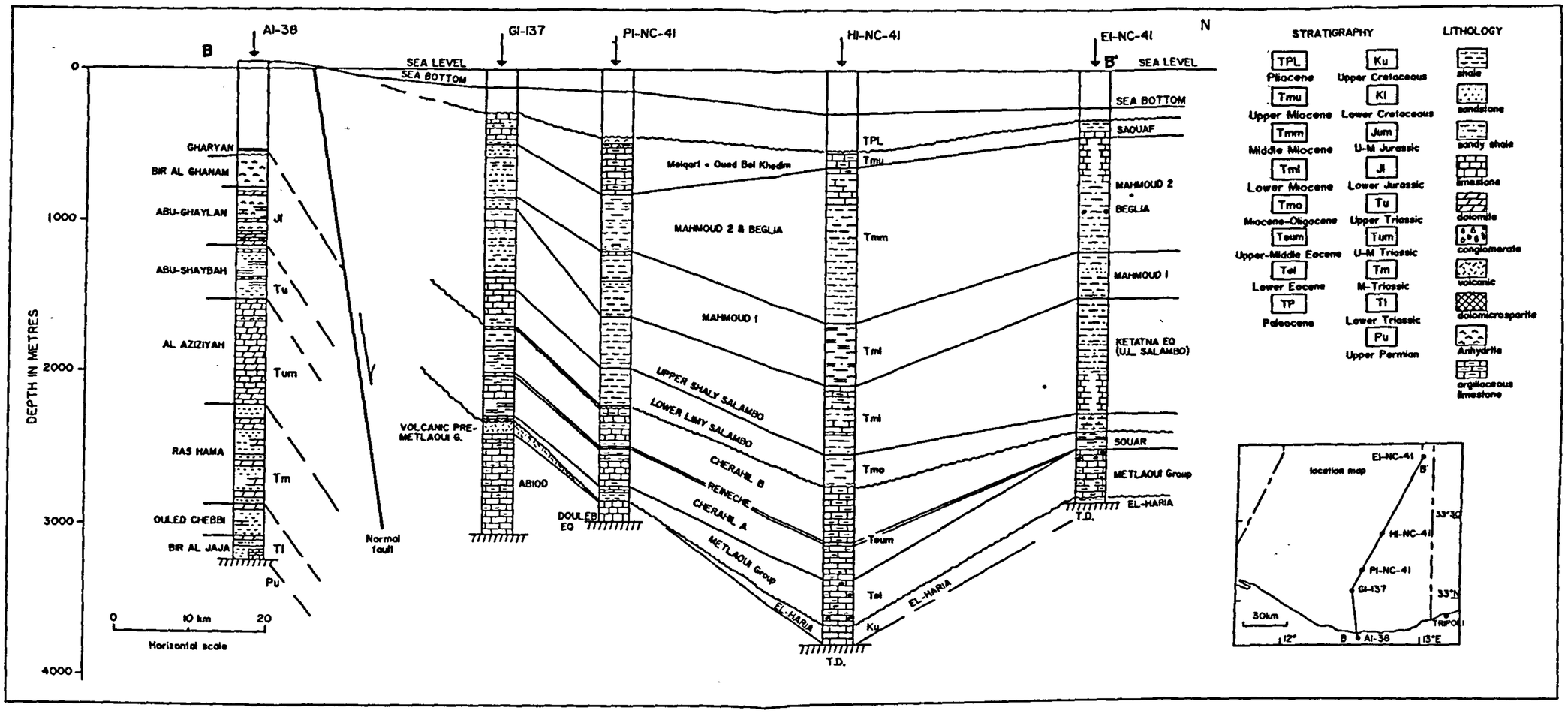

Figure 2.4: Diagrammatic section along the profile BB′ showing stratigraphy and lithology in the study area, Sabratah Basin NW-offshore Libya.

2.3 Stratigraphy and sedimentology

2.3.1 Regional palaeogeography

Triassic-Jurassic

The most complete Triassic-Jurassic sections in the southern border of the Sabratah Basin are known from boreholes in the Jeffara Basin (eg A1-38).

These are represented by the Bir El-Jaja, Ouled Chebbi (Lower Triassic), Ras Hama, Aziziyah (Middle Triassic), and Abu-Shaybah (Upper Triassic) Formations. South of well A1-38, near Gharyan City, the Abu-Shaybah Formation outcrops. The Triassic is represented by a successively sandy, dolomitic and evaporitic regressive sequence in the Jeffara Basin. At the continental margin of the Sabratah Basin (on the edge of the Saharan platform), the Triassic rocks are gently tilted, and a transition occurs from the Saharan continental facies to a marine facies. In the Sabratah Basin, only well L1-137 was penetrated to the Upper Triassic stratigraphic level, which is represented by the Abu-Shaybah Formation comprising shale, dolomite, and anhydrite with a total thickness of some 56 m. The Upper Triassic and the Liassic units are mainly shaly and anhydritic, and the Middle to Upper Jurassic units are mainly continental at the outcrops in the Jeffara Basin. The Lower to Upper Jurassic units are represented by the Bir-Al-Ghanam evaporitic Group and Tigi Group (shale and sandstone (well L1-137)).

Lower Cretaceous transgression

Lower Cretaceous sediments were encountered only in wells L1-137 and K1-137 (southern part), and are represented by the sandy dolomites and anhydrite of the Lower Zebbag Formation. This unit has been partially or entirely disturbed by volcanic activity.

Upper Cretaceous transgression

The major transgression of the Cenomanian-Turonian resulted in a link with the Gulf of Guinea through Nigeria (the trans-Saharan seaway) (Kogbe 1980), and deposited a blanket of limestone and dolomite on the northern margin of the Saharan craton. The Cenomanian deposits are often associated with volcanic units in the southern part of the study area (wells H1, H2, and L1-137, Figures 4.19 and 4.20). A deep pelagic environment was present in the central part of the Sabratah Basin in the Campanian. From the Santonian onwards the Sabratah Basin was disturbed by salt tectonic movements. The Upper Cretaceous is represented by the Abiod Fm., (Lower Maastrichtian-Campanian), the Aleg Fm., (Campanian to Santonian), Douleb Fm., (Turonian), and the Upper-Middle Zebbag Fm., (Cenomanian). In the Jeffara Basin the Upper Cretaceous is represented by a carbonate and evaporitic facies.

The Upper Cretaceous/ Tertiary unconformity

The Cretaceous/Tertiary unconformity is quite clearly observed all over the study area. The absence of Maastrichtian to Paleocene age deposits on top of some of the structures, is an indication of this erosional phase (eg J1-137, F1-137, and L1-137 Figure 2.4). Late Cretaceous to early Tertiary age strata are exposed in the Al Hamadah Al Hamra and Sirte basins of onshore Libya, where they comprise a carbonate-clay-calcilutite association with minor evaporites (Megerisi et al 1980).

Paleocene sequences

The Upper Cretaceous-Paleocene boundary lies within the red El Haria (volcanics tuff) Formation in well H1-137. In well G1-137 it is represented by the pre-Metlaoui volcanics (tuffs) and El-Haria Formations (see Figure 4.20, Chapter 4).

Eocene sequences

The Eocene sequence is represented by the Metlaoui Group (formerly the Farwah Group) transgressive sequence, and Cherahil Group (Tellil Group) regressive sequence. These groups are widely distributed in the Sabratah Basin, and were encountered in most of the wells drilled in the study area. They comprise a carbonate, shale, and limestone facies. The Metlaoui Group is economically the most important rock unit in the basin (for the production of hydrocarbons). It is thickest in the north and northeast , and thins towards the south and southwest along the profiles AA′ and BB′ (Figures 2.3 and 2.4). It overlies volcanic rocks in the south (wells H1 and H2-173, Chapter 4). In the western part *(the salt area)* of the study area the group is very thin or absent. The thinning and thickening of the Eocene sequences is due to the uplifting and erosion caused by salt tectonics in the western part of the study area. Therefore, the evolution of sedimentation was controlled by tectonic conditions.

Oligocene-Miocene sequences

These sequences are represented by the marker bed of *Nummulites vascus* (base of the Oligocene), Lower Shaly Salambo, Lower Limy Salambo, Upper Shaly Salambo, Ain Grab, Mahmoued, Beglia, Melqart, and Oued Bel Khedim Formations (Miocene sequences). The Oligocene-Miocene consists of a large regressive sequence with marine shales and sandstones (see Figures 2.3 and 2.4).

2.3.2 Stratigraphical and sedimentological description

Remarks on local nomenclature:

A terminology for the Tertiary to upper Cretaceous units of Tunisia was defined by Burollet (1965). The terminology has been applied in the past to the description of the lithological units present in western offshore Libya. However, this terminology for units in this region has been revised in a new publication on stratigraphic nomenclature for NW-offshore

Libya, by Hammuda et al (1985). The correlation of units is different parts of the region is shown in Figure 2.5

2.3.3 Lithological description

The main lithological units encountered in the wells drilled in the study area are shown in Figures 2.3 and 2.4, which show also the stratigraphic relationships between the units. The widely used terms for lithological units are shown in these Figures and used below. Equivalent terms (Hammuda et al 1985) are given in brackets after each name.

Triassic and Jurassic series

These series have only been reported from the southern part of the study area in well L1-137 (Figure 2.4). The top of the Triassic is represented by the Abu-shaybah Formation, which consists of brick-red anhydritic shales. The Lower to upper Jurassic series at L1-137 is represented by three members:

- A lower (Liassic) unit, the Bir-El Ghanam evaporitic group (anhydrite, dolomicrosparite, and shale) with a thickness of 360 m.
- A middle unit, the Tigi Group (Shale, and dolomitic pyritic with thin beds of sandstone) with a thickness of 157 m.
- An Upper Jurassic unit, equivalent to the Kiklah Formation, (dolomitic and argillaceous) with a thickness of 92 m.

Lower Cretaceous series

The Lower Cretaceous was also encountered in wells L1-137 and K1-137. It is called the Lower Zebbag Formation, which consists of 110 m of sandy dolomite in well L1-137, and 30 m of dolomicrosprite and anhydrite in well K1-137. The presence or absence of the

CORRELATION CHART OF MESOZOIC AND CENOZOIC ROCKS IN NORTHWEST LIBYA

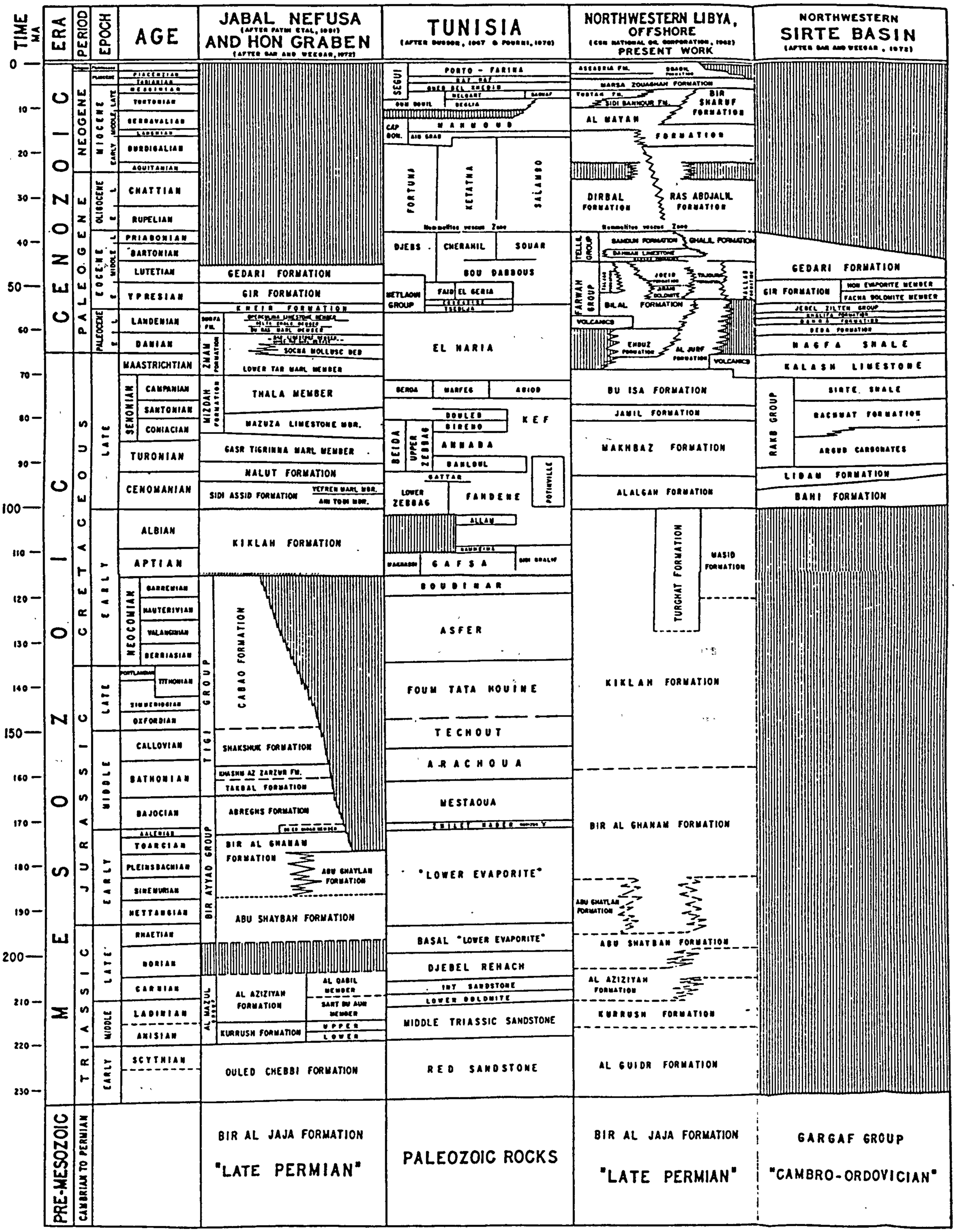

Figure 2.5: Correlation Chart of Mesozoic and Cenozoic rocks in northwest Libya. (*From Hammuda et al 1985*).

Lower Cretaceous in different parts of the study area is related to salt tectonics, which were an important process in this region. The Lower Zebbag Formation (lower Cretaceous) is overlain by an intrasedimentary volcanic unit (comprising volcanic conglomerate and anhydrite) in well L1-137, and underlain by an intrasedimentary volcanic unit (basaltic volcanic rock) in well K1-137.

The Zebbag (Alalgah) Formation. *Age : Cenomanian.*

The Zebbag Formation is a largely dolomitic facies, which extends over much of the western and southern parts of the Sabratah basin. Three intervals have been recognized within this Formation in well K1-137 . The lower unit is composed of dolomicrosparite with streaks of black shale. The middle unit is composed of grey, argillaceous dolosparite and massive anhydrite. The upper unit is composed of dolosparite and pyrite interbedded with thin layers of indurated, fossiliferous, black shale and dolomite. The middle Zebbag is frequently associated with volcanics. It is represented by a thickness of 207 m of volcanic material at well L1-137 Figure 2.3. The total thickness of the Zebbag Formation encountered in the southern part of the study area is 350 m. The upper part of the Zebbag Formation corresponds to formations which outcrop in the Jebel Nafusa (*Nalut Formation* Hammuda, et al 1985). The lower part corresponds to the Sidi As Sid Formation.

The Douleb (Makhbaz) Formation. *Age: Coniacian to Turonian.*

The Douleb Formation contains three units. The lower unit consists of microsparite, dolomitic at the base and interbedded with shale. The middle unit consists of micrite interbedded with shale, and the upper unit consists of argillaceous sparite, microsparite, pelmicrite and micrite (in well I1-137). The Douleb Formation is conformably underlain by the Zebbag Formation and conformably overlain by the Aleg (Jamil) Formation. It consists of a transitional zone between the shaly Aleg Formation and dolomitic Zebbag Formation. The total thickness of the Douleb Formation ranges from 33 to 184 m

The Aleg (Jamil) Formation. *Age: Santonian.*

The Aleg Formation consists of shales, marl and tight argillaceous limestones. The formation reaches a maximum thickness of 762m. It has been identified by seismic reflection data in the rim syncline between salt structures, and the thickness deduced from well data ranges from 380 m in well K1-137 to 125 m in well I1-137. In some rim-synclines between salt structures the Aleg can be more than 800 m. The Aleg Formation extends over the whole of the study area, halokinesis being active during this time (rim-syncline formation).

The Abiod (Bu Isa) Formation.

(Age: Campanian to Lower Maastrichtian.) The Abiod Formation, encountered in wells C1, I1, L1, G1, and H1-137, consists of micrite, argillaceous to biomicritic, marl overlain by micrite, and marl. This Formation thins slightly towards the west of the study area. In the southern part, along the continental shelf area at G1 and H1-137, the formation reaches a maximum thickness of 657 m (G1-137). It is overlain by the El Haria Group and the Metlaoui Group and underlain by the Aleg Formation.

The El Haria (Al-jurf) Group.

(Age: Upper Maastrichtian to Upper Paleocene)

The El Haria Formation consists of a shaly and marly series with limestone interbeds. This Formation is underlain by the Abiod *(Bu Isa)* Formation and overlain by the Metlaoui Group. The conditions of deposition of the El Haria Formation were controlled by tectonic and halokinetic movement in the study area. It thins out toward the south and southwest of the basin. It has a thickness of about 20 m in the south and south west rising to 414 m in the north and north east.

The Metlaoui (Farwah) Group.

(Age: Upper Paleocene to Lower Lutetian.)

This group is a carbonate sedimentary sequence bounded at the top by the shale and

limestone of the Cherahil Formation, and at the base by the shale and marl of the El Haria (Al Jurf) Formation. The Metlaoui Group comprises three formations: these are the Tsedlja and Chouabine Formations (*equivalent to the Bilal Formation*), and the Faid Formation (*equivalent to the Taljah Formation*). The Metlaoui Group is widely distributed in NW-offshore Libya and is encountered in most of the wells drilled in the central and southern Sabratah Basin. The group thins towards the south and southwest (very thin or absent in the well L1-137), and the western edge of the study area. It is thickest in the north and northeast. The conditions of deposition of the Metlaoui Group were mainly controlled by tectonic and halokinetic movements in the study area. The group is economically the most important rock in the NW-offshore Libya region. Oil is found in three formations of this group, in particular the nummulitic and dolomitic intervals (Hammuda et al 1985).

The Cherahil (Tellil) Group.

Age: Middle to Upper Eocene.

The Cherahil Group consists of a variety of interbedded lithologies including shale, siltstone, sandstone, dolomite, anhydrite and micrite lenses. The Lower unit is called the Cherahil A *(Harsha)* Formation, which consists predominantly of marl and dolomitic limestone with minor lenses of shale and anhydrite. In the middle part of the Cherahil Group occurs a nummulitic limestone bed, the Reineche (or Dahman) member, which is 23 to 60 m thick. The upper unit is the Cherahil B *(Samdun)* Formation, which consists predominantly of soft greenish shale and clay with lenses of siltstone, dolomite and anhydrite. This upper member is overlain by the Vascus Mbr *(base of the Oligocene)*. The total thickness of the Cherahil Group ranges between 400 m and 1116 m and decreases to the north.

Vascus Member. *Age: base of Oligocene.*

This is a nummulitic member, overlying unconformably the Eocene deposits. It comprises nummulitic limestones. This member is widely distributed and is encountered in most of

the wells drilled in the Sabratah Basin.

The Salambo Group. *Age: Lower Miocene to Oligocene.*

The Ketatna *(Dirbal)* Formation : This unit occurs below, above or within the Salambo Group. Its thickness ranges from 85 to 905 m, and its age ranges from Oligocene to Lower Miocene. This unit is named the Ketatna *(Dirbal)* Formation when it consists of biostromal limestones as observed in wells B1a-137, J1-137, and A1-NC-41, and the Salambo Formation, when it consists of a more argillaceous and deeper water facies. The Ketatna facies can be a lateral equivalent of any term of the Salambo Formation. The group is limited at its top by the Ain Grab intercalation corresponding to the Middle-Lower Miocene boundary and at its base by an intercalation of nummulitic limestone, the Vascus Mbr *(base of Oligocene)*. The Salambo Group has been divided into several formations according to the predominant lithology :

- Upper shaly Salambo Formation. *Lower Miocene.* Shaly or marly , but locally sandy and limy.
- Lower limy Salambo Formation. *Lower Miocene to Oligocene.* Characterized by an increase in shaly limestones and marls.
- Lower nummulitic Salambo Formation. *Oligocene.* Encountered in wells J1-137 and K1-137 only; it consists of a nummulitic tight limestone.
- Lower shaly Salambo Formation. *Oligocene.* This consists of shales which occur below the limy member.

The Beglia-Mahmoud (Almayah) Group.

(Age: Langhian to Tortonian (Middle to Upper Miocene).

In the particular study area and according to well information , there is no major break in lithology or in logs between the Beglia sand and the Mahmoud shale formation. Consequently these units have been grouped into one formation, called the Almayah Formation,

by Hammuda et al (1985). This consists of around 500 m of sand, shale and silty shale.

Melqart or Saouf (Tubtah or Bir Sharuf) Formation.

Age: Tortonian (Upper Miocene).

This formation occurs in wells A2, I1 and J1-137, and consists of 588 to 1097 m of white to grey, soft, chalky to marly bioclastic limestones. An alternative facies occurs in well E1a-137 where it is called the Saouf *(Bir Sharuf)* Formation. Its thickness is 805 m. The upper unit consists of micrite and biomicrosparite, the middle unit of interbedded light grey marl and the lower unit of white to cream biomicrite and biosparite.

Oued- Bel-Khedim (Marsa Zouaghah) Formation.

Age: Messinian (Upper Miocene).

The sequence was encountered at wells A2, J1, E1a-137, and P1-NC-41. It consists of 50 m of gypsum, interbedded with variegated shale, sandstone and marl. The Oued Bel-Khedim Formation, is absent in well I1-137. Therefore, it is concluded that the aerial distribution of this formation is not uniform.

2.4 Tectonics

The earliest attempt to model the development of the Alpine system using rigid plate rotations was by Smith (1971), based on the assumption that there was at all times only a single plate margin between Africa and Europe, using an idealized fixed rotation pole model. A model for the opening of the Atlantic was published by Pitman and Talwani (1972), based mainly on studies of ocean floor magnetic anomalies. Dewey et al. (1973), proposed a relative motion model based on the Atlantic history model of Pitman and Talwani (1972). They suggested the presence of numerous micro-plates, between Europe and Africa, and developed a model for the evolution of the Tethyan-Mediterranean-Alpine system covering the last 200 my. Biju-Duval et al. (1977) extended the work of Dewey et al. (1973), within the framework of plate kinematics, which is basically derived from the work of Pitman and Talwani (1972). Morgan's (1981 and 1983) model for the drift of

lithospheric plates around the Atlantic and the relative motion between hotspots during the past 200 m.y. Van Houten (1983) suggested that the Sirte Basin area (North central part of Libya) drifted over a fixed mantle hotspot in Early Cretaceous time (140 to 100 m.y. ago). Livermore and Smith (1985), described the motion of Africa relative to Europe, based on the Morgan (1981, 1983) hotspot framework. Dewey et al (1989), modelled the relative motion of the African and European Plates since the Middle Jurassic, and correlated the change of the direction of plate motion with the significant events in the evolution of the sedimentary basins in Pelagia.

2.4.1 Tectonic units of the Central Mediterranean (Pelagian Basin)

The principal tectonic elements of the Central Mediterranean (Pelagian Basin) are shown in Figure 2.6. These can be described as follows:

- The Pantelleria-Malta rift zone.
- The Malta-Medina Bank-Jeffara Medina Escarpment.
- The coastal and Jeffara fault system.
- The Kerkennah high-North and South Graben fault zones.
- The Jaraffa Basin.
- The Gabes-Sabratah Basin.

The Pantelleria-Malta rift zone

The large NW-SE Sicily Channel rifting phase, during the Miocene-Quaternary faulting activity affected the whole of the Pelagian Sea. It was also associated with volcanic activity in several parts *(eg Pantelleria and Linosa Islands)*. The major Grabens of Pantelleria, Linosa, Malta, and Medina, divide the Pelagian platform into two parts: the Tunisian platform-Hammamet basin and related features to the south and the Sicilian platform *(Ragusa Platform)* to the north.

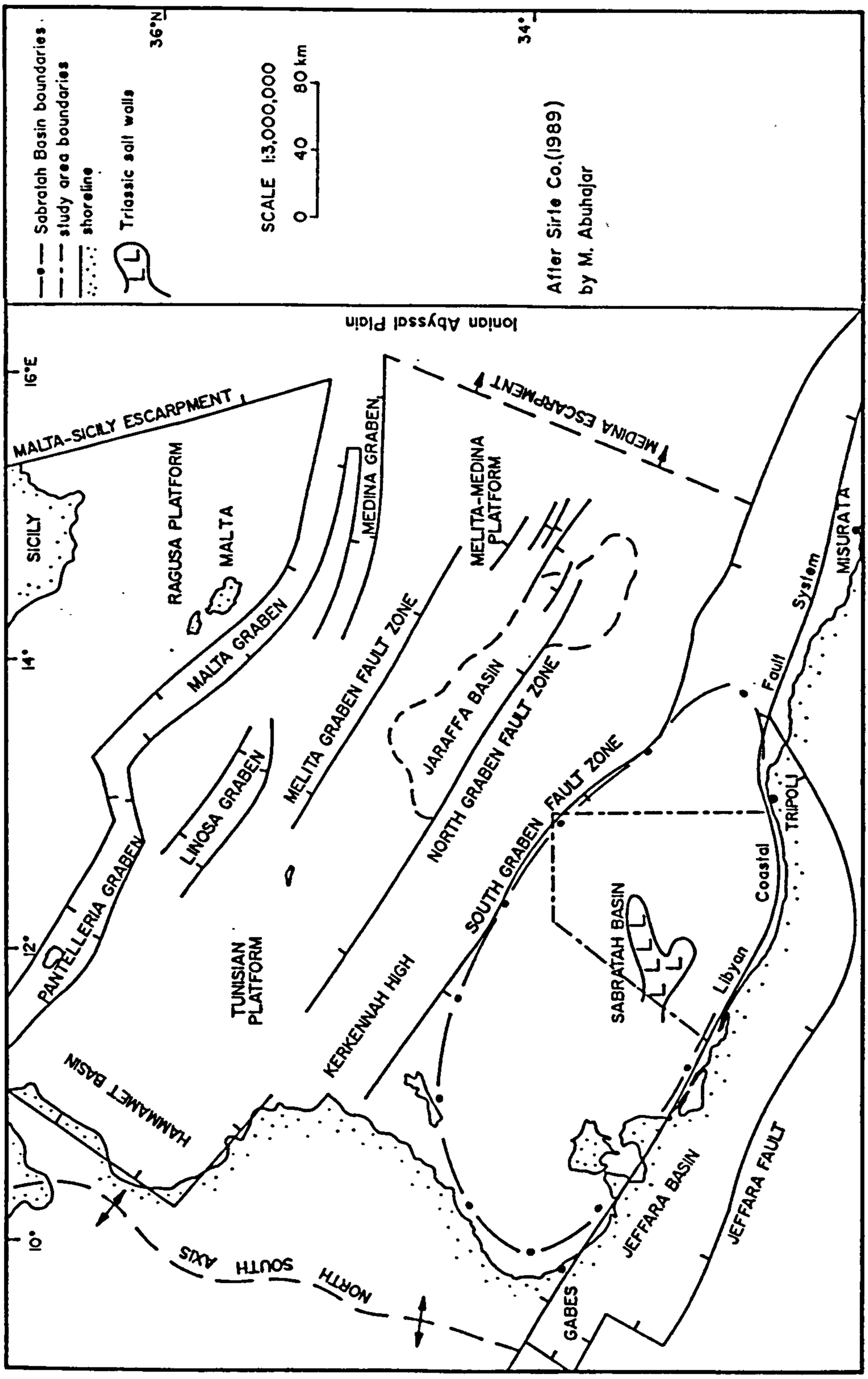

Figure 2.6: Schematic diagram showing principal tectonic elements of the Central Mediterranean region (Pelagian Basin). *After Sirte Co. (1989).*

The Malta-Medina Bank-Jeffara Medina Escarpment:

This area is affected by a normal regional fault system that diminishes its total displacement from Sicily to the Medina Mounts. South of the Ragusa plateau, an extensional fault system leads down to the Ionian abyssal area with a slope directly constituted by the fault plane (Finetti 1982). The water depth increases rapidly eastwards from 300 m to more than 1000 m. The Medina Mounts are comprised of a complex fractured horst system trending W-E. The northern escarpment of the Medina Mounts is the continuation of the Sicily Malta escarpment of Finetti, (1982). The Medina escarpment is linked to the north of the coastal City of Misurata.

Coastal and Jeffara Fault system.

At the southern flank of the Sabratah Basin, the Libyan Coastal Fault system has controlled the continental margin area (see seismic sections in Chapter 4) which is parallel to the Jeffara fault system in the southern part, and sub-parallel to the Triassic salt trend (W-E, WNW-ESE) in the central part of the Sabratah Basin.

The Kerkennah high-North and South Graben fault zones

A N-S trending belt of faults and folds (Alpine domain) in the northern and central parts of Tunisia, marks the division between the stable African platform to the east and the active Atlas folded belt to the west. The Kerkennah high and the North and South Graben fault zones have a WNW-ESE trend, related to Hercynian faulting, reactivated during the Plio-Pleistocene. These Graben fault systems have controlled the northern edge of the Sabratah Basin.

Jaraffa Basin

The Jaraffa basin is an elongate feature running along the northern margin of the North Graben fault zone. The basin occurs within the northern wing of the Sabratah Basin, and is probably related, indirectly, to basement (Hercynian) faulting (Sirte Oil Co. 1989).

Gabes-Sabratah Basin.

This geological unit extends from the Sfax-Gabes area to offshore Misurata. It is limited to the south by the regional extensional fault system of Gafsa-Jeffara, and to the north by the Kerkennah high and Graben fault zones system. This basin is considered to be result of old extensional geodynamical movements which occurred during the Hercynian event (a pull-apart between the coastal fault system and South Graben fault zone). The basin is characterized by evaporitic structures (salt walls, diapirs, and pillars) derived from piercement by Triassic salt along E-W, WNW and ENE fault trends (see Figure 4.9, Chapter 4.)

These basins and platforms are all underlain by cratonic or continental crust and are closely associated with the major structural features of the African continent.

2.4.2 Tectonic framework of the Sabratah Basin and the tectonic trends of the study area

Libya, situated on the Mediterranean foreland of the African shield, extends over a platform of cratonic basin belonging to the stable Saharan platform domain. The palaeogeographic evolution of Libya is directly connected with Caledonian, Hercynian and Alpine orogenic events (Goudarzi, 1980).

Caledonian orogeny. **This started in the Middle Silurian and affected all of Libya and its neighbouring countries. It was responsible for the initial genesis of the Sirte basin (Bellini et al 1980).**

Hercynian orogeny. This represents the second major tectonic phase. Its initial phases can be dated as Middle to Upper Carboniferous and Permian. The Hercynian orogeny caused uplifts, strong subsidence, tilting, faulting, and intrusions in the Jeffara and Sabratah basins.

Alpine orogeny. During the Kimmerian tectonic phase which caused the formation of the deep and complex graben of the Sirte basin (Upper Cretaceous-Eocene) the NW-SE Sirte fault system which runs parallel to the Red Sea and East African rifts developed. Post-Eocene to Holocene volcanic activity was recognized and dated by Goudarzi, (1980). He suggested that this volcanic activity was concurrent with movement along deep-seated fractures, perhaps associated with the Alpine orogeny.

Dewey et al., (1989) *(Rosa project, unpublished report)*, have divided the tectonic history of offshore Libya since the late Carboniferous into four general episodes:

- The Hercynian Event (Late Carboniferous late-Permian).
- Late Permian to Middle Triassic.
- Late Triassic to mid Cenomanian.
- Mid-Cenomanian to the present day.

The Sabratah Basin formed during the late stages of the Hercynian event, in response to a phase of lithosphere extension, predetermined by the initial stretching factor and the pre-stretching thicknesses of the crust and lithosphere (Dewey et al 1989). The lithospheric extension model is adequately explained by Mckenzie (1978), Roden and Keen (1980), and Barton et al (1984).

The subsidence of the basin since the Jurassic, is documented by well and seismic data, but there is no available direct information below the mid-Cretaceous interval. Deep seismic reflection and seismic refraction data are required, to investigate the nature of the Crust under the great thickness of low density sediment in the basin, which must be compensated by a rise in the level of the Mantle beneath the basin. The tectonic history of the

Sabratah Basin was derivative from the tectonic history of the Pelagian Basin, since late in the Hercynian event (late Carboniferous). It provides a plate-tectonic framework model for the evolution of the Tethyan Mediterranean system. This model has been illustrated by a series of paleo-plate-tectonic reconstructions by several investigators. The Sabratah Basin was initiated as a pull-apart basin between WNW trending faults of Hercynian origin, developed by left-lateral motion in the late Triassic, and has continued to subside to the present day (Dewey, et al. 1989). The tectonic and structural elements related to earlier tectonic stages (Triassic-Liassic rifting, Jurassic-Cretaceous passive margin drifting) of the Sabratah Basin, are shown in Figure 2.7. The general framework of the dominant tectonic trends of the Sabratah Basin, are described below:

- *The Sirtic tectonic trend*: A NW-SE trend is present in the north-eastern part of the study area. It is related to the third extensional geodynamic evolution phase in the central Mediterranean of Cretaceous age, and to opening of the Sirte basin (Finetti, 1982). It is marked by extensional faults with large throws and graben.

- *The Jeffara tectonic trend*: A W-E trend is present to the south, and characterized by block-faulting towards the north (Jeffara fault system). This system is related to the second extensional phase of Jurassic age.

- *The salt tectonic trend*: An E-W trend is present in the western and central part of the study area . It is related to halokinetic movements of Triassic salt.

Tectonic trends of the study area

The structural trends of the study area will be described in detail in the discussion of the structural domains and salt configuration sketch maps (Figures 4.7 and 4.9); also the two structural time maps of the Base of Oligocene *(Salambo/Cherahil interface)* and the top of Zebbag (Figures 4.4 and 4.5). These trends can be briefly described as the follows:

- A major west-east (WNW-ESE) *salt Tectonic* trend associated with a major fault trend, which extends between the Sabratah and Gabes basins in the west-central

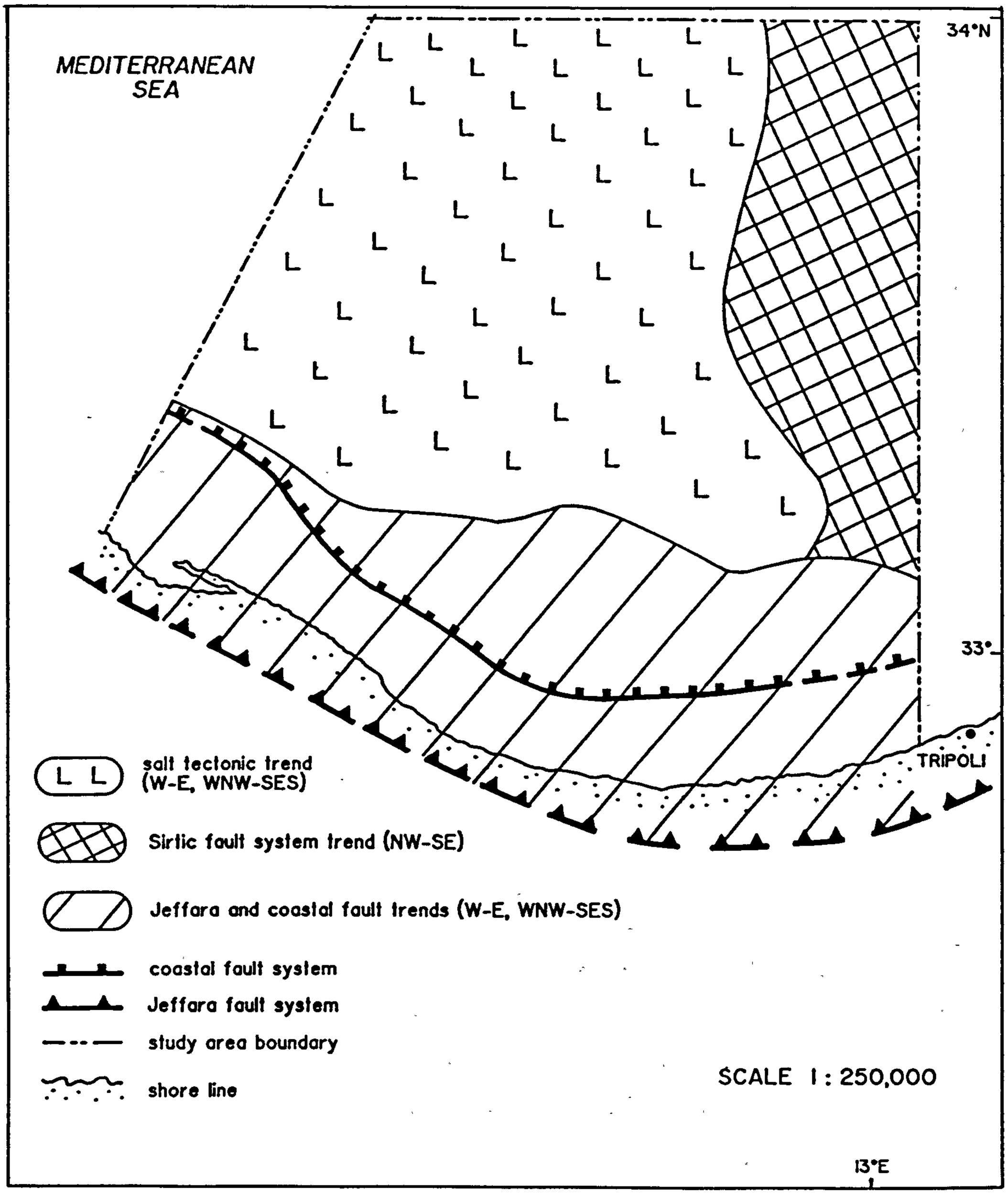

Figure 2.7: Tectonic elements of the Sabratah Basin (study area).

part of the study area, parallel to the Coastal Fault System in the continental shelf area.

- A minor west-east salt tectonic trend in the northern part of the study area.
- The major west-east Coastal Fault System, is located in the southern part of the study area, sub-parallel to the Jeffara fault system (onshore).
- A thick (Upper Cretaceous/Tertiary) sedimentary basin, is located in the eastern part of the study area with a north-west south-east direction, which is represented in the deepest part of the study area (10 km of sediments). Seismically, there is less faulting in this area, with no observed effects of the NW-SE Sirtic fault system (Upper Cretaceous age) in the eastern part of the study area.

2.5 Summary

The geological history of the Central Mediterranean based on the plate tectonics model, has been described by several investigators. The tectonic history of offshore Libya (since the late Carboniferous), has been divided into four general episodes: The Hercynian Event (Late Carboniferous-Late Permian), Late Permian to Middle Triassic, Late Triassic to mid Cenomanian, and Mid-Cenomanian to the present day.

The Sabratah Basin formed during the late stages of the Hercynian event, during upper Triassic to late Jurassic times by normal faulting, in response to a phase of whole lithosphere extension. The basin was initiated as a pull-apart basin between WNW trending faults of Hercynian origin, by left-lateral motion in the late Triassic, and continued to subside to the present day. The seismic and well data indicate the subsidence of the basin since the Jurassic.

The general framework of the dominant tectonic trends of the Sabratah Basin, can be summarized as follows: (i) the NW-SE Sirtic tectonic trend (north-eastern part). This is marked by extensional faults with large throws and graben (Cretaceous age). (ii) the W-E Jeffara tectonic trend (southern part) which is characterized by block-faulting

towards the north (Jeffara fault system of Jurassic age), and (iii) the W-E salt tectonic trend (western and central parts). This is related to halokinetic movements of Triassic salt.

The tectonic trends of the study area are (i) A major west-east (WNW-ESE) salt tectonic trend associated with a major fault trend, which is parallel to the Coastal Fault System of the continental shelf area. (ii) A minor west-east salt tectonic trend in the northern part. (iii) A major west-east coastal fault system, (southern part), sub-parallel to the Jeffara fault system, and (iv) A thick (Upper Cretaceous/Tertiary) sediment trend, (eastern part), which represents the deepest part of the study area.

Generally, the study area is characterized by W-E to WNW-ESE salt tectonic and fault system trends (in the Late Triassic-Early Jurassic and Mid-Upper Cretaceous), which were sub-paralleled to the Jeffara fault system (Permian-Triassic age).

Chapter 3

A review of salt tectonics.

3.1 Introduction

Salt structures in the Sabratah Basin are recognized as masses of salt which have intruded into overlying strata. Little information has been published regarding the diapirs in the basin. A large quantity of information is held by the National Oil Corporation of Libya and their associated companies, but only a small part of this material specifically concerns the origin and development of salt basin diapirs. An understanding of salt tectonics in NW-offshore Libya requires a fairly detailed knowledge of the tectonics of the adjacent regions to the Sabratah Basin, i.e. the Sirte Basin, Jeffara Basin, Central Mediterranean, and Tunisia.

This chapter seeks to provide the reader with an overview of the principles of evaporite basins and the salt tectonics, through the work of many authors. Additionally, the relevance of these principles to the Sabratah Basin, is considered by reference to the seismic interpretation results, as well as subsurface data from wells.

The initiation of the salt movement in the Sabratah Basin began in the Upper Cretaceous (Cenomanian/Turonian times). The salt basin was deformed as a result of halo-tectonics (compressive tectonic forces), and halokinesis (autonomous, isostatic salt

movement). These descriptive terms were proposed first by Trusheim (1960).

3.2 Evaporite Basins

The origin of major evaporite deposits in the geological record has been studied by several investigators, including Murray (1961), Halbouty (1967), Schmalz (1969), Hsu (1972), Kendall (1978b), Taylor (1984) and Sonnenfeld (1985). Jenyon (1986) summarized the principal marine evaporite deposition theories as follows: The *first model* is that of a shallow basin, shallow water situation, with a layer of denser brine sinking to the bottom of the shallow water layer, (Figure 3.1 (a)). Syndepositional subsidence of the basin is

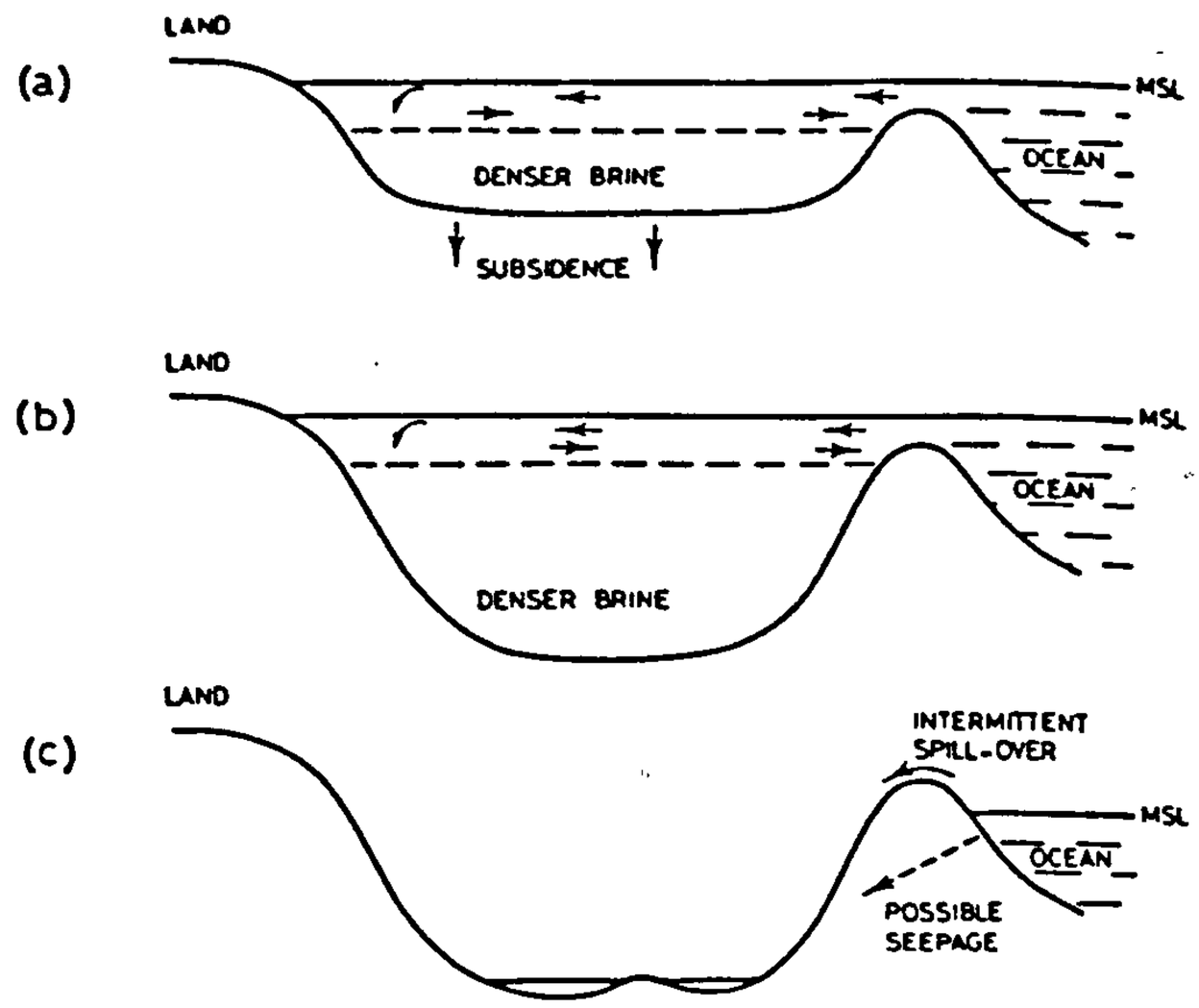

Figure 3.1: The three principal models to explain the origin of major evaporite basins. (a) the shallow basin-shallow water model. (b) the deep basin-deep water model. (c) the deep basin-shallow water model *(after Jenyon, 1986)*.

required in order to allow very thick deposits of evaporites to develop by surface and bottom nucleation of crystals. The *second model* shown in Figure 3.1 (b), is that of a deep basin with deep water as proposed by Schmalz (1969). This model has the advantage over the previous one of requiring no basinal subsidence for the build up of thick deposits.

Schmalz considered that the Salina and Castile evaporites of the USA, and the Zechstein evaporites were formed in this way. He suggests the development of a deep basin-deep water model in several stages (Figure 3.2). The *third model* is that of the deep basin-shallow

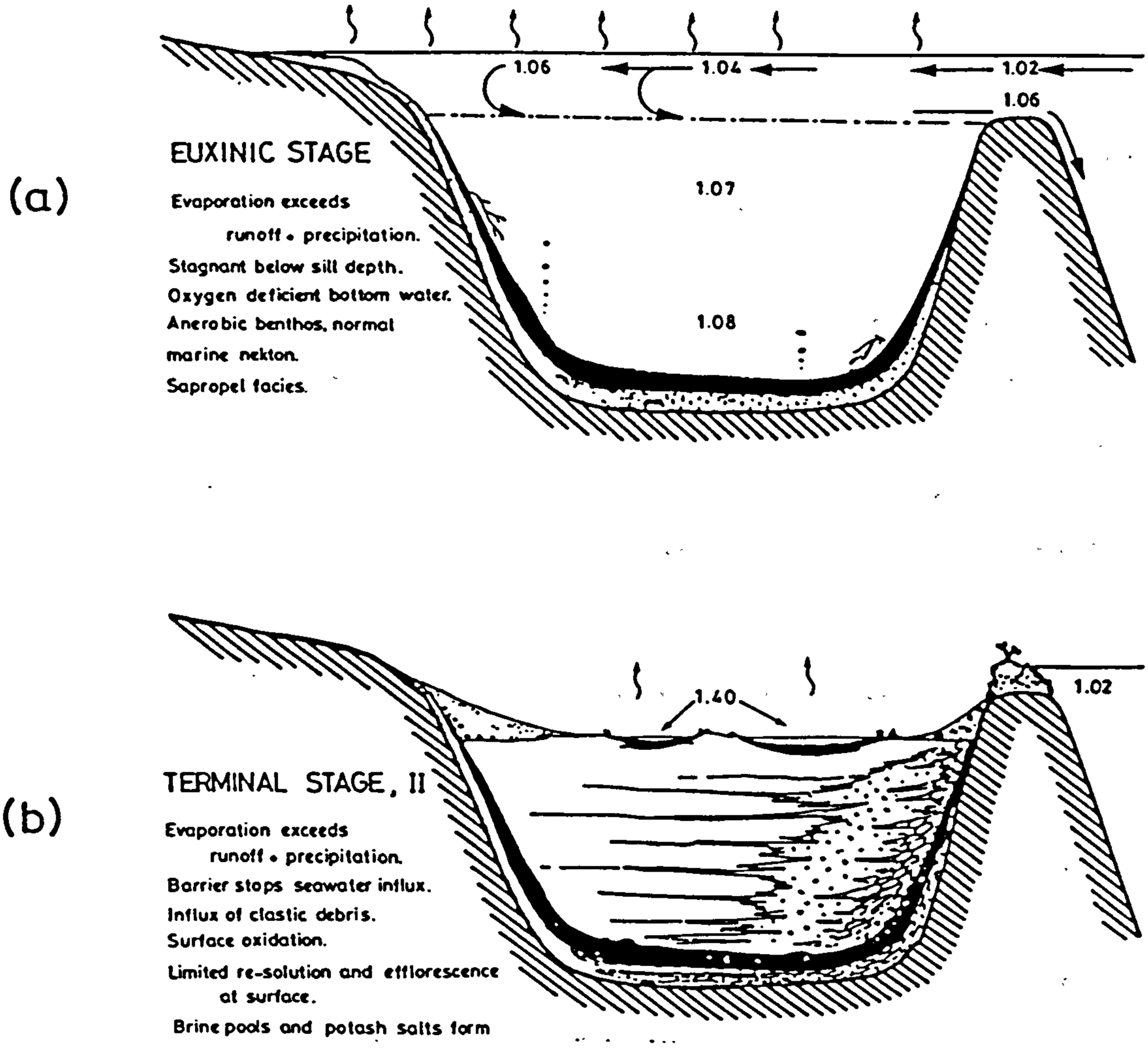

Figure 3.2: Sketches showing the principal of a deep basin-deep water origin for evaporites. (a) an early stage with free water circulation and euxinic sediment deposition, and (b) one of several alternative late stages with the basin filled and desiccating. *(From Schmalz, 1969, after Jenyon 1986).*

water type (or desiccating deep basin). Hsu (1972) advocates this model to explain the origin of the Messinian stage (Miocene) evaporites of the Mediterranean. The model is illustrated in Figure 3.1 (c). In this model the deposition of evaporites is supposed to take place in widespread playas and desert lakes covering the floor of the basin, which receives

intermittent inflows of sea water when the sea level rises above the level of the restricting sill (c.f. Hsu 1972, for more detailed discussion).

Assereto et al (1971), described the stratigraphy of pre-Cenomanian sediments of NW-onshore Libya (Jabel Nafusa), comprising lateral variations of the Upper Abu-Shaybah Formation and the lower part of the Abu-Ghaylan Formation from an onlap marine sequence with basal continental sediments passing into transitional and shallow marine sediments. As shown in the vertical profile, which also reflects lateral facies during deposition, continental alluvial to marine environments coexisted (Figure 3.3). The progression of environments is illustrated by red alluvial mudstones, green lacustrine clays, supratidal flat dolomicrites and evaporites, low supratidal-intertidal stromatolitic dolomites and laminated pelmicrites, lagoonal or coastal flat pelmicrites, and shoal and tidal channel, porous, oolitic and intraclastic calcarenites. He suggests that this sequence shows a similar pattern to those detrital-evaporite-carbonate sequences occuring in the Arabian Gulf (Illing et al 1965) and in Shark Bay Western Australia (Logan et al 1970).

In the Sabratah Basin, drilling has not penetrated very far beyond the very top of the Triassic salt *(only 78 m in well L1-137)*; therefore there is only a limited amount of data on pre-Triassic salt history. Consequently the discussion of the Sabratah evaporites basin given here relates primarily to the above reviews, particularly the model of Assereto et al (1971). Generally, the Sabratah evaporites can be classified as conforming to the shallow basin-shallow water model. The Triassic transgressive phase is represented by exposed marine rocks in the area south of Tripoli. They include the Ras Hamia, Azizia, Abu-Shaybah, and Bir-Al Ghanam Formations.

During the Late Triassic to Early Jurassic time, the basin was affected by extensional faults which related to cratonic rifting, and was characterized by considerable subsidence (Figure 4.18). This subsidence has allowed very thick deposits of evaporites to develop by surface and bottom nucleation of crystals (Schmez 1969).

Many important hydrocarbon accumulations throughout the world are associated with evaporite basins, particularly since hydrocarbon source rocks may be included as

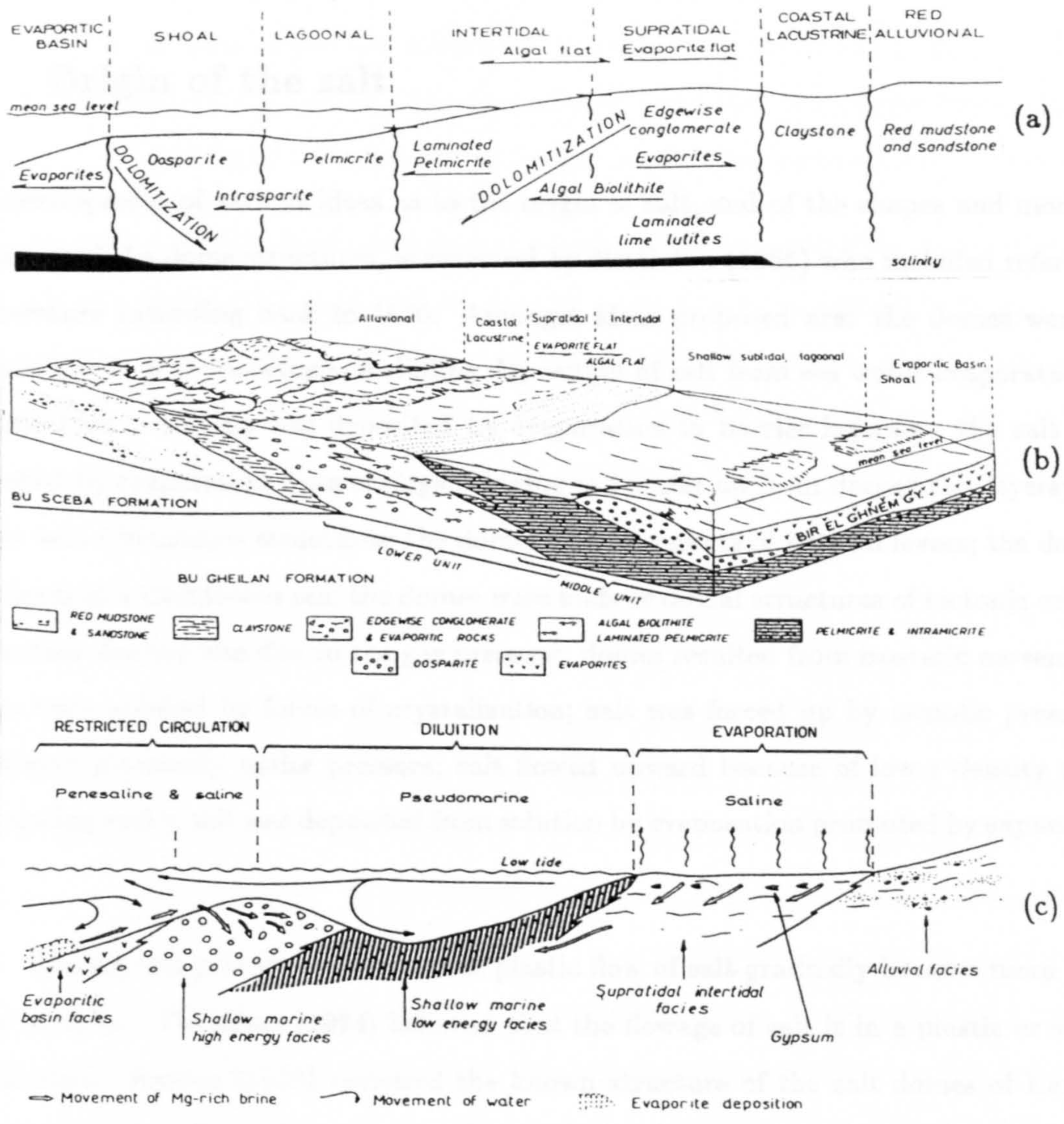

Figure 3.3: (a) Interpreted lateral variation across depositional strike showing the relation between the Bu-Ghaylan Facies. (b) Block diagram of proposed lateral relation between Abu-Shaybah, Abu-Ghaylan and Bir-Al Ghanam Formations, and interpreted depositional environments. (C) Proposed model of dolomitization of Bu-Ghaylan Formation. *(From Assereto et al 1971).*

members of the evaporite cycle.

3.3 Origin of the salt

The development of various ideas as to the origin of salt, and of the shapes and mode of formation of the dome structures, is reviewed by Nettleton (1955) who included reference to literature extending back to 1860. Amongst ideas proposed are: the domes were of volcanic origin with variations, including deposition of salt from sea water evaporated by volcanic heat ; the salt was deposited by evaporation in barrier lagoons ; the salt was deposited by evaporation from springs bringing salt water up from deeper salt layers; the domes were Cretaceous structures; the domes were remnants of natural levees; the domes were lands in a Cretaceous sea; the domes were folds or domal structures of tectonic origin; the surface doming was due to the gas pressure; domes resulted from isostatic movement; domes were uplifted by forces of crystalization; salt was forced up by osmotic pressure; salt flowed plastically under pressure; salt flowed upward because of lower density than surrounding rocks; salt was deposited from solution by evaporation promoted by expanding gas.

During this period, the concept of plastic flow of salt gradually became more generally accepted. DeGolyer (1924) believed that the flowage of salt is in a plastic or semi-plastic state. Barton (1926) reviewed the known structure of the salt domes of Europe and the style of geologic structure; he rejected all the theories of origin except the upward intrusion consequent upon plastic yielding.

Several model experiments were carried out to simulate the form of the salt or the deformation of the surrounding sediments. The earliest experiments were based on the concept that the motivating force of salt flowage was primarily tectonic (the salt was forced up through the surrounding sediments). (Torrey and Fralich, 1926; and Link, 1930).

Barton (1933) developed the ideas of salt dome mechanics. Barton's idea was that the salt mass rises in general contemporaneously with the deposition of sediments around

the salt and along with the sinking of the sedimentary basin as whole. He postulated that the top of the dome may have been at approximately constant absolute level, with the rise of the salt taking place at about the same rate as the sinking of the basin. He pointed out that the salt was of lower density than the sediments and that the motive force resulting from this density difference would increase as the salt column became longer.

Nettleton (1934) constructed several models to illustrate the fluid mechanical concept, with movement depending only on internal forces due to differences in density. The origin of his concept was the association of salt domes with negative gravity anomalies which very clearly and definitely established the fact that the salt is of lower density than the sediments. Nettleton constructed the first models to produce artificial salt domes by purely gravitational forces and without external pressure.

Hubbert (1937), reviewed the mathematical requirements of salt dome laboratory models, and applied scale model theory to several previously published geologic model experiments. Dobrin (1941), applied scale model theory to the fluid salt-dome model with a scale ratio 1 inch to 1 mile. Nettleton (1943) reviewed the geological, geophysical, and experimental evidence accumulated in the ten years since the fluid model of dome formation was first developed. The geological evidence included further detailed knowledge of the structure of salt and sediments and of sand thicknesses, further suggesting the rather general occurrence of rim-synclines or peripheral sinks. The geophysical evidence included some rather striking examples of dips and faults around domes which indicated well-developed rim-synclines. Other workers such as Nettleton and Elkins (1947), and Cloos (1955) have constructed salt-dome models of a wide variety of types.

Parker and McDowell (1955), postulated that domes are initiated by (i) irregularities on the surface of the salt bed. (ii) differences in overburden thickness, and (iii) lateral differences in overburden density.

Trusheim (1960) introduced the term *halokinesis* as a collective term for all processes connected causally with the autonomous, isostatic movement of salt. Halokinetic structures are contrasted with *halotectonic structures*, which result from compressive tec-

tonic forces. He proposed a model for the history of salt structures from their origin throughout all stages of development. Sannemann (1965) introduced a classification of salt-stock families, which typically consist of several salt stocks grouped around the genetically oldest stock *(mother, daughter, and grandchild salt stocks)*. Biot and Ode (1965), considered the mathematics of salt-dome dynamics. Gussow (1968), has advanced the idea that salt does not rise diapirically until it has reached depths of about 7600 m, where it reaches a temperature of about 300° C and becomes plastic. Bishop (1978), described the theory of diapirism to explain the emplacement of piercement diapirs, he formalized some of the mechanical processes necessary to develop a piercement model. A detailed discussion of the internal features of salt diapirs, is given by Braunstein and O'Brien (1968).

Seni and Jackson (1983), note that controversy surrounds the emplacement history of diapirs, and hinges on whether the dominant processes were intrusion, extrusion, alternation between intrusion and extrusion *(down building)*...; or related very closely to the depositional history of the surrounding sediments. Jenyon (1986), discussed the use of seismic data in the interpretation of geological features relating to salt tectonics. Lerche and O'Brien (1987) present a comprehensive treatment of the various aspects of the genesis and development of salt structures.

3.4 The physical properties of the salt rock

Salt rock is formed mainly from the mineral halite, which in its pure form has a hardness of 2.5, and a density of approximately $2.17 g/cm^3$. The apparent salt rock density increases with increasing burial depth, within normal clastic sequences and depends on the lithologies involved. The density of salt rock decreases with increase in temperature. At 300° C salt is plastic and its melting point is 800° C. Salt has a high thermal conductivity.

The remarkable consistency of seismic velocity throughout an evaporitic interval is clearly demonstrated by the acoustic velocity log shown in Figure 3.4. Over the whole interval the log trace gives an interval transit time value of about 50 microsecond per

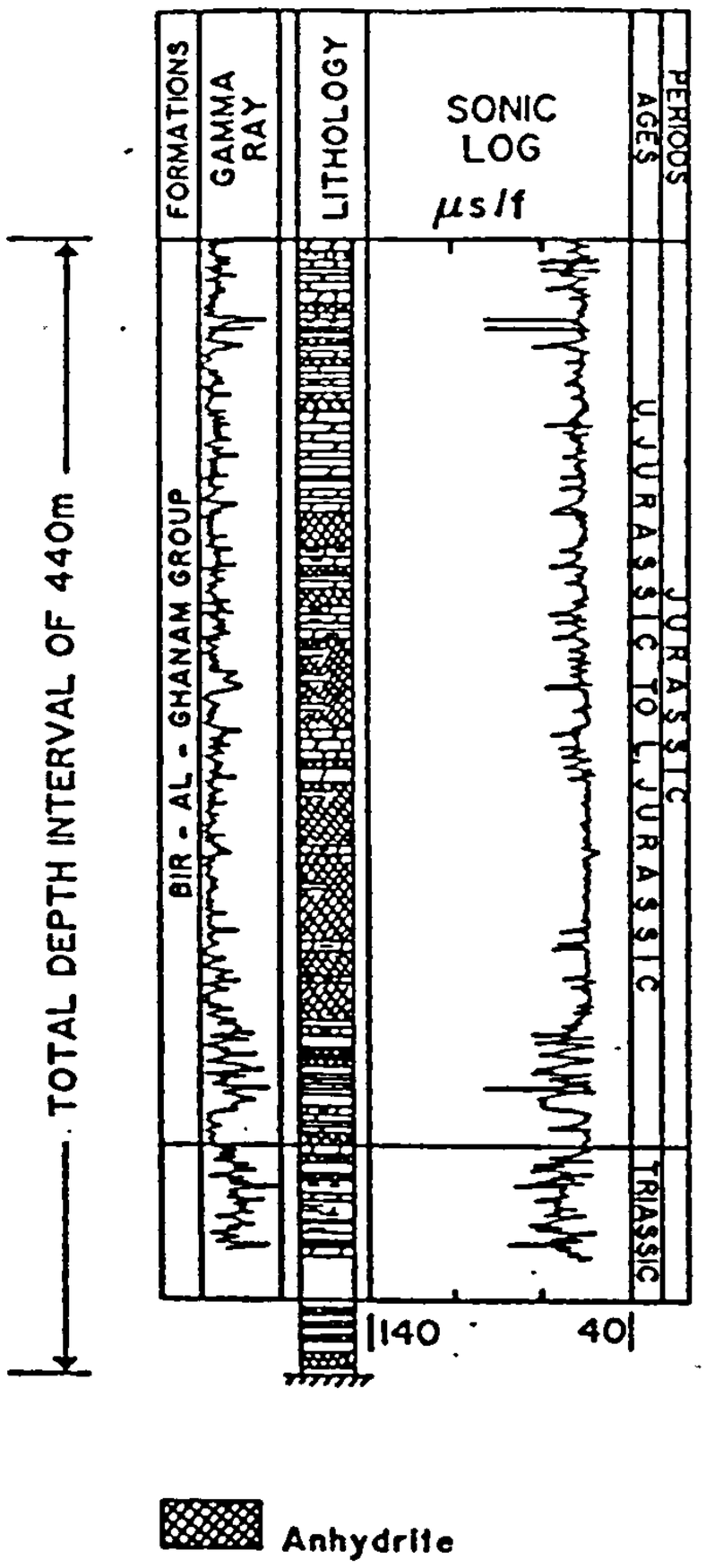

Figure 3.4: Tracing of an acoustic velocity log through an evaporite group interval (well L1-137). Note the remarkably constant sonic transit time of the log trace for the Jurassic Bir Al-Ghanam evaporite group.

foot, equivalent to a seismic interval velocity of 20,000 ft/s (6000 m/sec). For pure halite, the seismic (compressional P-wave) velocity is of the order of 4500 m/s. Impurities are commonly present, however, the most common of these being anhydrite, which in its pure form has a density of about 2.98 g/cm^3 and a velocity of the order of 20,000 ft/s (6000 m/s), as shown in Figure 3.4.

3.5 Distribution of salt evaporite basins and salt diapirs

The distribution of the major salt basins and salt diapirs of all parts of the world has been compiled by Halbouty (1967) and O' Brien (1968), as shown in Figure 3.5. The age and geographic location of the salt deposits are listed in Table 3.1.

As shown in this table, the major salt basins of the world lie in the Mediterranean Sea region, Northwest Germany, the North Sea, West Africa, and Gulf of Mexico (United States and Mexico).

Seismic exploration of the Sabratah Basin has proved that the diapiric phenomena are related to halokinetic movement of the Upper Triassic/Lower Jurassic salt (see Chapter 4).

3.6 The development of the salt structures.

Parker and McDowell (1955) demonstrated that the development of one salt diapir could initiate a whole series of others (Gulf coast basin of U.S.A). Later Trusheim (1960), discussed the development of a single salt stock, as shown in Figure 3.6. As salt becomes mobile under the load of overburden, a salt pillow is formed. At its periphery, the displacement of the salt causes a rim syncline *primary peripheral sink* to develop. As the accumulation of salt continues, it causes the sedimentary cover to break at the top of structure and the diapir rises. At the same time the surrounding strata subside, again causing the formation of a pronounced rim-syncline, the so-called *secondary peripheral sink,* in which sedimentation characteristically is thickest closest to the salt stock. In contrast, sedimentation which is thinnest closest to the salt stock is indicative of the primary rim syncline, the age equivalent of the salt pillow stage.

Sannemann (1965), considered Trusheim' model for a single salt stock development, and extended this to the development of multi-salt stocks. He represented this process in a schematic diagram (see Figure 3.7). In this model the lowermost section corresponds to the

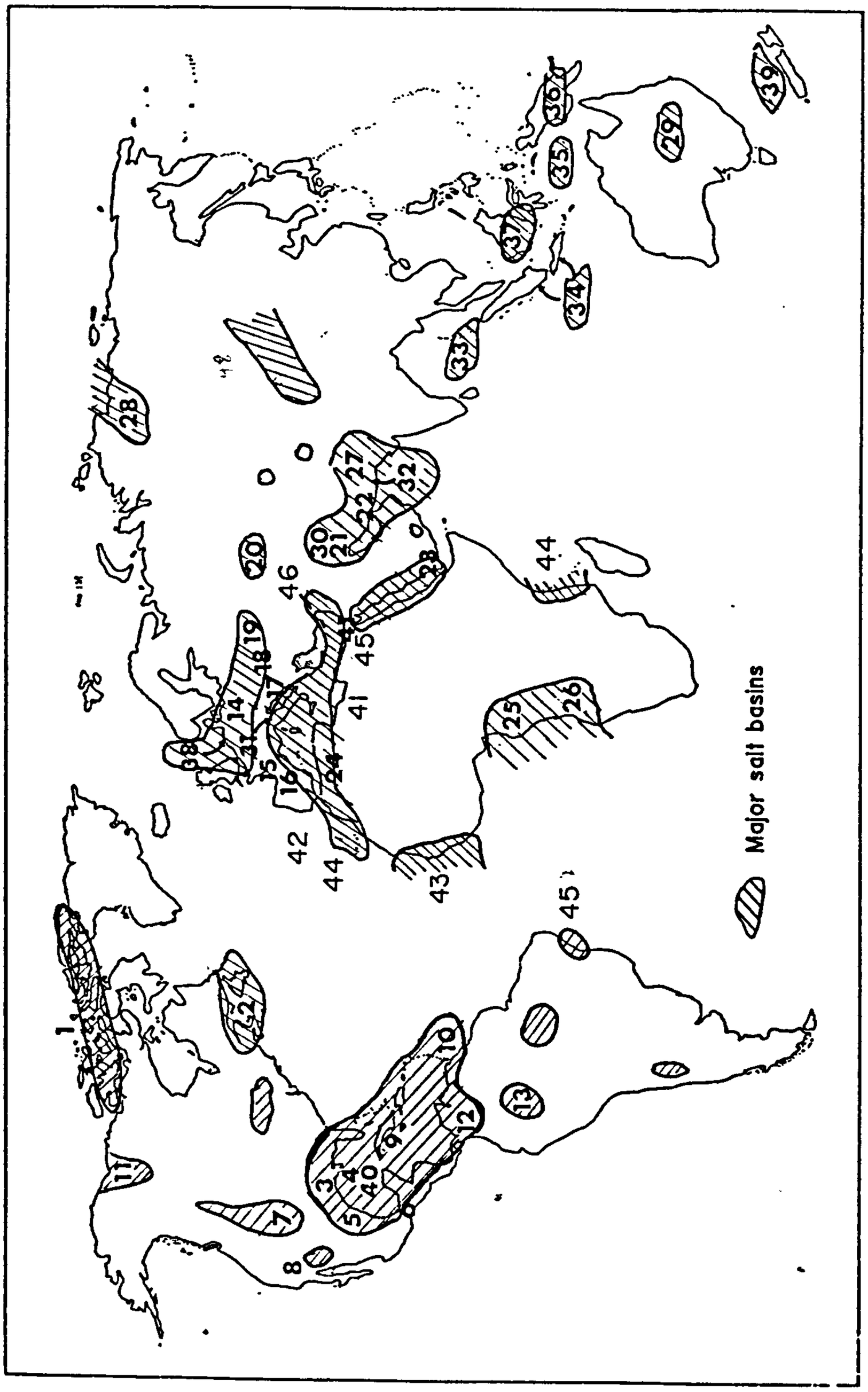

Figure 3.5: Map shows locations of the major salt basins and diapiric structures. Numbers indicate localities listed in Table 3.1 (Modified after Halbouty (1967) and O' Brien (1968)).

Table 3.1: A listing of the geographic locations/ages of the salt deposits of the world (*After O'Brien 1968.*)

Locality (Fig. 2)	*Geologic Feature*	*Geologic Setting*	*Geographic Location*	*Type of Diapir*	*Diapiric Material*	*Age of Diapiric Material*	*Reference*
1	Gypsum domes	Sverdrup basin	Canadian Arctic Islands	Domal	Gypsum	Ordovician	Gould and deMille, this vol.
2	Salt anticlines	Moncton basin	Maritime Provinces, Canada	Anticlinal-domal	Salt	Mississippian	Gussow, 1953
3	Shale domes	U. S. Gulf Coast basin	Onshore and offshore, Gulf of Mexico	Domal	Salt, shale	Jurassic or Triassic; Tertiary	Murray, this vol.
4	Mudlumps	Mouth of Mississippi River	Gulf of Mexico	Domal	"Mud"	Recent	Morgan, this vol.
5	Gypsum anticlines	Coahuila marginal folded belt	Northeastern Mexico	Anticlinal-domal	Gypsum	Jurassic or Triassic	Wall *et al.*, 1967
6	Salt domes	Isthmian Salt basin	Isthmus of Tehuantepec, Mexico	Domal	Salt	Jurassic	Contreras and Castillon, 1960 (trans., this vol.)
7	Salt anticlines	Paradox basin	Western Interior, U. S.	Anticlinal	Salt	Pennsylvanian	Elston *et al.*, 1962
8	Serpentine diapirs	Diablo Range	California	Domal	Serpentine	?	Oakeshott, this vol.
9	Salt domes		Camaguey Province, Cuba	Anticlinal-domal	Salt	Jurassic or Triassic	Meyerhoff and Hatten, this vol.
10	Mud flows, diapiric anticlines		Trinidad	Anticlinal-domal	Mud	Oligocene	Suter, 1954
11	Pingoes, ice diapirs	MacKenzie River delta	Northwest Territories, Canada	Domal	Ice	Pleistocene	Müller, 1959
12	Mud volcanoes		Northwest Colombia; East Venezuela	Domal	Mud	Miocene	Gansser, 1960
13	Salt domes	East flank of Andes	Peru; Colombia	Domal	Salt	Permian	Benavides, 1962
14	Salt domes	Hannover basin	Northern Germany, North Sea	Domal	Salt	Permian	Sannemann, this vol.
15	Salt diapirs	Aquitaine basin	Southern France	Anticlinal	Salt, marl	Triassic	Dupouy-Camet, 1953
16	Diapirs	Pyrenees, Cantabrian, Andalusian Mtns.	Spain	Anticlinal-domal	Salt, marl	Triassic	Loegters and Brinkman, this vol.
17	Serpentine masses	Inner Dinaric Alps	Yugoslavia	Anticlinal	Serpentine	?	Milovanovic and Karamata, 1960
18	Diapirs	Carpathian Mtns.	Rumania	Anticlinal	Salt	Miocene	Voitesti, 1925
19	Salt domes	Dneiper-Donets basin	Southeastern Russia	Domal	Salt	Devonian	Kityk, 1959
20	Salt domes	Emba region	South-Central Russia	Domal	Salt	Permian	Sanders, 1939
21	Diapiric anticlines	Foothills of Zagros Mtns.	Eastern Iran	Anticlinal	Salt, anhydrite	Miocene	O'Brien, 1957
22	Salt plugs	Persian Gulf area	Southern Iran	Domal	Salt	Cambrian	O'Brien, 1957
23	Salt plugs	Yemen, Farson Islands	Southern Red Sea area	Domal	Salt	Triassic	Wade, 1936
24	Domes, anticlines, and laminae	Atlas Mtns.	North Africa	Anticlinal	Marl, gypsum, salt	Triassic	LaCoste, 1934
25	Salt anticlines	Congo basin	Gabon, Africa	Anticlinal	Salt	Cretaceous	Pegand and Reyre, 1959
26	Salt anticlines	Cuanza basin	Angola, Africa	Anticlinal	Salt	Cretaceous	Brognon, Verrier, and Masson, 1959
27	Salt anticlines	Punjab salt range	Pakistan	Anticlinal	Salt	Eocene or Cambrian	Krishnan, 1962
28	Salt dome	Nordvick Bay	North Siberia	Domal	Salt	Silurian	Tolmachoff, 1926
29	Salt diapirs	Amadeus basin	Northern Territory, Australia	Domal	Salt	Precambrian	McNaughton *et al.*, 1962
30	Mud volcanoes	Southeast Caucasus	USSR; Norhern Iran	Domal	Mud	Miocene	Goubkin, 1934
31	Clay diapirs	Po basin	Northern Italy	Anticlinal	Clay	Cretaceous	Weidenmayer, 1950
32	Mud volcanoes	Makran Coast range	Southern Iran; Pakistan	Domal-anticlinal	Mud	Miocene-Oligocene	Snead, 1964
33	Mud volcanoes	Burmese-Andaman trend	Burma; islands in Bay of Bengal	Anticlinal	Clay	Oligocene-Miocene	Chibber, 1934
34	Mud volcanoes		Sumatra; Java	Anticlinal	Clay	Miocene	Höfer, 1909
35	Clay diapirs	Molucca, Banda Sea	Indonesia	Domal	Clay	Miocene	Heim, 1940
36	Mud volcanoes		New Guinea	Anticlinal	Clay	Miocene	Höfer, 1909
37	Mud volcanoes		Borneo	Anticlinal	Clay	Miocene	Höfer, 1909
38	Peat diapirs	Flevoland	Netherlands	Domal	Peat	Recent	Paine, this vol.
39	Mud volcanoes		New Zealand	Anticlinal	Clay	Miocene	Höfer, 1909
40	Diapiric structures	Sigsbee Deep, upper continental slopes	Gulf of Mexico	Domal-anticlinal	Salt (?)	Jurassic (?)	Ewing *et al.*, 1966
41	Clay diapir	East edge of Libyan Desert, Palmyrean chain	Egypt; Syria	Anticlinal	Clay, gypsum, and anhydrite, with clay and marl	Jurassic	Omara, 1964

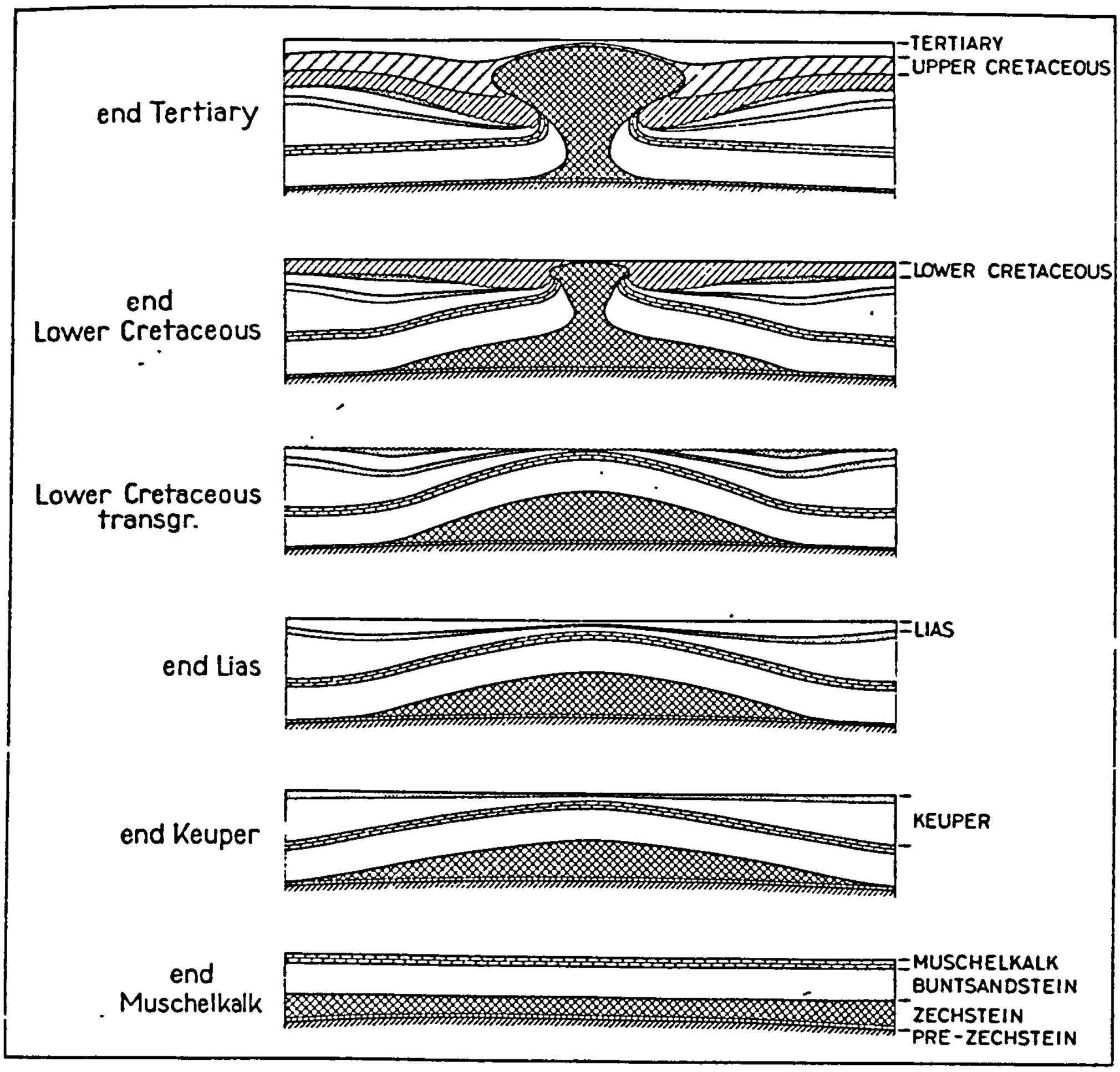

Figure 3.6: Diagrammatic development of single salt stock, in the Northwest Zechstein Basin, West Germany. (*after Trusheim, 1960*).

final stage of Sannemann model shown in Figure 3.6. The sedimentary cover which dips toward the salt stock produces a strong differential pressure causing centrifugal migration of the salt away from the salt stock. At a certain distance, new salt accumulation and salt-pillow formation take place. The new salt pillow in turn is transformed into a diapir (middle section of Figure 3.7), thereby creating a situation favoring the formation of another salt pillow. This process continues like waves travelling centrifugally away from the central salt stock, the so-called *mother salt stock*. Around the mother salt stock are grouped younger salt stocks. Ideally in the form of rings, the age of which decreases with distance from the center. A genetic unit of this kind is termed *a salt stock family*.

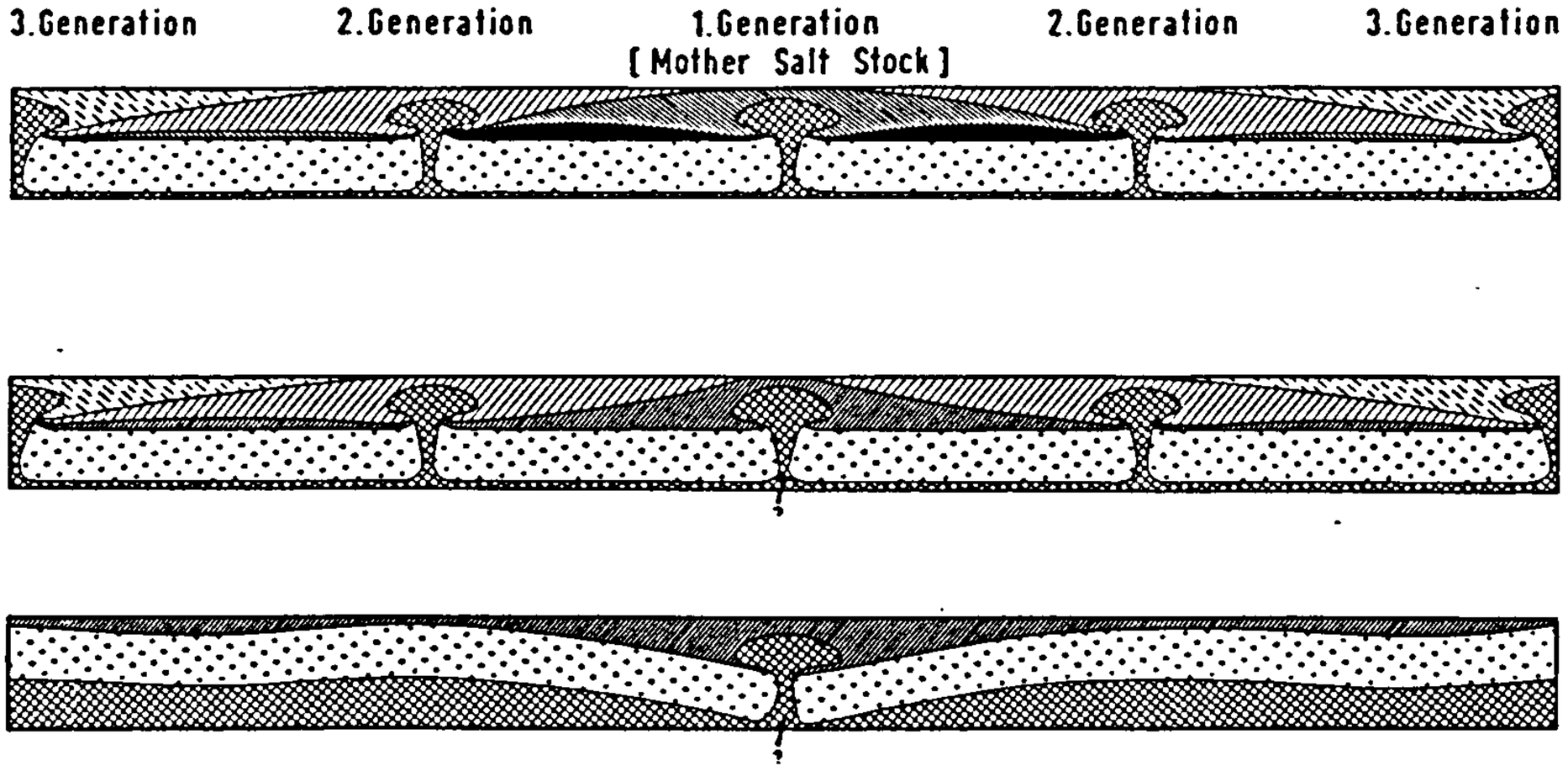

Figure 3.7: Schematic diagram of development of a salt stock family. ***Sannemann (1965).***

3.7 Summary

The Mediterranean includes one of the world' s largest salt structure provinces. Upper Triassic to Lower Jurassic evaporites were deposited in the Sabratah Basin and the adjoining areas of Tunisia and Algeria. They are characterized by diapiric phenomena. The initiation of the salt movement is believed to have been in the Upper Cretaceous (Cenomanian/Turonian).

The origin of major evaporite deposits has been modelled by several investigators, the Sabratah evaporite basin being classified as a shallow basin-shallow water type.

In the Sabratah Basin, drilling has not penetrated very far beyond the very top of the Triassic salt; therefore there is only a limited amount of data on pre-Triassic salt history. The Triassic transgressive phase is represented by exposed marine rocks in the area south of Tripoli. They include the Ras Hamia, Azizia, Abu-Shaybah, and Bir-Al Ghanam Formations.

Chapter 4

Seismic Investigation and interpretation

4.1 Introduction

In 1968, the Libyan offshore area was opened to oil exploration and at the same time, the National Oil Corporation of Libya (NOC) and Elf Aquitaine group were granted the offshore Zuwarah concession (Concession 137) which forms the western and central part of the study area of this thesis. In 1974, the Agip Oil Company was granted (Concession NC-41) the eastern part of the study area. In 1983, the NOC initiated the *Rosa project*, which was undertaken by the Sirte Oil Company. The Rosa project covered most of the offshore Libyan area including the present study area. It involved seismic, gravity, and magnetic surveying.

The seismic reflection data used for the present study comprises parts of various surveys conducted between 1968 and 1985 by the different companies mentioned above. These data were shot with different sources and parameters and different gridded networks over the entire study area, depending on the exploration company. The shot point location map of the various seismic lines is shown in Figure 4.1. The aims of the seismic

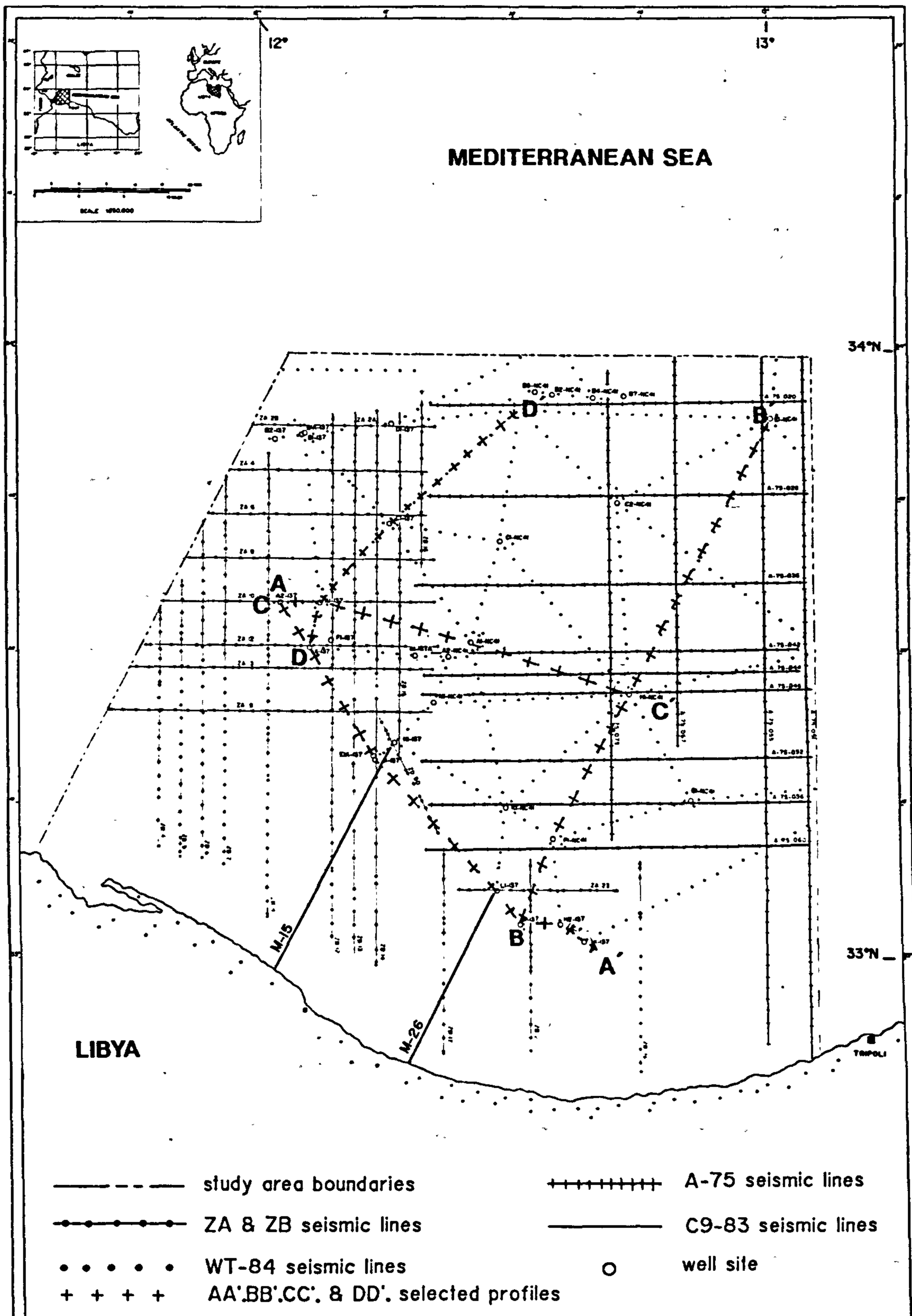

Figure 4.1: Shot point location map

reflection study embodied in this thesis are: Firstly, to investigate the extent of the salt structure configuration and particularly its influence on sediment sequence development and petroleum accumulation in the study area; secondly, to produce structural contour maps of some selected geological horizons; and finally, to give a regional picture of the tectonics and structure of the study area, locating the salt domes, folds and faults,

4.2 Seismic sources and types of data

The National Oil Corporation of Libya (NOC) has provided the essential seismic and well log data for this study as shown in the shot point location map of Figure 4.1. The geophysical data available include:

A- Seismic data:

1. *Rosa project seismic lines (WT-84):*

   A total of 1000 kms of seismic lines include:

   - Two-way time unmigrated seismic sections.
   - Two-way time migrated seismic sections.
   - Depth seismic sections.

2. *Elf-Aquitaine seismic lines (ZA, ZB):*

   A total of 1100 kms of seismic lines include:

   - Two-way time unmigrated seismic sections.

3. *Agip Company seismic lines (A75):*

   - A total of 800 kms of two-way time unmigrated seismic sections.

4. *Mobil Company lines (C9-83):*

   - Two migrated seismic sections crossing the continental shelf (and tied with K1 and L1-137).

B- Well logs:

Well log data were available from a total of 20 boreholes drilled in the study area. These logs include:

- **Composite logs.**
- **Formation density logs.**
- **Formation velocity logs.**

4.3 Data acquisition

a. Recording parameters:

Table 4.1 summarises some of the source types and recording parameters which were used for these surveys.

Parameters	*ZA & ZB*	*A-75*	*Wt-84*
Shooting date	1968	1975	1984
Energy Source	Flexotir Vaporchoc	Air Gun (930 cu in)	Air Gun (1200 cu in)
Cable length	2300–2400 m	2400 m	3200 m
Fold of coverage	24 & 48	48	60
Group interval	50 m	50 m	13.33 m
Shot Pt.interval	25 m	200 m	26.67
Sample rate	2 ms	4 ms	2 ms

Table 4.1: Seismic source and recording parameters used in the surveys.

b. Processing parameters:

Routine processing has been done for the exploration companies, this incorporates demultiplexing, deconvolution, velocity analysis, and migration for some selected lines.

4.4 Data quality

As several seismic surveys were carried out by different companies over a period of time (see section 4.1), the quality of the seismic data varies. It can be described as follows:

WT-84 data quality

The Rosa project seismic lines (WT-84) represented the highest quality and resolution of any of the seismic data in the study area. It provides both migrated and depth sections. The grid used was designed to tie in most of the control wells drilled in the study area. In general, the quality of data for horizons below the Mid-Cretaceous (i.e below the Zebbag Formation) is poor. Several lines have been selected and converted to migrated time and depth sections. Examples of two seismic sections showing the difference of the quality between unmigrated and migrated sections are given in Figures 4.2 and 4.3. Figure 4.2, the unmigrated time section, shows the anticline (crest T) of the deformed overburden sequence, (S) is an adjacent syncline. (A), (B) and (C) are apparent antiformal structures created by the partial diffraction pattern. The complex nature of reflection events associated with a salt diapir (D) makes the boundaries and the shape of the diapir difficult to estimate. On the other hand, in Figure 4.3 which represents a migrated time version of the section example of Figure 4.2, the artifacts (A), (B) and (C) are removed by the migration process. The syncline (S) and the overburden flank up to (T) are clarified together with a better estimated position for boundaries of the diapiric salt structure.

ZA and ZB data quality

These lines are located at the western and central part (Salt Domain area, see section 4.8.2.1) of the study area, as shown in Figure 4.1. The data were shot in 1968–1970, when 600% or 1200% stacks were used. The quality, as reported in the R.G.n.56 Aquitaine Company unpublished report, was generally poor. In the 1976–1979 period, the improvement by use of 4800% stack enhanced the data quality. The available seismic data of ZA

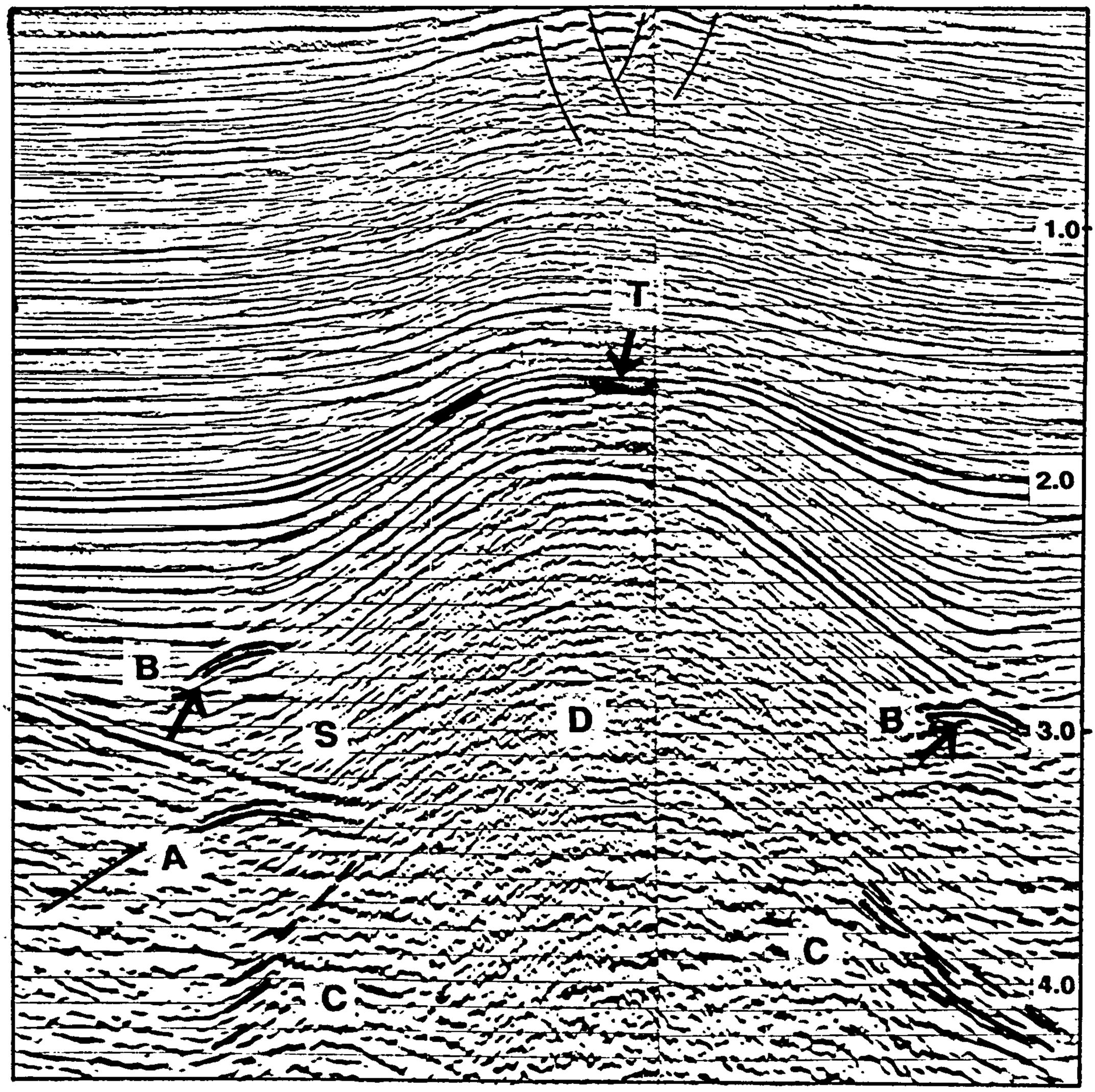

Figure 4.2: An example of an unmigrated seismic section located on profile AA'. It indicates the complex nature of reflection events associated with a salt diapir (D). (A), (B) and (C) are partial diffraction patterns, (T) marks the location of the crest of the deformed overburden anticline and (S) is an adjacent syncline (NOC section).

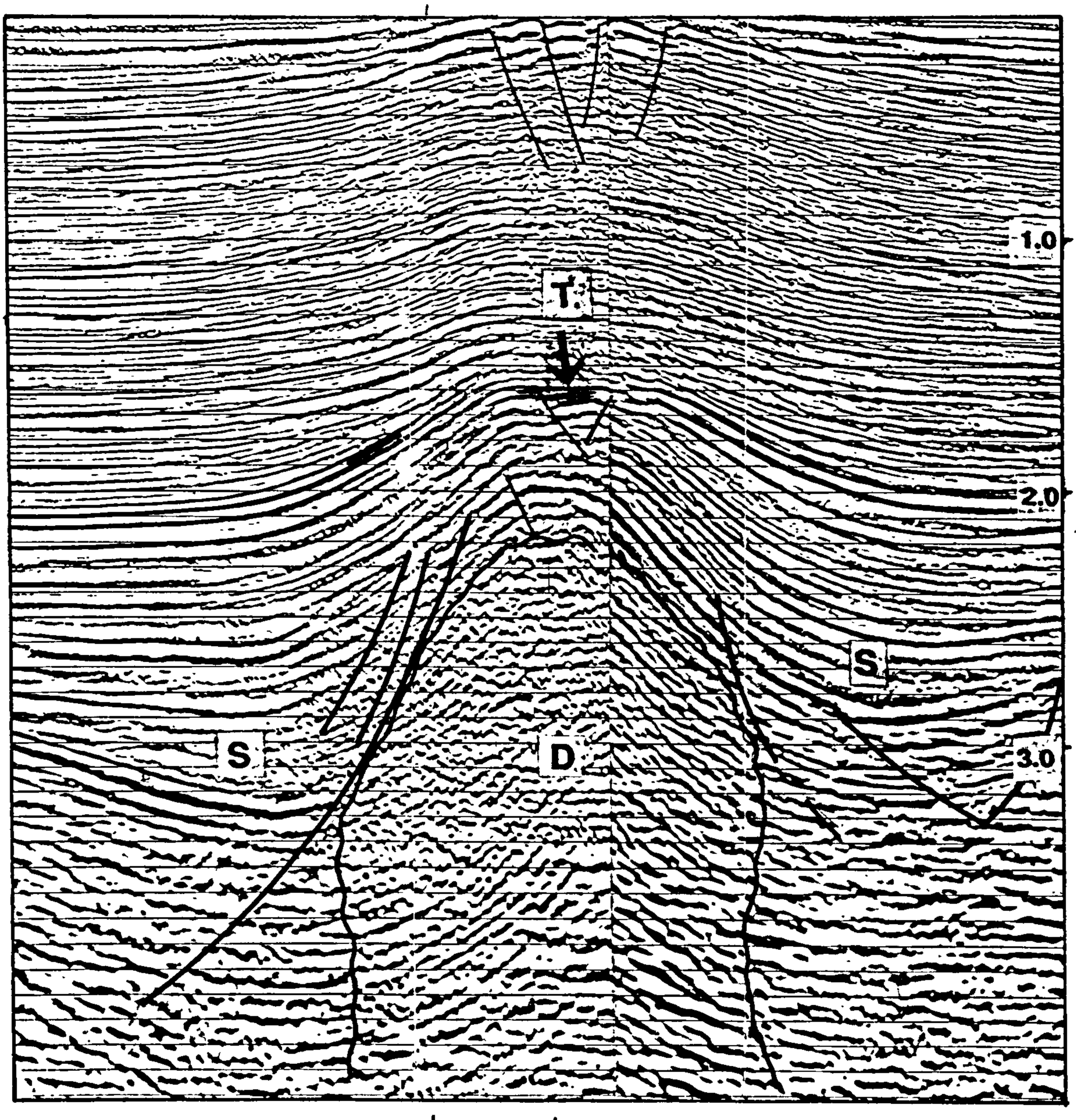

Figure 4.3: An example of a migrated version of the section example of Figure 4.2, with estimated boundaries of the diapiric salt and faults. (NOC section).

and ZB are unmigrated sections. In general, the quality of unmigrated seismic data is poor, particularly in the western part (Salt Domain, see section 4.8.2.1). In the southern part (Continental Shelf Domain see section 4.8.2.2) of the study area, the poor quality is related also to complex faulting. It is impossible to distinguish seismic events below the Zebbag Formation (Mid-Cretaceous).

In the Salt Tectonics Domain, the stacking routine in a standard seismic processing route cannot deal with reflection events which are very steeply dipping. Where a salt feature with vertical, or very steep flanks, has steeply dipping or even overturned overburden units truncating against it, none of the very steep events will be seen in the final time section display. Structures which dip at more than 45° could not be recovered by the correction routine effected prior to the stacking process, and so would not appear on the seismic section (Jenyon, 1986). The migration process is essential to help resolve these ambiguities.

A-75 data quality

A-75 lines are situated in the east central part of the study area. The data comprise 48 fold unmigrated sections of fair to good quality. In the eastern part of the study area the Zebbag Formation was out of range of the seismic response, due the thick sediment sequences (6 km) overlying it. The quality of seismic data below the Abiod Formation was, in general, poor. Therefore, the tentative interpretation of units below this horizon should be treated with caution for A-75 lines.

4.5 Horizon picking

In seismic interpretation, the resolution of the sediment sequences are very important for exploration, especially in the region of salt tectonic structures and particularly at the sediment flanks of the salt structures. Therefore, during this study, ten horizons were commonly picked, between the top of the salt structure (Base of Oligocene) and the

Age	*Tunisian names*	*Offshore Libyan names*
L.Miocene	Salambo or Ketatna	Dirbal or Ras Abd-jalil
Oligocene	Base of Oligocene	Base of Oligocene
U.Eocene	Cherahil (B) Fm.	Samdun Fm.
M.Eocene	Reineche Mbr.	Dahman Mbr.
M.Eocene	Cherahil (A) Fm.	Harsha Fm.
L-M.Eoc.to Paleo	Metlaoui Group	Farwah Fm.
Pa leo-U.Cretace.	El-Haria Group	Al-Jurf Fm.
U.Cretaceous	Abiod Fm.	Bu Isa Fm.
U.Cretaceous	Aleg Fm.	Jamil Fm.
U.Cretaceous	Douleb Fm.	Makhbaz Fm.
U.Cretaceous	Zebbag Fm.	Alalgah Fm.

Table 4.2: The formational names of seismic reflectors which have been interpreted in the study area, and their equivalent names in adjacent Tunisian area.

lowermost horizon which could be readily distinguished (i.e top of the Zebbag Formation), as shown in Table 4.2.

In subsequent analysis of these eleven horizons, only two seismic reflecting horizons have been mapped: Firstly, the base of the Oligocene (the Salambo/Cherahil interface), and Secondly, the top of the Zebbag Formation (Alalgah Fm.) (Upper Cretaceous).

4.6 Seismic tie lines

As the study area includes different sources of seismic data which were shot and processed by various companies, therefore, there is a possibility of mis-ties. This has been considered and avoided by use of synthetic seismograms (available for use in this study by authority of NOC) and well tie control with depth seismic sections.

4.6.1 Closed loops

WT-84 lines **represent good quality data. The grid was designed to tie in all the wells. A series of closed loops between the wells and seismic lines has been achieved, and no mis-tie has been observed at the seismic line intersections. The *ZA,ZB lines* are close together; they represent different scale sections which were tied with the other sections through well control points. For the *A-75 lines*, most of the loops of the picked horizons have been closed, except for deeper horizons (below the Abiod Formation) in the eastern part of the study area (the Thick Sediment Domain).**

4.6.2 Seismic ties with borehole data

The data in the seismic sections can be tied directly with the borehole data through the use of synthetic seismograms. Borehole information, such as composite log, formation density log, compensated sonic log, and a few synthetic seismograms, is available from 20 wells and assisted in the identification of seismic reflectors in the seismic lines. The seismic lines have been tied to each well control point by using the available synthetic seismogram data. In the absence of a synthetic seismogram, the seismic depth sections have been used to determine the depth, and confirm it with the corresponding actual depth in the drilled wells.

4.7 Velocity analysis and depth conversion

In this particular study, no new velocity analysis has been done. The interpretation of the seismic velocity data was studied in detail when WT-84 lines were converted to depth (Rosa project report, 1989). These depth sections have been used to confirm the depths of the formations on the seismic sections and boreholes. The available sonic logs (formation velocity logs), together with formation density logs constitute the essential physical parameters to define the acoustic impedance of the rock units and are therefore the fundamental factors in the construction of the synthetic seismograms.

4.8 Seismic interpretation

4.8.1 Introduction

One of the seismic interpretation objectives of this thesis was to produce structural maps (isochrons) for selected geological horizons, and to describe the geological features and salt tectonics of the study area. These were then used for integrating with other geophysical data (gravity and magnetic maps). After the selected horizons ((A) Base of Oligocene and (B) Zebbag Formations) had been identified on the cross lines, and treated all the way around the closed loops, all the sources of mis-closure were examined. The horizons were continued on the sections. The two way time structural maps of horizons A and B were then constructed, as described below.

4.8.2 Regional structural maps

The two structural maps of the Salambo/Cherahil interface and top-Zebbag Formation are shown in Figures 4.4 and 4.5. From the interpretation of these maps, the study area was divided into three areal domains: *the Salt Domain*, *the Continental Shelf Domain* and the *Thick Sediment Domain*, as shown in Figure 4.6. The most effective way of discussing the use of seismic data in the interpretation of geological features is to present examples of the seismic response to various geological structures. The three domains are described individually below, using appropriate examples.

4.8.2.1 The Salt Domain (salt basin)

This area is located in the western part of the study area, near the Tunisian offshore border, as shown in Figure 4.6. The area is characterized by the presence of strong halokinetic salt structures. The action of the salt is particularly marked in the western part, where the piercements continue up to the Miocene. Several salt phenomena have been found in the Sabratah Basin of NW-Offshore Libya. Seismic Profile AA′ across the

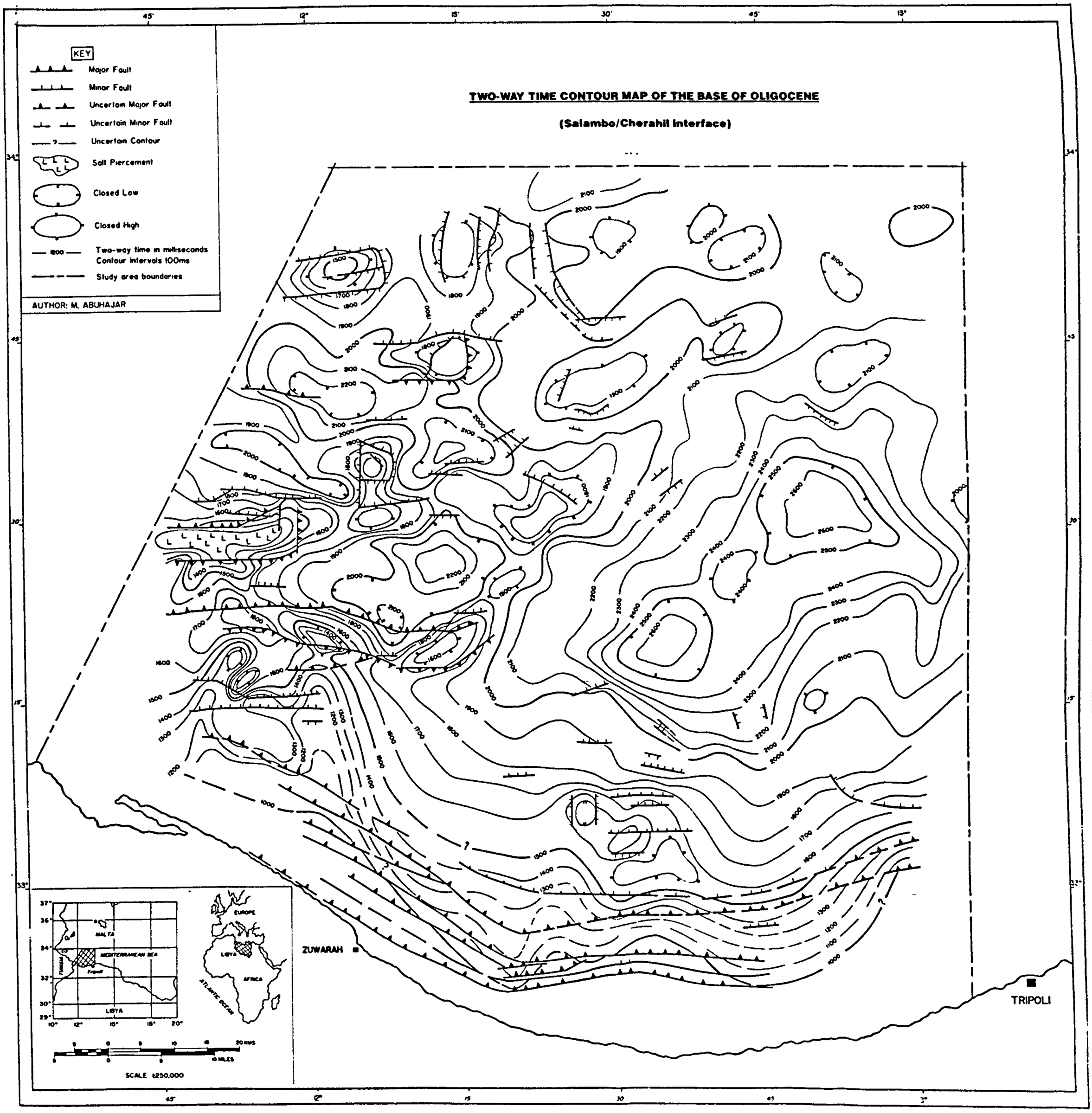

Figure 4.4: Two-way time structural map of the Salambo/Cherahil Formation interface. (Horizon (A), base Oligocene). *This is reduced copy of the full scale map available in Appendix 2.*

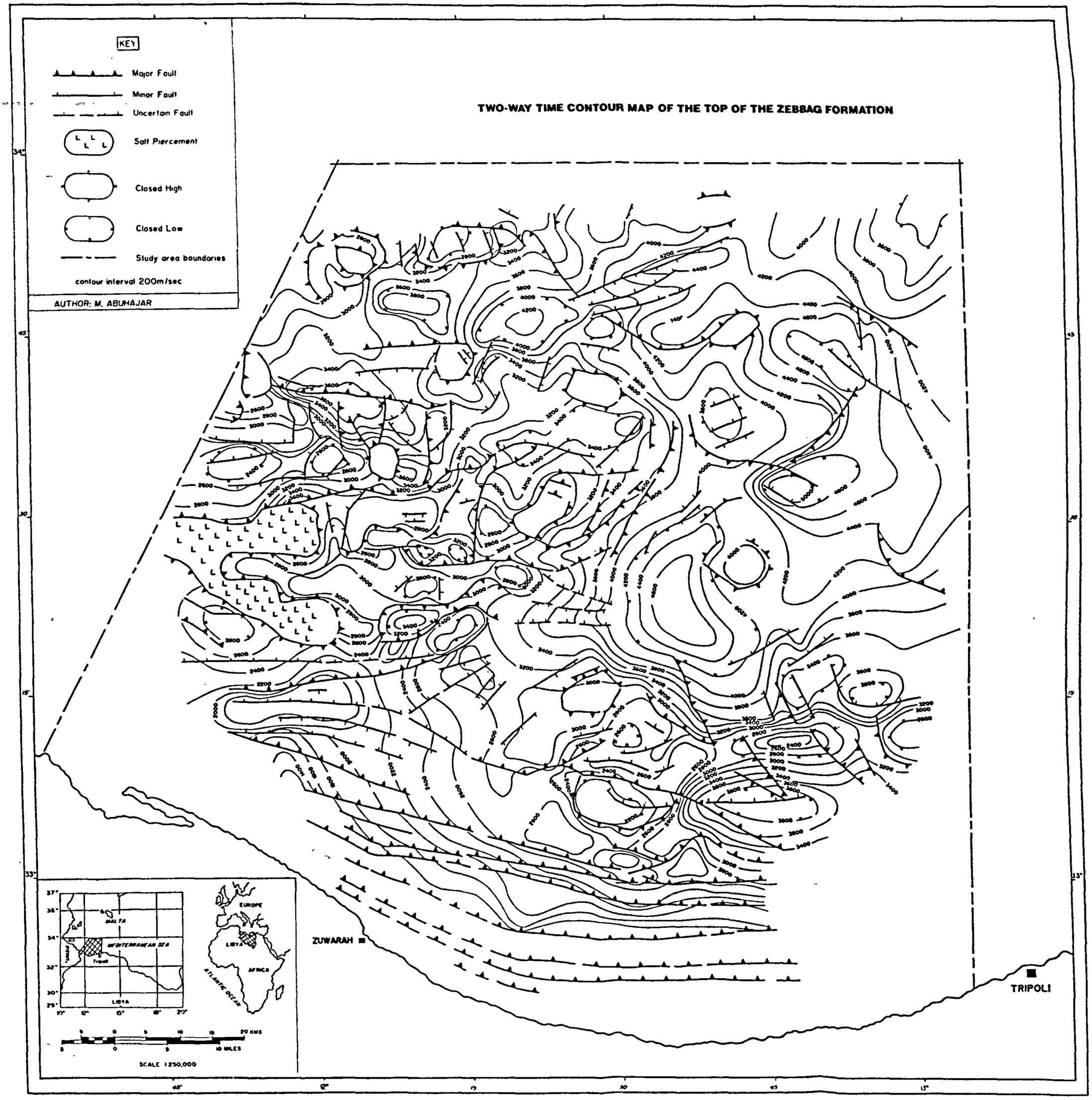

Figure 4.5: Two-way time structural map of the top the Zebbag Formation. (Horizon (B), Upper Cretaceous). *This is reduced copy of the full scale map available in Appendix 2.*

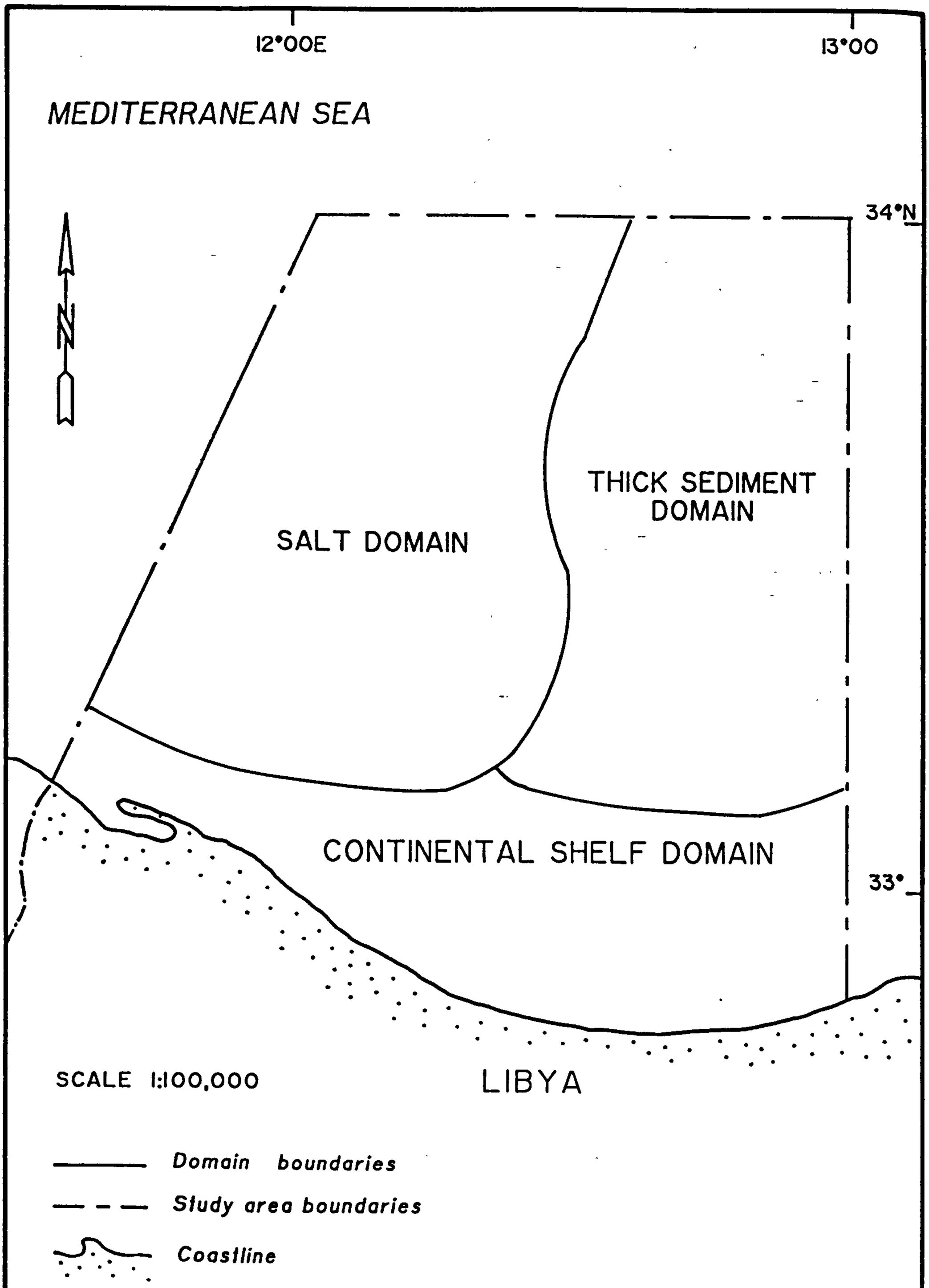

Figure 4.6: Sketch map of the structural domains of the study area.

salt domain in a NW-SE direction, is provided as a good example for the salt structure in this part of the study area (Figure 4.7). The reflection data along this profile, indicate several key features in the salt domain area, related to salt tectonics, are seen in the northern and central parts ((N) and (C)) of the AA′ profile, which are represented by the salt diapirs (D1), (D2), and (D3). A major normal fault system (F), is associated with the salt diapir (D1), showing increased throw with depth. These faults were active in Upper Cretaceous times (the same age as Triassic salt movements). The distribution of the selected horizons (base of Oligocene and top of Zebbag Formations), which have excellent reflection signatures delineate the salt structures and provided a good picture of the salt deformation in the salt domain area. Profile AA′ provides strong evidence that the Triassic salt mobility action was starting in the upper Cretaceous (below the Zebbag Formation). This is seen in the strong reflector of the Zebbag Formation (cap rocks C) overburden crest, and the continuity of the same reflector in the lower part of the salt diapir flanks, which are overlain by thick sediment sequences (rim-syncline S). The boreholes A2, I1, E1a, and J1-137, have been used as control points to tie in the seismic reflectors and to indicate the seismic sequences, their velocities, and densities controls, as shown in the sketched section of profile AA′ in Figure 4.8. Asymmetrical development of the salt diapir (D1), is associated with fault activity. Asymmetrical development of the salt diapir (D2), is associated with folds, a less faulted zone, and clear seismic sequences at the rim-syncline (S) on the left hand side of the structure. None of the salt diapir tops have reached the sea floor in profile AA′ . The salt diapirs have approximate widths, of 5 km, 4 km, and 3 km, respectively for D1, D2, and D3 on profile AA′. They occur at about 3 km below the sea floor, and have average heights of 3 km. The southern part (S) of the AA′ profile demonstrates the beginning of the uplifted structure associated with faulting.

Consideration of the seismic interpretation leads to development of the the configuration map (Figure 4.9) which has been derived to show the salt distribution in the study area categorized into three types, as described below:

- Salt walls.

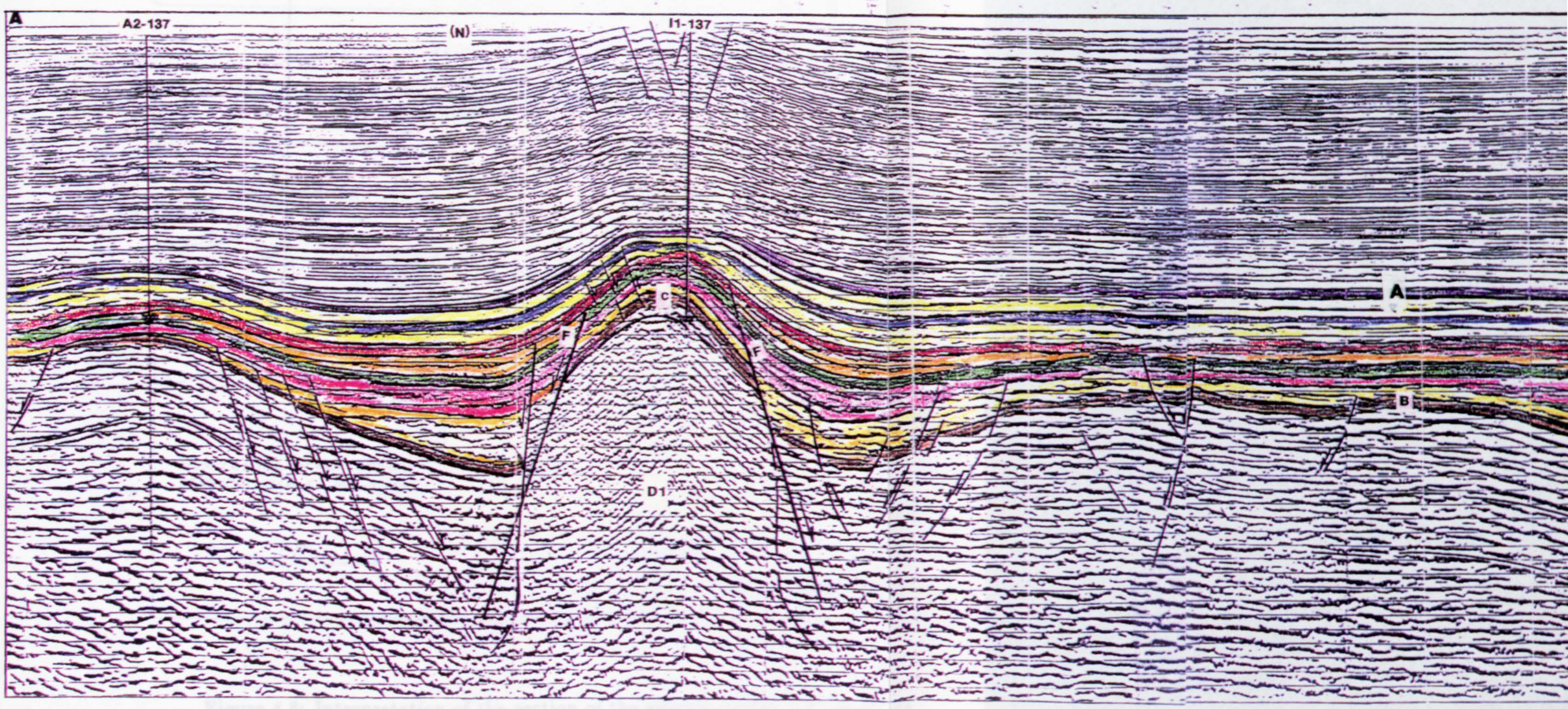

Figure 4.7: Seismic profile AA′ across the salt domain in a NW-SE direction, indicates the salt phenomena which are represented by the salt diapirs (D1), (D2) and (D3).

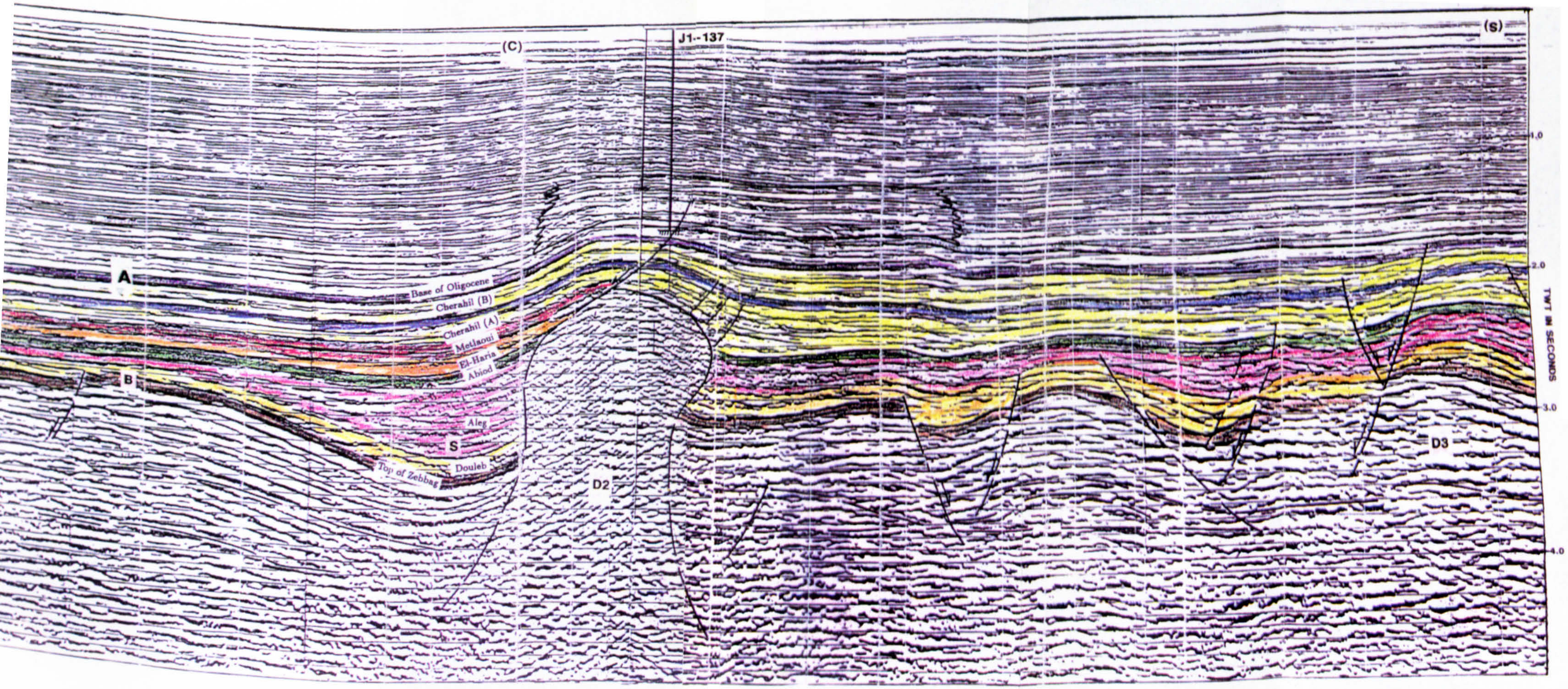
(C)
J1--137
(S)
A
B
S
Base of Oligocene
Cherahil (B)
Cherahil (A)
Metlaoui
El-Haria
Abiod
Aleg
Douleb
Top of Zebbag
D2
D3
1.0
2.0
3.0
4.0
TWT IN SECONDS

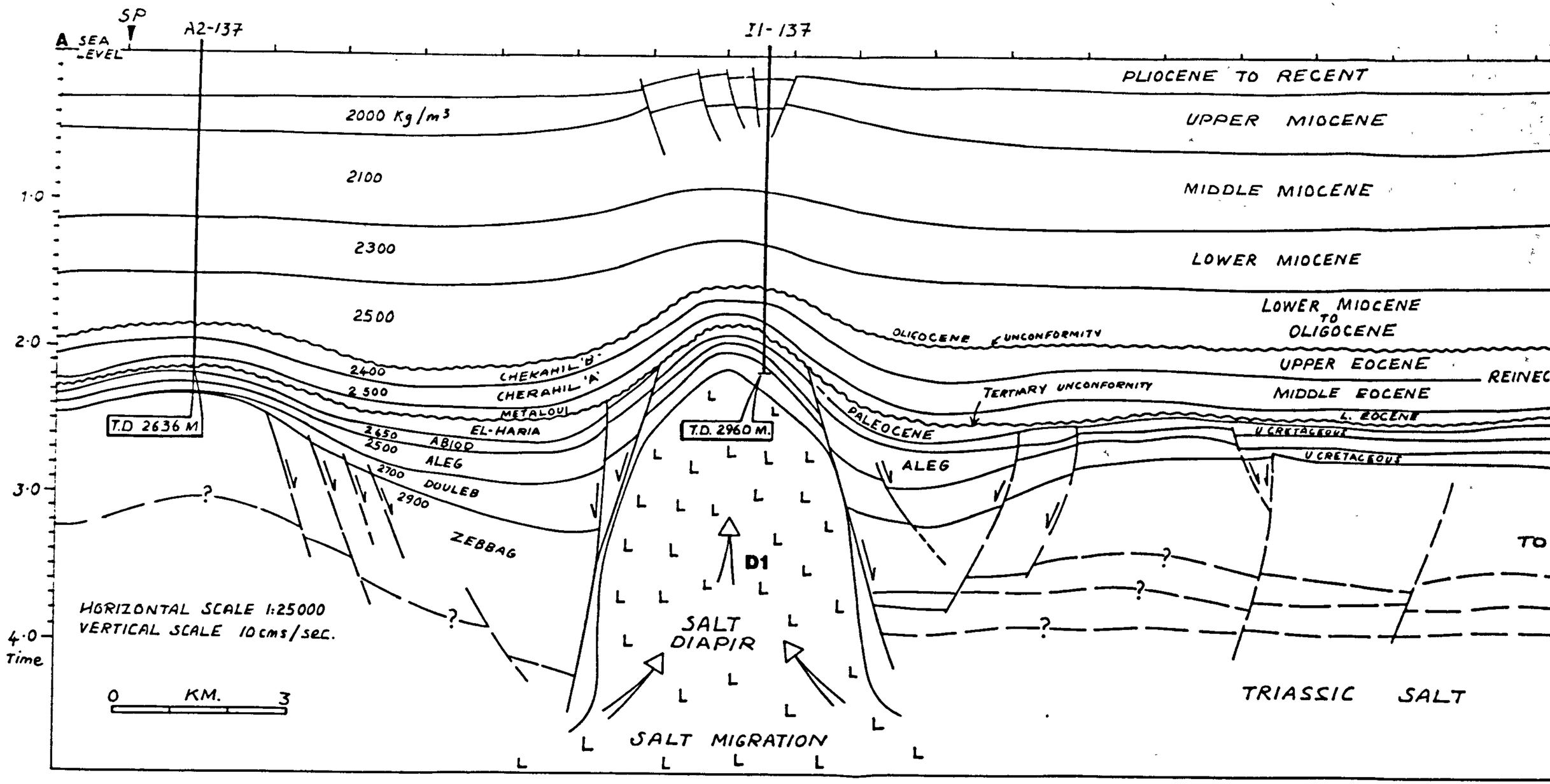

Figure 4.8: Interpretation of the section of the seismic profile AA′ shown in Figure 4.8.

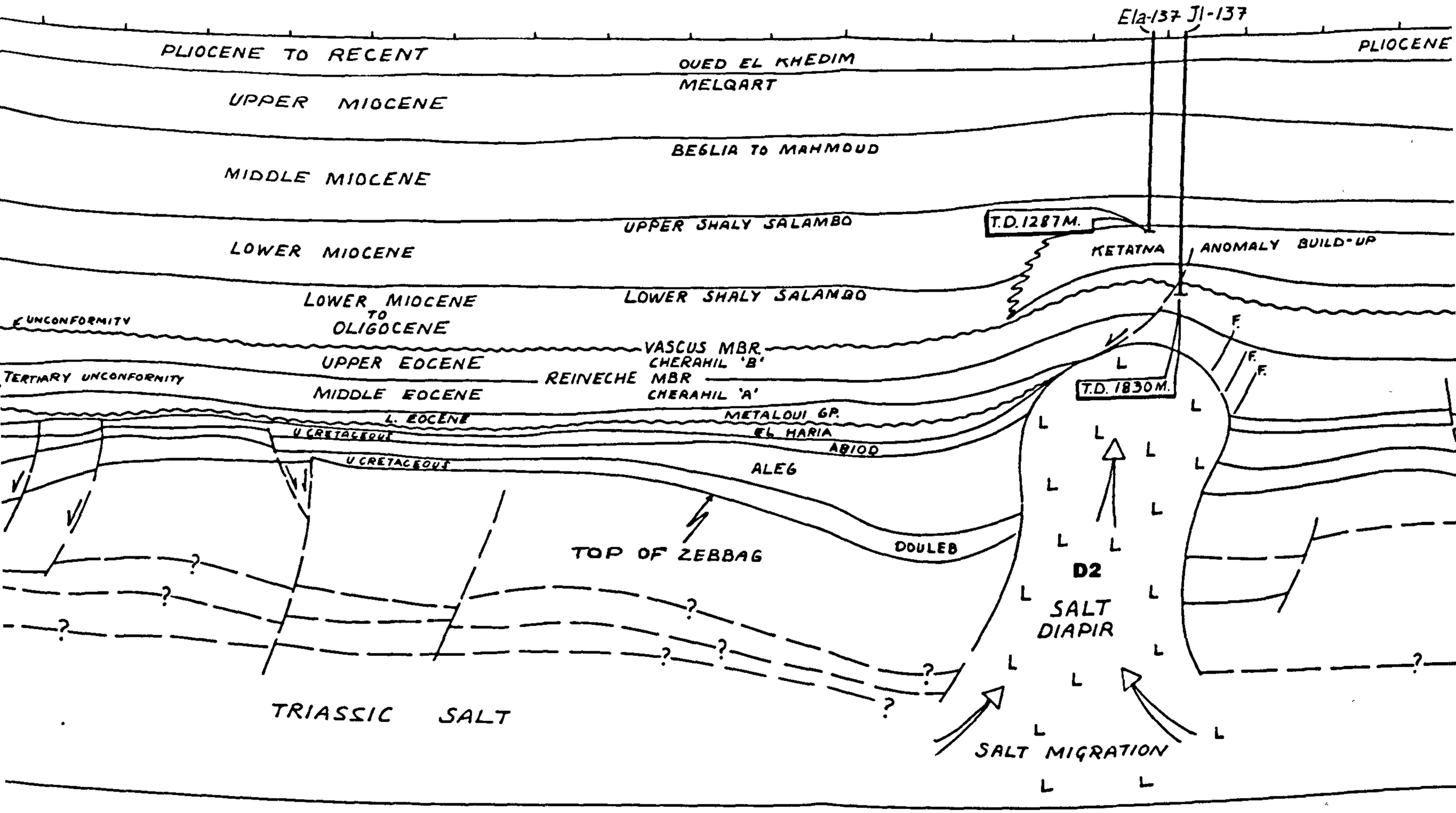
Ela-137
J1-137
PLIOCENE TO RECENT
PLIOCENE
OUED EL KHEDIM
MELQART
UPPER MIOCENE
BEGLIA TO MAHMOUD
MIDDLE MIOCENE
UPPER SHALY SALAMBO
T.D. 1287 M.
KETATNA
ANOMALY BUILD-UP
LOWER MIOCENE
LOWER SHALY SALAMBO
LOWER MIOCENE TO OLIGOCENE
UNCONFORMITY
VASCUS MBR.
CHERAHIL 'B'
UPPER EOCENE
REINECHE MBR
TERTIARY UNCONFORMITY
MIDDLE EOCENE
CHERAHIL 'A'
METALOUI GP.
L. EOCENE
EL HARIA
U CRETACEOUS
ABIOD
U CRETACEOUS
ALEG
TOP OF ZEBBAG
DOULEB
T.D. 1830 M.
D2
SALT DIAPIR
TRIASSIC SALT
SALT MIGRATION

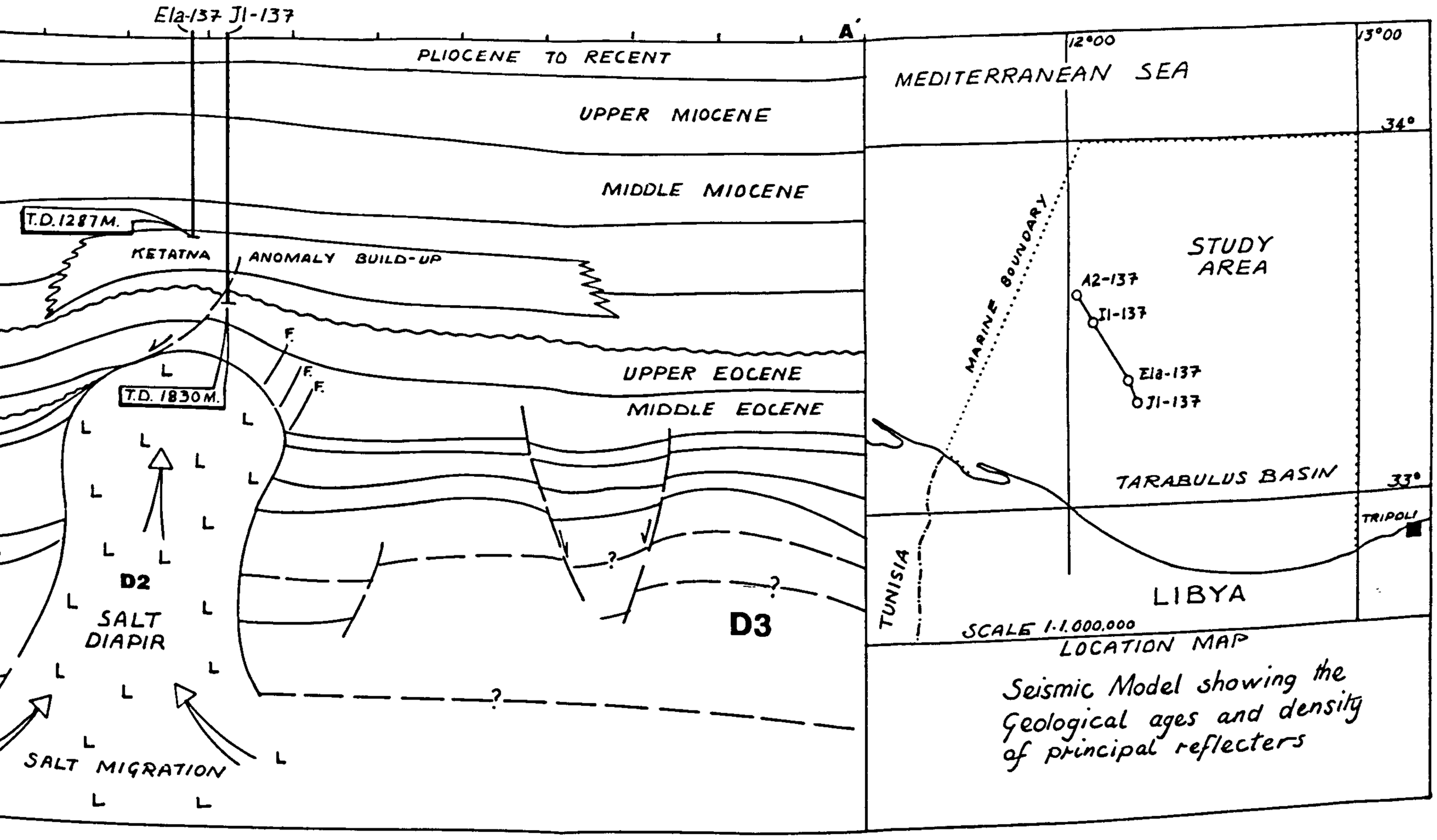

Seismic Model showing the Geological ages and density of principal reflecters

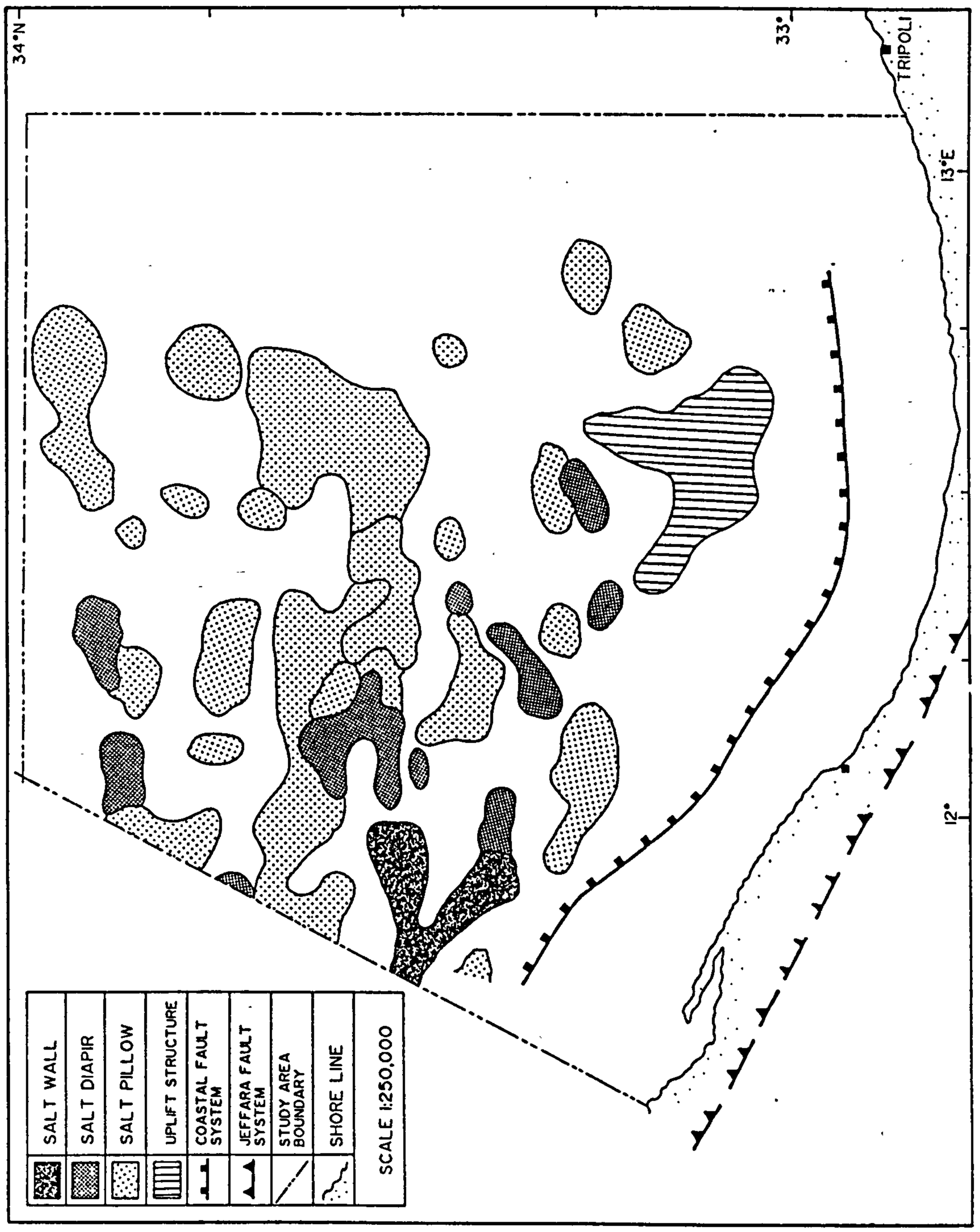

Figure 4.9: Sketch map showing the seismic indications of salt configuration. The alignments of salt features indicate the strong relationship between the salt movement and tectonic elements (expressed by major faults) sub-parallel to the Coastal Fault system, and the Jeffara Fault system.

- Salt diapirs.
- Salt pillows.

Salt Walls

A major bifurcating salt wall, trending west-east, is located in the western part of the study area. The interpretation of the seismic lines, indicates that the salt piercement of the Tertiary and Upper Cretaceous series in the western part of the study area disappears towards the eastern part. Salt walls are not a common type of salt structure in the Sabratah basin, existing only in the western part of the study area, (extending into the adjacent Gabes basin, as shown in the salt configuration map, Figure 4.9). Details of the salt wall are shown in Figure 4.10, showing the seismic lines across the salt walls, as in a N-S direction *(lines 4, 5, 6, 7, 8 and 9)*, and Figure 4.11 showing the lines run in a W-E direction (*line 13 and 15*).

Line No.4. This line indicates only one diapiric salt wall (D),which is probably a piercement through to the sea floor.

Line No.5. This line shows two piercement salt walls (D1) and (D2), which are separated by the sediment sequences. The salt flanks have been affected by faults and folds.

Line No.6. Two separate diapirs were active at the same time, but in asymmetrical developments, and the rim syncline between (D1) and (D2) contains more sediments. Salt walls (D1) and (D2) are very shallow, extending to approximately 300 m beneath the sea floor.

Line No.7. This particular line gives a very good illustration of the two separate diapiric salt walls, the anticlines of the structures underlain by the salt domes and the well-defined rim synclines. The important change seen in line 7 is the deformation of the sediment overlying the salt dome, probably as a result of the dissolution of invading salt and collapse of the overburden. Shallow structural graben, normal and antithetic faults are present on both of the salt walls.

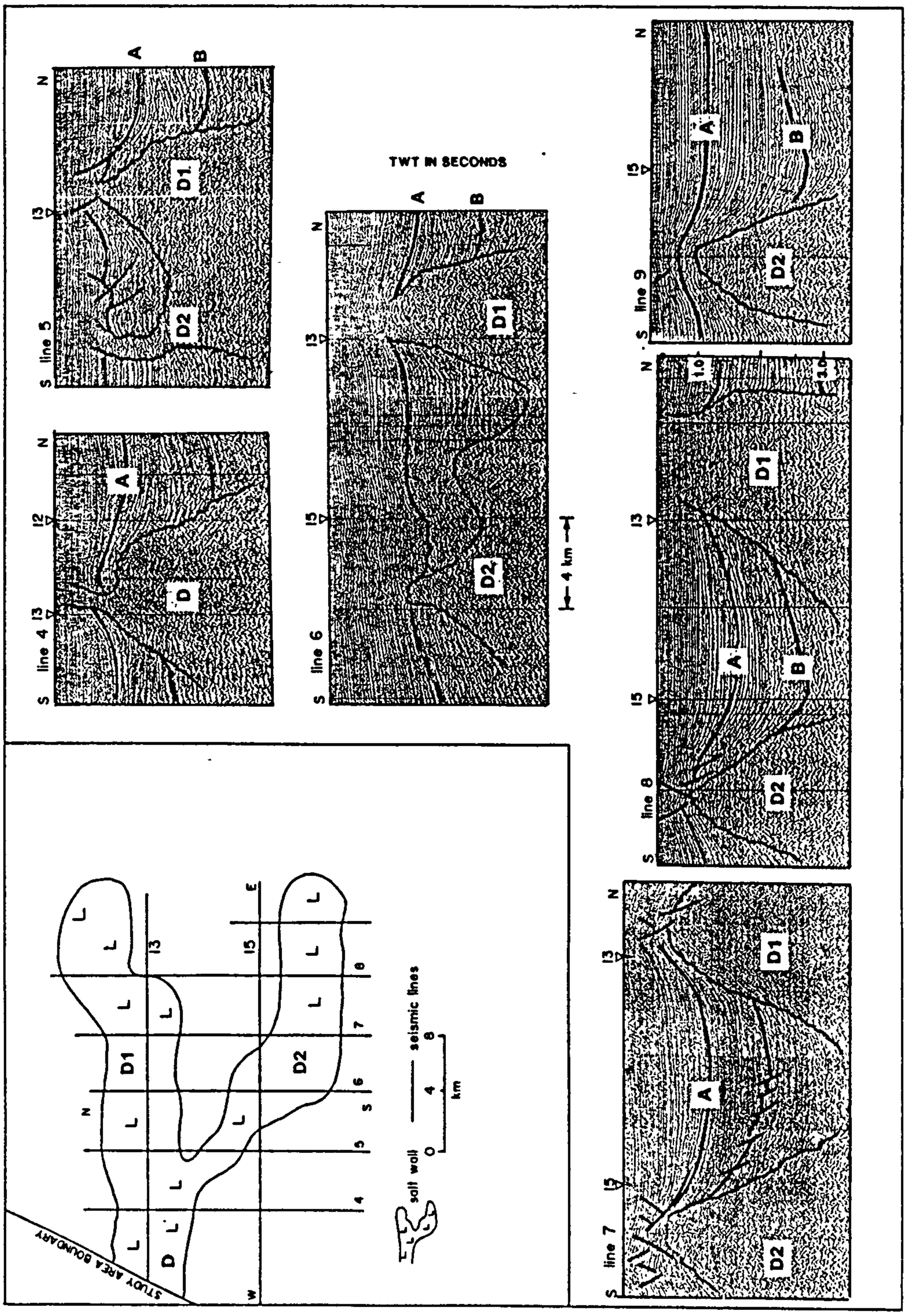

Figure 4.10: An example of seismic lines crossing the salt wall trends, in a N-S direction in the salt domain area, as shown in the sketch map (*NOC section*).

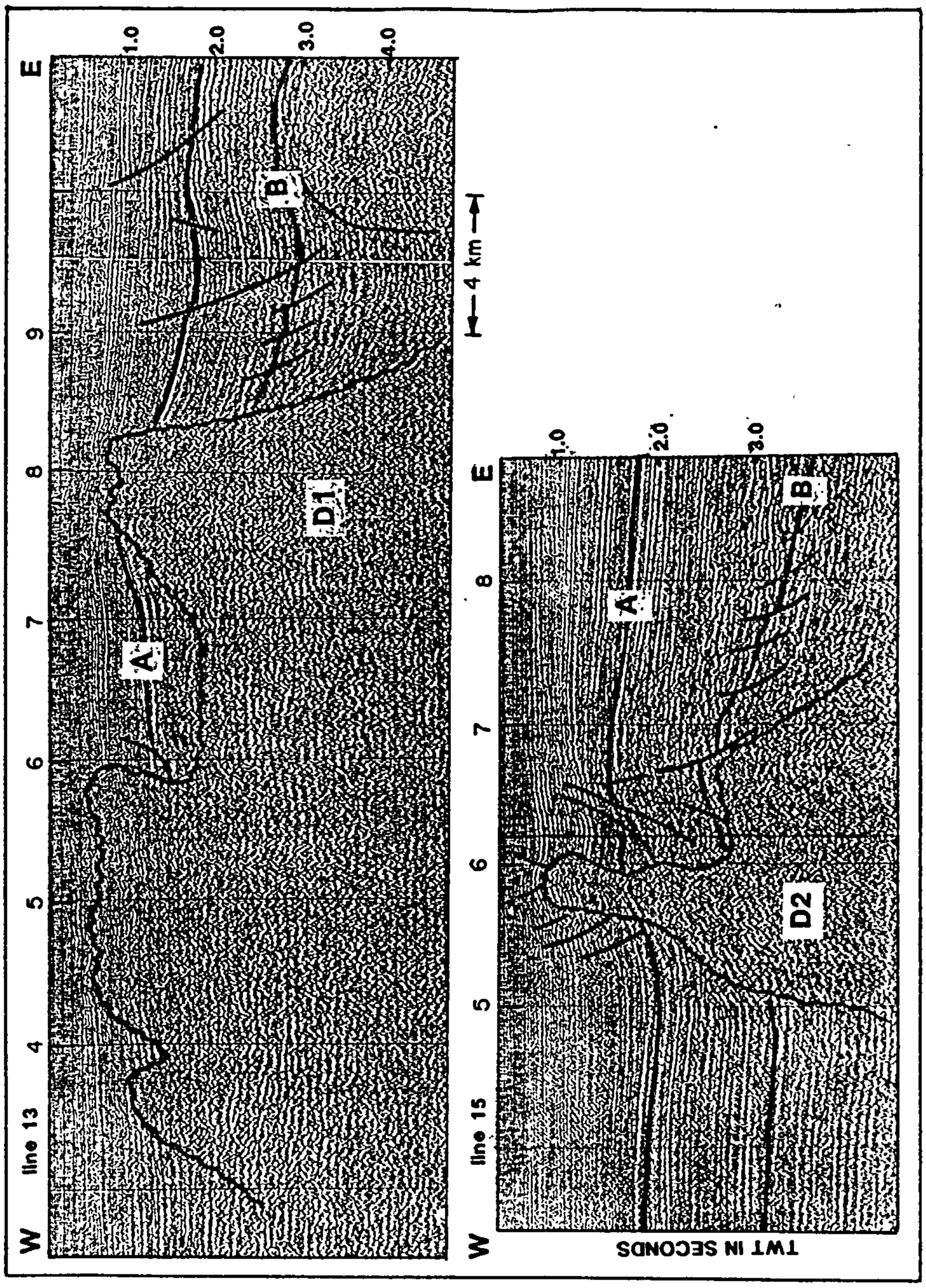

Figure 4.11: An examples of seismic lines across the salt wall trends, in a W-E direction of the salt domain area, as shown on the sketch map of Figure 4.10. (*NOC section*).

Line No.8. A full development is seen of (D1), the salt piercement having reached to the sea floor, due to overloading of the thick sediments separating the salt walls.

Line No.9. Only (D2) appears on this line; it has a well-defined shape, and rim-syncline, and strong continuity of the (A) and (B) horizons with a clear seismic sequence between. Shallow overburden sediment on the crest of the salt is less faulted.

Line No.13. This line crosses the salt wall (D1) from the west to the east as shown in Figure 4.11. At the western edge of line 13, at the line 4 intersection, the reflection data were poor, probably due to the high seismic velocity of the huge quantity of the salt mass itself. Seismically, this area is a reflection free zone. The intersection with line 5 indicated the final stage of the diapric salt wall (D1), which is represented by the very shallow location of the salt beneath the sea floor. The intersection with line 7, indicates a thin sediment sequence which partially separates the two parts of the salt wall. The salt wall disappears between the lines 8 and 9 intersections.

Line No.15. This line crosses the D2 wall in a W-E direction. The line 6 intersection provided a good tie over a diapiric salt wall (D2), and displays a well-defined rim syncline at the left side. More deformation (normal and antithetic faults), and thick sediment deposition is present on the right side. The diapiric salt wall trend changes to a NW-SE direction over D2, as shown in Figure 4.11.

Salt Diapirs

Usually the salt wall region is adjoined by salt diapirs which take the same trend as that of the salt walls, particularly in the central western part of the study area. The salt diapirs are generally elongated with an E -W directional trend sub-parallel to other important tectonic trends such as the coastal fault system and Jeffara fault system. This observation strongly implies that the initiation of salt movement was halotectonic.

The major trend of the salt diapirs in the central part, and the minor trend in the northern part of the salt domain area, are shown in Figure 4.9. The seismic profiles cross the salt domain in different directions, which usefully serves to indicate several

features of the salt diapirs. Profile AA′ gives two examples of features of a salt diapir, as represented by Figures 4.12 and 4.13. On Figure 4.12, (D) is a well-defined piercement salt diapir and (S) the late depositional feature (rim-syncline). The onlap of the Tertiary unconformity is affected by a subsidence fault. Horizon (A) is a strong and continuous reflector indicating the salt diapir crest and a thin sediment layer overlying the salt diapir. The Zebbag reflector horizon (B) represents the depression in the surface of the mobile layer ("primary peripheral sink", according to the definition of Trusheim, Chapter 3), overlain by thick sediment sequences. This is seen as a rim-syncline (S). This structure developed as an asymmetric diapir associated with a gentle fold on the left side, without a major fault. No cap rocks are present, and the onlap configuration of the Tertiary unconformity is seen in the (O) position. Figure 4.13, indicates the salt diapir (D) as located in profile AA′ of Figure 4.7. A reflection (C) represents the cap rocks at the crest of the diapir, which is the same formation as seen in the structure′s flanks. Reflector (B) represents the top of the Zebbag Formation (Primary peripheral sink), overlain by the rim-syncline sediments (S). Extensional fractures, forming the graben structure (E), and its associated faults, resulting from salt piercement through the overlying beds, are seen in the shallow part of the section. The area of diapir development has been deformed, and is associated with two major faults (F) on either side of the salt's flanks.

Profile CC′ (Figure 4.16), shows the disappearance of the diapiric features toward the eastern part (Thick Sediment Domain) of the study area. This is best seen on the NW side of the profile CC′ which shows strong evidence of diapiric salt existing at the A1 and A2-137 locations. Gradually the depth increases along the central and eastern parts of the profile, salt diapirs disappearing and joining with deep salt pillows overlain by thick sediments.

Profile DD′, is drawn across the northwestern part of the study area in a NE-SW direction, as shown in the location map, Figure 4.1. This profile is represented in Figure 4.14, which provides an example of two salt diapiric stages, separated by a thick sediment sequence. The salt diapirs are located at the positions of wells I1-137 and A1-137 ((D1) and (D2)), and the salt pillow (D) is sited at the C1-137 location. The depth section version of this profile, shows the increase in the depth of the basin along the

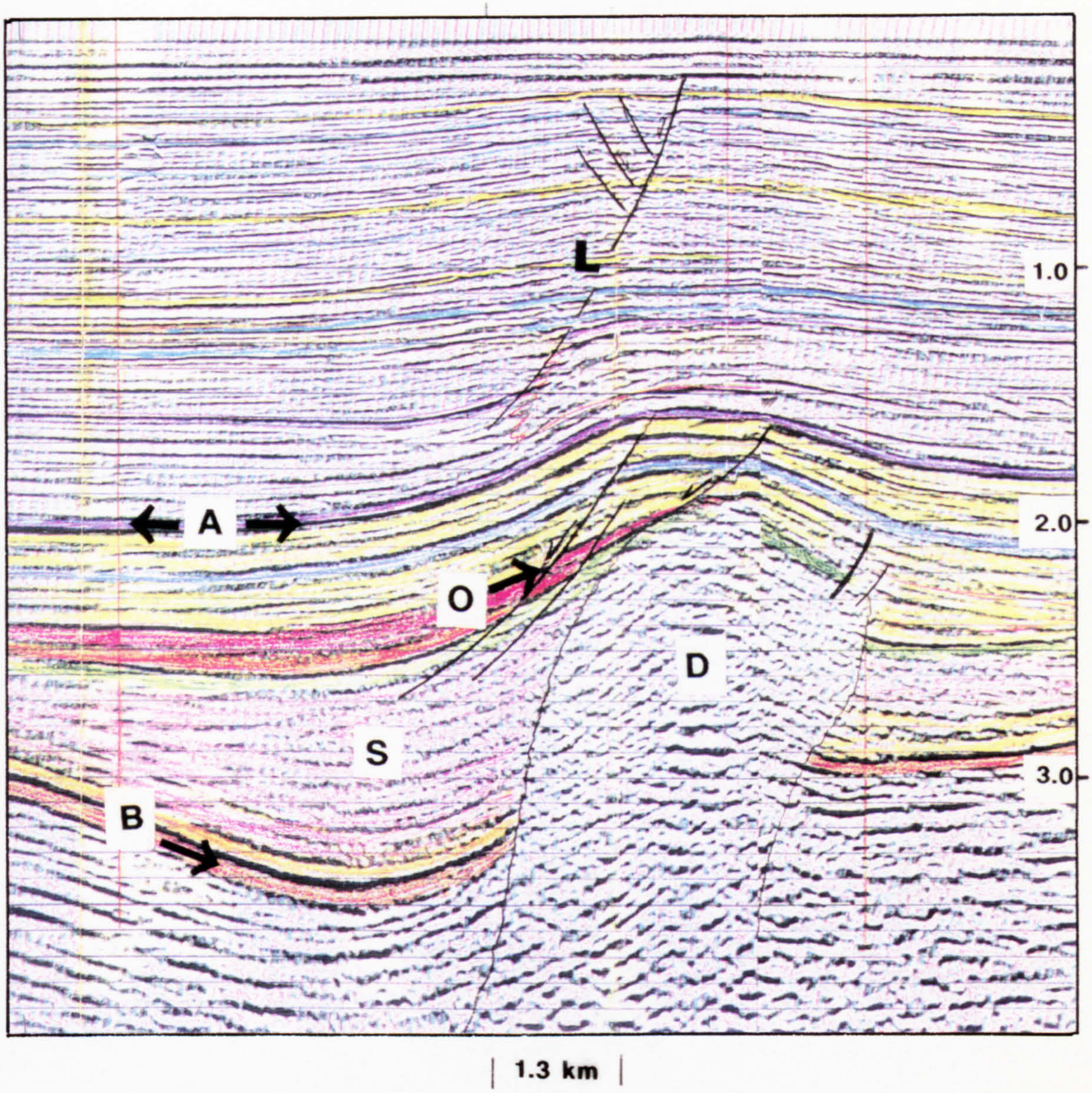

Figure 4.12: An example of a migrated seismic section, showing a salt diapir (D), a strong reflector (B) (top Zebbag Formation) and a strong continuous reflector (A) (Salambo/Cherahil interface). The salt influence is believed to largely terminate at the latter level (A). A well-defined rim-syncline sequence (S) is present. This structure developed as an asymmetric diapir (note onlap configuration of Tertiary unconformity to the left position (O)).

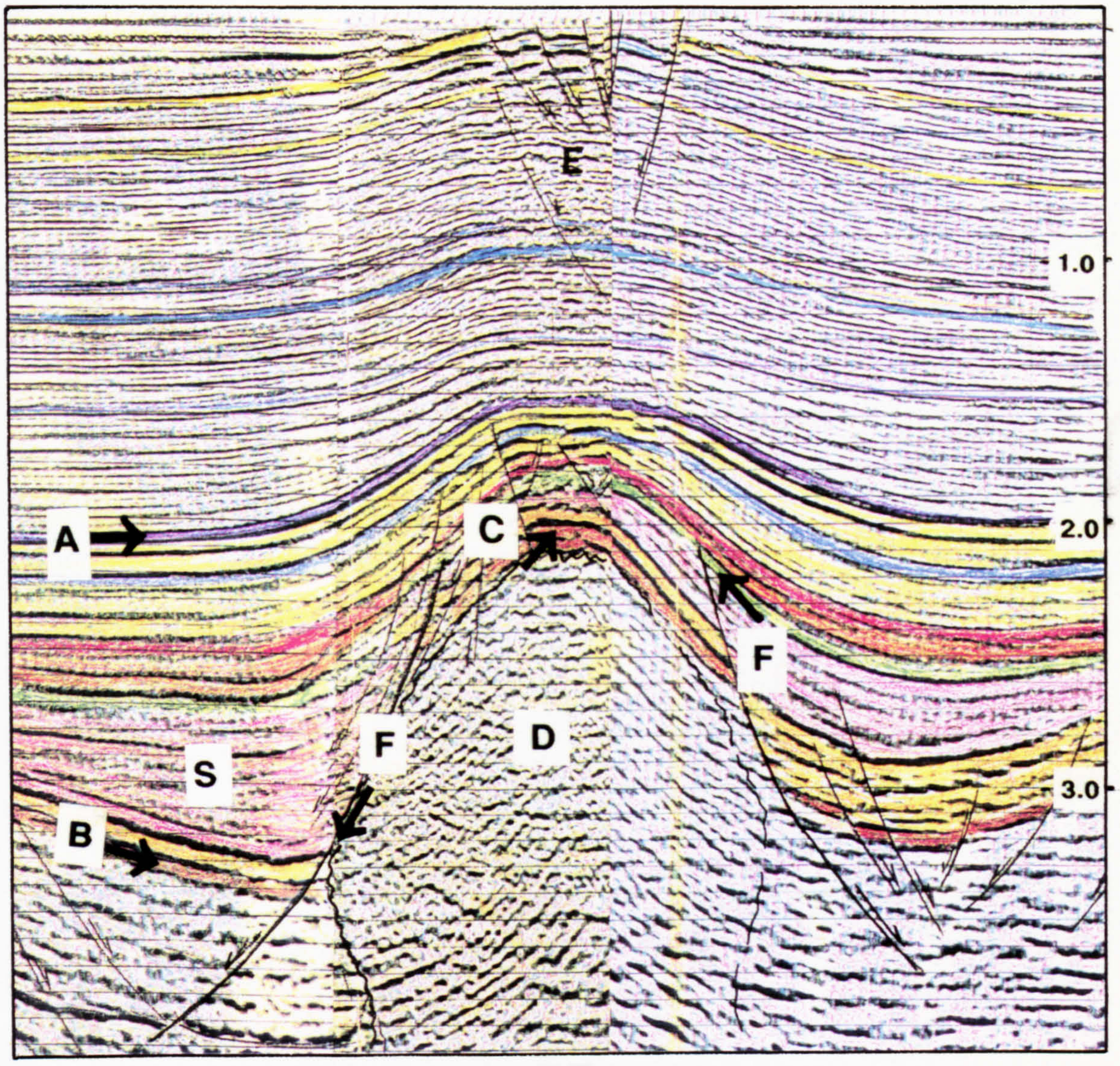

Figure 4.13: An example of a migrated seismic section, illustrating the salt diapir (D), located in profile AA′ of Figure 4.8. The reflection (C) represents the Zebbag Formation cap rock at the crest of the diapir; the same formation is seen at the base of the rim-syncline (S). Extensional fractures, graben structures (E), and faults in the shallow part of the section are visible.

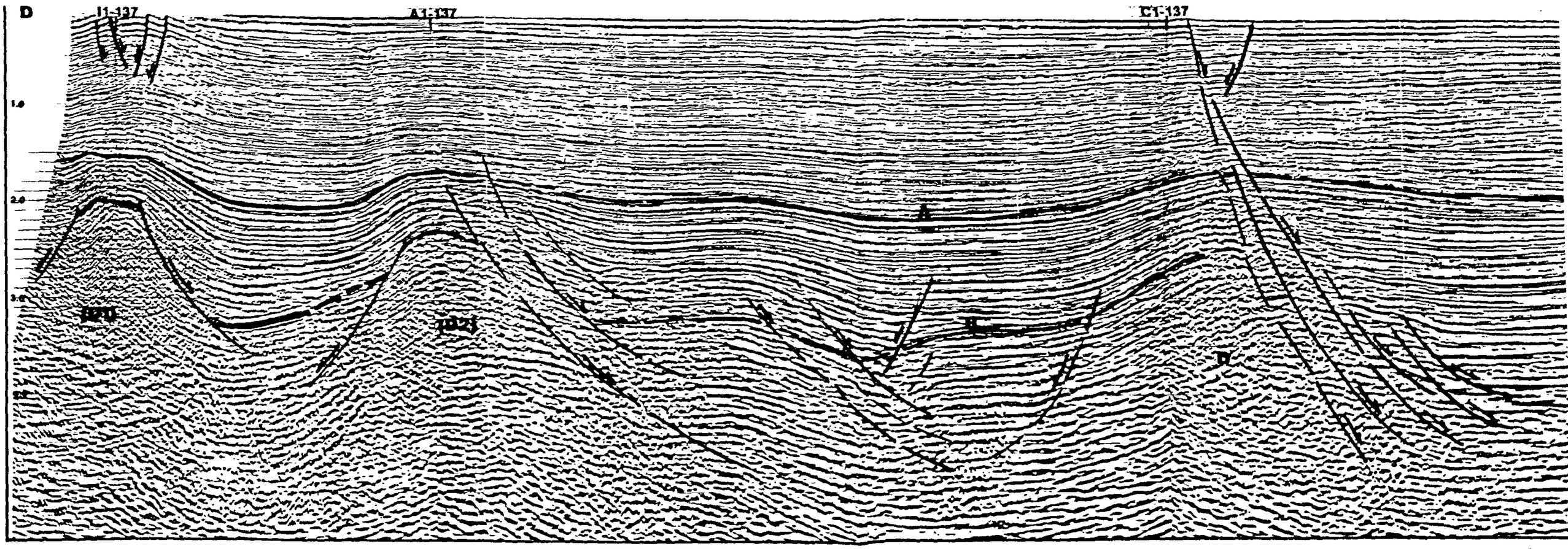

Figure 4.14: The seismic profile DD′ across the north western part of the study area, as shown in Figure 4.1, showing salt diapirs and salt pillow, separated by thick sediment sequences.

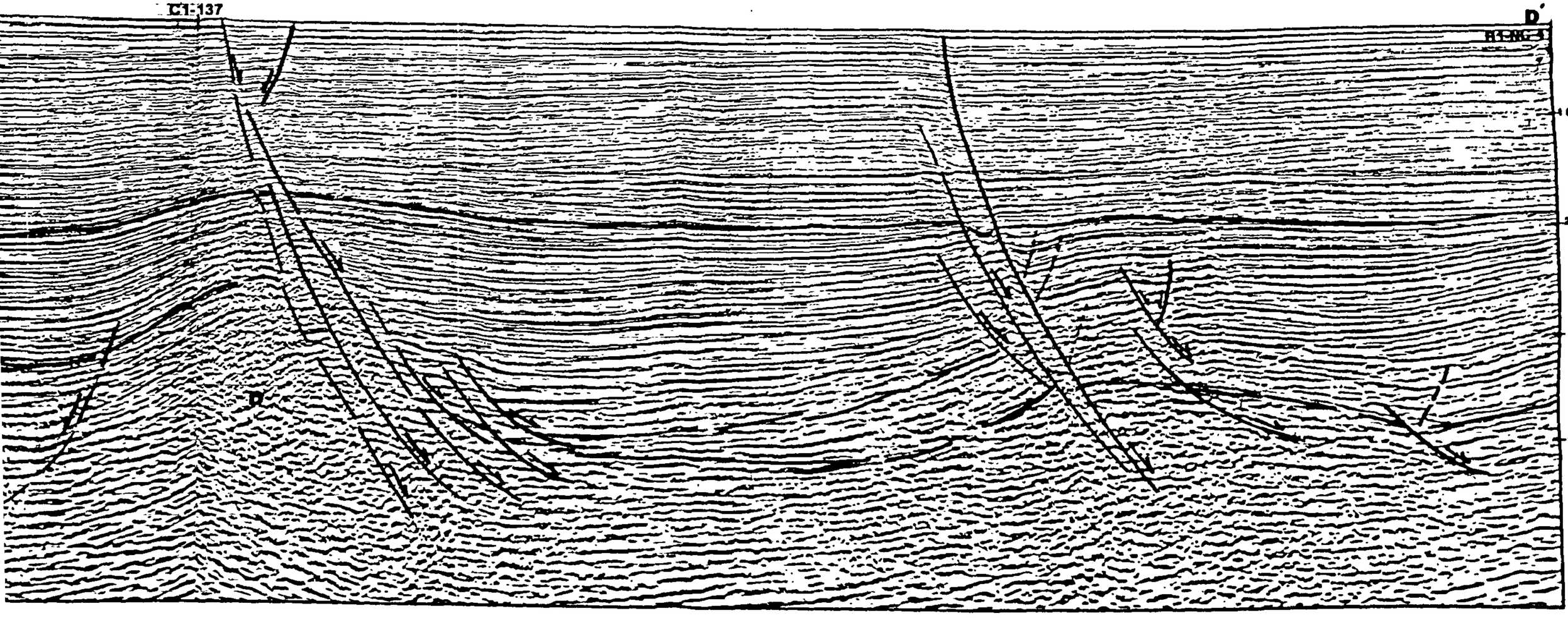
C1-137
D'
1.0
2.0
4.0
TWT IN SECONDS

northern part of the study area (Figure 4.14). The particular depths over this profile have been determined by the distribution of the top Zebbag Formation depths at the boreholes locations. The approximate depths (below sea floor) of the top Zebbag Formation along profile DD′ are: at A1-137, 2800 m; at C1-137, 4000 m, and in the central part of the profile 5500 m. These depths represent the variation in thickness of the sediments overlying the Zebbag Formation.

Seismically, the development history and origin of the salt structures below the mid-Cretaceous units was impossible to analysis for two reasons: firstly, the limitation of seismic response below the Zebbag Formation (Mid-Cretaceous), which is believed to be the same age as that of the salt movement. Secondly, none of the boreholes penetrated the salt level, except at the base of well L1-137, where the salt level has been dated as Upper Triassic, and consists of anhydrite, dolomites and shales. The base of the Oligocene (Salambo/Cherahil interface) reflector (A), is taken to be represent the latest horizon to be affected by the salt diapirism. Since the Zebbag Formation (B) is the deepest reflector to have been interpreted as a primary peripheral sink (the depression in the surface of a mobile salt layer), then, seismically speaking, the diapirism probably commenced in the Early Cretaceous and continued up to the Tertiary in the study area.

Salt Pillows

Salt pillow structures are the most common salt configuration in the study area, as shown in Figure 4.9. The salt pillow represents the first stage of the salt flowage mechanism, as described by Thersium (1960), and Sannemann (1965), and reviewed in Chapter 3. The example of the seismic section Figure 4.15, indicates three adjacent salt domes at different stages of development, the first stage (D1) salt pillow, the second stage (D2) salt diapir, and the third stage (D3) salt wall. (A) and (B) are the two mapped reflectors (Salambo/Cherahil interface and the Zebbag Formation respectively). Profile CC′ across the salt domain and thick sediment domain in a WNW-ESE direction includes the boreholes, as shown in Figure 4.1. This illustrates the development of the geological features of the salt domain and a thick sediment domain areas. Figure 4.16, shows an interpretation of profile CC′ which indicates the salt diapir structure (D) in the NW part of the

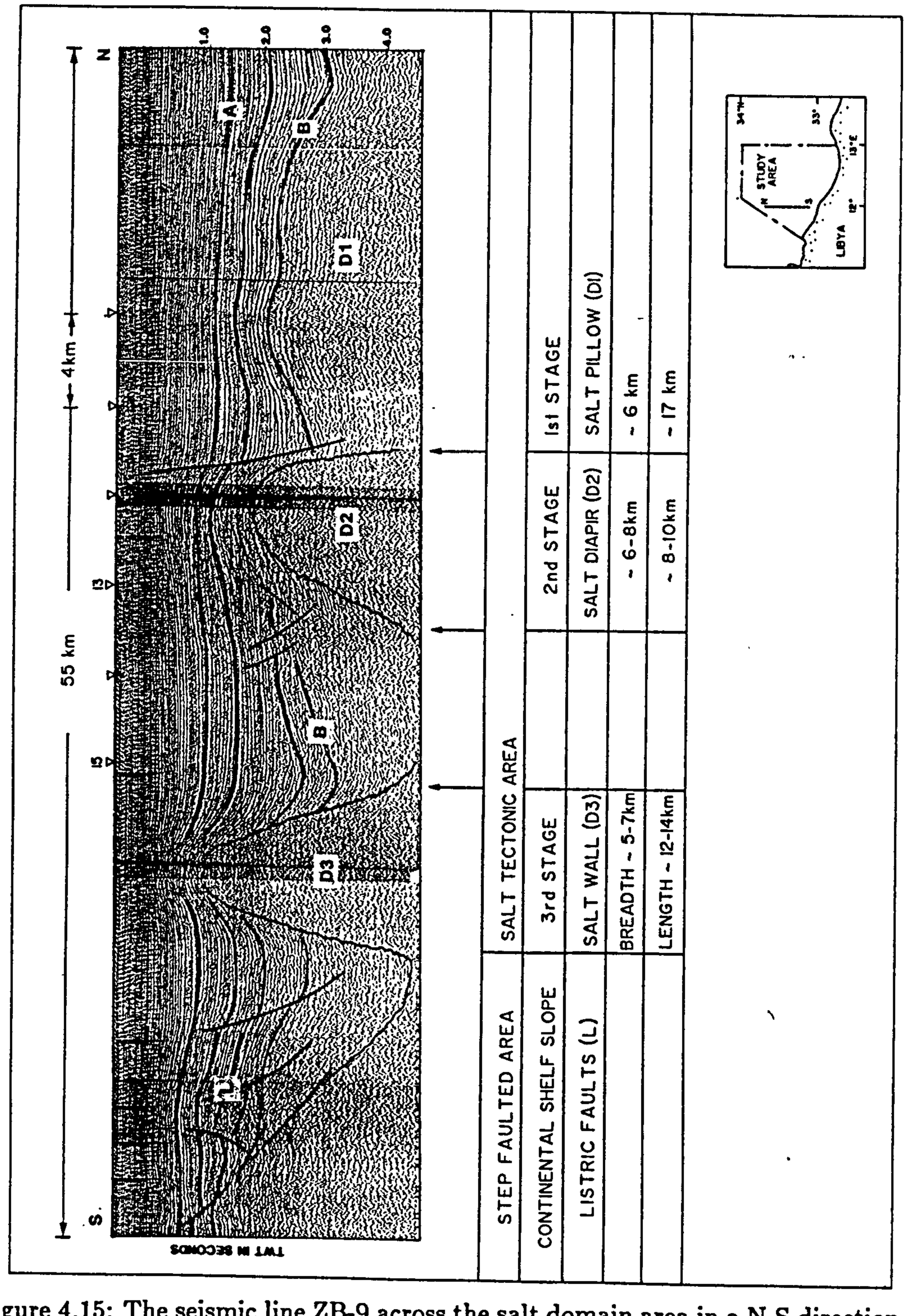

Figure 4.15: The seismic line ZB-9 across the salt domain area in a N-S direction, showing the development of three adjacent salt structures in different stages, as shown in the inset sketch map. (A) and (B) are the base of Oligocene and the top of Zebbag Formations, respectively. (L) is a step-faulted zone (continental slope).

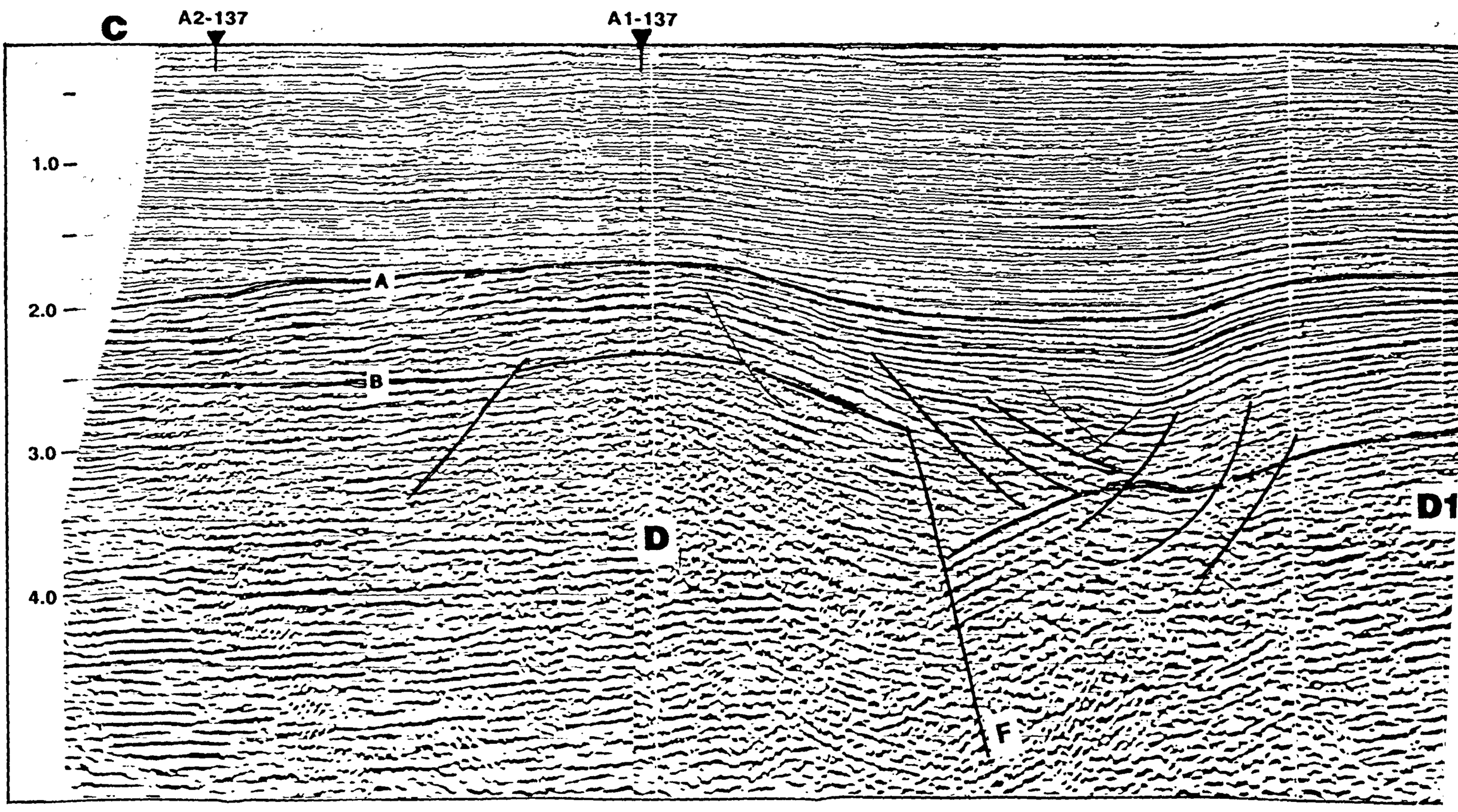

Figure 4.16: Migrated seismic profile CC′ across the salt and thick sediment domains area in WNW-ESE direction, D, D1, and D2, represent the salt diapir and the salt pillows respectively. F is the major fault.

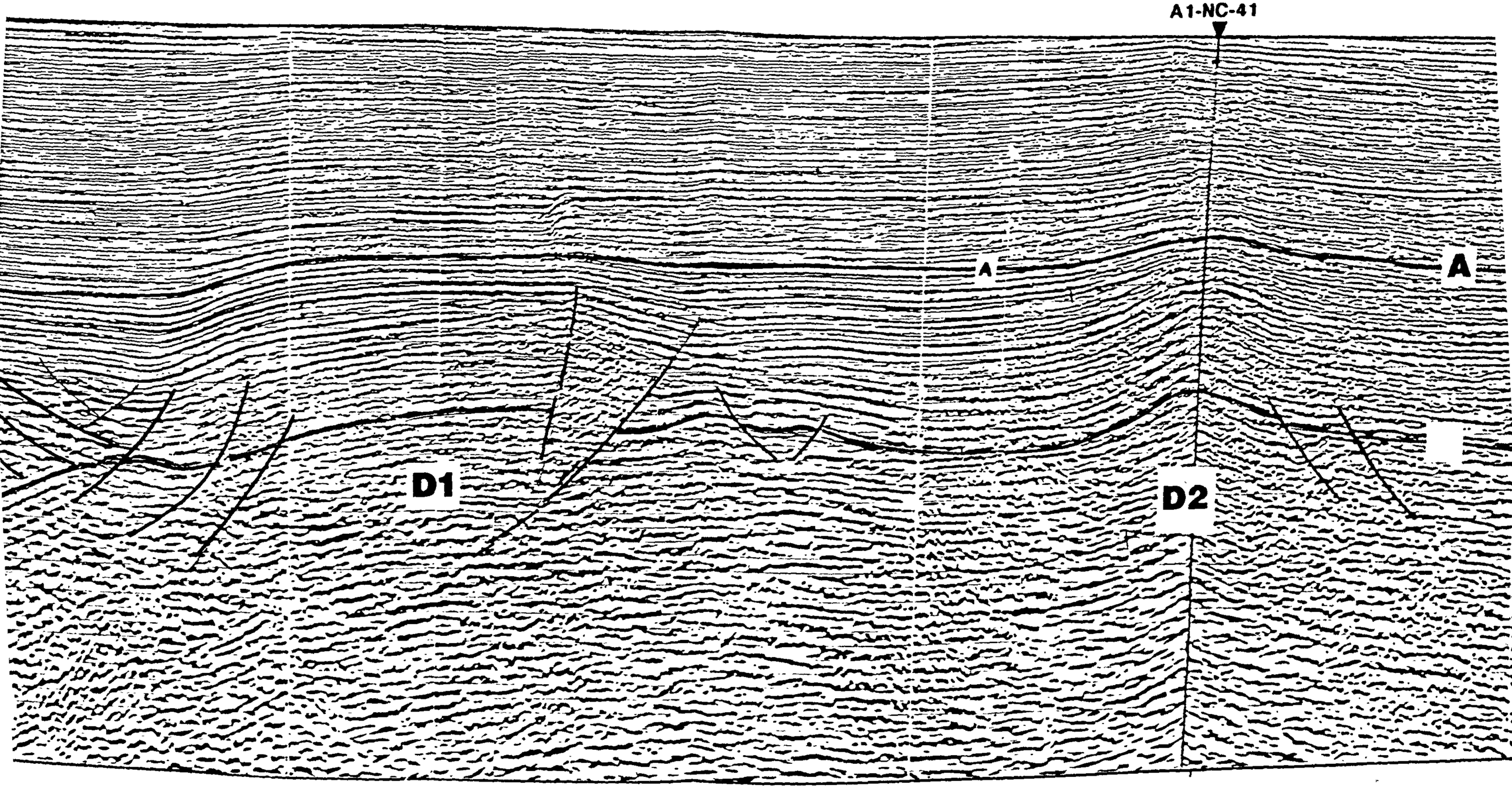
A1-NC-41
A
A
D1
D2

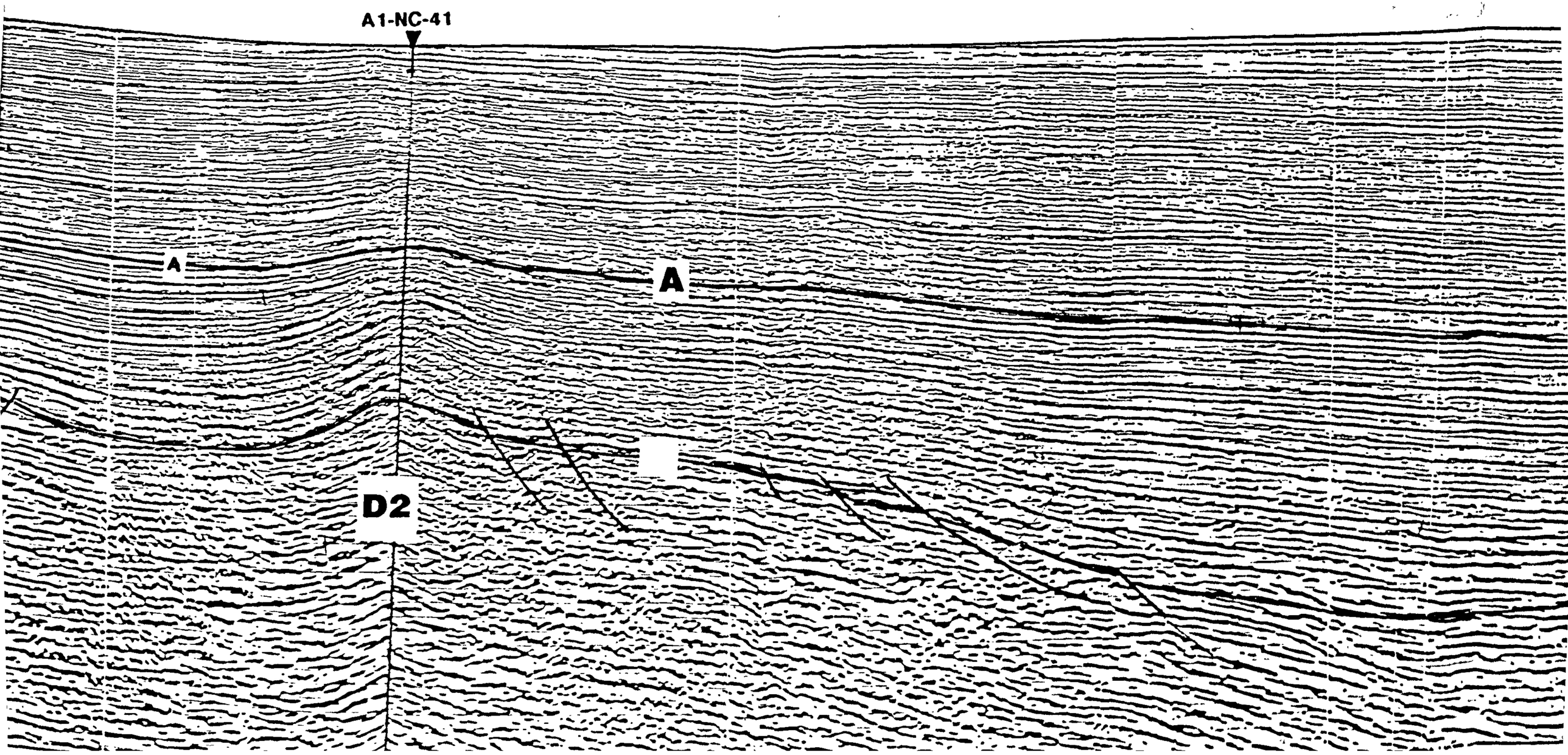
A1-NC-41
A
A
D2

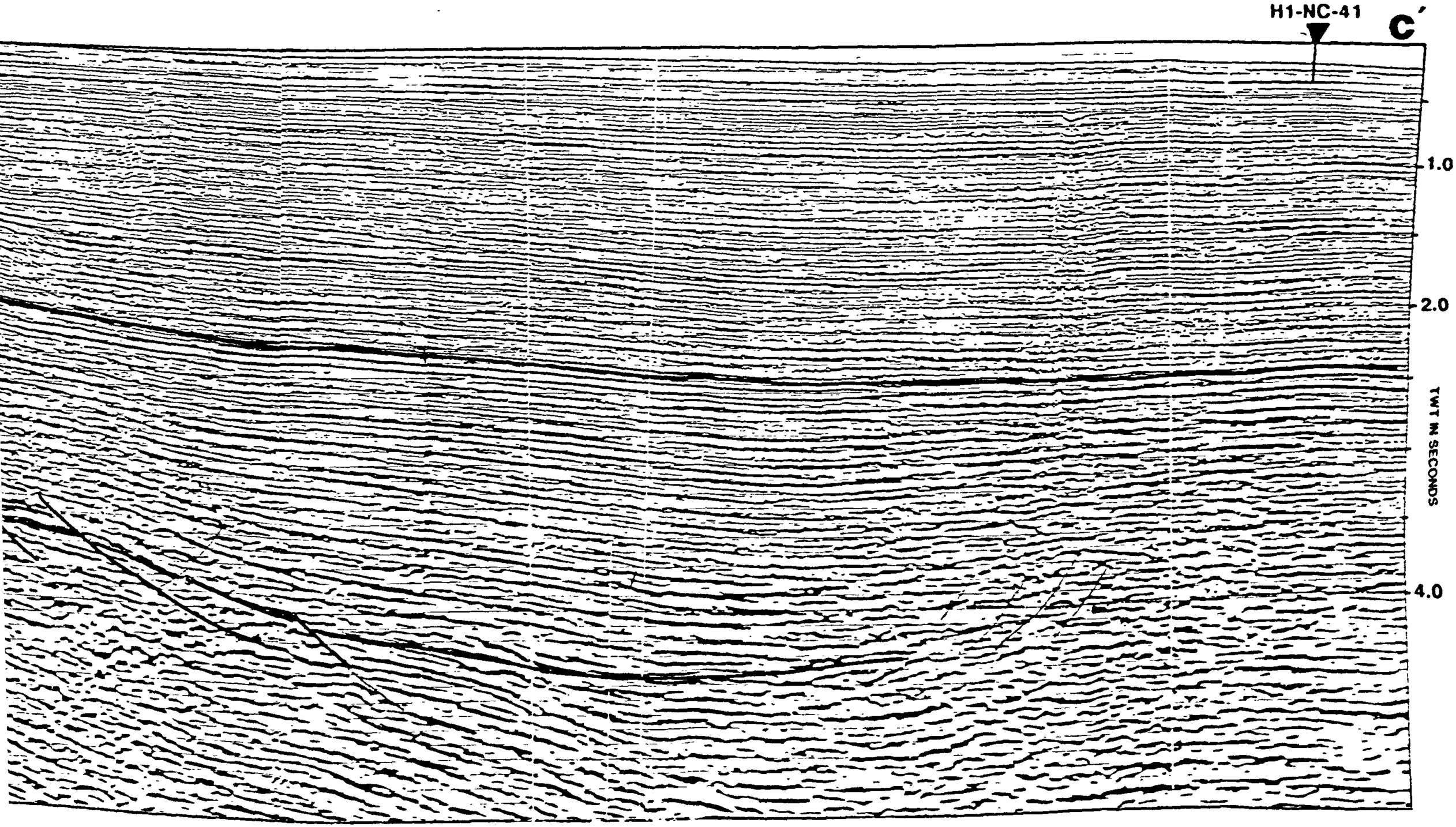
H1-NC-41
C´
1.0
2.0
4.0
TWT IN SECONDS

area, at locations A1 and A2-137, adjoined by the salt pillows (D1 and D2). The diapir is associated with a major fault of very large throw (over 1000 ms two-way time), affecting the top of the (B) Zebbag Formation on the upthrown side. The strike-slip reactivation of the relatively minor faulting at the Zebbag level, together with increasing overburden loading may have initiated the salt movement. Listric growth-faults related to the rising salt structure, and a thick sediment cover overlying the salt pillow (D), are seen at the right side. A deep salt pillow (D2) is seen at A1-NC-41, which does not pierce through the overlying sediment. The Zebbag Formation (B) dips slightly towards the Thick Sediment Domain. Because of shortage of information to confirm the top of the Zebbag formation, this reflector cannot be identified as reliably in the Thick Sediment Domain area. Profile CC′ crosses the thick Tertiary/Cretaceous sediment sequences, which includes a significant thickness of mature source and reservoir rocks (for instance, the Metlaoui, and El-Haria Formations). The Salambo/Cherahil interface (unconformity) appears and is continuous over the whole of this profile. The salt pillows disappear along the eastern part of the study area. Thick Triassic salt layers existed in the eastern part, but were overloaded by the thick sediment sequences and forced to migrated into the Salt Domain area (western part of the study area) in the Late Triassic/Early Jurassic times. The available seismic and borehole information, have been used together to deduce the basin depth along the CC′ profile, which can be described as follows:

- In the western part of profile CC′ at A2 and A1-137 locations, the top of the Zebbag Formation lies at 3576 m and 2800 m, respectively.
- In the flank between A1-137 and A1-NC-41, the top of the Zebbag lies at 4600 m.
- At location A1-NC-41, the top of the Zebbag is at 4250 m.
- Along the eastern part of profile CC′ on the flank between locations A1 and H1-NC-41, the Zebbag depth is approximately 7000 m.

It is clear that the depth increase towards the eastern part of the study area (from 3000 m to 7000 m).

4.8.2.2 The Continental Shelf Domain

The continental shelf domain is located in the southern part of the study area, as shown in Figure 4.6. It is a part of the African continental margin, developed during Late Triassic or Early Jurassic times. It has been affected by extensional faults related to cratonic rifting, and has been characterized by considerable subsidence and volcanic activity. The passive continental margin was examined in this study from a few available seismic lines. The structural maps of the two horizons (A) and (B) are shown in Figures 4.4 and 4.5. These indicate the position of the E-W Coastal Fault System and the pronounced uplift structure sited at well locations L1, H1, G1-137. Three seismic lines (M-26, M-15, and ZB-21) crossing the continental shelf domain area, are shown on the location map in Figure 4.1. They are illustrated in Figure 4.17, which shows the major aspects of geological features which extend from the southern (coastal) part to the K1 and L1-137 wells. The major structural features along these lines are described below, from south to north below. The coastal fault system, is represented by normal and listric faulting to the north along an east-west trending zone. The area seaward (north) of the coastline has continued to subside since Late Triassic time, receiving a total of more than 5 km of sediment, while the area landward (south) has remained near sea level. The two anticlines (representing salt and uplift structures) are located at wells K1 and L1-137, respectively.

Coastal Fault system

The coastal fault system is shown in Figures 4.4 and 4.5. It is clearly visible paralleling the coastline's east-west direction, and is represented by listric growth faults which are the dominant structural style along the continental shelf zone, where they have produced numerous tilted fault blocks. Many of these faults continued to be active in the Pliocene, but rarely propagate to the sea floor. Most of the faulting took place in Miocene times. Associated with these listric faults are some antithetic faults which resulted in the graben features, seen in the shallower parts of the sections. The major faults have been readily identified, but the minor faults could not be traced so reliably, and have simply been assigned trends similar to those of the major features which were parallel to the Jeffara

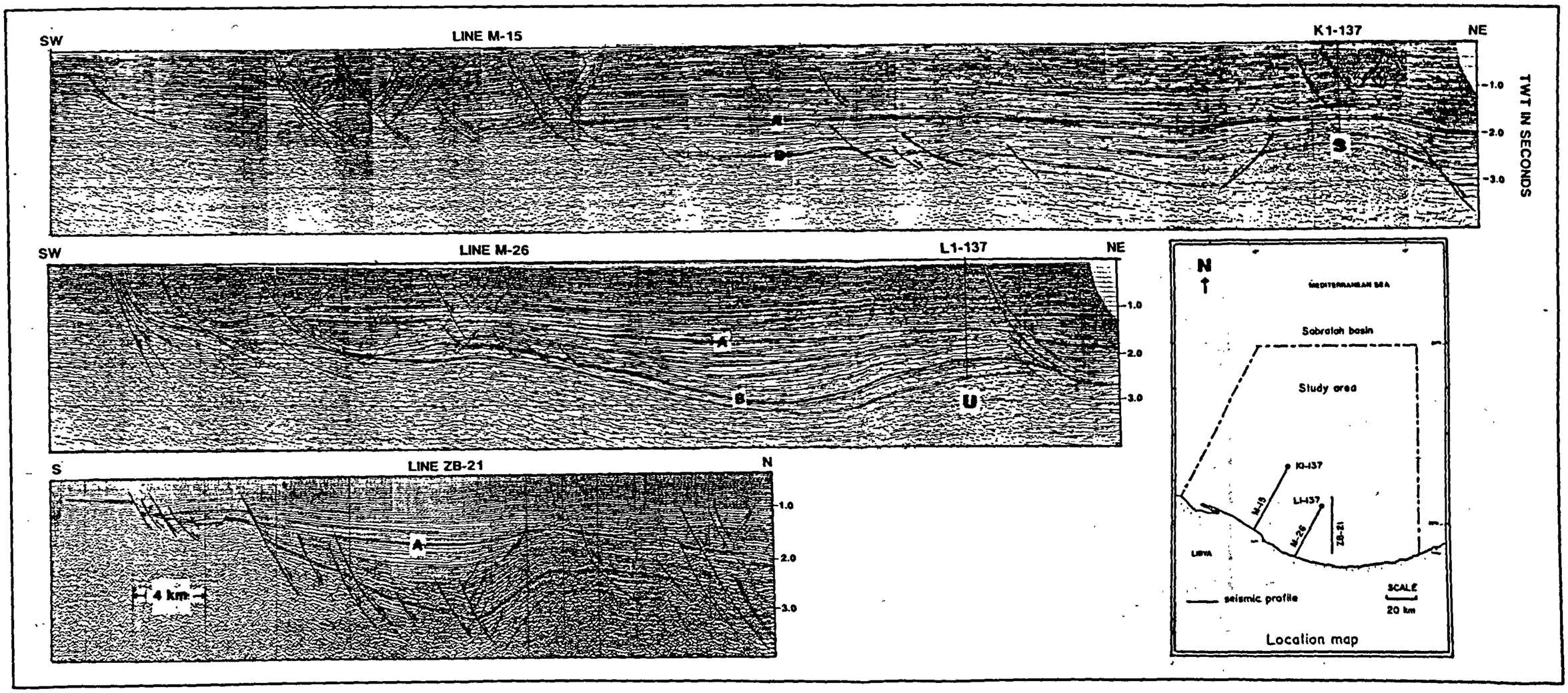

Figure 4.17: Seismic lines (M-26, M-15, and ZB-21), crossing the Continental Shelf Domain in three different locations. A and B are the base of Oligocene and top of the Zebbag respectively. (U) is the uplift structure which associates with high positive magnetic anomaly at L1-137 location. (S) is a salt structure which associates with a negative gravity anomaly and negative magnetic anomaly at the K1-137 location

fault system. The development of listric growth faulting associated with subsidence is an important element in continental margin tectonics, where salt basins are found along the strike of the continental shelf or slope. Jenyon, (1986), has discussed and modelled the association of growth faulting with subsidence. He describes the development of a growth fault in the overburden in a continental slope setting, where the salt in a small basin has moved in the downslope direction, resulting in subsidence and related to up-slope salt flow and subsidence effects.

In this particular study area, the salt basins are found along the strike of the continental slope, and the relationships between faulting and salt movement in the continental shelf zone has been established through the seismic sections described previously, particularly in the migrated section M-15 shown in Figure 4.17. The interpreted section of this line through well K1-137 to the coastline, is shown in Figure 4.18. The Sabratah Basin was formed during the Late Triassic or Early Jurassic by E-W trending normal faults (N) to the north, as shown in Figure 4.18 (I). The Listric growth faults (L) associated with antithetic faults (E), in the step-faulted area relate to upslope salt flow and subsidence effects. The sedimentary overburden subsidence sequence deposited on this passive margin is seen in the middle of the section (subsidence and sediment accumulation area). The salt tectonic structure (D) resulted through salt movement under the sediment load.

Therefore, a geological model for the Libyan continental shelf can be constructed, based on seismic line M-15 and available data from well K1-137 (Figure 4.18 (I)). This interpretation relies greatly on consideration of previous work on the evolution of the Libyan margin and geological history of the area, (Elf-Aquitaine (1979), Agip (1984) and Sirte (1985) Oil companies, Burollet et al (1978), and Pitman et al (1981)).

Figure 4.18 (II) shows the proposed geological model for the development of the Libyan continental slope, from Late Triassic/Early Jurassic time through to the present time. This is discussed below.

The first stage, described by Burollet et al (1978), notes that a fundamental change in the palaeogeography of northern Libya occurred during Carboniferous times. Prior to the Visean, the whole of the Saharan platform, covered by open epicontinental seas, was gently

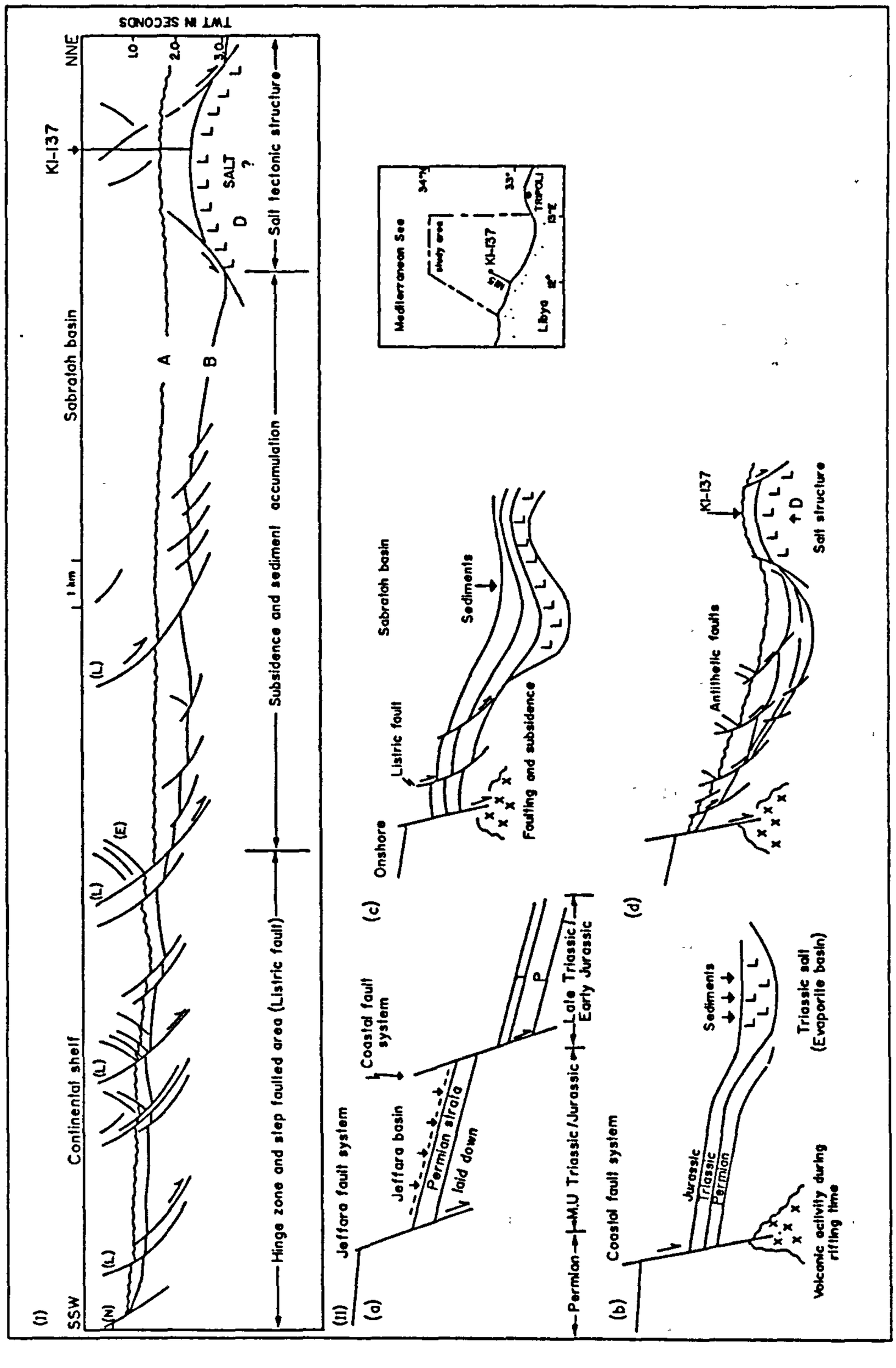

Figure 4.18: (I)- The geoseismic section deduced from the migrated seismic line (M-15), showing the structural elements of the Libyan continental shelf in a SSW-NNE direction, as shown in the location map. A and B are base of Oligocene and the top of Zebbag, respectively. (N), (L), and (E) are normal, listric, and antithetic faults. (II)- The geological model of the Libyan continental shelf, indicates the stages of the development, from Late Triassic/Early Jurassic to the present time. (*the ages are approx. in Fig II (a) to (d)*).

subsiding. At the end of the Visean the area north of Hammada El Homra was uplifted by prerift epeirogeny and the Carboniferous beds eroded. In the Jeffara, a subsidence basin appeared north of this partially faulted flexure. The upper Carboniferous and Permian strata were laid down, (Figure 4.18 II, (a)). During Triassic and Liassic times subsidence of the northern Jeffara trough continued, and was marked by carbonate sedimentation. Pitman et al (1981) discuss the nature of the North Africa hinge zone. Basically they imply that the Pelagian basin (including the Sabratah basin) was formed near the end of the Triassic or early in the Jurassic, by normal faulting (Coastal Fault System) to the north along an E-W trending hinge zone. The area seaward (north) of the hinge zone, has continued to subside since that time receiving a total of more than 5 km of sediment.

The Triassic salt basin is believed to have been filled from the continental region, and existed along the strike of the continental slope, as shown in Figure 4.18 II (b). The area seaward (north) of the coastline to K1-137 has continued to subside and receive sediment. The sediment sequence prograded seawards across the shelf. Sketch (c) in Figure 4.18 (II) shows the initiation of the salt movement at the seaward margin of the basin. Further deposition and subsidence effects due to the salt withdrawal lead to the occurrence of gravitational normal faults of growth-type above the landward margin of the basin, as in sketch (d) of Figure 4.18 (II).

Magmatic activity and uplift structures

The Late Cretaceous/Early Tertiary and the Middle/Upper Cretaceous magmatic phases, have been inferred from migrated seismic sections in time and depth, tied to data from wells K1, L1, G1, H2, and H1-137. Drilled intervals in these wells confirm the presence of these magmatic units. An example of a migrated depth section, WT-84-1-6, across the uplift structure through wells H1 and H2-137 is shown in Figure 4.19. V1 and V2 are represent the Tertiary/Cretaceous, and Middle/Upper Cretaceous volcanic intervals respectively. The well correlation shown in Figure 4.20 gives the depths and the thicknesses of the volcanic intervals in the study area. The thickest volcanic interval penetrated in borehole L1-137 represents 207 m of basaltic conglomerate, assigned a Middle Cretaceous

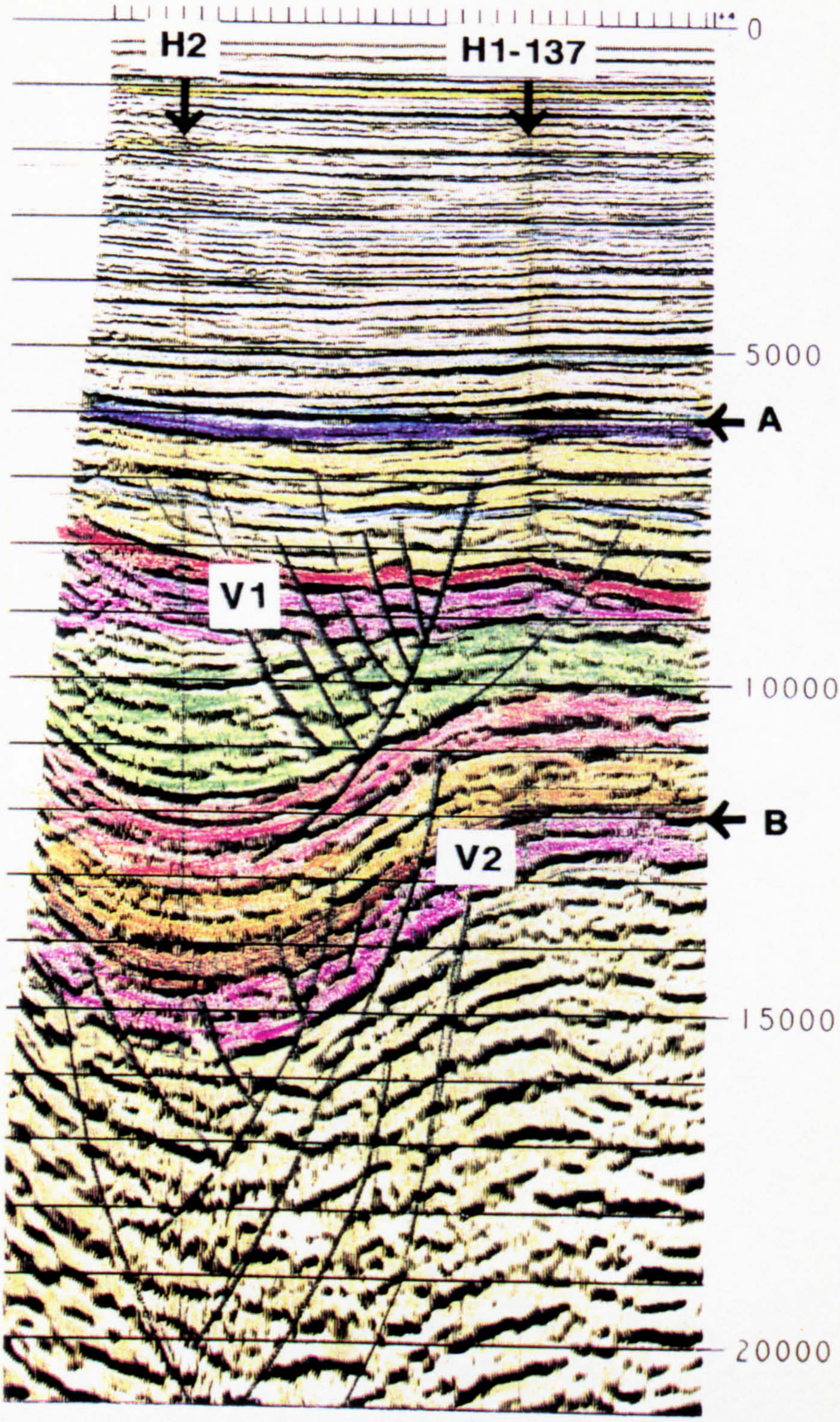

Figure 4.19: An example of a migrated depth section, showing the volcanic intervals, (the Tertiary/Cretaceous interval (V1) and Upper Cretaceous interval (V2)). The depths have been confirmed from wells H1 and H2-137. A and B represent the base of the Oligocene, and the Zebbag Formations, respectively.

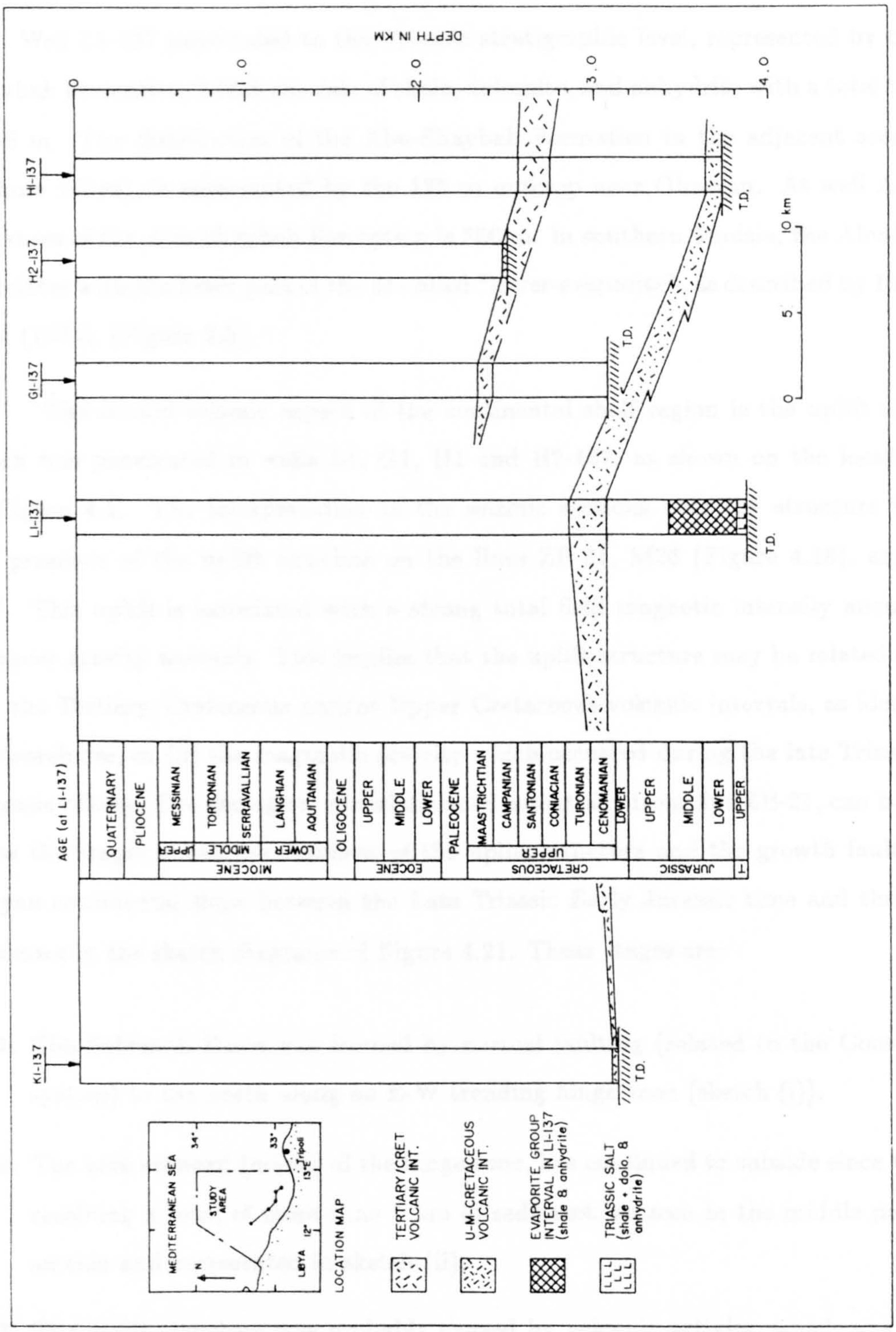

Figure 4.20: Diagramatic section showing the volcanic intervals, deduced from five wells located in the southern part of the study area, as shown in the sketch location map.

age. Well L1-137 penetrated to the Triassic stratigraphic level, represented by the Abu-Shaybah Formation, which consists of shale, dolomite, and anhydrite with a total thickness of 56 m. The distribution of the Abu-Shaybah Formation in the adjacent areas (NW-onshore Libya), is represented by the 125 m outcrop near Gharyan. At well A1-38 the thickness of the Abu-Shaybah Formation is 356 m. In southern Tunisia, the Abu-Shaybah correlates with the lower part of the so-called "lower-evaporite", as described by Hammuda et al (1985), (Figure 2.5).

The second seismic aspect of the continental shelf region is the uplift structure, which was penetrated in wells L1, G1, H1 and H2-137, as shown on the location map in Figure 4.1. The interpretation of the seismic sections over the structure indicates the presence of the uplift anticline on the lines ZB-21, M26 (Figure 4.18), and profile BB′. This uplift is associated with a strong total field magnetic intensity anomaly and Bouguer gravity anomaly. This implies that the uplift structure may be related either to (i): the Tertiary/Cretaceous and/or Upper Cretaceous volcanic intervals, as identified in the boreholes, or (ii) the magmatic activity which occurred during the late Triassic/early Jurassic rifting. The geological model deduced essentially from line ZB-21, can be used to show the stages of the development of the uplift structure and the growth faults on the Libyan continental slope between the Late Triassic Early Jurassic time and the present, as shown in the sketch diagrams of Figure 4.21. These stages are:

1. The Sabratah Basin was formed by normal faulting (related to the Coastal Fault system) to the north along an E-W trending hinge zone (sketch (i)).

2. The area seaward (north) of the hinge zone, has continued to subside since that time receiving a total of more than 5 km of sediment, as seen in the middle part of the section and represented in sketch (ii).

3. The uplift structure was probably caused by volcanic activity, which was initiated during the Late Triassic rifting process.

It should be noted that well L1-137 did not penetrate to this level, and the seismic lines revealed the structure of the anticline only at limited depth. Only the strong magnetic

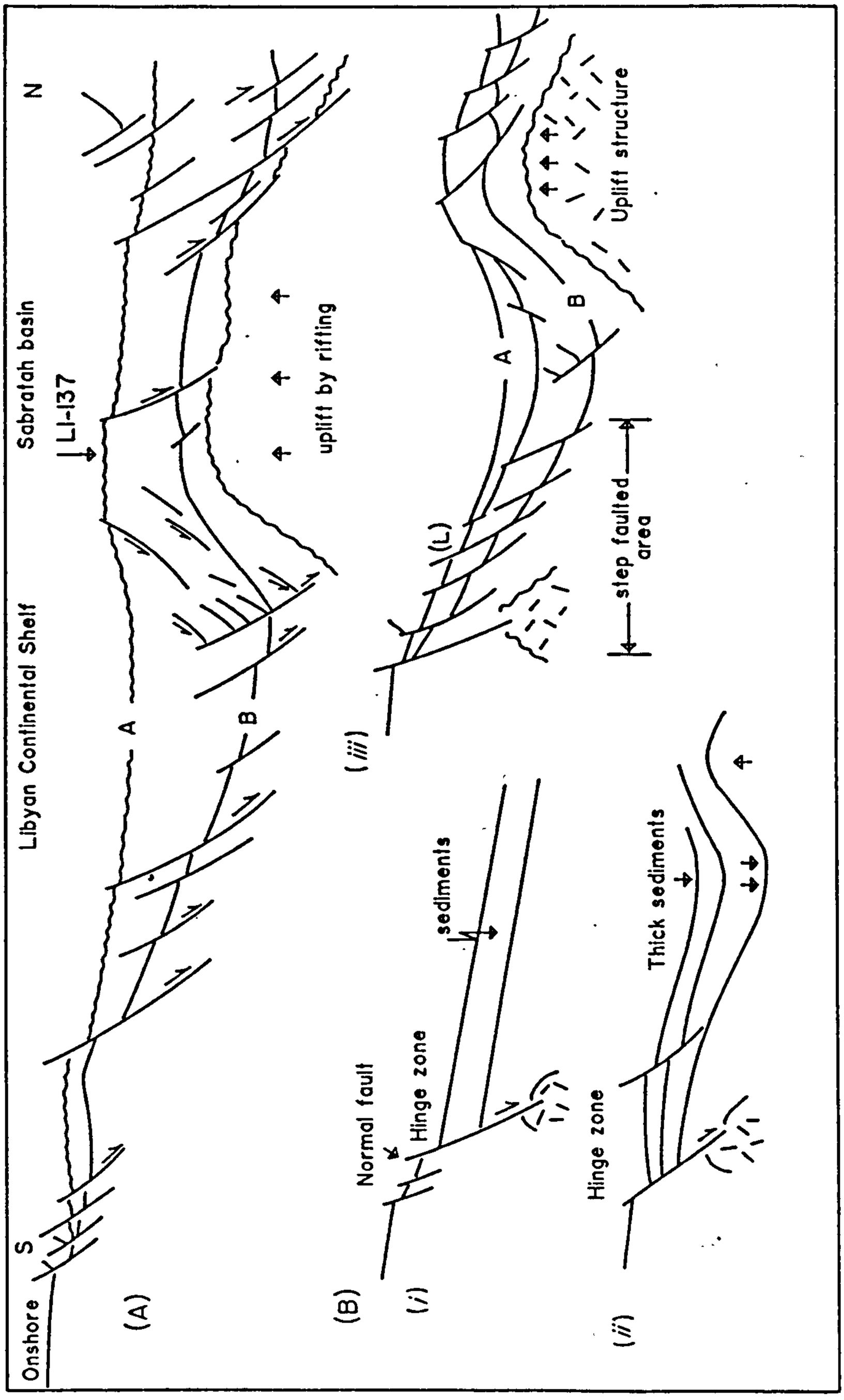

Figure 4.21: a-The geoseismic section sketched from the seismic line ZB-21, which is located along the Continental Shelf near well L1-137 in a S-N direction, as shown in Figure 4.17. b-The development stages of the Libyan Continental Shelf, between the Late Triassic/Early Jurassic and the present. (L) is the listric curvature growth fault.

and gravity anomaly over the structure seen in the total field intensity magnetic and Bouguer gravity maps, suggest that this structure results from high density (volcanic) rocks. Listric faults are common in the step-faulted area overlying the structure, due to the tectonic activity as shown in sketch (iii).

4.8.2.3 The Thick Sediment Domain

A thick sediment domain is located in the east-central part of the study area as shown in Figure 4.6. The seismic profile BB′ (Figure 4.1) is the most useful profile to examine the geological features and the tectonics of this part of the study area. The reflection data along this profile, shown in Figure 4.22, indicates a complete transect of a thick Tertiary and Upper Cretaceous basin, as in the central part (C), which is relatively less deformed. Halokinetic phenomena are less intense than in the western part, probably due to the greater thickness of the sediments in the central and northeastern part of the deep basin. Salt pillow structures are common and characterized by arched structures without piercement, which are a good target for oil exploration. The salt influences disappear towards the eastern part of the study area. The major aspects of the seismic sequences seen in profile BB′ are:

- **The study area is underlain by Mesozoic and Tertiary sequences, which are represented by a thick sedimentary unit lying between the Salambo/Cherahil Formation (base of Oligocene), and the Zebbag Formation(U-Cretaceous). The thick sediment region (C), is relatively less deformed than the southern area (S).**

- **Thick Triassic salt layers probably occur low in the sequence (eg base of the well L1-137 lies in an evaporite group). These were overloaded and compacted by the sediments and during the late Cretaceous the salt was forced to migrate into the western part (*salt area*).**

This interpretation implies that the salt movement in NW-Libya was from eastern to western parts. Borehole data have provided good ties with profile BB′ and with many

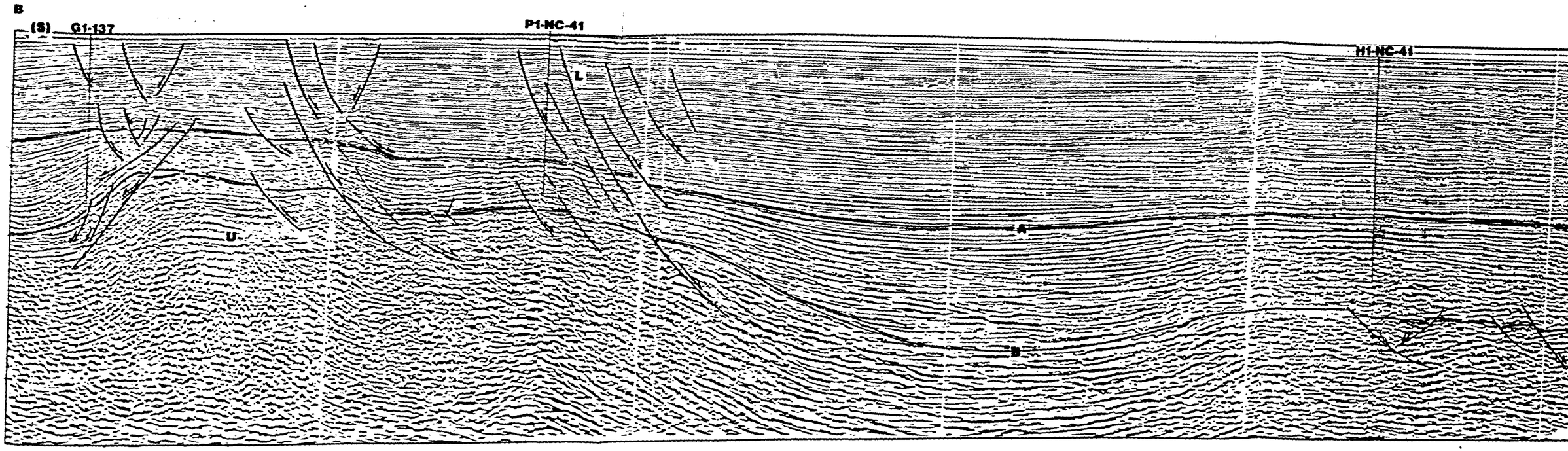

Figure 4.22: Migrated seismic profile BB′ across the study area in a NE-SW direction, as shown in Figure 4.1.

B'

E1-NC-41

(M)

(C)

NC-41

reflectors, particularly the base of the Oligocene Formation, which has a clear distribution over the area. The Zebbag Formation, appears clearly in the southern part of the area (S), as described in the previous section.

4.9 Salt and fault association.

The relationship between faults and salt features in the Sabratah Basin are very close, the alignment of salt features being sub-parallel to the direction of the controlling tectonic elements of the Coastal Fault system (offshore) and Jeffara fault system (onshore). The structural maps of Figures 4.4 and 4.5, show this relationship. Thus an E-W major trend of the salt and fault system is seen along a major salt wall and diapirs in the west-central part of the study area (salt domain), which indicates a strong relationship between salt movement and tectonic activity. This provides a good indication that the initiation of salt movement and diapirism were both halotectonic (controlled by tectonic forces), and halokinetic (controlled by gravity) processes. The E-W Coastal Fault system in the southern part is sub-paralled to the regional E-W salt trend of the west-central part, and the Jeffara fault system of NW-onshore Libya. Various cases of fault-related salt movement have been demonstrated in the study area, such as major dip-slip, strike-slip, listric and antithetic, and subsidence faults. Several examples of migrated time seismic sections have been described to show the fault association with salt structure. An example of a migrated seismic section was shown in Figure 4.13, which indicated a major feature present in faults (F and F′) of very large throws (over 500 ms, two-way time) affecting all salt structure sequences up to Oligocene in age. Another example of a migrated seismic section at the Continental Shelf Domain and the edge of the Salt Domain, was shown in Figure 4.12. This indicates the presence of a listric fault which affects all levels up to those of Miocene age, and is often related to overburden subsidence. The listric curvature of the main fault (L) induced some antithetic faulting which resulted in the graben feature seen in the shallower section. Figure 4.13 is a migrated section, which shows the overburden faulting related to salt movement (E) is a small collapse graben structure above the crest of a salt pillow.

4.10 Summary

The seismic investigation has included the detailed interpretation of several seismic lines which cross the study area. These have been tied to available borehole data. Two-way time structure contour maps have been produced, as a result of the seismic interpretation. According to these maps, the study area can be divided into three structural domains:*the Salt Domain*, *the Continental Shelf Domain*, and the *Thick Sediment Domain.* The Salt Domain represents the salt tectonic phenomena in the western and central part of the study area. Selected seismic profiles crossing this domain confirm the distribution of the salt structures and different stages of salt piercement. The salt configuration map of the study area, has been used to classify the distribution of the salt in this area into: (i) *Salt Walls*, (ii) *Salt Diapirs*, and (iii) *Salt Pillows.* Several salt structure examples have been used to demonstrate the salt type, shape, and size.

The Continental Shelf Domain is located in the southern part of the study area, which consists of a part of the African continental margin which developed during Late Triassic or Early Jurassic time. This has been affected by extensional faults related to cratonic rifting and is characterized by considerable subsidence and volcanic activity. It was examined by the few available seismic lines, and a geological model has been established. The magmatic activity phases (Late Cretaceous/Early Tertiary and Middle/Upper Cretaceous) have been investigated by both migrated seismic sections and well data. The Thick Sediment domain is located in the east-central part of the study area; the reflection data for this area indicates a complete section of upper Cretaceous deposits and a thick Tertiary basin, which represents the ideal condition for source rock maturation. The hydrocarbon is believed to have accumulated in the deepest part of the basin (thick sediment sequences), and migrated to the northern part. The salt migration occurred from the eastern part to the western part of the study area, under the overload of the thick sediment sequences in the eastern part. The major tectonic elements are the Coastal Fault system and the sub-parallel salt trend which, has a dominantly E-W trend in the study area.

The seismic investigation gives a regional picture of the salt tectonics and the structural geology (salt structures) of the study area, as well as an indication of the salt configuration in the area. The limitation of the seismic response below the middle Cretaceous makes the interpretation uncertain below this , particularly in the Thick Sediment Domain. Since the present seismic data do not reveal seismic events below the middle Cretaceous, it is not possible to deduce the history of salt structures and their stages of development below this level. Deep seismic reflection and refraction surveys are to be recommended for future work in this study area.

Chapter 5

Gravity and Magnetic data processing and modelling techniques.

5.1 Introduction

This chapter describes the methods used for processing and interpreting the gravity and magnetic data from the study area. Various filtering and other analytical methods have been used to delineate regional and local anomalies. These include the methods of *polynomial surface fitting, Chebyshev series representation, second-derivative calculation, upward continuation and power spectral analysis.* The low and high pass filtered anomalies are presented as a reasonable representation of the gravity and magnetic anomalies arising from the deep and shallow sources respectively. Two dimensional modelling techniques have been used to improve the geological interpretation of these anomalies.

The broad purpose of the study is to produce a geological interpretation of the gravity and magnetic data, delineating the deep, intermediate and shallow structures of the study area. The interpretation involved an analysis of gravity and magnetic intensity data sets, making use of various derived maps including regional and residual, upward continued, second derivative and low and high pass filtered.

5.2 Sources of data

All the available gravity and magnetic data for this study have been provided by the National Oil Corporation of Libya. The types of data are listed below:

5.2.1 Gravity data

The gravity data for the study may be summarized as follows:

(a) Maps at scales of 1:500.000 and 1:250.000 of:

- Bouguer gravity.
- Free air gravity.

(b) Formation density logs.

5.2.2 Magnetic data

Combined marine and aeromagnetic survey data sets (1975 – 1986); including the following:

(a) Maps at scales of 1:500.000 and 1:250.000 of:

- Total field magnetic anomaly intensity.
- Total field magnetic anomaly reduced to the pole.
- Second vertical derivative of anomalous magnetic field reduced to the pole.

(b) Borehole cuttings samples.

The gravity and magnetic surveys of the NW-offshore Libya, were undertaken between 1975–1988 by the Sirte , Elf-Aquitaine, Mobil, and Agip Oil Companies. This thesis utilizes the 1mGal contour interval Bouguer gravity map and the 5 nT contour interval total magnetic field intensity map, produced by the Sirte Oil Company (1988).

5.3 Data processing and reduction of gravity and magnetic maps

The gravity and magnetic data used in the study were processed by Robertsons Research Group PLC., in 1988. The processing procedures adopted are as the follows:

5.3.1 Basic data processing

(a) Gravity data :

1. Despiking
2. Meter constant and Eotvos correction
3. Meter inverse filtering
4. Latitude and free air correction
5. Deletion of bad data spots caused by acquisition errors
6. Bouguer correction
7. Merging with previous data sets
8. Gridding and contouring

(b) Magnetic data:

1. Despiking
2. Base station correction
3. Internat. Geomag. Reference Field (IGRF) removal
4. Deletion of line ends (affected by ship turning varying ship' field at sensor)
5. Merging with previous data sets
6. Gridding and contouring

5.3.2 Data reduction

The original Bouguer anomaly map is shown in Figure 5.1, which uses a 1 mGal contour interval, and has been digitized on a 1 km rectangular grid, as shown in Figure 5.2. The resultant (70x70) array of gravity values was contoured, the X axis along the W-E direction and the Y axis along the N-S direction, using the GINOSURF contouring package. The shape and amplitude of the anomalies in the original and digitized maps are in very close agreement. This rectangular area has been selected to cover the negative anomalies in the western and central parts, and the positive anomalies in the southern part of the study area.

The original total field magnetic anomaly map is shown in Figure 5.3 which is plotted with a 5 nT contour interval. This has been digitized on a 1 km rectangular grid, as shown in Figure 5.4. The rectangular area was digitized on a 1 km grid, the X axis along the W-E and the Y axis along the N-S direction. The rectangular areas have been selected in order to apply different analytical methods. The resultant (85x85) and (55x55) array of total field magnetic anomaly values was contoured, using the GINOSURF contouring package. Comparison of these maps with the original maps in Figure 5.3 reveals general good agreement in the shape and amplitude of the anomalies featured.

The grid values used affect the computation time. The main disadvantages of using a finer grid is that it would exceed the capacity of the available software.

5.4 Possible sources of gravity anomalies

Gravity anomalies in the study area might be expected to arise from the following sources:

1. Salt diapiric structures, which have been demonstrated from seismic data to occur extensively in the western part of the study area. Salt is typically of lower density than the surrounding sediments and so should give rise to gravity lows.

TWO-WAY TIME CONTOUR MAP OF THE TOP OF THE ZEBBAG FORMATION

KEY

- Major Fault
- Minor Fault
- Uncertain Fault
- Salt Piercement
- Closed High
- Closed Low
- Study area boundaries

contour interval 200m/sec

AUTHOR: M. ABUHAJAR

ZUWARAH

TRIPOLI

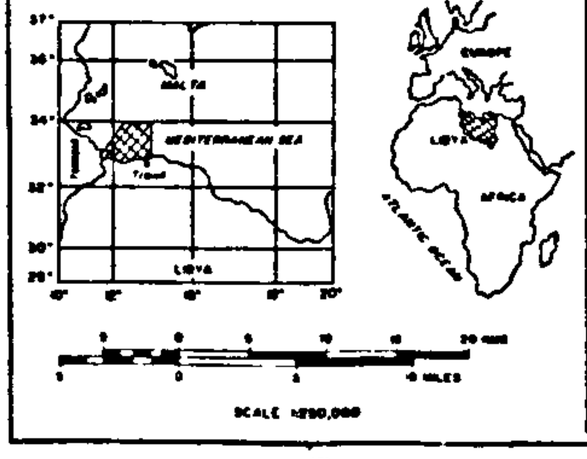

SCALE 1:250,000

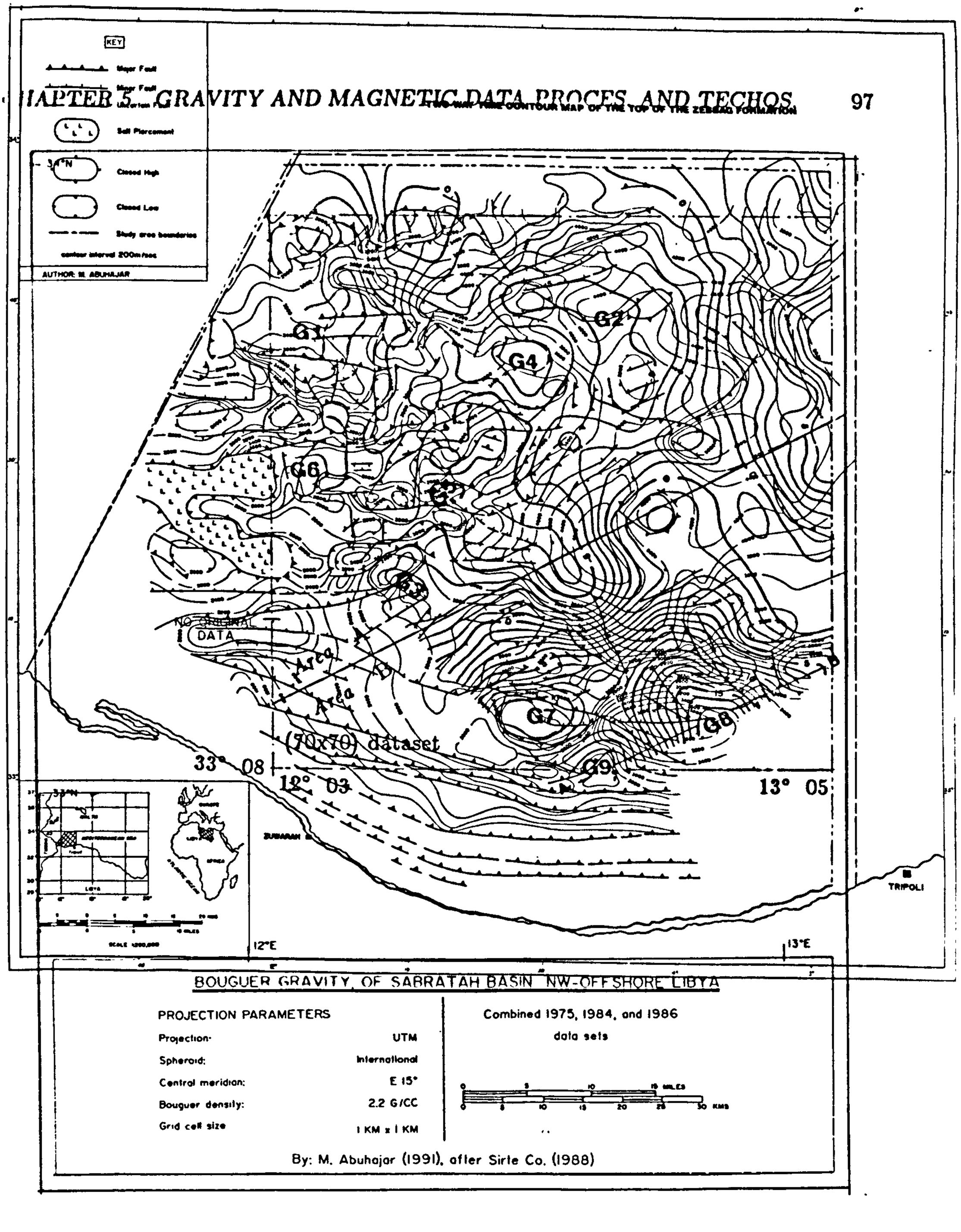

Figure 5.1: The original Bouguer gravity map of the study area, showing the rectangular area (70x70) defined for the application of the analytical methods. Contour interval 1 mGal. G1–G9 are the conspicuous gravity anomalies. *This is reduced copy of the full scale gravity map (1:500.000).*

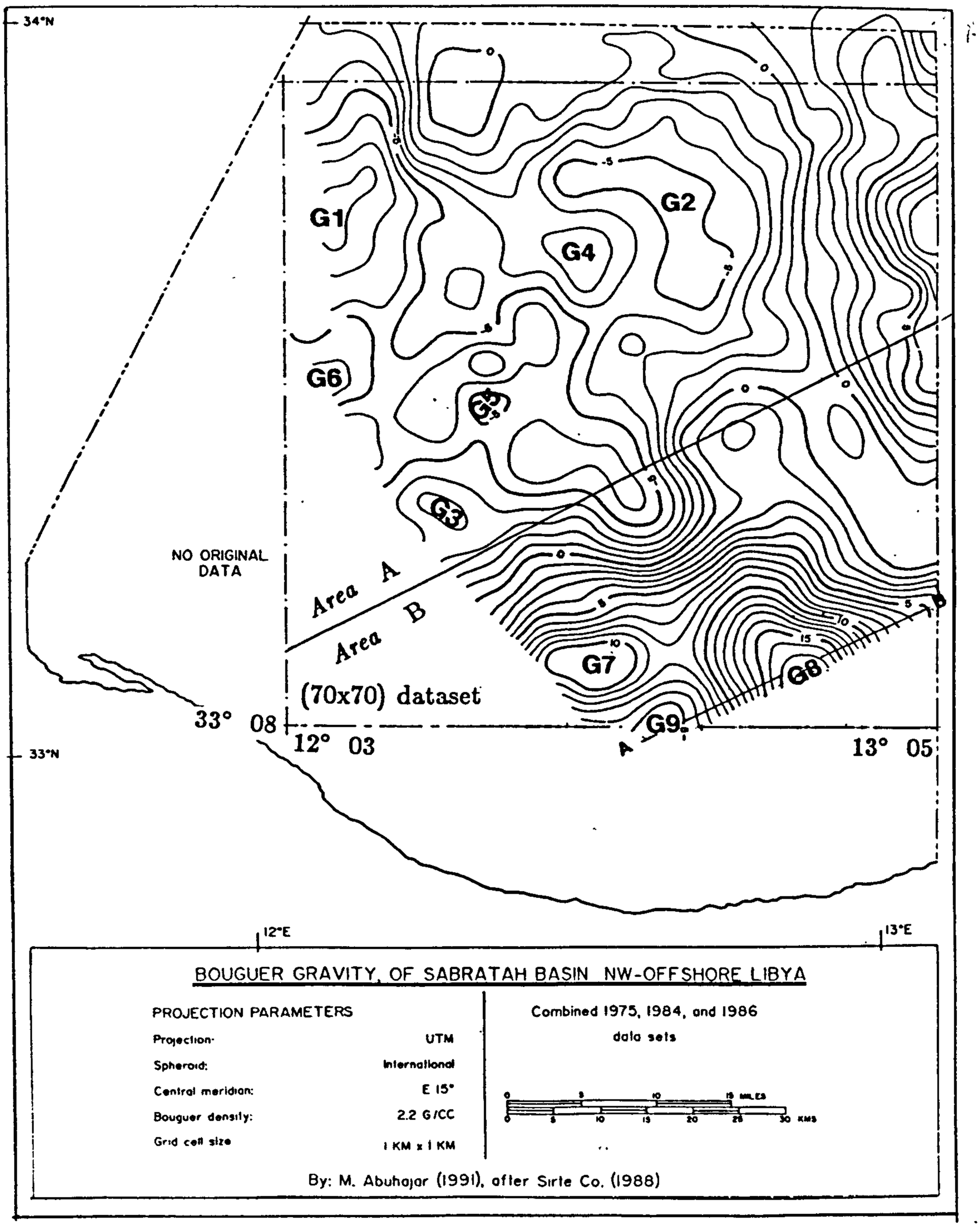

Figure 5.1: The original Bouguer gravity map of the study area, showing the rectangular area (70x70) defined for the application of the analytical methods. Contour interval 1 mGal. G1–G9 are the conspicuous gravity anomalies. *This is reduced copy of the full scale gravity map (1:500.000).*

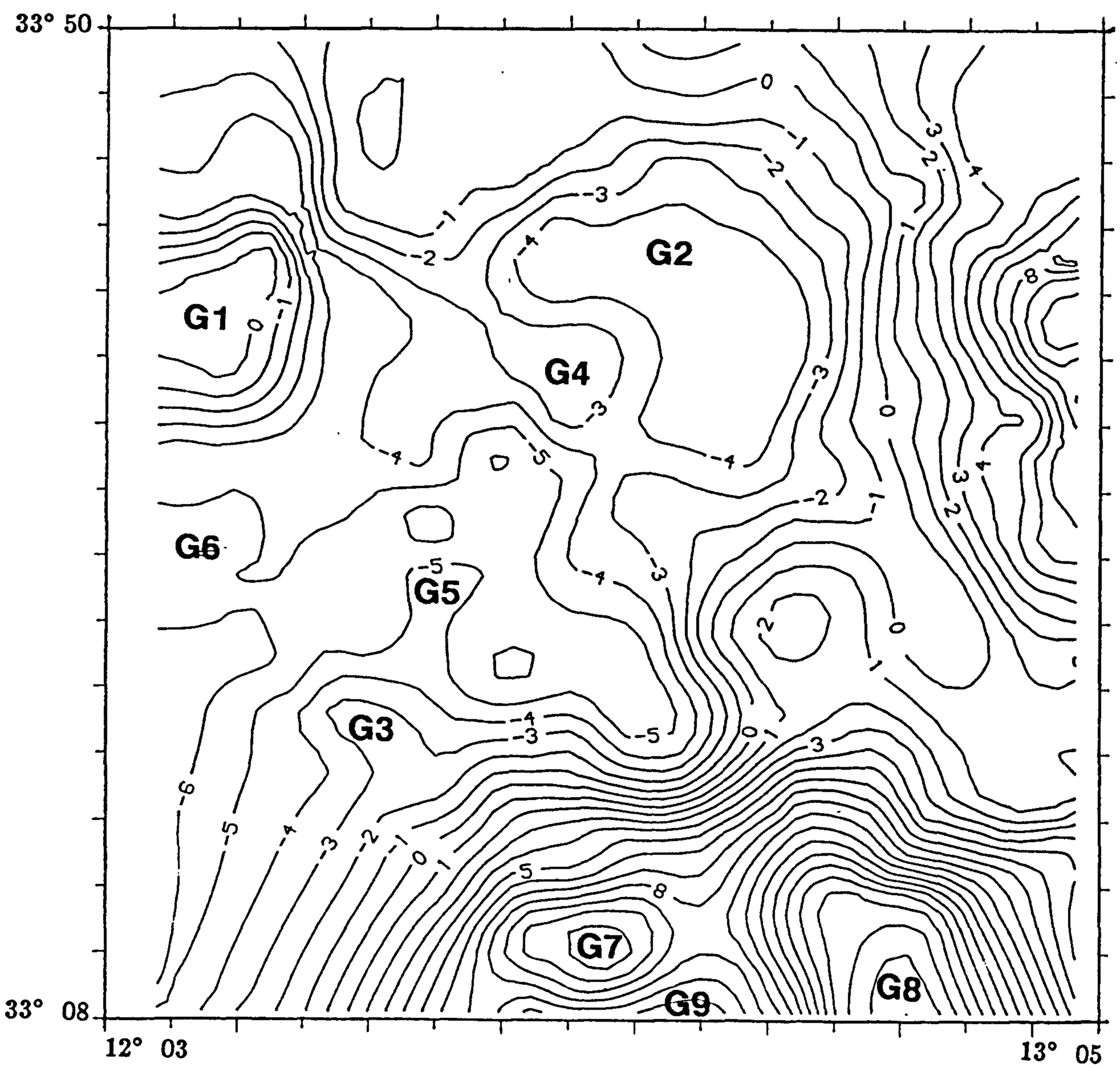

Figure 5.2: The digitized Bouguer gravity map of the study area. Grid spacing 1 km. Contour interval: 1 mGal.

TWO-WAY TIME CONTOUR MAP OF THE TOP OF THE ZEBBAG FORMATION

KEY

- Major Fault
- Minor Fault
- Uncertain Fault
- Salt Piercement
- Closed High
- Closed Low
- Study area boundaries

contour interval 200m/sec

AUTHOR M. ABUHAJAR

ZUWARAH

TRIPOLI

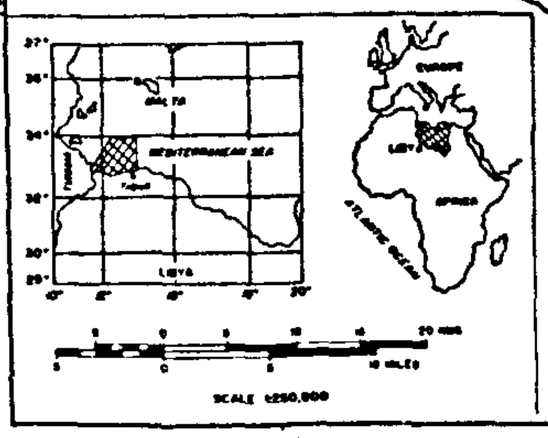

SCALE 1:250,000

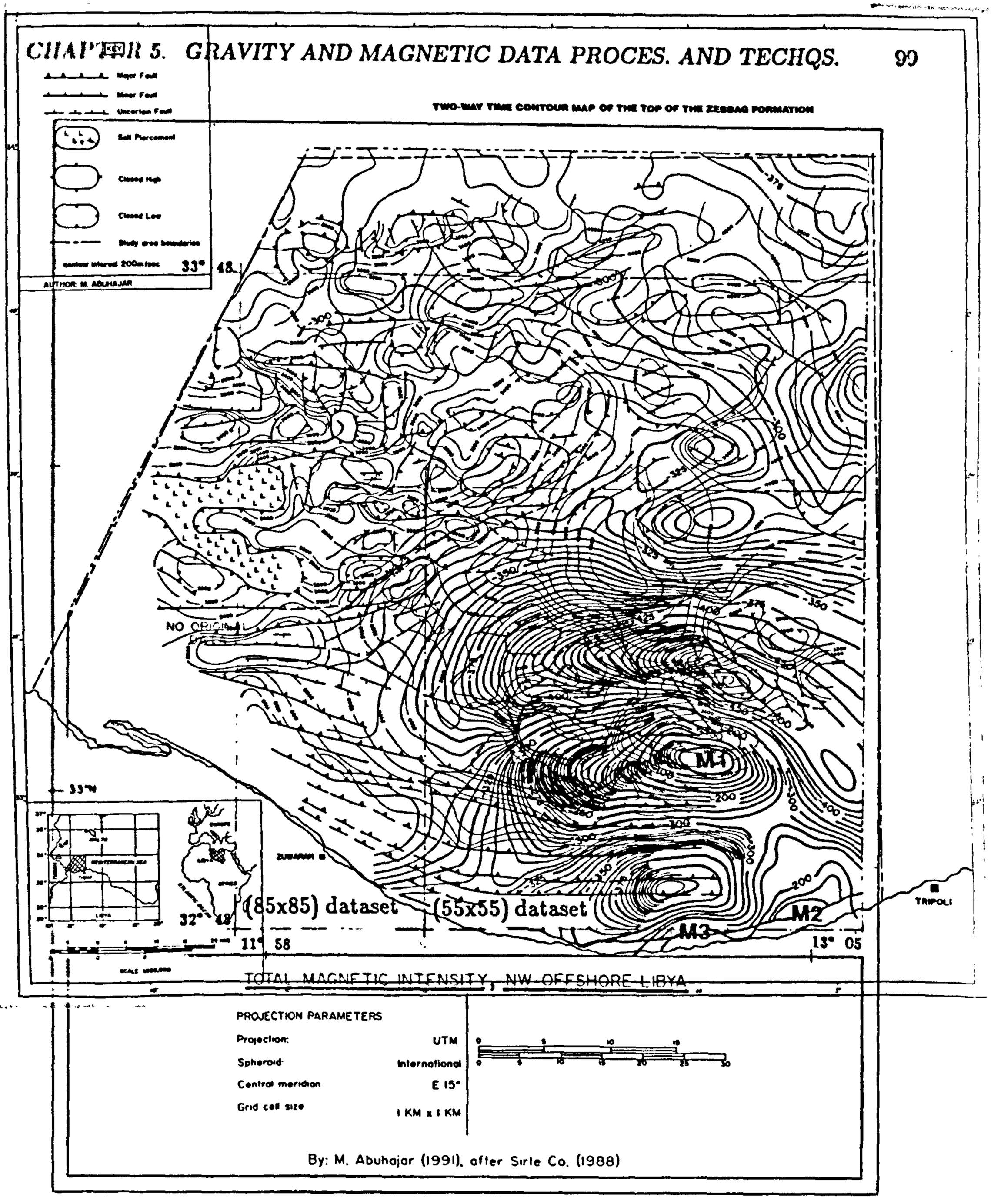

Figure 5.3: The original total field magnetic anomaly map of the study area, showing the rectangular areas (85x85 and 55x55) defined for the application of the analytical methods. Contour interval 5 nT. M1, M2, and M3 are the possible sources of magnetic anomalies. *This is reduced copy of the full scale magnetic map (1:500.000).*

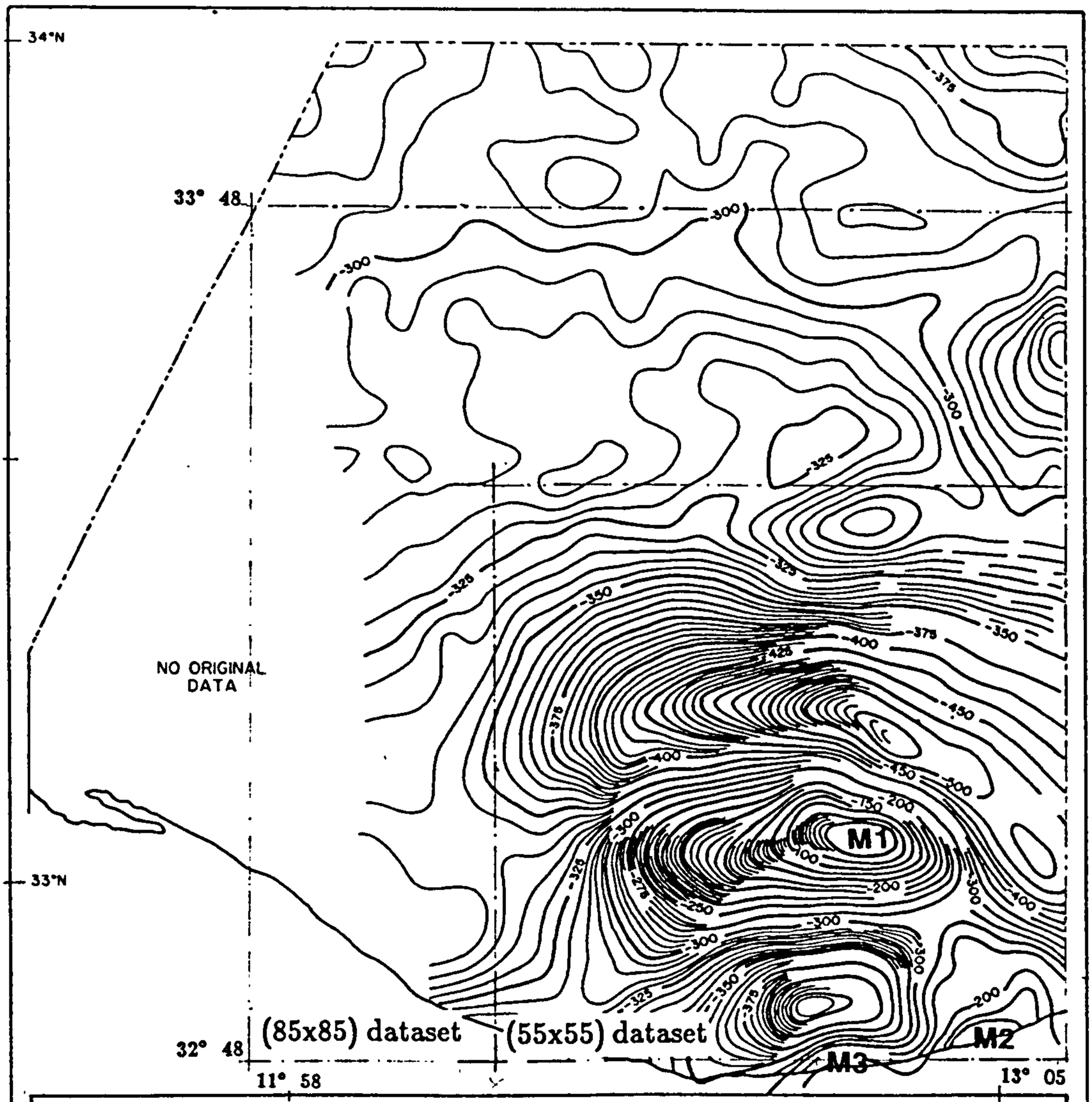

Figure 5.3: The original total field magnetic anomaly map of the study area, showing the rectangular areas (85x85 and 55x55) defined for the application of the analytical methods. Contour interval 5 nT. M1, M2, and M3 are the possible sources of magnetic anomalies. *This is reduced copy of the full scale magnetic map (1:500.000).*

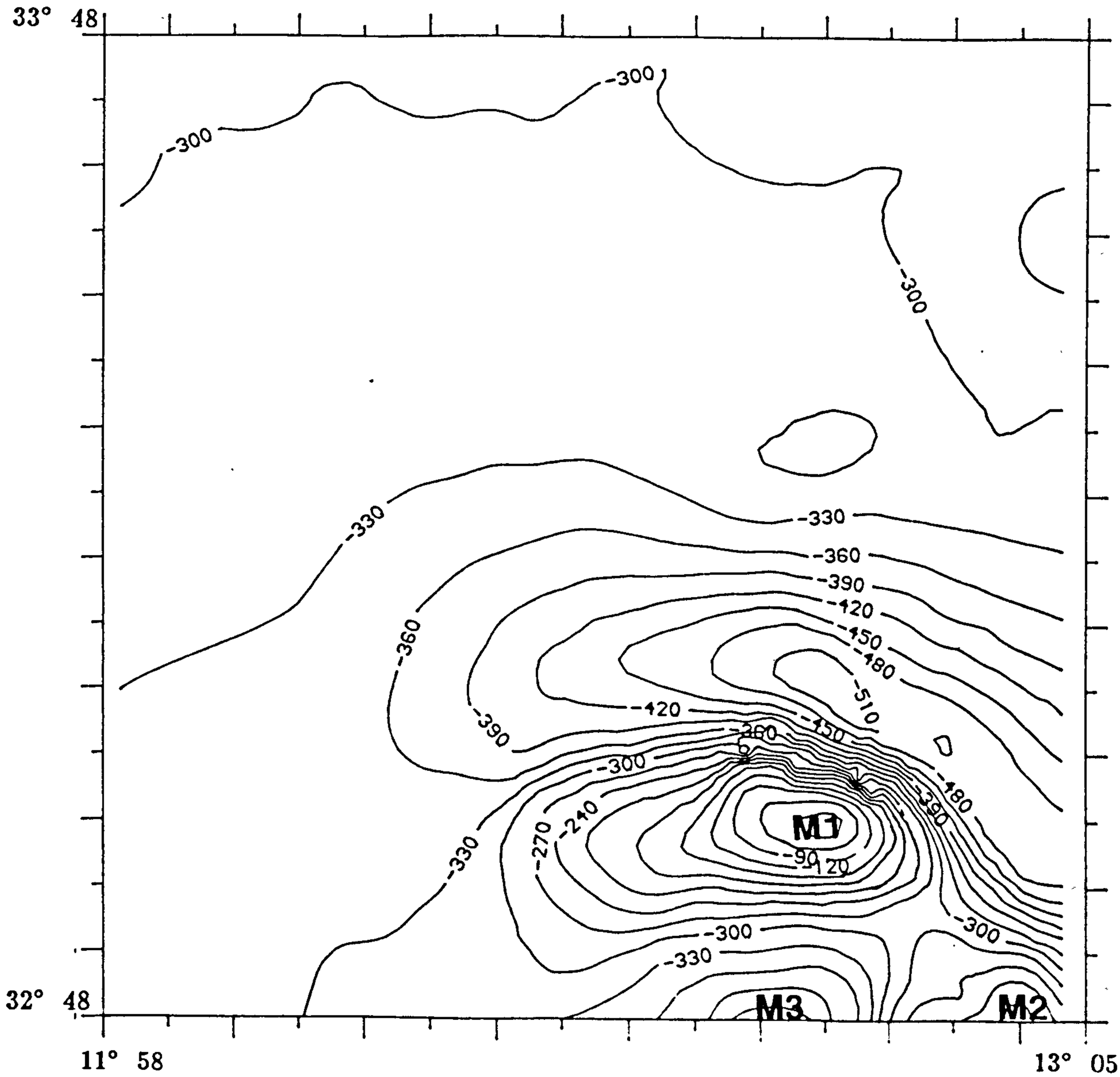

Figure 5.4: The digitized total field magnetic anomaly map of the study area. Grid spacing 1 km. Contour interval: 30 nT. Individual magnetic highs (M1, M2, and M3) are identified.

2. Infilled Basins involving larger than usual accumulations of sediments (approx. 10 km), typically of lower density than underlying basement.

3. The cap rocks above the crest of the salt structures give rise to a higher density than that of the surrounding sediments at the same level and hence may result in a localized positive anomaly above the center of the salt structure.

4. Major basic intrusive or extrusive volcanics, will give rise to gravity highs. Some of the features identified on the seismic profiles as basement horsts could be such intrusives, of which the most likely candidate is the uplift structure apparent in the southern part, associated with magnetic anomalies M1, M2 and M3 of Figure 5.3.

5.4.1 Description of Bouguer anomaly map

According to the two-way time structural maps, shown earlier (Figures 4.4 and 4.5), the main negative gravity anomalies are clearly associated with the Salt and Thick Sediment Domains, located in the western and central parts of the study area, respectively. The main positive gravity anomaly is possibly associated with the intrasedimentary volcanics intervals, and the uplift structure in the southern part (Continental Shelf Domain).

The Bouguer gravity map (Figure 5.1) has numerous positive and negative anomalies which are labelled for ease of reference and listed in Table 5.1. The 0 mGal gravity contour separates the negative Bouguer values of the Thick Sediment Domain (north-central) and Salt Domain (west), from the positive Bouguer values of the uplift structure in Continental Shelf Domain (southern part), as shown in Figure 5.1.

The negative gravity anomalies are concentrated in area (A) are and attributed to the Thick Sediment Domain and the structures in Salt Domain.

Anomaly G1 is attributed to the low density of the rim-syncline of the salt dome flanks, which produces negative anomaly values lower than -5 mGal.

Anomaly G2 is attributed to the deepest part of the basin (eastern part), defined by seismic data.

Area	*Anomaly code*	*H/L*	*Geographical location*	*Source*
A	G1	L	Western part (Salt Domain)	Flank of rim-syncline
A	G2	L	Central part (Thick Sediment Domain)	Thick sedimentary infilled of basin
A	G3	L	K1-137 location	Salt diapir + cap rock
A	G4	L	C1-NC-41 location	Salt pillow
A	G5	L	A2-NC-41 location	Salt diapir + cap rock
A	G6	L	I1-137 location	Salt diapir + cap rock
B	(G7,G8,G9)	H	Southern part (Continental Shelf Domain)	Intrasedimentary volcanics or basement uplift structure

Table 5.1: A listing of the geographical location and possible source of the most important gravity anomalies shown in Figure 5.1. H is high and L is low.

Anomalies G3, G4, G5, and G6, are attributed to salt structures (salt diapirs). Seismic interpretations presented in Chapter 4 establish that there is no likely cause for such gravity features other than salt structures (domes). However, as the top of these structures (cap rocks) are so shallow, it is probable that the uppermost part of the salt has a higher density than that of the surrounding sediments at the same level, hence giving rise to a positive anomaly above the center of the dome (Nettleton 1976; Dobrin 1976). The cap rock over the salt structures might produce a definite positive gravity effect which is more or less central within the surrounding negative anomaly due to the salt. The cap rock effects can be separated out by estimating the magnitude of the positive components which depend on the depth, thickness and breadth of the cap rock. Nettleton (1976) and Dobrin (1976) suggest that a common magnitude for such cap-rock anomalies is 2 mGal.

The salt structure anomalies (G3, G5, and G6) represent shallow structures associated with the cap rocks; these thick cap rocks may produce a small and rather broad

negative gravity effect, within which there are strong positive anomalies.

The large positive anomaly area (B), which includes anomalies G7, G8, and G9 in the southern part (Continental Shelf Domain), appears to be associated with the intrasedimentary volcanic intervals, and basement uplift structure. The anomalies G8 and G9 are incomplete due to the termination of the survey along the Tripoli coastal line. The maximum amplitude of the anomaly is 18 mGal. An overall NW-SE trend is observed in the Bouguer anomaly map.

5.4.2 Description of Free Air gravity map

The Free Air gravity map, on a scale of 1:500.000 (Figure 5.5) shows large negative values of Free Air anomalies in the central part (G2, G4 and G5) associated with the main sedimentary basin, and in NW part, anomaly G1 associated with a thick rim-syncline. However, the salt trends in the western part (G6 and G3) produce less negative values than the surrounding rock, particularly on the tops of the salt diapirs (due to cap rock effects). In the southern part (G7 and G8) clearly identified structures occur, with range of amplitude between 5 and 10 mGal.

5.4.3 Borehole formations density logs

Since the the densities and density contrasts are fundamental factors controlling gravity anomalies, reliable density values are required for the gravity modelling. These can be determined from the formation density log data. Several well density logs (compensated neutron formation density logs) are available for this study. The densities encountered in some boreholes are listed in Table 5.2.

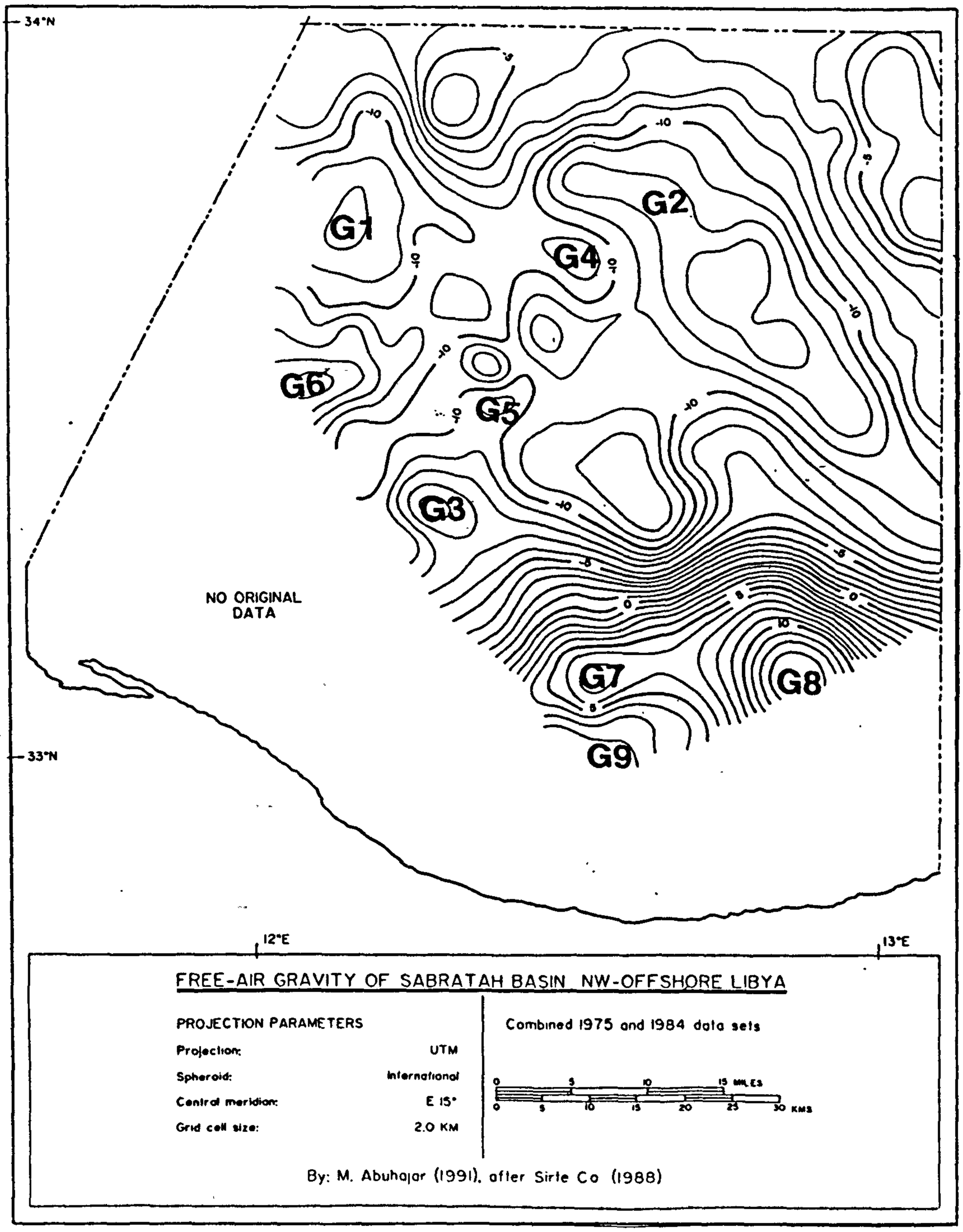

Figure 5.5: Free Air anomaly map of the study area. Contour interval 1.0 mGal. *This is reduced copy of the full scale Free Air map (1:500.000).*

Geological unit	*Ave. density* (kg/m^3)
Mahmoud to Beglia	2140
Ain Grab	2400
Upper shaly Salambo	2260
Lower limy Salambo	2450
Ketatna	2550
Cherahil (B)	2470
Reinche	2500
Cherahil (A)	2550
Metlaoui	2650
Volcanics	2550
El-Haria	2600
Abiod	2650
Aleg	2500
Douleb	2700
Zebbag	2850
Volcanics	2650

Table 5.2: Density of various rocks in the study area. (determined from formation density log data.

Anomaly code	*Geographical location*	*Source*
M1	Southern part (Continental Shelf Domain)	Intrasedimentary volcanics, and basement uplift structure
M2	Western Tripoli (Continental Shelf Domain)	probably intrusive volcanics and shallow basement
M3	Western Tripoli (Continental Shelf Domain)	probably intrusive volcanics and shallow basement

Table 5.3: A listing of the geographical location/source of the most important magnetic anomalies shown in Figure 5.3.

5.5 Possible sources of magnetic anomalies

1. Intrasedimentary volcanic, extrusive lavas and volcaniclastics occur within the sedimentary section. If sufficiently basic and thick, these could give rise to detectable magnetic anomalies, though these are likely to have low-amplitudes.

2. Igneous intrusives: Igneous rocks intrude the sedimentary section , and are characterized by higher susceptibility and a stronger remanent magnetization than the sediments.

3. Shallow basement uplift structures.

5.5.1 Description of the total field magnetic intensity anomaly map

Figure 5.3 shows the total field magnetic anomalies; the codes of the anomalies are listed in Table 5.3. Anomaly M1 is attributed to the occurrence of intrasedimentary volcanic rock and the basement uplift structure, discussed in chapter 4. Intrasedimentary volcanic rocks are known from drilling and seismic data to occur in the Paleocene and at the base of the Upper Cretaceous. The upper interval is likely to produce only small amplitude and short

wavelength features due to the low magnetic susceptibility and remanent magnetization of the rocks (as determined from laboratory measurement- see Chapter 6). The major strong anomaly is attributed to the lower volcanic interval which has a stronger susceptibility and NRM intensity, and also is expected to be much thicker than the upper interval. The basement uplift structure, may also be associated with a high magnetic intensity anomaly.

Anomalies M2 and M3 are attributed to the magmatic activity associated with shallow basement, which occurred with the rifting and subsidence of the Sabratah Basin during Jurassic and Cretaceous times. The anomalies have large amplitude, ranging between up to 300 nT. They are believed to be caused the intrusive volcanic plugs which penetrated the overlying sediments. The Thick Sedimentary and Salt Domains areas, are associates with low amplitude magnetic intensity anomalies ranging between (-275 and -325 nT).

5.5.2 Description of reduced-to-pole-anomaly map

The shape of a magnetic anomaly caused by induced magnetization changes with latitude due to the changing inclination of the Earth's magnetic field vector. In consequence of an inclined magnetization vector it is usual for a magnetic anomaly to be centred away from the apex of the causal body though the amount of offset depends also on the shape of the source body (Baranov et al, 1964). On the reduced-to-the-pole anomaly map (Figure 5.6), the anomalies appear as if the Earth's magnetic field were vertical or as if the area was located at the magnetic pole. The magnetic highs are thus located over the bodies which cause them.

The high intensity magnetic anomalies M1, M2, and M3 in the total magnetic reduce-to-the-pole map represents the real position of the causal bodies. Therefore, the magnetic profile AB selected for modelling has been marked on this map across the M1 anomaly.

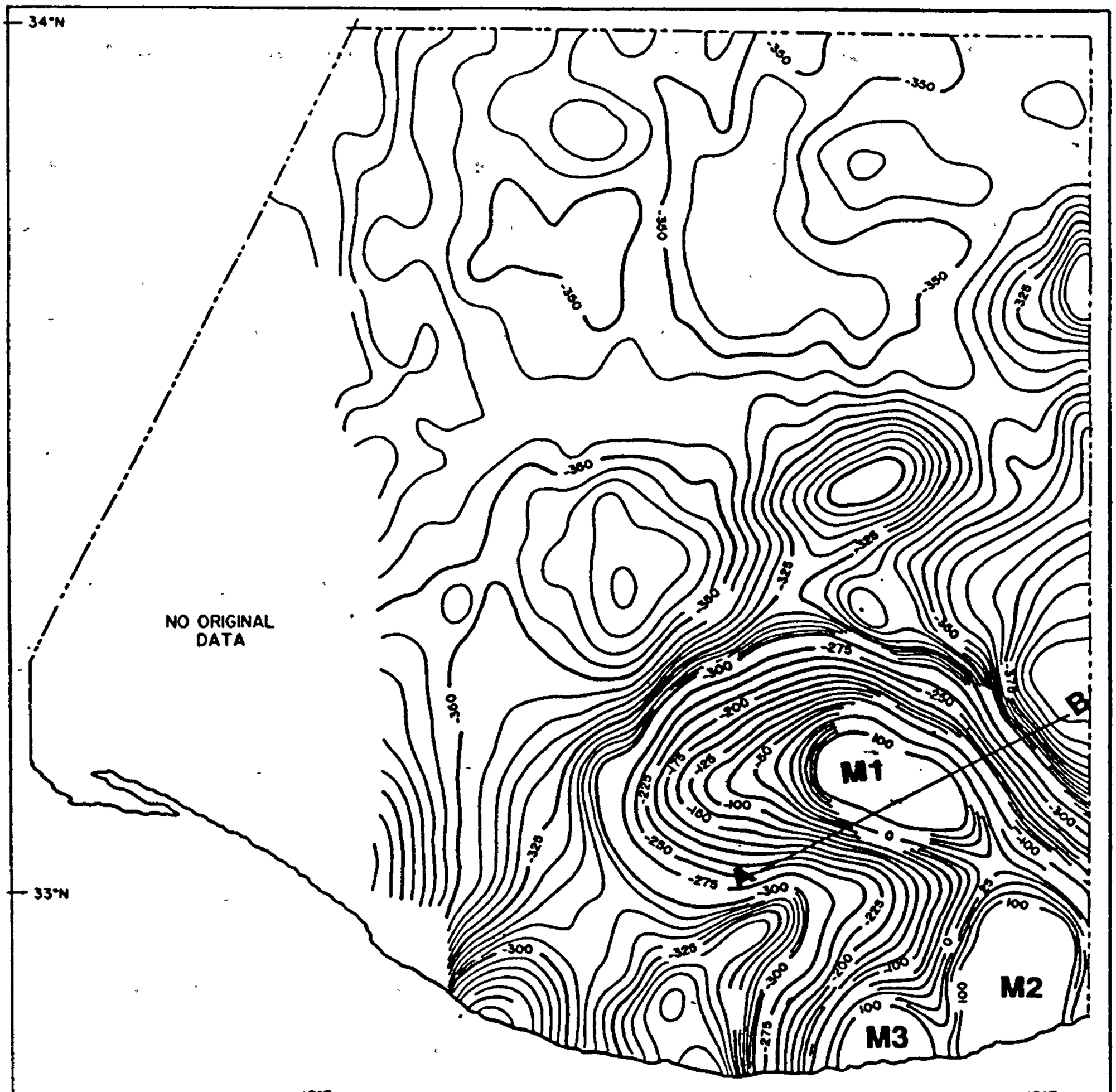

Figure 5.6: Map of total field magnetic anomaly reduced-to-the-pole, for the study area. Contour interval (5 nT). M1, M2, and M3 are possible sources of magnetic anomalies. *This is reduced copy of the full scale map (1:500.000).*

5.5.3 Magnetic susceptibility from borehole cuttings samples

In order to interpret or model the magnetic anomalies, some knowledge of the magnetic properties of samples from the well sites is required. A number of samples from the boreholes K1, L1, H1-137, are available. The susceptibility and NRM intensity of these samples has been measured on a Highmoor magnetic susceptibility bridge, and Molspin magnetometer, respectively. The results are presented in Tables 5.4 5.5 5.6 5.7 and 5.8.

5.6 Filtering and analytical methods applied to potential field maps

The gravitational and magnetic anomalies are both potential fields. The potential at any point is defined as the work necessary to move a unit mass or pole from an infinite distance to that point through the ambient field (eg Kearey et al 1984).

An essential initial stage in gravity and magnetic interpretation is that of identifying and isolating individual anomalies of interest. This requires removal regional effects, in order to leave the remaining residual anomalies. The operation of separation of regional and residual anomalies is mathematically similar to the filtering effect of electric circuits (Dean, 1958; Grant and West 1965; Fuller 1967). Original graphical methods have now been largely replaced by numerical methods. Nettleton (1954) pointed out the advantage and limitation of both classes of treatment.

In the present study computer programs were used for the purpose of applying various analytical methods to the two-dimensional gravity and magnetic data described in the preceding sections. Application of these analytical methods, combined with geological and seismic considerations, can most successfully delineate individual anomalies. Some description of the analytical methods, and of the computer programs for applying them to the gravity and magnetic maps, is gives in the following sections.

Specimen code	$KX10^{-3}SI$ *(whole sample)*
8430	1.15
8490	0.59
8500	0.53
8550	0.57
8600	3.45
8650	5.19
8700	11.61
8750	11.12
8800	8.28
8850	7.31
8900	14.93
8950	10.62
8970	8.65
9000	8.40
9050	9.42

Table 5.4: Magnetic properties of the samples from well H1-137 (*whole sample).* The average susceptibility from the 15 specimens is: $5.855X10^{-3}SI$. The NRM intensity (single measurement for a small cutting sample) is 14.606 mA/m.

Depths of interval (ft)	$KX10^{-3}SI$ *(Magnetic concentrate)*
8510–8950	34.67
8610–8640	33.22
8660–8690	37.56
8710–8740	36.11
8760–8770	39.00
8780–8790	37.56
8810–8830	46.23
8840–8860	46.23
8870–8870	49.10
8890–8890	43.34
8910–8910	54.90
8940–8960	52.00
9010–9040	44.80

Table 5.5: Magnetic properties of samples from well H1-137 (*magnetic concentrate)*. The average susceptibility for the 13 intervals is:$42.16X10^{-3}SI$. The NRM intensity (single measurement for a small cutting sample) is 14.606 mA/m.

Specimen code	$KX10^{-3}SI$ *(whole sample)*
9450	6.32
9500	4.66
9550	2.71
9600	2.63
9650	1.29
9700	1.13
9750	3.80
9800	5.07
9850	15.21
8900	5.39
9950	6.66
10000	4.75
10050	2.33

Table 5.6: Magnetic properties of samples from well L1-137 (*whole sample*). The average susceptibility from the 13 specimens is:$3.81X10^{-3}SI$. The NRM intensity (single measurement for a small cutting sample) is 281.651 mA/m.

Depths interval(ft)	$KX10^{-3}SI$ *(Magnetic concentrate)*
9530–9640	52.00
9760–9820	43.34
9840–9890	144.446
9910–9920	144.466
9930–9990	144.466

Table 5.7: Magnetic properties of samples from well L1-137 (*magnetic concentrate).* The average susceptibility from the 5 intervals is:$92.56X10^{-3}SI$. The NRM intensity (single measurement for a small cutting sample) is 281.651 mA/m.

Specimen code	$KX10^{-3}SI$ *(whole sample)*
10160	0.41
10170	0.40
10180	1.90
10190	0.36
10200	1.16
10208	0.63

Table 5.8: Magnetic properties of samples from well K1-137 (*whole sample).* The average susceptibility from the 6 specimens is: $1.872X10^{-3}SI$. Only one single NRM measurement (a small cutting sample) was made, giving a value of 0.114 mA/m.

5.6.1 Filtering methods

Computer programs have been used in this study for the purpose of applying various analytical methods to the two dimensional gravity and magnetic data. The description of the filtering techniques, and of the computer programs used for applying them to the gravity and magnetic maps, is given in the following sections.

5.6.1.1 Polynomial surface fitting of potential field data

One of the analytical techniques used for determining regional gravity is polynomial fitting. The separation of the regional and residual anomalies can be achieved by determining the regional field as a low-order polynomial surface (Agocs, 1951). In most cases a second degree fitting is found to be satisfactory (Telford et al 1976). In the present study, the calculations of the first and second degree regional and residual field for gravity and magnetic maps will be demonstrated in Chapter 6.

5.6.1.2 Chebyshev series representation of the original field

The Chebyshev series expansion is made in order to calculate the regional field of the gravity and magnetic maps (see Maltezou 1986). A computer program was written by Maltezou (1986), to calculate the Chebyshev polynomial surface-fitting of gravity and magnetic maps. This program was used in the present study. Maltezou (1986) pointed out that this method is superior compared to the commonly used linear polynomials fitting. This method is provides an accurate mathematical procedure for surface fitting analysis, particularly revealed when a trend surface of higher than second degree is required.

5.6.1.3 Second derivative of potential fields

The calculation of the second vertical derivative of a potential field provides a method for isolating local effects, caused by smaller and/or shallower geologic features relative to

larger, regional features (Peters 1949, Henderson and Zietz 1949, Elkins 1951, Rosenbach 1953, Nettleton 1954, and Garland 1977).

Let a potential field be denoted by U (X,Y) in spatial coordinates. Since a potential field U satisfies Laplace's equation, for any potential field in a space free of sources:

$$\nabla^2 U = 0 \tag{5.1}$$

In the case of gravity, this expression can be written as

$$\nabla^2(\Delta g) = \frac{\partial^2(\Delta g)}{\partial X^2} + \frac{\partial^2(\Delta g)}{\partial Y^2} + \frac{\partial^2(\Delta g)}{\partial Z^2} = 0 \tag{5.2}$$

Where Δg is the anomalous gravity field

so that:

$$\frac{\partial^2(\Delta g)}{\partial Z^2} = -[\frac{\partial^2(\Delta g)}{\partial X^2} + \frac{\partial^2(\Delta g)}{\partial Y^2}] \tag{5.3}$$

Since the expression on the right hand side of equation (5.3) is the total curvature of the gravity anomaly surface, calculation of the second vertical derivative reflects the curvature of the anomaly surface and consequently enhance the local, near-surface sources expressed as anomalies of greater curvature. The second vertical derivative is positive over local maximum anomalies, with the zero-contour corresponding to the zero curvature points, usually marking the edges of anomalous structures. Several methods have been published for second derivative calculations. All these methods used similar procedures: averaging of potential field values obtained on grid points lying on circles of different radii and then multiplication of the average values by a set of weighting coefficients. Such a set of coefficients was published by Peters (1949). Henderson and Zietz (1949) calculated the second derivative of the total magnetic field by expanding it in terms of a Fourier-Bessel series and proposed another set of coefficients. Elkins (1951) proposed a method for determining the second derivative graphically and presented a set of numerical coefficients equivalent to the graphical method. Further sets of coefficients have been proposed by Rosenbach (1953), Henderson (1960) and Agarwal and Lal (1971). A more recent method for second derivative calculation is applied in the frequency domain. This method depends on the Fourier harmonic expansion of a potential field in two dimensions from the observed values

on a plane. It was firstly applied to gravity data by Tsuboi (1959, cited in Bhattacharyya, 1965).

In the case of gravity data, let the gravity function in two dimensions be denoted by $g(x,y)$ with the Fourier transform $G(u,v)$.

$$G(u,v) = \int_{-\infty}^{\infty}\int_{-\infty}^{\infty} g(x,y).\exp\left[-i\,(ux+vy)\right] dxdy \tag{5.4}$$

with the corresponding inverse Fourier transform as:

$$g(x,y) = \frac{1}{(2\pi)^2}\int_{-\infty}^{\infty}\int_{-\infty}^{\infty} G(u,v).\exp\left[+i\,(ux+vy)\right] dudv \tag{5.5}$$

where u and v are the angular frequencies in the x and y directions respectively. The second vertical derivative of the gravity field can be obtained by differentiating equation (5.5) twice and using Laplace's equation

$$\nabla^2 g = 0$$

we then get:

$$\frac{\partial^2 g}{\partial z^2} = \frac{1}{(2\pi)^2}\int_{-\infty}^{\infty}\int_{-\infty}^{\infty}[u^2+v^2].G(u,v).\exp\left[i\,(ux+vy)\right] dudv \tag{5.6}$$

from the equation (5.6), if we denote the Fourier transform of the second vertical derivative as $G_2(u,v) = (u^2+v^2).G(u,v)$, then the frequency response of the second derivative is:

$$h(u,v) = \frac{G_2(u,v)}{G(u,v)} = u^2+v^2 \tag{5.7}$$

(Swartz, 1954 in Agarwal and Lal, 1972).

As can be seen from equation (5.7) the method accentuates the higher frequency components and is therefore sensitive to any random errors present in the data. Agarwal and Lal (1972) introduced a smoothing parameter λ and calculated the modified amplitude response function of the second derivative as:

$$h\,m\,(u,v) = (u^2+v^2).\exp[-\lambda(u^2+v^2)] \tag{5.8}$$

They showed that any sets of coefficients introduced by the space domain methods can be obtained by varying the smoothing parameter λ. As an example, they showed that the

results from Elkins' (1951) method are very close to those obtained from the frequency domain method calculations using $\lambda = 0.23$ in equation (5.8). In this case the smoothing operation provides the desired filtering at high frequencies, acting as a low-pass filter and thus revealing the relatively deeper structures.

The analysis of potential field data in the frequency domain has been widely applied (Dean 1958, Mesco' 1965, Bhattacharyya 1965, Darby and Davis 1967, Fuller 1967, Mufti 1972; and Agarwal and Lal 1972). It is widely used today in gravity and magnetic field studies by employing computer programs.

5.6.1.4 Continuation of potential fields

In principle any potential field can be projected on to another plane, above or below the measurement plane. The continuation process is used in order to enhance the effects of the anomalous sources of interest and reduce field variation unrelated to the problem. The result of this processing can be an aid to map the subsurface geological structure by interpreting the continued anomaly which has been brought to a suitable elevation above or below the level of original observation.

Upward continuation gives a smoother field and downward continuation a sharper field than that at the surface of measurement. Upward continuation provides a form of smoothing as a basis for anomaly separation.

Downward continuation is also applied for anomaly separation. This process can be carried out to a level just above the source, where the effects of the source would be greatest. Down ward continuation depends on emphasizing small effects at the measured surface. If such effects are present from shallow sources and the field is continued below their depth of origin, then the shallow sources contribute large false components to the continued field (Nettleton 1976). Several published methods of continuation have been designed by weighting the field values using calculated sets of coefficients (Peters 1949, Henderson and Zietz 1949 and Henderson 1960). Some other methods developed in the wavenumber domain (Dean 1958, Fuller 1967, Oldham 1967, and Mufti 1972) failed to

provide a generalized procedure for field continuation. With the advent of the Fast Fourier transformation (FFT) (Cooley and Tukey 1965) a more generalized method has been achieved.

The continuation process is effected by multiplying the Fourier transform of the potential source field by the frequency response of the continuation operator and then taking the inverse Fourier transform to return to the spatial domain. For the upward continuation we have:

$$k(u,v) = G(u,v).Yup(u,v) \tag{5.9}$$

where $k(u,v)$, $G(u,v)$ $and Y$ $up(u,v)$ are the Fourier transforms of the measured field, the source field and the continuation function respectively. The frequency response of the upward continuation is the Fourier transform of the continuation function$W$ $up(x,y)$where:

$$Wup(x,y) = \frac{h}{[2\pi(h^2+x^2+y^2)^{3/2}]} \tag{5.10}$$

The Fourier transform of this is given by:

$$Y_{up}(u,v) = \int_{-\infty}^{\infty}\int_{-\infty}^{\infty} \frac{h}{[2\pi(h^2+x^2+y^2)^{3/2}]}.\exp^{-1(ux+vy)}.dxdy = \exp^{-h\sqrt{(u^2+v^2)}} \tag{5.11}$$

By using the downward continuation we are interested in finding the source field. In this case:

$$G(u,v) = k(u,v).Ydown \tag{5.12}$$

from (5.12) using (5.9) and (5.10) the frequency response of the downward continuation is found to be:

$$Ydown(u,v) = \exp^{+h\sqrt{(u^2+v^2)}} \tag{5.13}$$

5.6.1.5 A computer program for upward continuation and second derivative calculations

In the present study a computer program modified by Maltezou (1986) was further modified by the author and used for second derivative, upward and downward continuation of the gravity and magnetic fields.

A brief description of the program follows: *Subroutine* PLANE, is called prior to the Fourier transformation, to remove the best-fitting plane from the data, thus removing the excess amount of power at long wavelengths. This procedure can also attenuate the amplitude of those wavenumber components whose wavelengths are greater than twice the length of the data, and which therefore cannot be accurately represented by Fourier series coefficients. *Subroutine* EXKSYM mirrors the original data along the X and Y axes, thus creating an array with period twice the size of the original data. *Subroutine* MULFFT is then called to compute the Fourier transform of the enlarged array using the mixed-radix MULFFT algorithm. *Subroutine* CONDER is used to calculate the frequency response of the second derivative operation as well as the upward continuation operation. By calling this routine, second derivative and field continuation calculations can be made for any size of array. The expanded array in this subroutine was changed from a 1-D to a 2-D array to be consistent with the form it has in subroutine EXPSYM and the range of frequency values was rearranged to correspond to the 2-D array values. Subsequently, by calculating the inverse Fourier transform, the results for the original data array are given in the space domain. The version of the program so modified is called UPDOWN and is listed in Appendix 1.

5.6.1.6 Wavenumber filtering of potential field data

The use of wavenumber filtering techniques for gravity and magnetic data has been examined in the work of (Dean 1958, Byerly 1965, Mesco 1965, Bhattacharrya 1966, Derby and Davies 1967, Fuller 1967, Spector and Grant 1970, Ellis and Kearey 1984, and Maltezou 1986).

Nettleton (1976) pointed out the basic reasons which makes wave-number filtering useful. Since the advent of the Fast Fourier Transformation (Cooley and Tukey 1965) filtering is employed in the frequency domain. The Fourier-Transform operation is precisely equivalent to determining the best least-squares harmonic trend. The main types of filter are low-pass (wavenumbers below the cut-off frequency), high-pass (wavenumbers above the cut-off frequency), and band-pass (wavenumbers within a range of frequencies). The

radially-averaged power spectrum is used to define cut-off frequency values for low-pass and high-pass filters. The computer program is used to for power spectral calculations and filtering.

5.6.2 Power spectral analysis

5.6.2.1 Wavenumber spectra

The applications of wavelength filters to potential field data by using power spectra analysis, have been described by Bhattacharyya (1966); Spector and Grant (1970); Ellis and Kearey (1984), and Maltezou (1986).

Bhattacharyya (1966) obtained the 2D spectrum of a magnetic anomaly caused by a rectangular prismatic body, and the separation of the effects of near surface structures (as high-wavenumber components in the spectrum) from the effects of deeper (low wavenumber sources).

Spector and Grant (1970) defined the regional and residual in the frequency domain, and calculated the power spectra from gridded total intensity aeromagnetic data. They also showed the estimated depth of the individual sources. The group of such sources is treated by statistical theory and reduced to a power spectrum. The result of the analysis is plotted on a logarithmic scale against the frequency. On such a plot, if a group of sources has a similar depth, they will fall into a line of constant slope. Thus, if there are groups of sources with the individual groups at different depths, the plot will be separable into parts with different slopes and the magnitude of the slope is a measure of depth.

Ellis and Kearey (1984) used the radially averaged 2-D amplitude spectrum plotted on logarithmic scale against the wavenumber for identifying groups of magnetic sources at different depths.

Maltezou (1986) also used power spectral methods for investigating regional and local structures of the Rhodope region of NE Greece. She obtained depths of the deep

and shallower potential field sources.

5.6.2.2 A computer program for power spectral calculation

A computer program used by Maltezou (1986) for filtering and power spectral calculations, was used in this study to calculate the power spectrum of the gravity and magnetic maps. The program computes the 2D power spectrum and radially-averaged log power spectrum for the gravity and magnetic data. An estimate of the maximum possible depth can be generated from the equation:

$$\frac{\Delta log_e.P}{\Delta K} = -2h$$

By defining linear segments in the graph of $log_e P$ against the wavenumber K, their gradients can be used in the depth estimations.

5.7 Modelling techniques

5.7.1 2D methods

Several forward modelling methods have been suggested for interpreting gravity data by using two-dimensional bodies of irregular cross-section with uniform density (eg Talwani et al 1959, Talwani and Ewing 1960, Grant and West 1965, Bhattacharyya and Navolio 1975, and Murthy et al 1979). A widely used method is the polygon method of Talwani et al (1959), which calculates the anomalies over two-dimensional bodies, which are assumed to extend to infinity in the strike direction. Talwani et al (1959) suggested that the length of the geologic structure must be approximately five times that of its maximum width. Grant et al (1965) suggested that the 2 D body must be five or more times the greatest cross-sectional dimension. Telford et al (1976) considered that the strike length should be about twenty times all the other dimensions. Dobrin (1976) suggested that the strike length should be ten times greater than any other dimension.

The Talwani et al (1959) approach has been widely used, and improved by Won

and Bevis (1987). In the present study a computer program for two-dimensional gravity and magnetic data has been provided by the Oceanography department, Southampton University, which was written by Helena Bagg et al (1987), Reading University. The program HPP1A computes the gravity effect, in gravity units, of (up to) ten *two-dimensional* bodies, striking perpendicular to the direction of the x-axis and compares this with experimental data. Full theory is derived by Grant and West (1965). The MPL2A program computes the magnetic effect of such abody in nanoTesla. Fully theory is given by Talwani and Heirtzler (1963).

The profile AB across the gravity and the magnetic anomalies (Figures 5.1 and 5.6) has been selected for modelling, on the basis of seismic and well data which demonstrate the presence of intrasedimentary volcanic rocks in the study area (detailed in Chapter 6).

5.8 Summary

The filtering and modelling analysis of the gravity and magnetic data in this area includes various analytical methods such as, power spectral analysis, low-pass and high pass filtering, second-derivative calculation, upward continuation, and 2-D modelling. In order to apply these analytical methods, selective rectangular areas from the study area have been digitized onto a 1 km grid, and the resultant datasets of gravity and magnetic values contoured.

The purpose of these analytical methods is to produce a geological interpretation of the gravity and magnetic data by different techniques, using constraints provided by the surveys, and well data. In particular they were used to estimate the depths of the anomaly sources.

The expected gravity and magnetic anomaly sources in the study area might be include salt diapiric phenomena in the salt basin, the cap rocks above the crest of the salt structures, the large accumulation of sediments in the basin, uplift structures, or any major igneous intrusives or extrusives such as the intrasedimentary volcanic units and

in the southern part of the study area. The Bouguer map in Figure 5.1 shows that the major negative gravity anomalies are associated with the salt structures and the thick sedimentary basin area, whereas the major positive gravity anomaly appear to be associated with the intrasedimentary volcanic units and uplift structure in the southern part. These numerous positive and negative anomalies have been labelled for ease of reference and are listed in Table 5.1.

The total field magnetic anomaly intensity map (Figure 5.4) illustrates the magnetic anomalies; the codes of these anomalies are listed in Table 5.3. The major strong anomaly M1 is attributed to the occurrence of intrasedimentary volcanic rock units, and the uplift structure. The large magnetic anomalies M2 and M3 have been attributed to the igneous activity associated the initial rifting and subsidence the of Sabratah basin during Jurassic times. The total field intensity magnetic map shows a generally low amplitude anomaly field associated with the thick sedimentary basin and salt structures area. The magnetic susceptibility and NRM intensity of the cuttings samples from boreholes have been measured and the results are presented in Tables 5.4 to 5.8, in order to assist with the interpretation and modelling of the magnetic anomalies (Chapter 6).

The analytical method of second vertical derivative calculation, is a method for isolating local effects, and the field continuation process is used in order to enhance the effects of the anomalous sources of interest and to reduce field variations unrelated to the problem of interest. In the present study a computer program utilized by Maltezou (1986) and modified by the author is used for second derivative and upward continuation of the gravity and magnetic fields. Profile AB across the gravity and magnetic anomalies, was selected for interpreting the potential field data by using two-dimensional bodies. All these modelling methods require suitable geometry and knowledge of appropriate physical parameters (density and susceptibility) for the geologic structures, as part of the input.

The interpretation of the various derived maps and the modelling of the gravity and magnetic data, will be described in the next chapter.

Chapter 6

Interpretation of gravity and magnetic data

6.1 Introduction

The interpretation of potential field data described in this thesis involves the qualitative analysis of the Bouguer gravity and total field magnetic intensity anomalies maps, using the methods of trend surface analysis, second derivative, upward continuation, power spectrum, and wavenumber filtering. Quantitative interpretation of a specific magnetic anomaly (55x55) dataset has been attempted, together with interpretation of selected magnetic and gravity profiles, using 2-D models for magnetic and gravity anomalies.

6.2 Analytical interpretation of gravity and magnetic maps

Wavenumber filtering and spectral analysis of gravity and magnetic data is applied to the rectangular study areas shown on the gravity and magnetic maps (Figure 5.1 and Figure 5.3).

6.2.1 Part 1: Gravity

6.2.2 Analysis of gravity map

The gravity map of the study area, for interpretation purposes, is that considered as a rectangular area (70x70) km shown in Figure 5.2. This is chosen in order to apply the analytical methods. This rectangular area (70x70) dataset represents the best available gravity data in the study area. It shows the negative gravity anomalies in the western and the central parts, and the positive anomalies in the south-eastern part. The results of the application of the analytical methods and their interpretation is given in the following sections.

6.2.2.1 Polynomial surface fitting:

The polynomial surface fitting method is one of the most useful analytical techniques for determining the regional gravity field. The observed data are used to compute the polynomial surface giving the closest fit to the gravity field; this surface is the considered to represent the regional gravity field, and the residual field is the difference between the observed and regional field. The calculations of the first degree regional and residual field (k,1) = (1,1) for the gravity map shown in Figures 6.1 and 6.2, respectively, are based on the Chebyshev series representation (where K = degree of polynomial). The removal of the first order regional field does not appear to have isolated the local negative anomalies of interest.

The second degree ((k,1) = (2,2)) regional and residual maps are shown in Figures 6.3 and 6.4, respectively. The removal of the second degree regional field has more effectively isolated the local negative and positive anomalies of interest, such as: G1 (thick sediment (rim-syncline)), G6 (salt diapir trend), G3 and G5 (salt diapirs), and G7 and G8 (intrasedimentary volcanic units). A general NE-SW trend is observed in the central part of the study area; this correlates with the location of the major sedimentary basin.

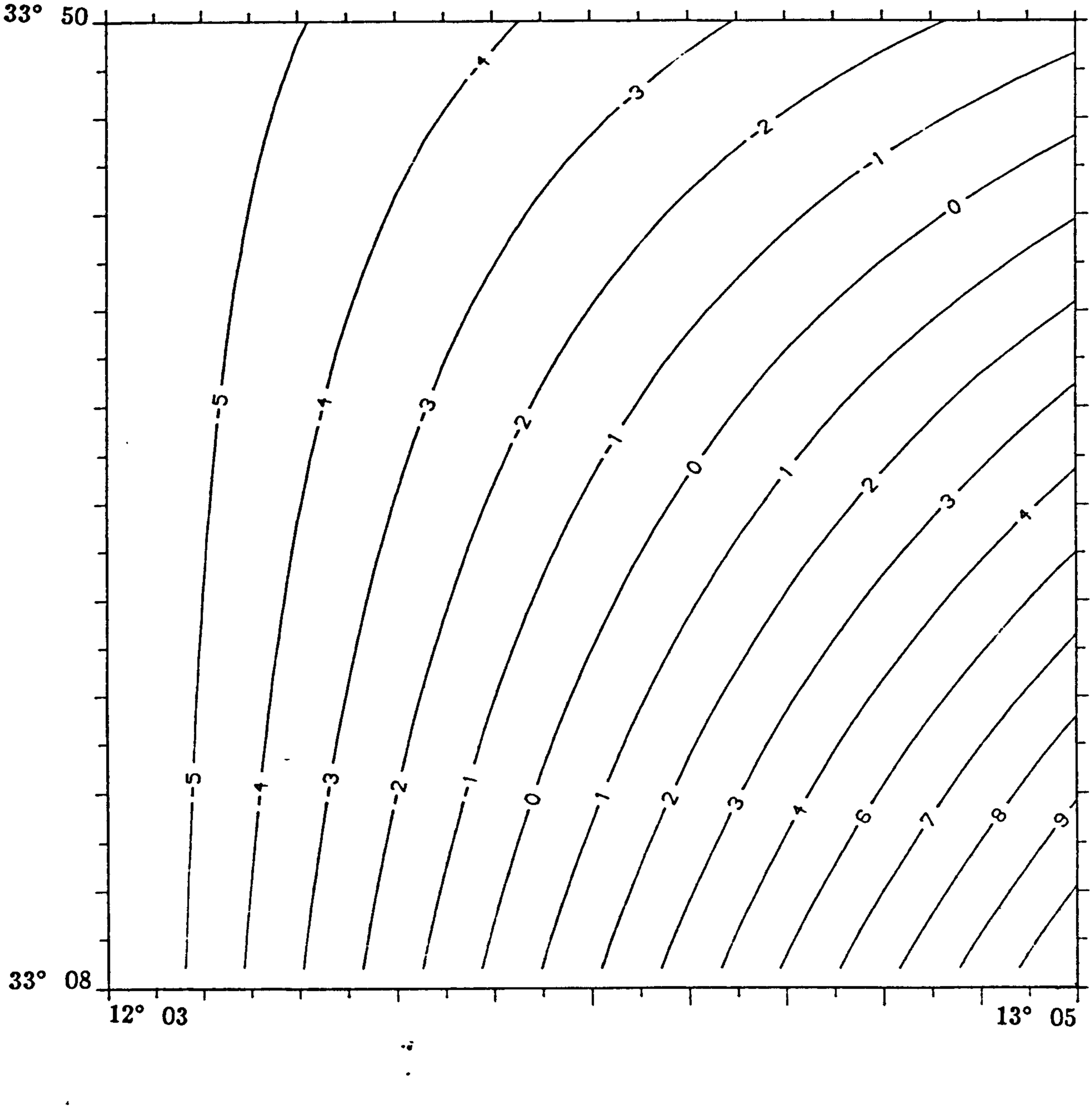

Figure 6.1: First degree (k,1 = 1,1) regional gravity field of the study area, (70x70) dataset.

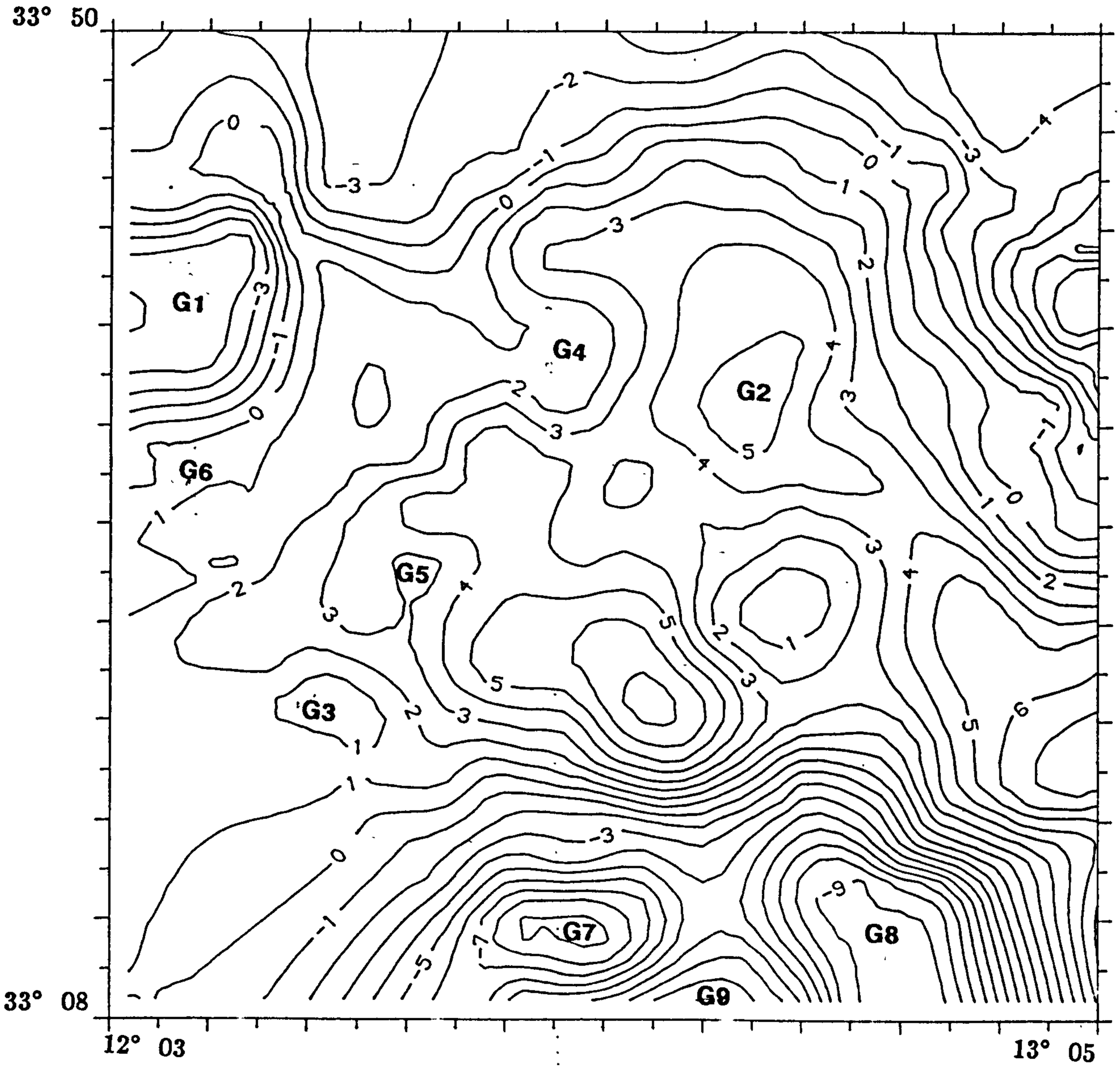

Figure 6.2: The residual gravity anomaly corresponding to the first degree regional. Individual anomalies (G1–G9) are identified.

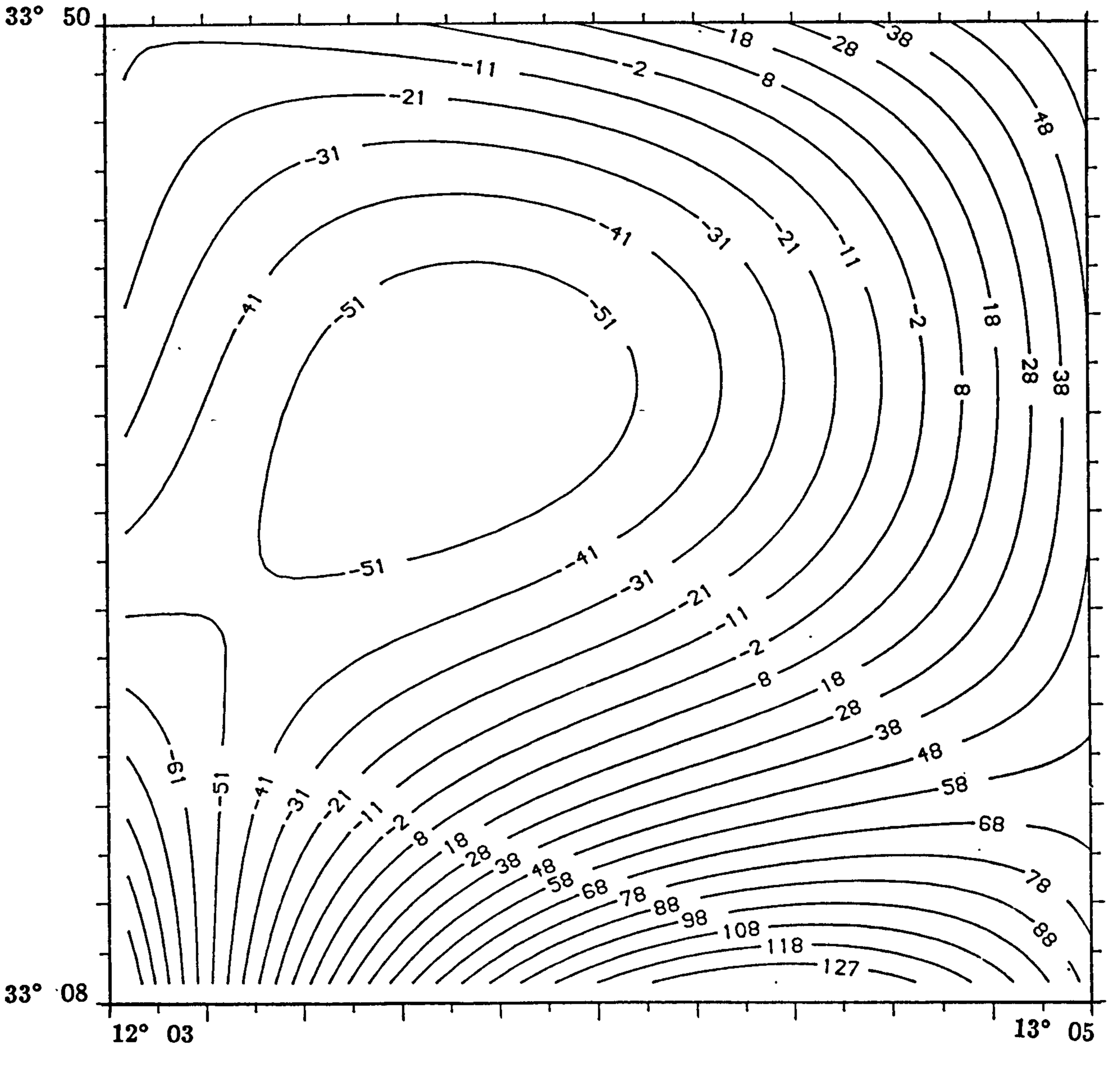

Figure 6.3: The second degree (k,1 = 2,2) regional gravity field of the (70x70) dataset. Contour interval= contour value x 10^{-1} mGal.

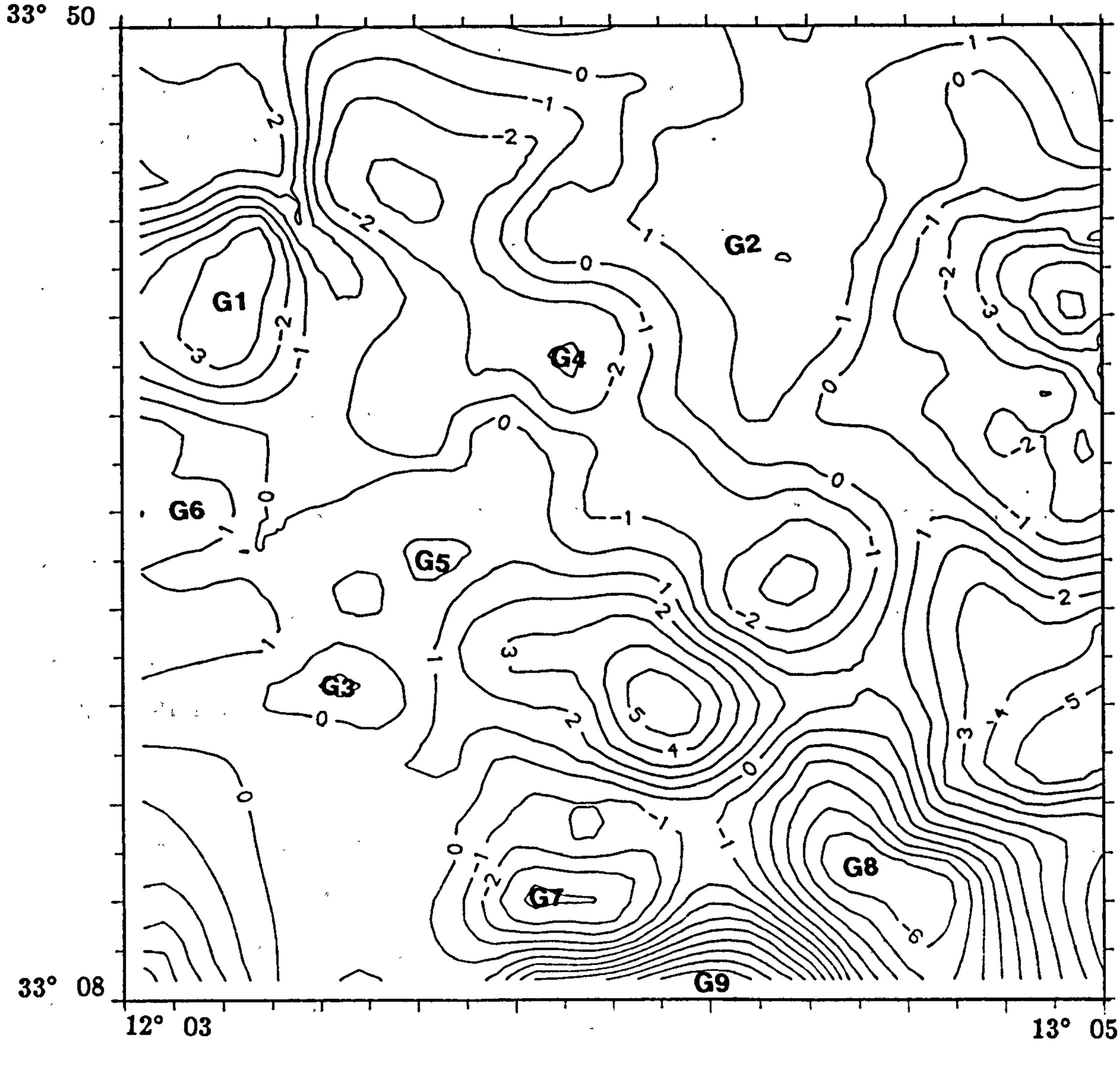

Figure 6.4: Residual gravity anomaly corresponding to the second degree regional. Contour interval= 1 mGal. Individual anomalies are identified (G1–G9), see text.

6.2.2.2 Second derivative calculation:

The second vertical derivative gravity map is shown in Figure 6.5. The calculation of the second vertical derivative of the gravity field should isolate local effects, but in this case the map does not exhibit features of particular interest. Earlier workers commenting on similar observations suggest " this is mainly due to the interpolation of the data from a contour map onto a grid which, together with the large spacing of the stations which produced the original maps, has already applied a degree of smoothing to the small local gravity anomalies in the area" (Maltezou, 1986).

6.2.2.3 Upward continuation

The gravity field has been continued upwards to 1, 3, 5 and 7 km (Figures 6.6, 6.7, 6.8 and 6.9) respectively. On the 1 km continued map (Figure 6.6), the Salt Domain and Thick Sediment Domain boundaries are clearly identified (G3, G5, G4, and G2), which represents the maximum negative gravity anomaly is apparent in the central-western part of the study area. The positive anomalies G7 and G8 are still identified as two separate sources.

The 3 km continued map (Figure 6.7), demonstrates the Salt and Thick Sediment Domains boundaries in the central part with NE-SW thick sediment trend. The positive (G7 and G8) anomalies are apparent as one anomaly (G8) with a large amplitude (7.52 mGal) in the central part of the G8 anomaly.

The gravity field, when continued upwards to 5 to 7 km, (Figures 6.8 and 6.9) shows also the clear boundaries of the Salt and Thick Sediment Domains (negative values). The 0 mGal contour separates the positive (intrasedimentary volcanic units and uplift) from the negative (Salt and Thick Sediment Domains) anomalies. The G8 anomaly still has a relatively high amplitude, as shown in the 7 km continued map (Figure 6.9).

The continuation maps did not identify or isolate any particular anomaly in the Salt and Thick Sediment Domains, because of the smoothing of the original gravity data

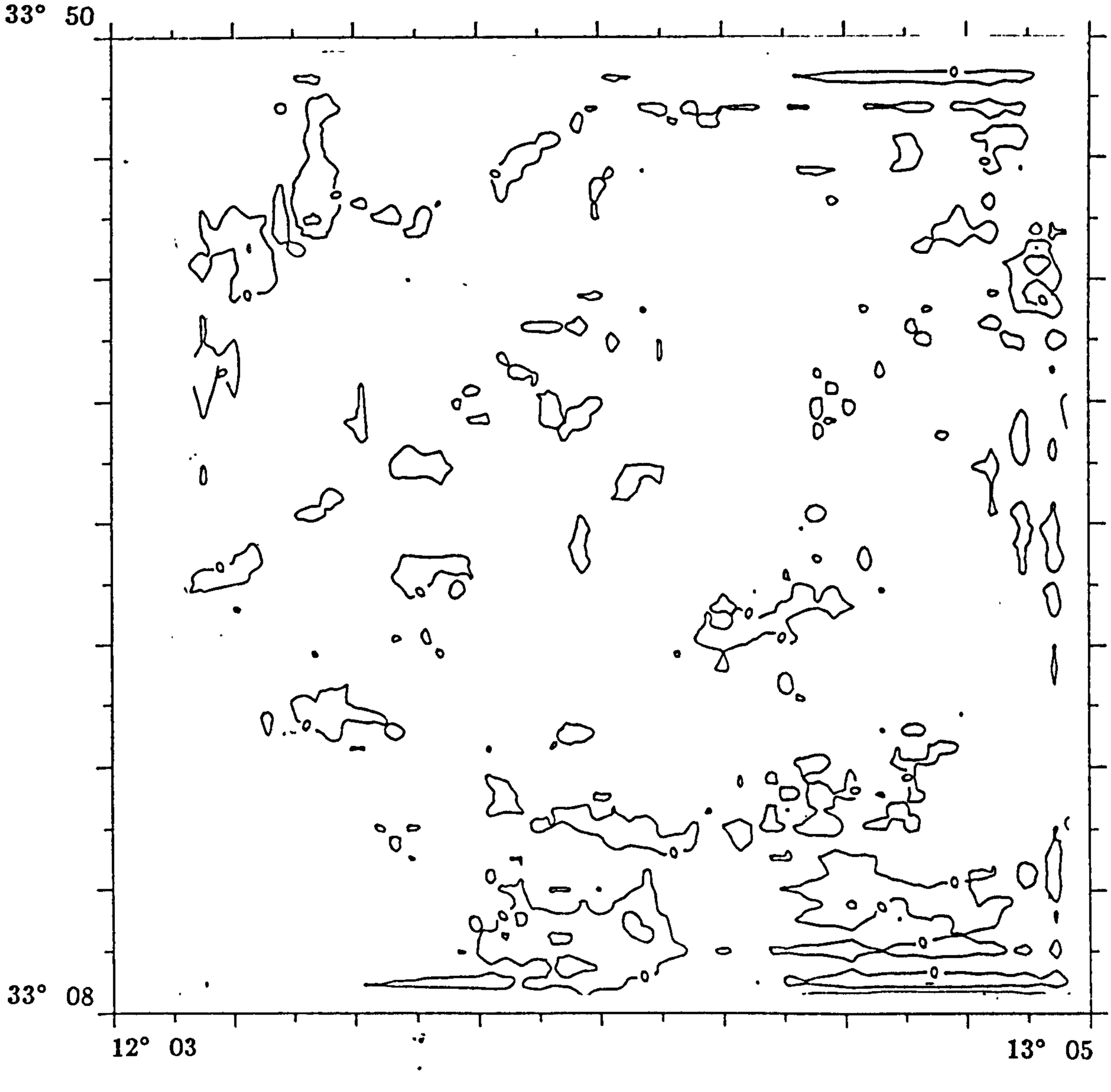

Figure 6.5: The second vertical derivative gravity map of the (70x70) dataset.

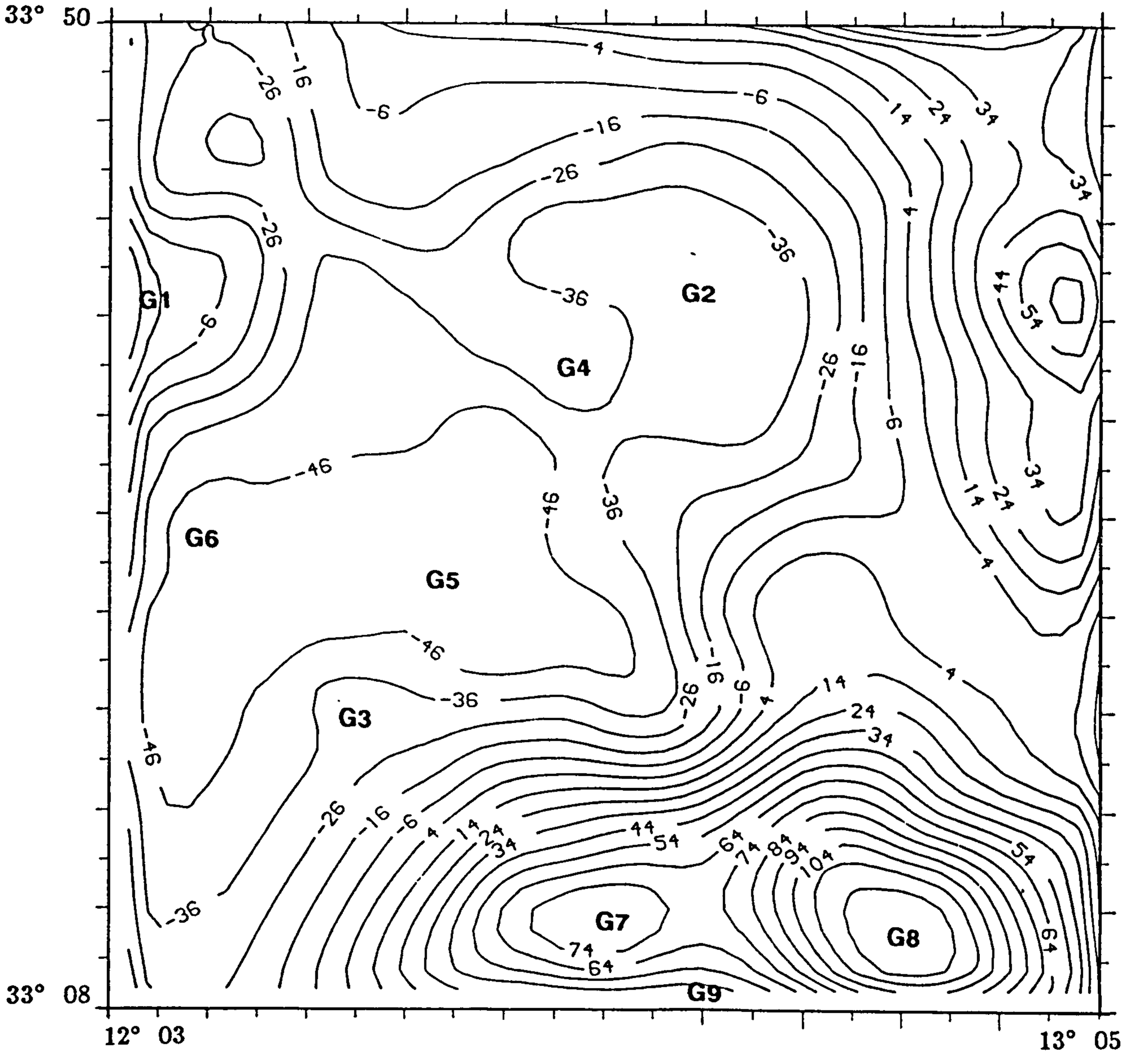

Figure 6.6: Upward continued gravity map of the (70x70) dataset. Level of continuation: 1 km. Contour interval= contour value x 10^{-1} mGal.

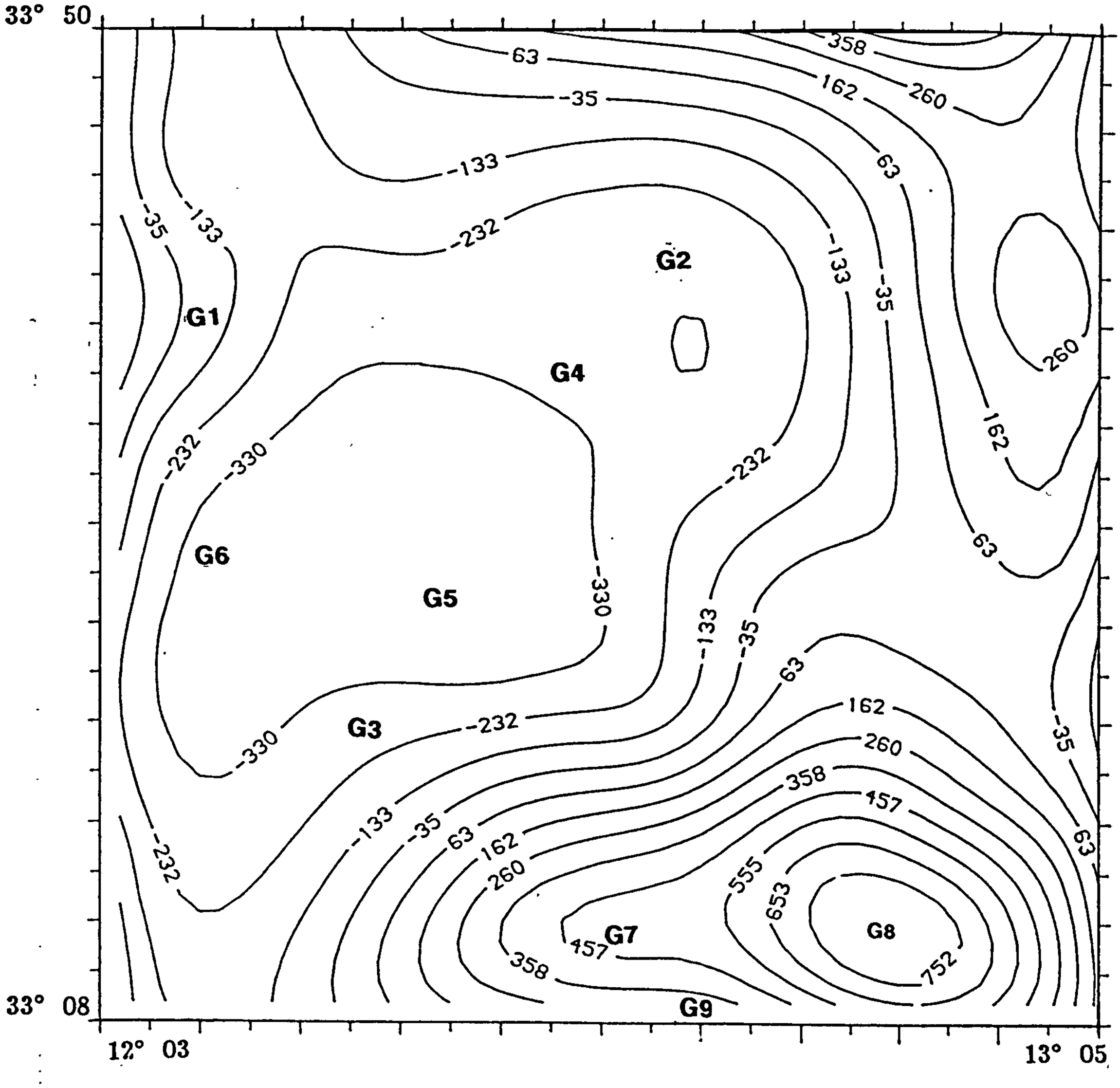

Figure 6.7: Upward continued gravity map of the (70x70) dataset. Level of continuation: 3 km. Contour interval= contour value x 10^{-1} mGal.

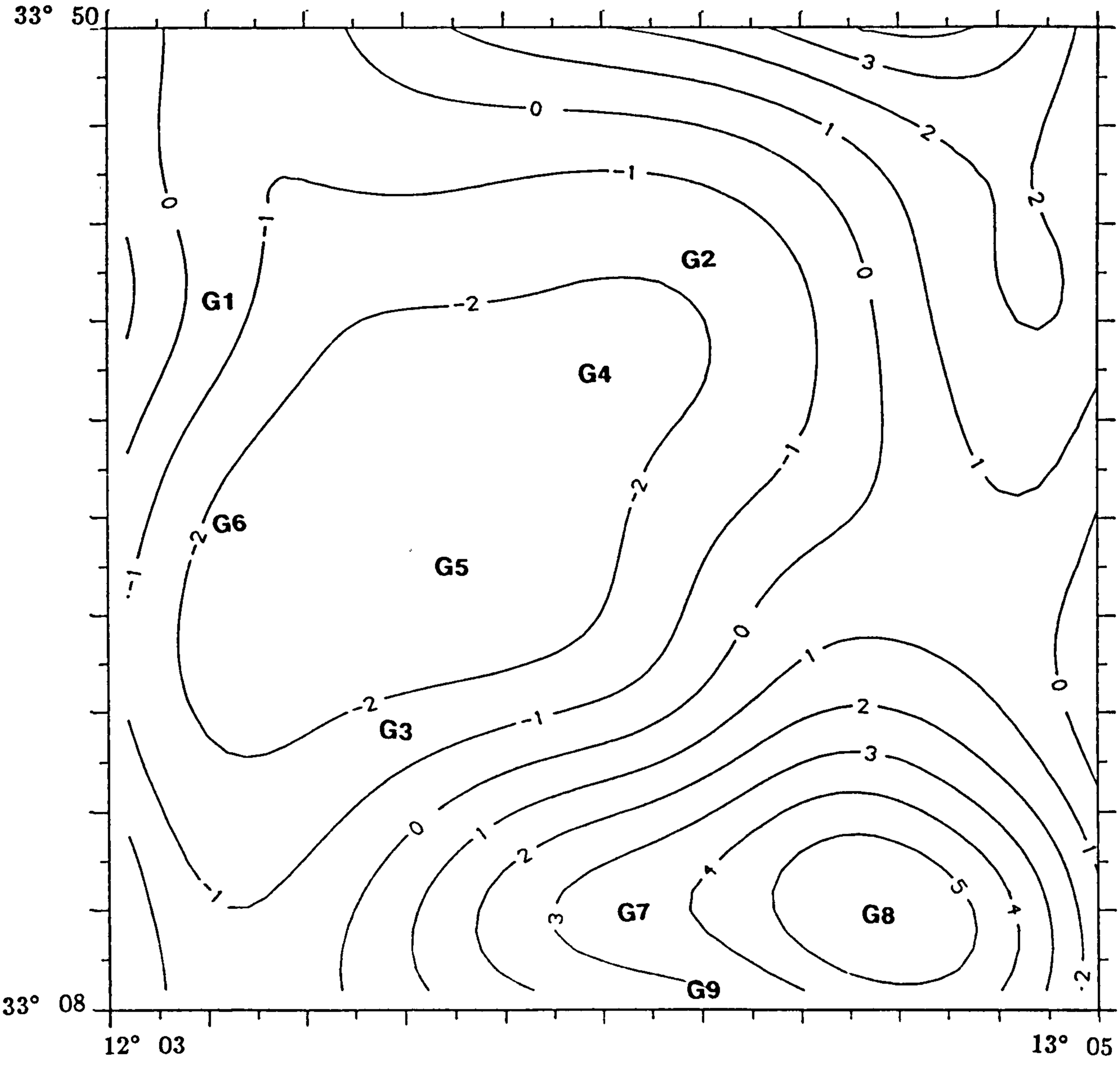

Figure 6.8: Upward continued gravity map of the (70x70) dataset. Level of continuation: 5 km. Contour interval= contour value x 10^{-2} mGal.

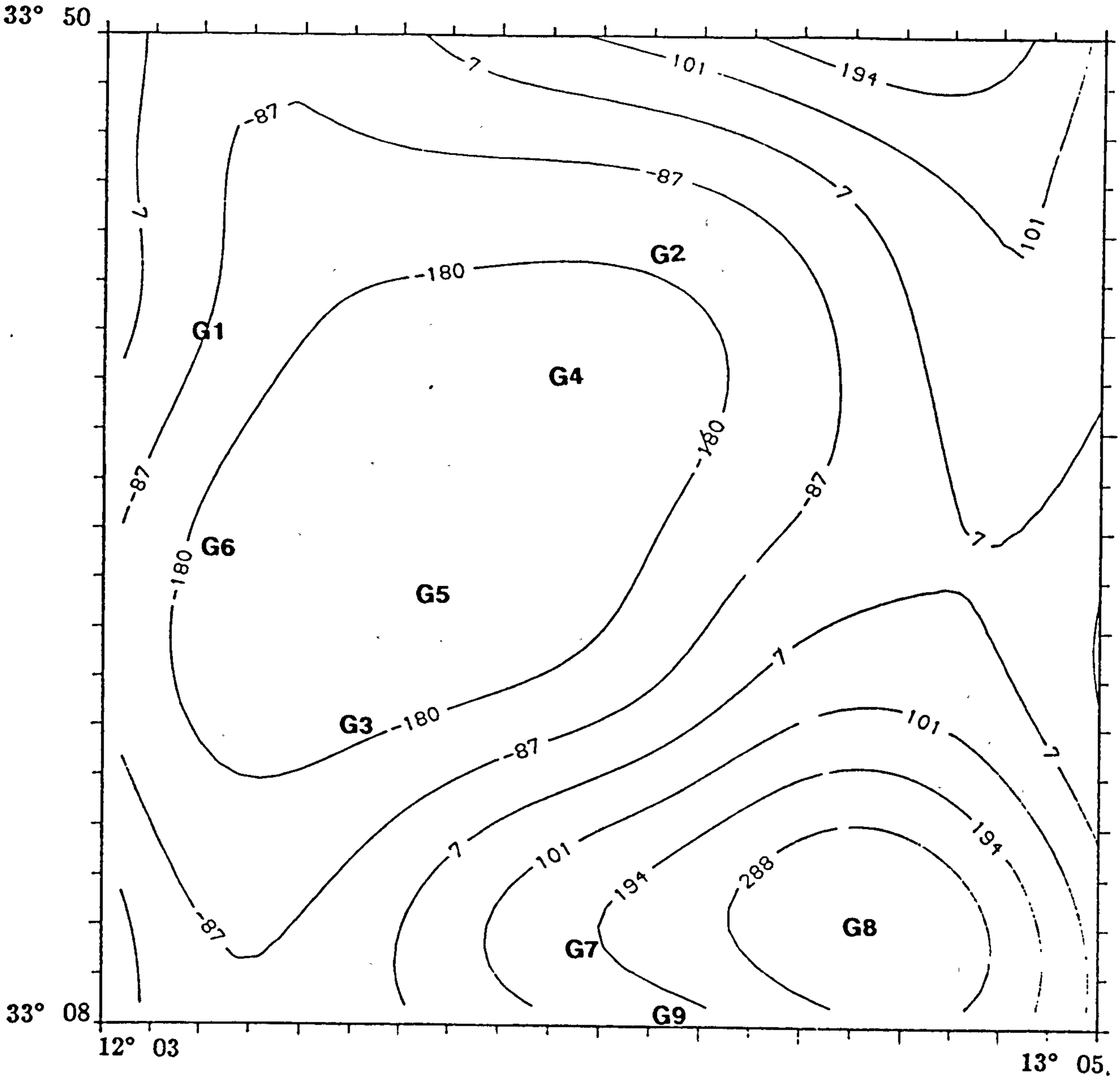

Figure 6.9: Upward continued gravity map of the (70x70) dataset. Level of continuation: 7 km. Contour interval= contour value x 10^{-2} mGal.

over this area. However, in the southern part the G7 and G8 anomalies are associated with intrasedimentary volcanic units and uplift structures.

6.2.2.4 Power spectral calculation and wavenumber filtering:

The gravity anomaly of the 70x70 dataset was digitized at 1 km intervals, in order to calculate the power spectrum using the computer program described in section (5.6.2.2). The dataset obtained covers the main parts of the negative anomalies (Salt Domain area, north), and the positive anomalies (the intrasedimentary and uplift structure, south). The power spectrum of this dataset was computed and averaged azimuthally in wavenumber K *and* $log_e P$ as shown in Figure 6.10.

Figure 6.10 (b) shows graph of the logarithm of the azimuthally averaged spectrum, $log_e\ P$ against K. Depth estimates were made using the method of Spector and Grant (1970) guided by the applications of Ellis and Kearey (1984) and Maltezou (1986). Depth estimates to statistically discrete sources, were obtained from the gradients of the linear segments defined on Figure 6.10 (b). These indicate the presence of three groups of gravity sources at (0.800), (2.587), and (4.777) kms, respectively. The same line segments were used to define cutoff wavenumbers for low-pass and high-pass filters.

The low-pass and high pass filtered gravity maps are shown in Figures 6.11, and 6.12, respectively. The low-pass filtered gravity maps of Figure 6.11 (cutoff: a -0.13, b - 0.34) represent the gravity anomaly arising from deep sources. The high-pass filtered gravity map of Figure 6.12 (cutoff 0.13) reflects the gravity anomaly arising from shallow sources.

6.2.3 Part 2: Magnetic

6.2.4 Analysis of magnetic map

The total field intensity magnetic map of the study area can be used to define two rectangular datasets (85x85) and (55x55) (Figure 5.3). These were chosen in order to apply

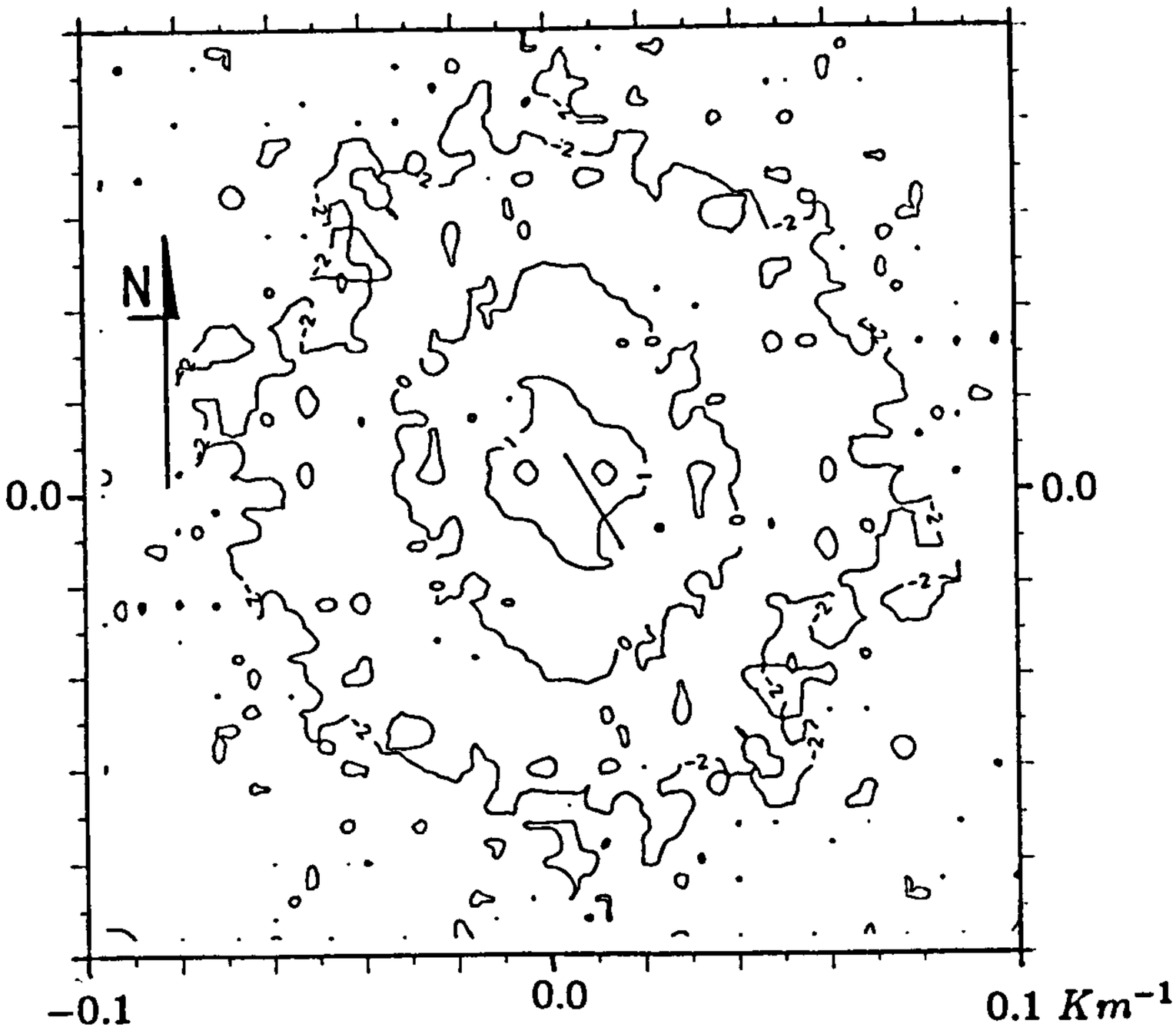

(a)

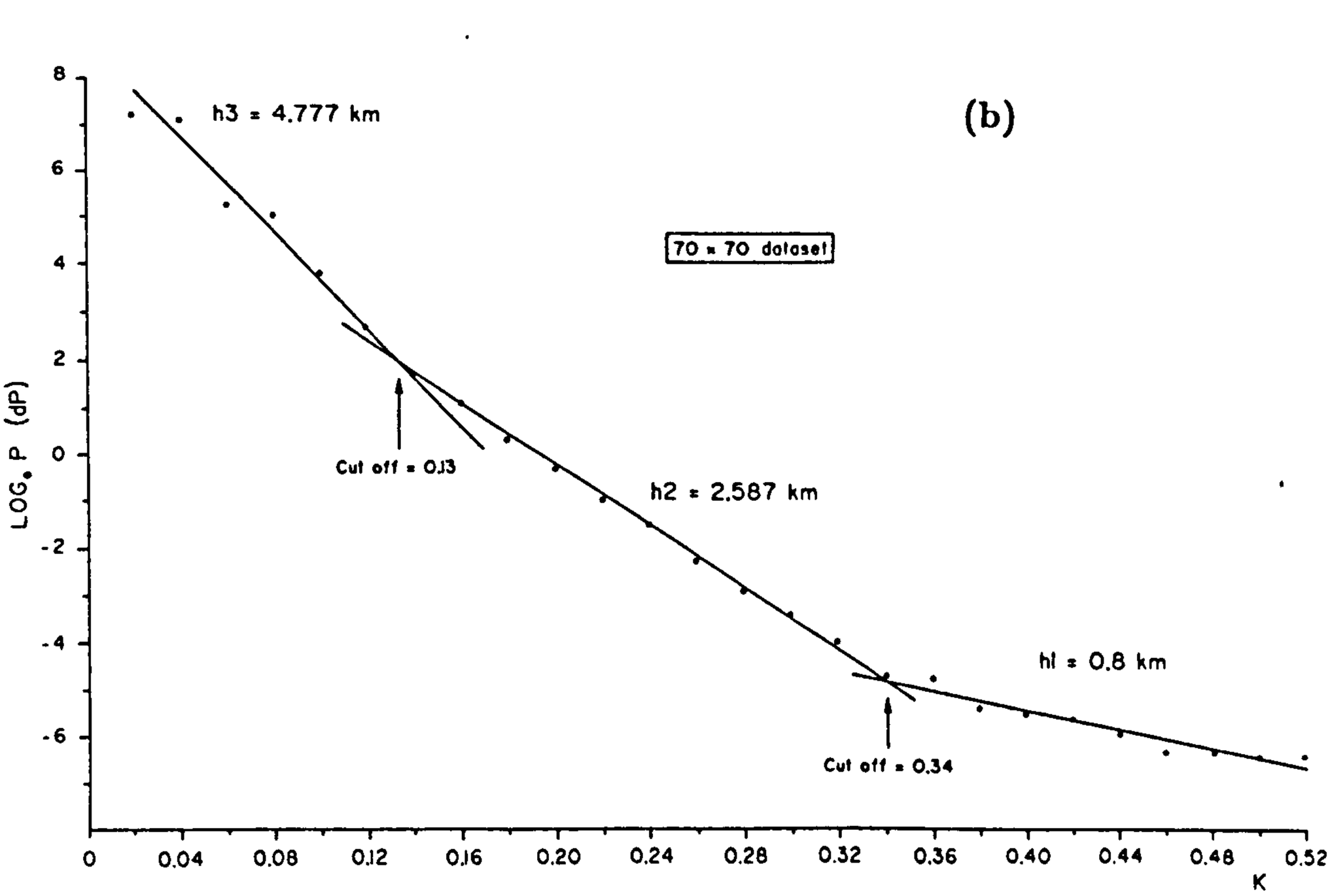

(b)

Figure 6.10: (a)- 2-D log power spectrum. (b)- Radially-averaged log power spectrum versus wavenumber $K = \sqrt{u^2 + v^2}$ for (70x70) dataset of the gravity map. The units are based on a decibel scale.

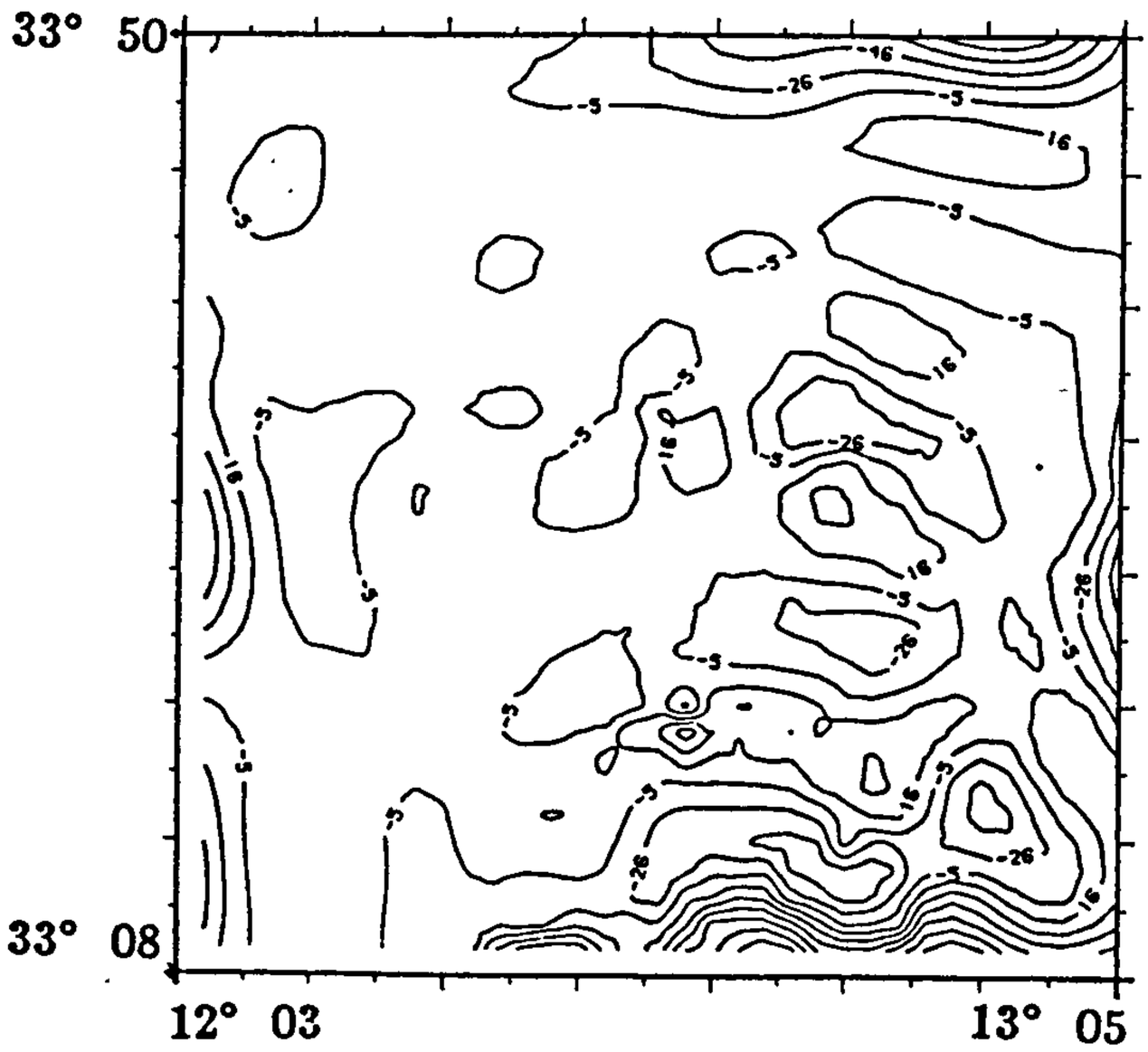

Figure 6.11: Low-pass filtered gravity maps defined by a square (70x70) dataset. Wavenumber filter cutoffs: a - 0.13, and b - 0.34.

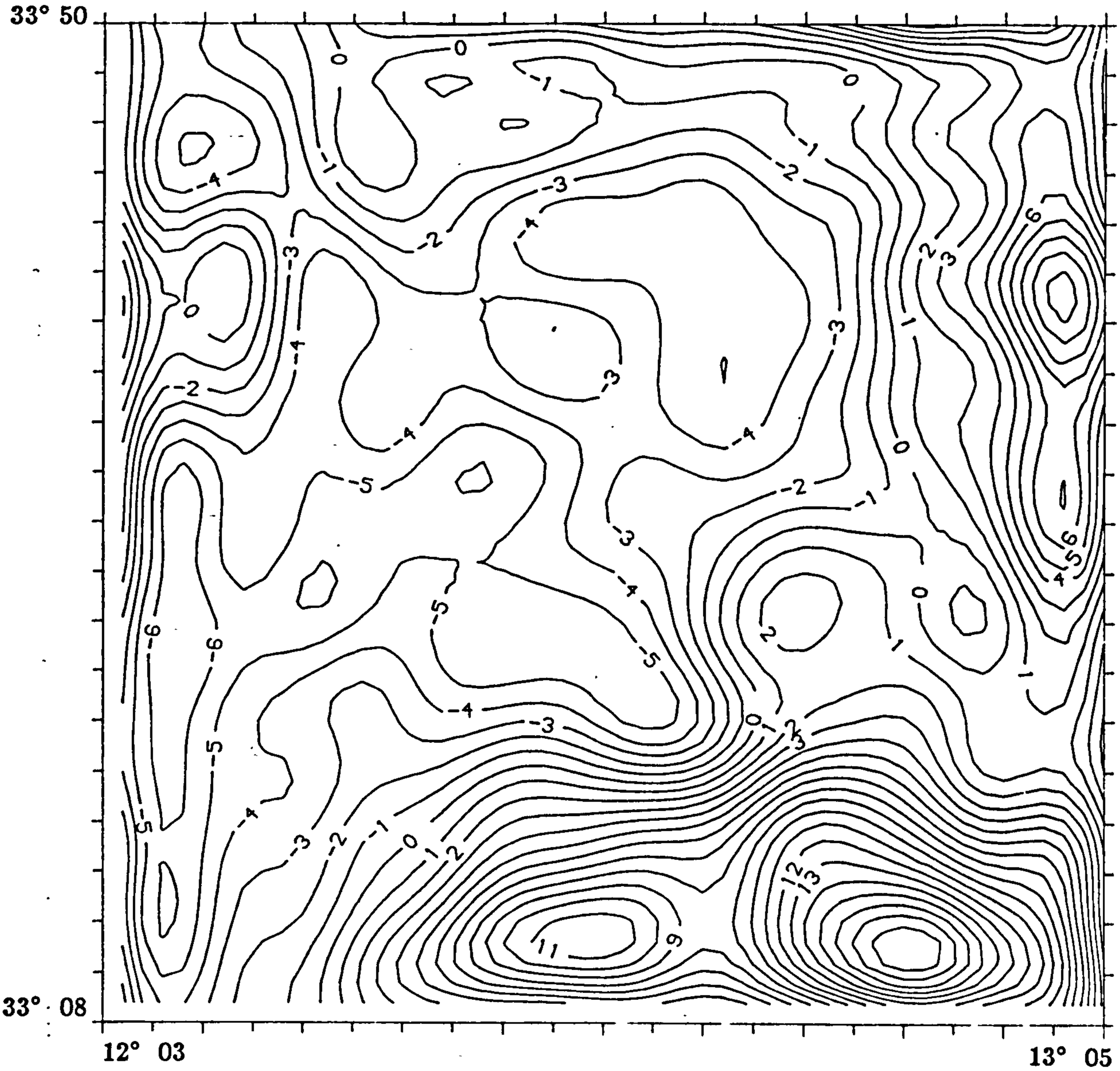

Figure 6.12: High-pass filtered gravity map defined by a square (70x70) dataset. Cutoff: 0.13.

the analytical methods. The first, larger, rectangular (85x85) dataset comprises all the available magnetic anomaly data in the study area. Low amplitude magnetic anomalies occur in the western and the central parts and the higher amplitude magnetic anomalies in the south-eastern part. The second rectangular (55x55) dataset comprises the magnetic anomaly of particular interest (believed due to the intrasedimentary volcanic units and the uplift). This is associated with a high intensity magnetic anomaly. The digitized total field magnetic anomaly map of the (55x55) dataset is shown in Figure 6.13. The results of the application of the analytical methods will be described in the follow sections:

6.2.4.1 Polynomial surface fitting:

Regional and residual maps have been produced for the rectangular (55x55) dataset defined in Figure 5.3. The first degree regional field and residual field of the magnetic map are shown in Figures 6.14 and 6.15, respectively. A maximum regional field level of - 236 nT is observed in the southern part, and a minimum of - 413 nT in the northern part (Figure 6.14). The residual field magnetic map (Figure 6.15) shows a close agreement with the original magnetic data map (Figure 6.13).

6.2.4.2 Second derivative calculation:

Second vertical derivative maps have been produced for the rectangular (85x85) and (55x55) datasets, as shown in Figures 6.16 and 6.17. The zone of high second derivative values delineate the boundaries of anomalies M1, M2, and M3 in the southern part of the area, associated with the intrasedimentary volcanic units and uplift structure.

6.2.4.3 Upward continuation:

The results of continuing the (85x85) dataset magnetic field maps upwards to 1, 3, and 5 kms, are shown in Figure 6.18, 6.19 and 6.20, respectively. The results of continuing the (55x55) dataset, magnetic field maps upwards to 2, 4, and 6 kms, are shown in

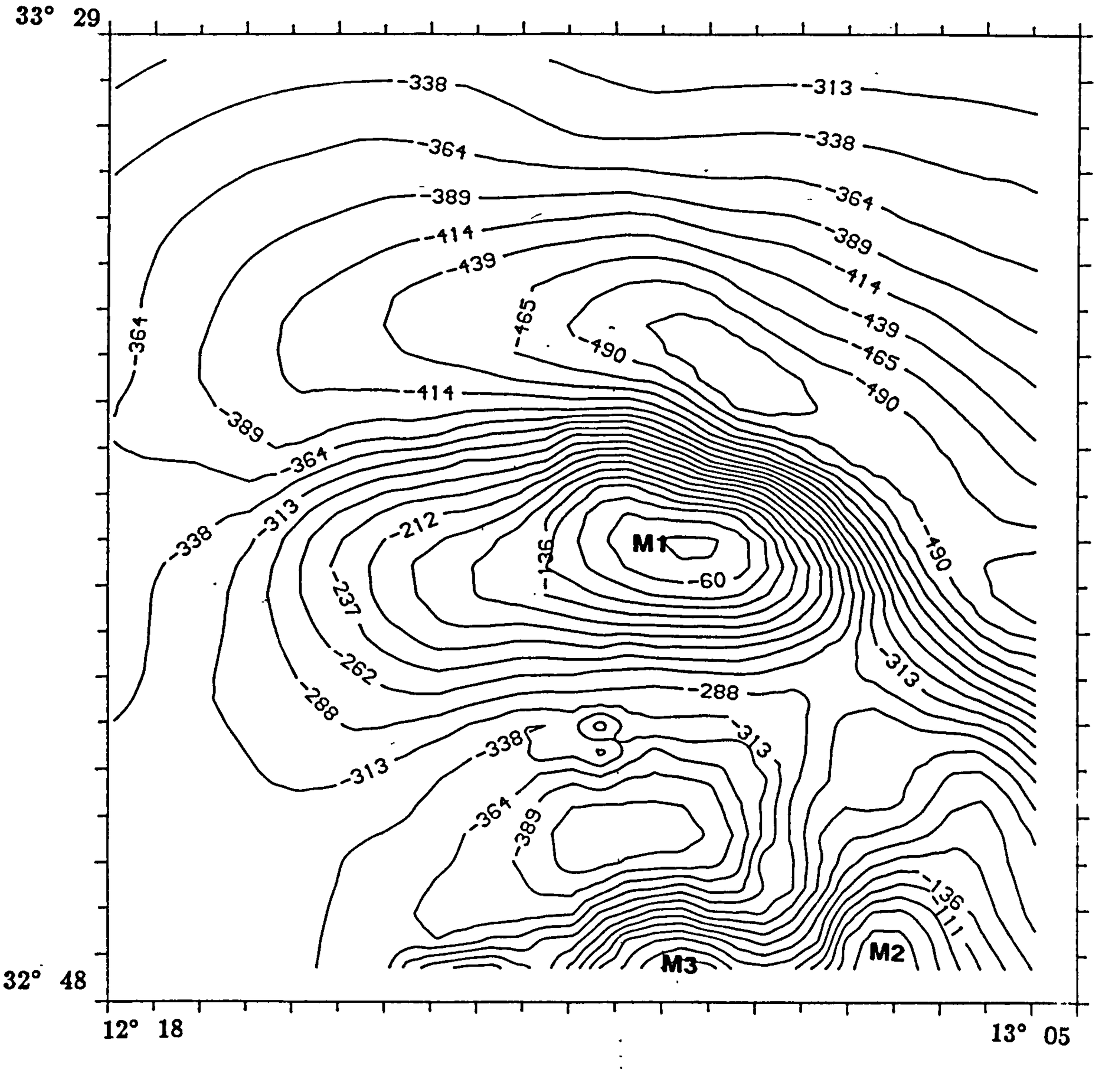

Figure 6.13: Digitized magnetic map of the defined rectangular (55x55) dataset in the southern part of the magnetic map of the study area (Figure 5.3). Contour interval: 25 nT.

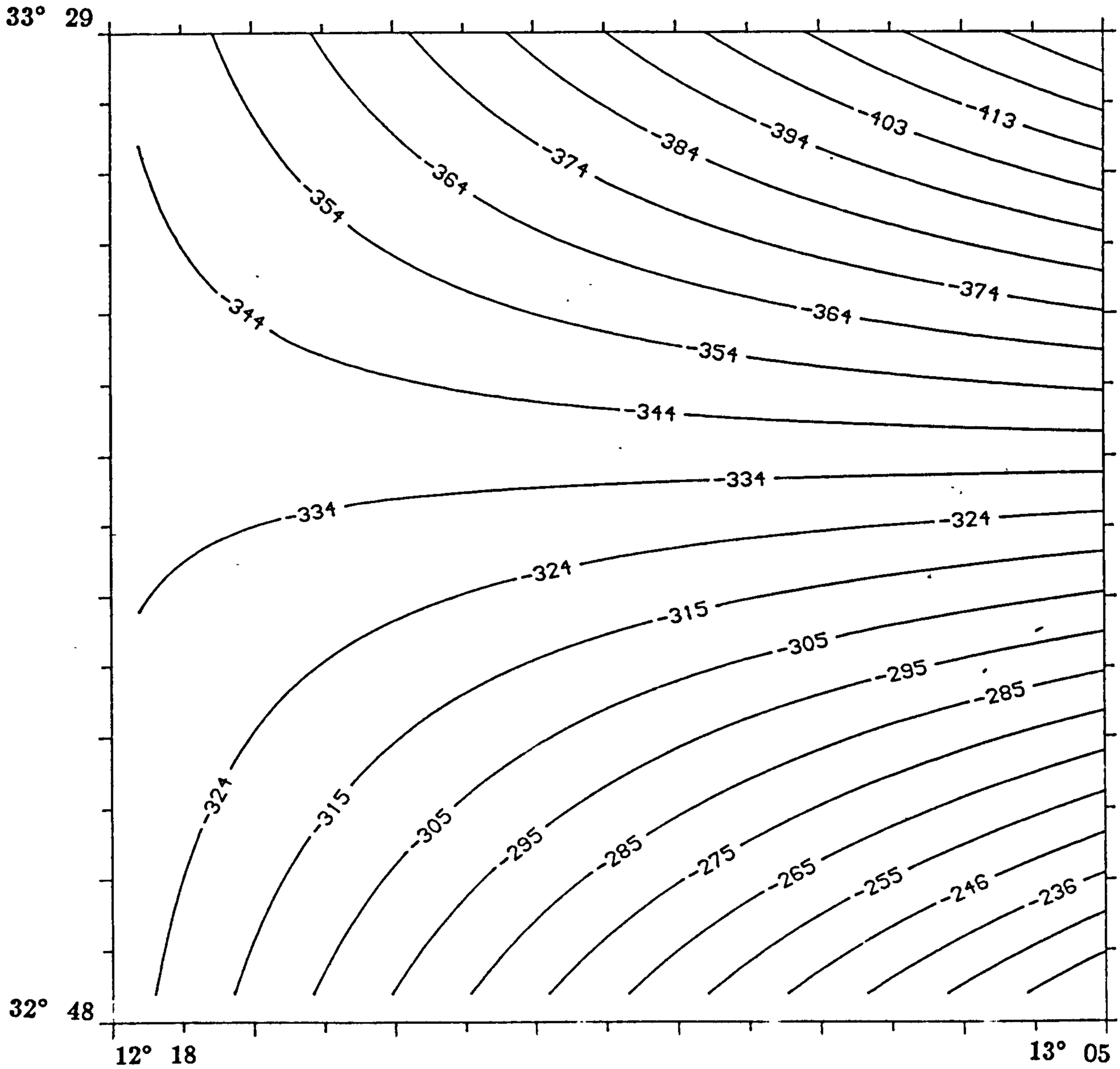

Figure 6.14: First degree (k,1 = 1,1) regional magnetic field of the (55x55) dataset.

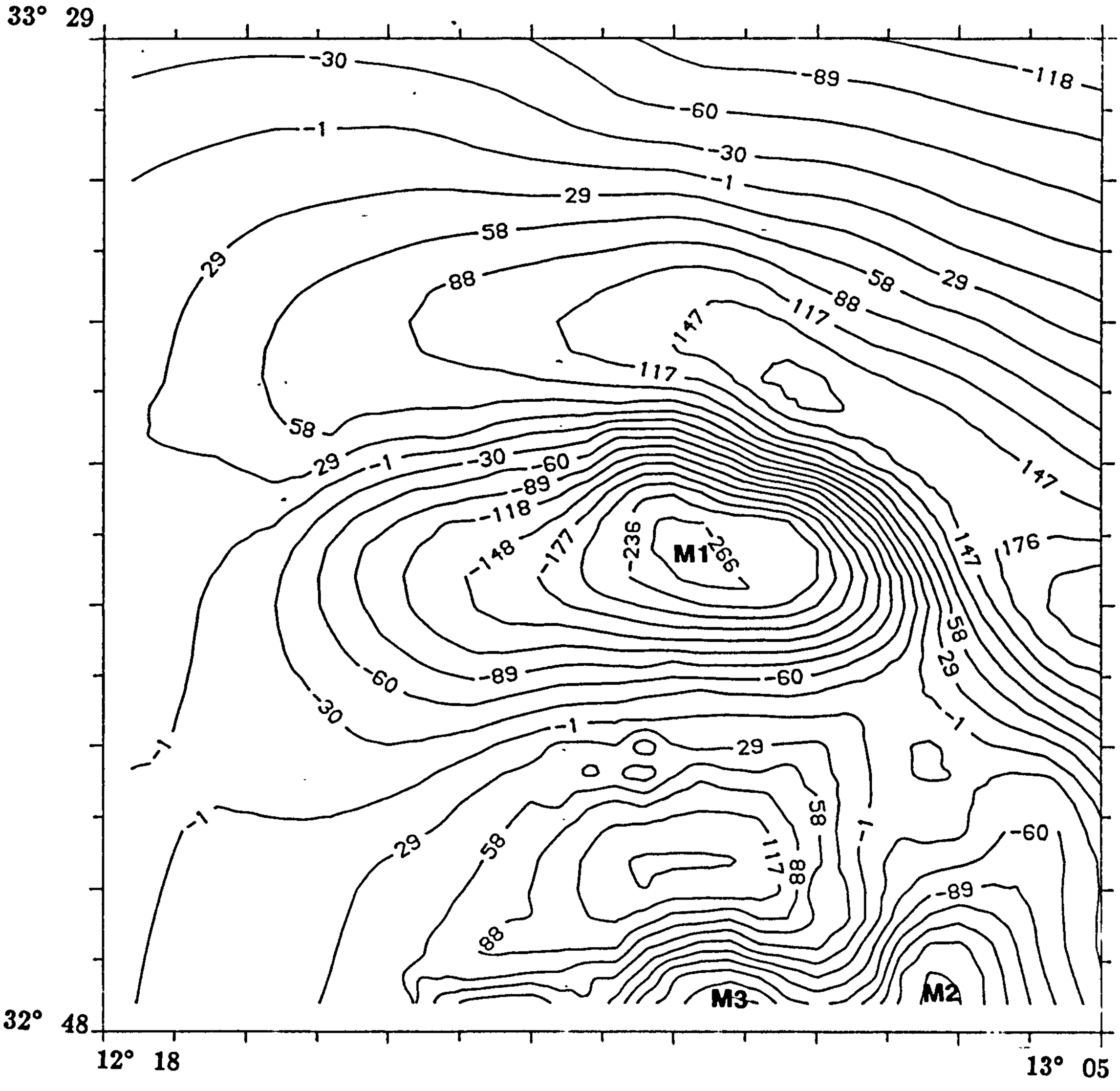

Figure 6.15: Residual magnetic map of the (55x55) dataset corresponding to the first degree Chebyshev polynomial regional. Contour interval: 30 nT. Individual anomalies (M1, M2, and M3) are identified.

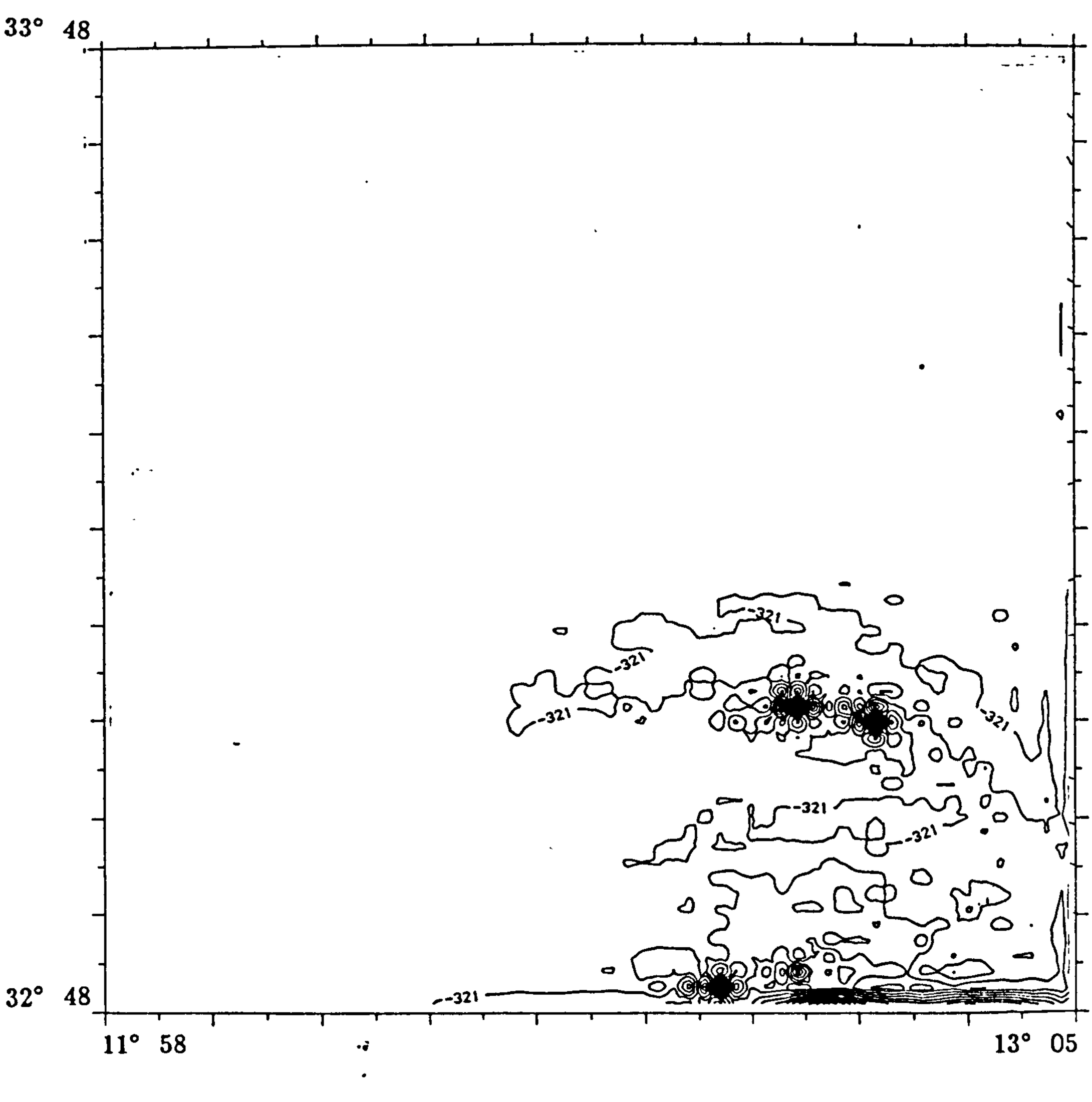

Figure 6.16: Second vertical derivative magnetic map of the (85x85) dataset. Contour interval: 40 nT/Km^2.

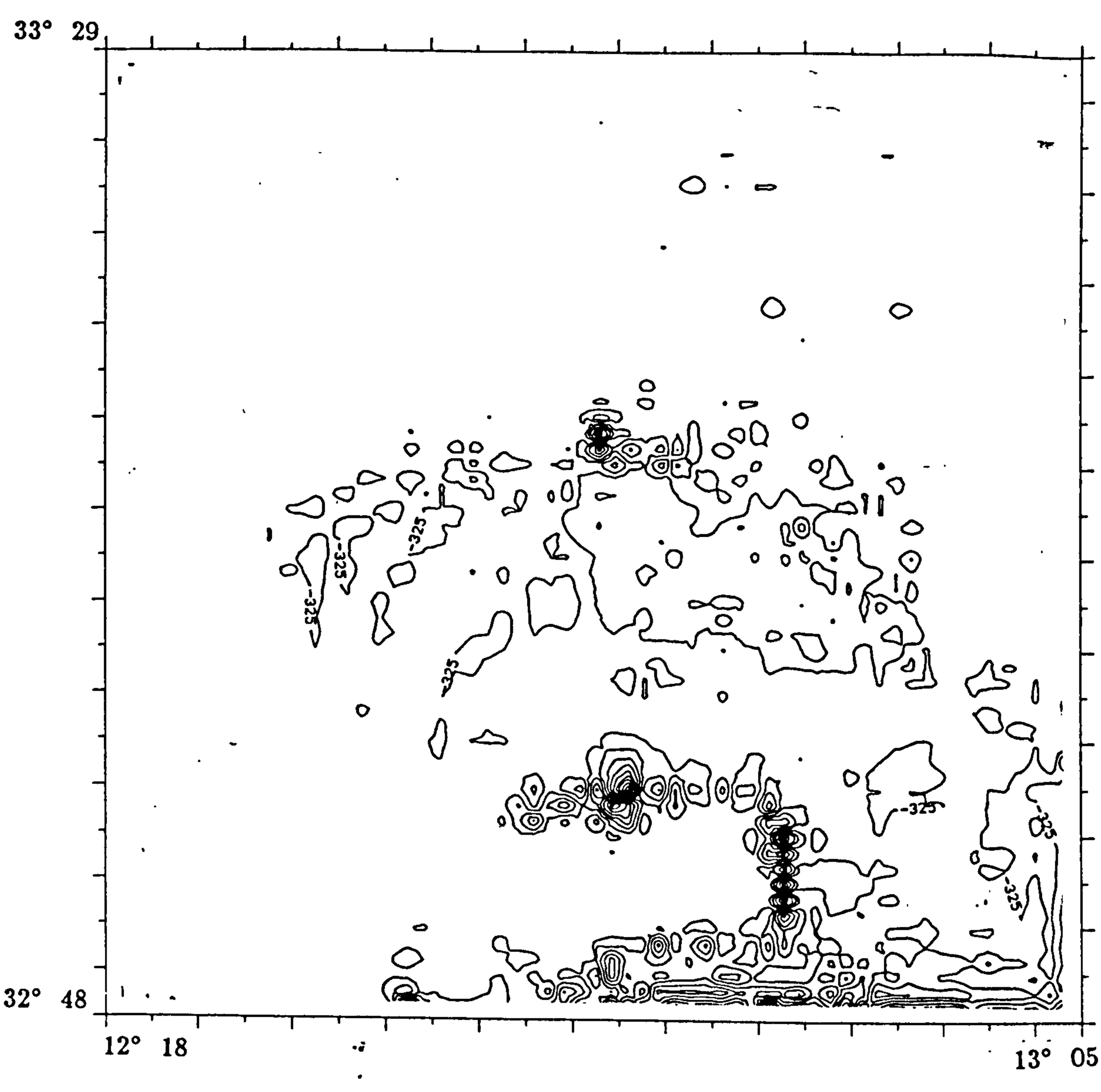

Figure 6.17: Second vertical derivative magnetic map of the (55x55) dataset. Contour interval: 40 nT/Km^2.

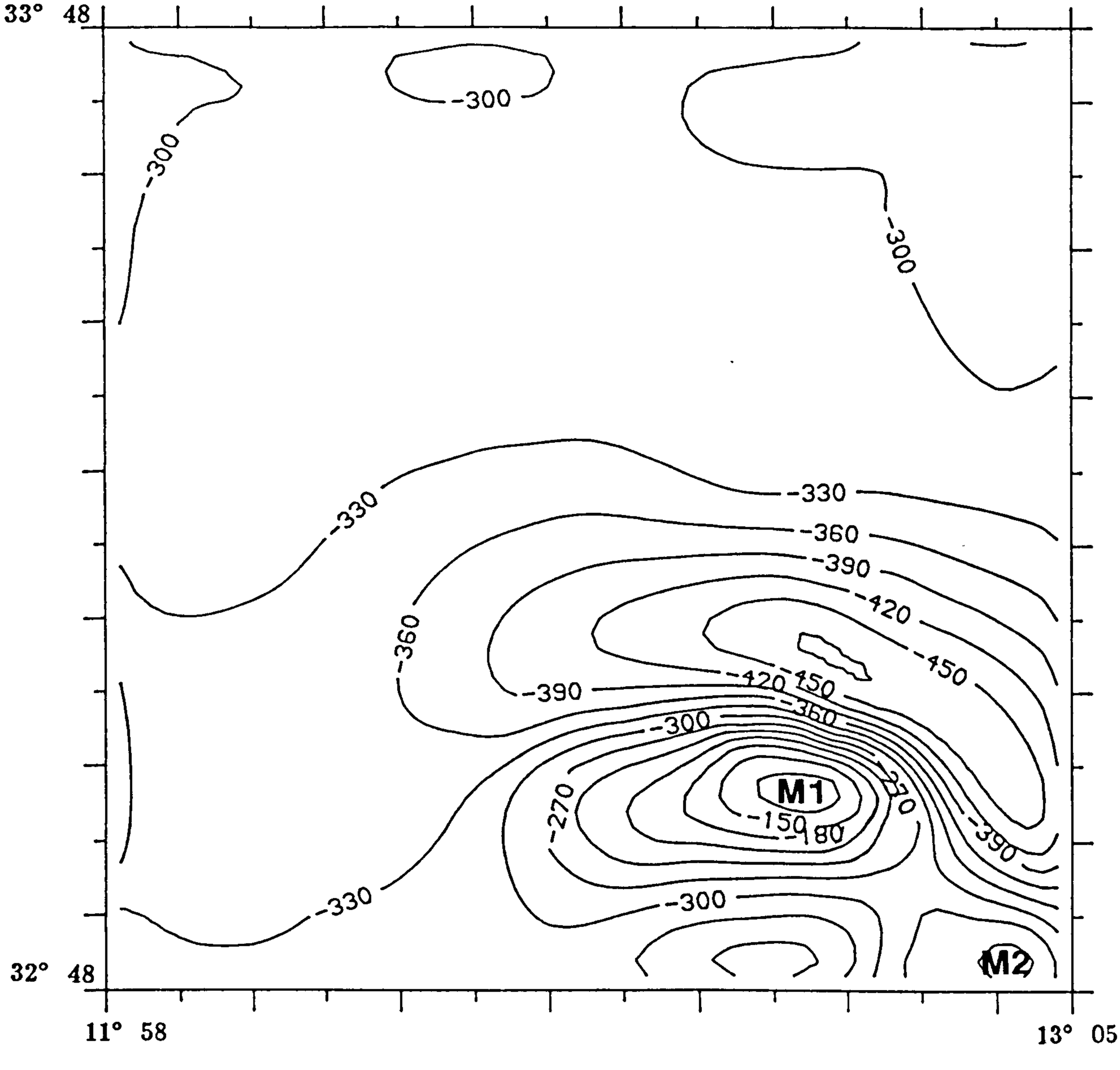

Figure 6.18: Magnetic map of the (85x85) dataset continued upwards by 1 km. Contour interval: 30 nT. Individual magnetic highs (M1 and M2) are identified.

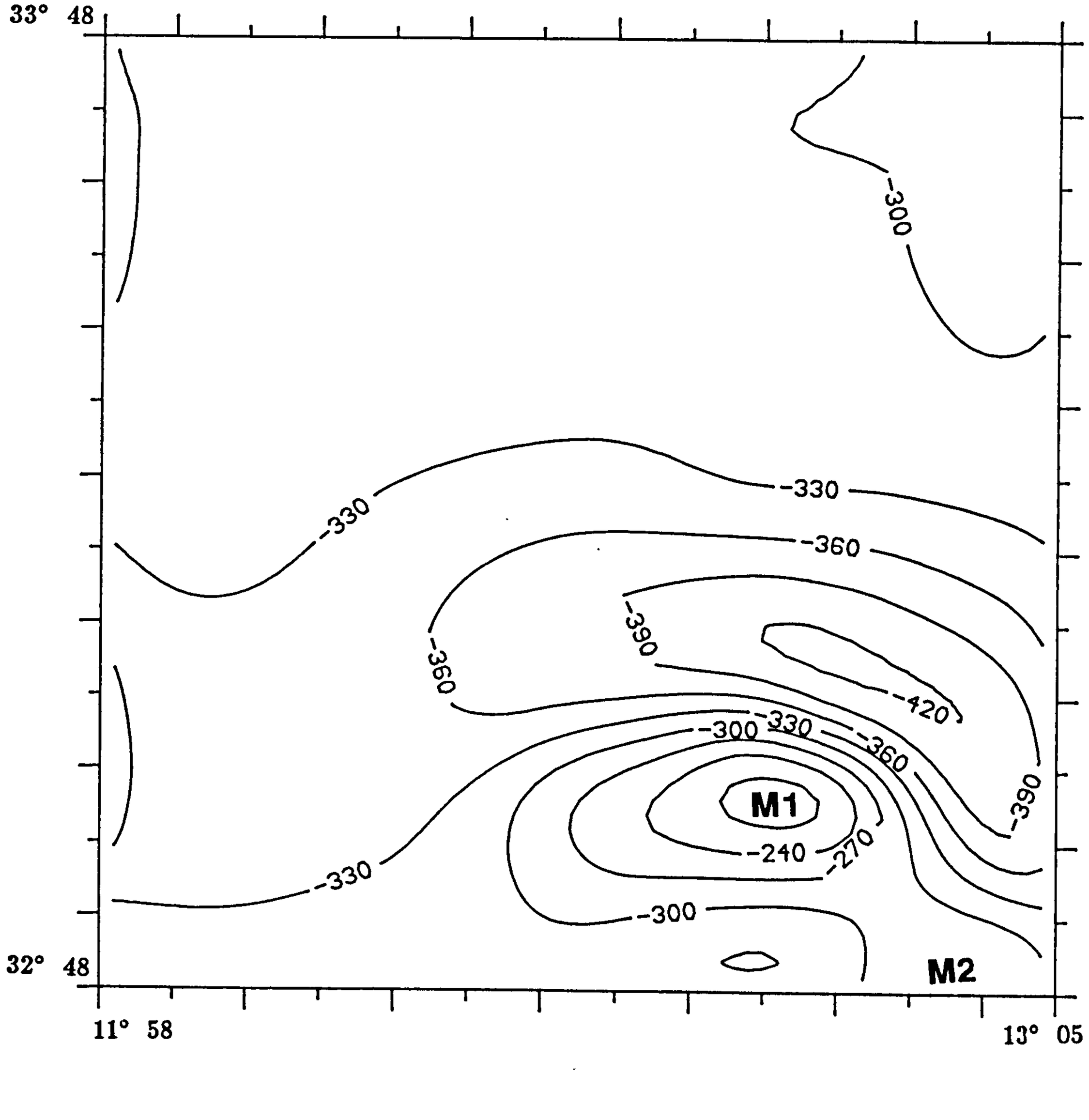

Figure 6.19: Magnetic map of the (85x85) dataset continued upwards by 3 km. Contour interval: 30 nT. Individual magnetic highs(M1 and M2) are identified.

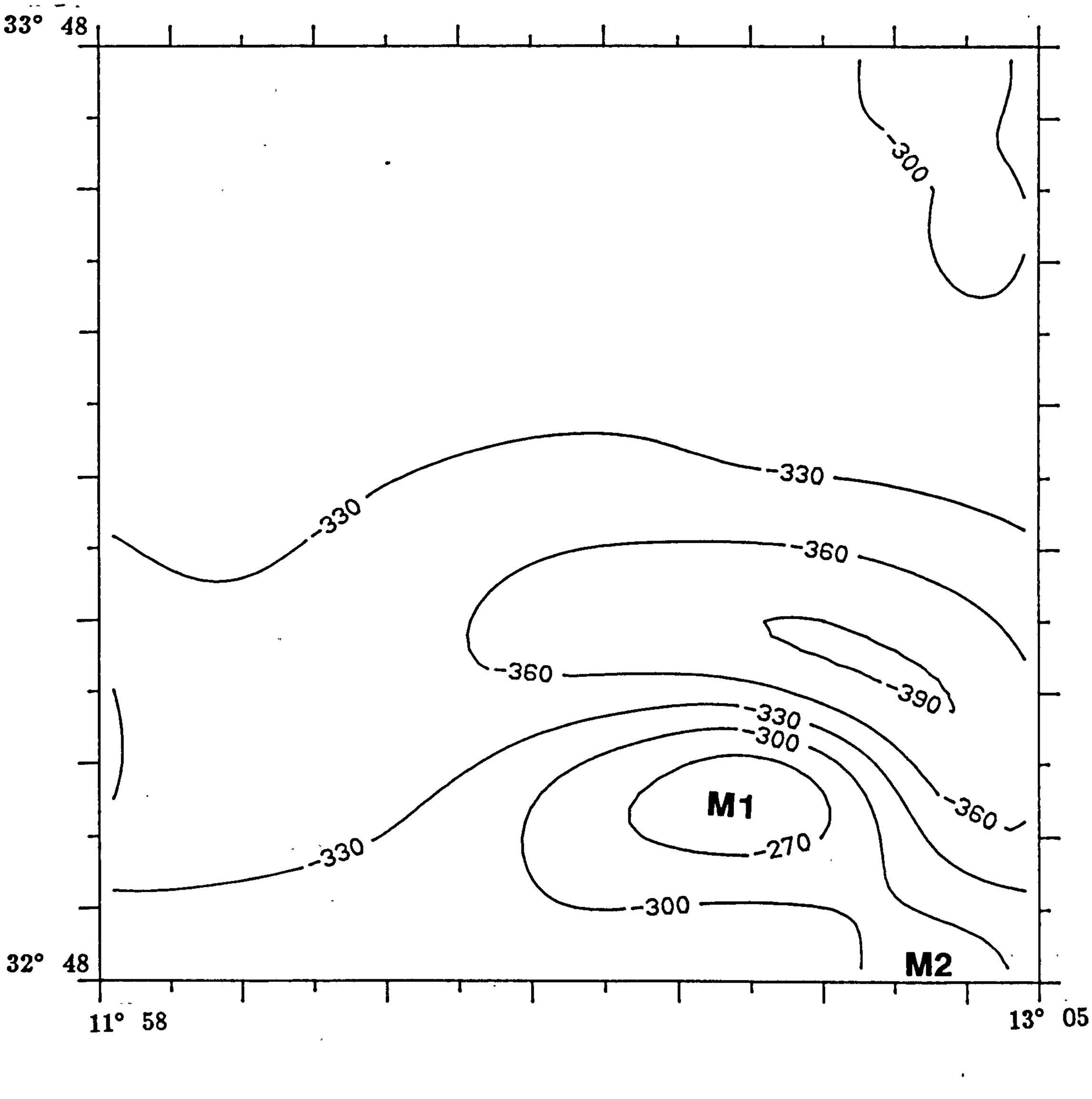

Figure 6.20: Magnetic map of the (85x85) dataset continued upwards by 5 km. Contour interval: 30 nT. Individual magnetic highs (M1 and M2) are identified, see text.

Figures 6.21, 6.22 and 6.23, respectively.

For the 1, 3, and 5 kms upward continued maps (Figures 6.18, 6.19, and 6.20), the anomalies M1, M2, and M3 are apparent as three discrete sources bodies, believed to be associated with the magmatic activity. The northern part is characterized by a low magnetic anomaly attributed the Salt and Thick Sediment Domains.

For the 2, 4, and 6 kms upward continued maps (Figures 6.21, 6.22, and 6.23) of the (55x55) dataset, the M1 and M2 anomalies define a general NW-SE trend, surrounded to the west and north by low magnetic anomalies in the range - 320 to - 370 nT.

The major magnetic anomaly (M1) which is attributed to the intrasedimentary volcanic units and the uplift structure, is clearly identified by continuation in the range 1 to 6 kms.

6.2.4.4 Power spectral calculations and wavenumber filtering

The power spectrum for each dataset (85x85 and 55x55) was computed (Figures 6.24 and 6.25).

Figure 6.24 (b) and Figure 6.25 (b) show graphs of the logarithm of the radially averaged log power spectrum $log_e P$ against wavenumber K. The graph for the (85x85) km dataset demonstrates three linear segments, indicating the presence of three groups of magnetic sources at different depths, h1= 0.663 km (negligible), h2 = 2.0 km, and h3 = 5.9 km. The graph for the (55x55) km dataset comprises two linear segments, providing depth estimates (h2) of 2.0 km and (h3) of 3.3 km. A possible interpretation of the increase in h3 value for the (55x55) compared to the (85x85) dataset is that the upper surface of the deeper group of sources slopes outwards from a point beneath the centroid of the anomaly and contributions to the power spectrum are made from progressively deeper components. An alternative explanation is that the wavenumbers generated by the deeper group of sources extend to very low values which only appear in the spectrum as the area of sampling increases (Ellis and Kearey 1984).

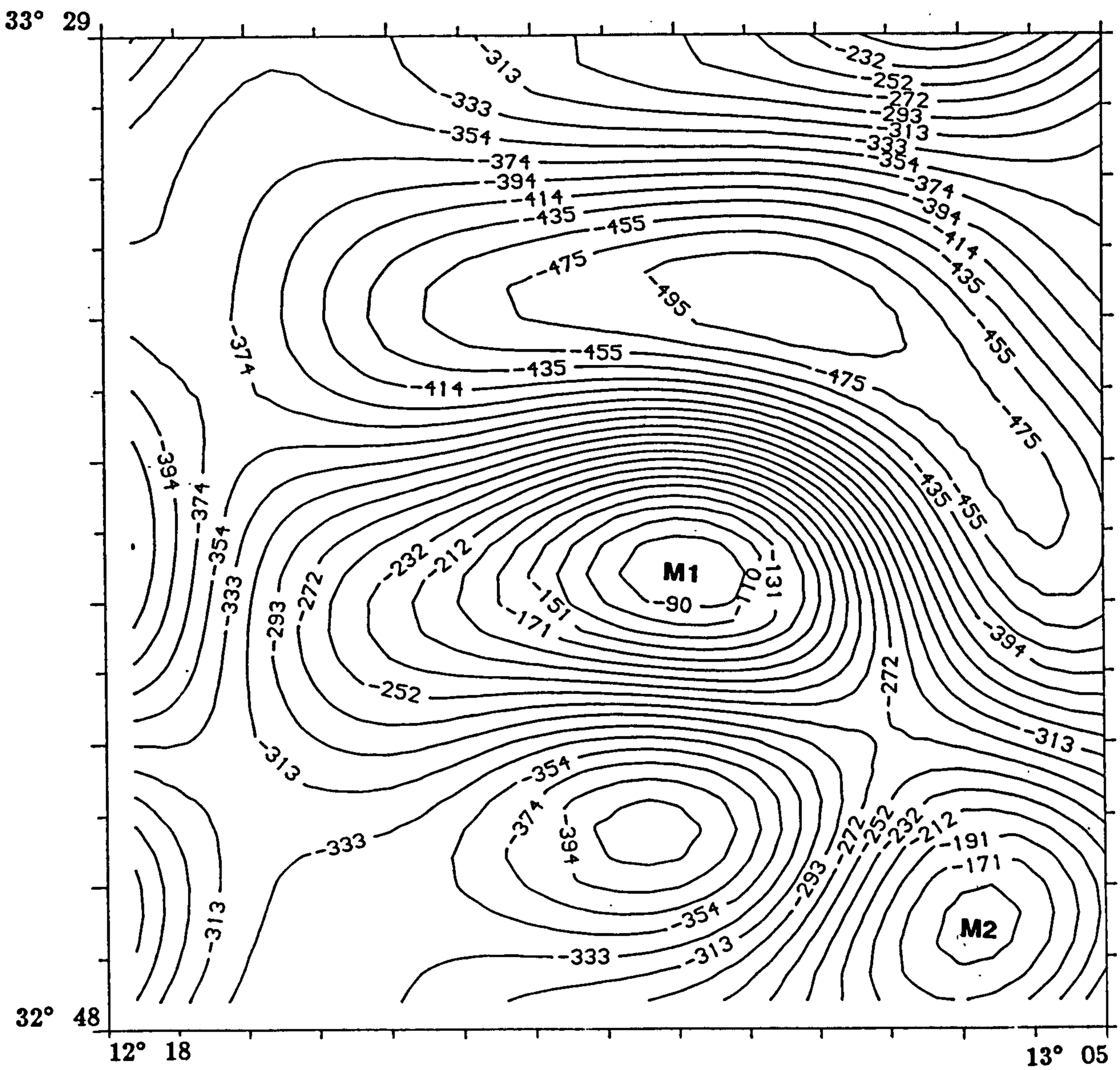

Figure 6.21: Magnetic map of the (55x55) dataset continued upwards by 2 km. Contour interval: 20 nT. Individual anomalies (M1 and M2) are identified.

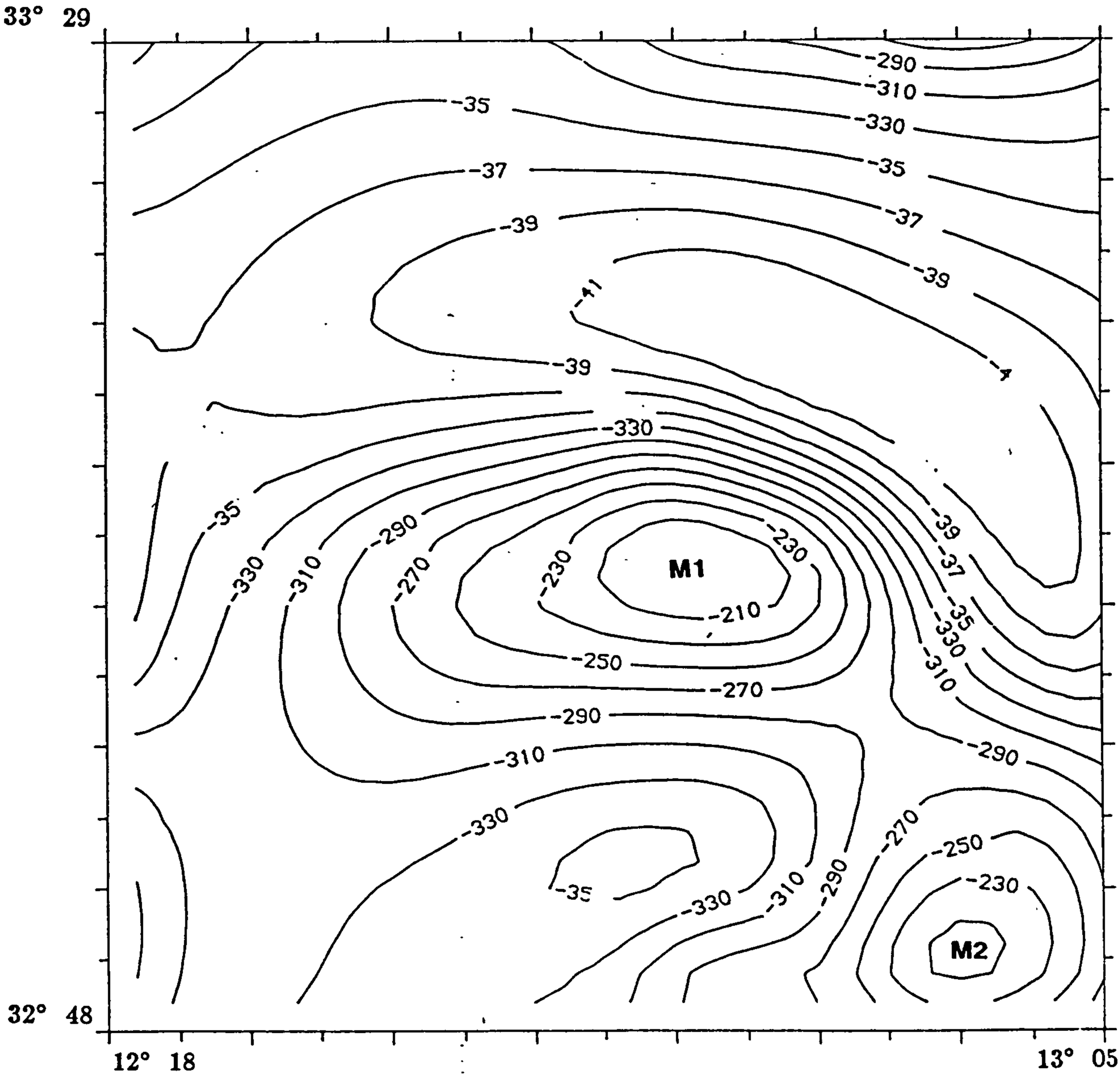

Figure 6.22: Magnetic map of the (55x55) dataset continued upwards by 4 km. Contour interval: 20 nT. Individual anomalies (M1 and M2) are identified.

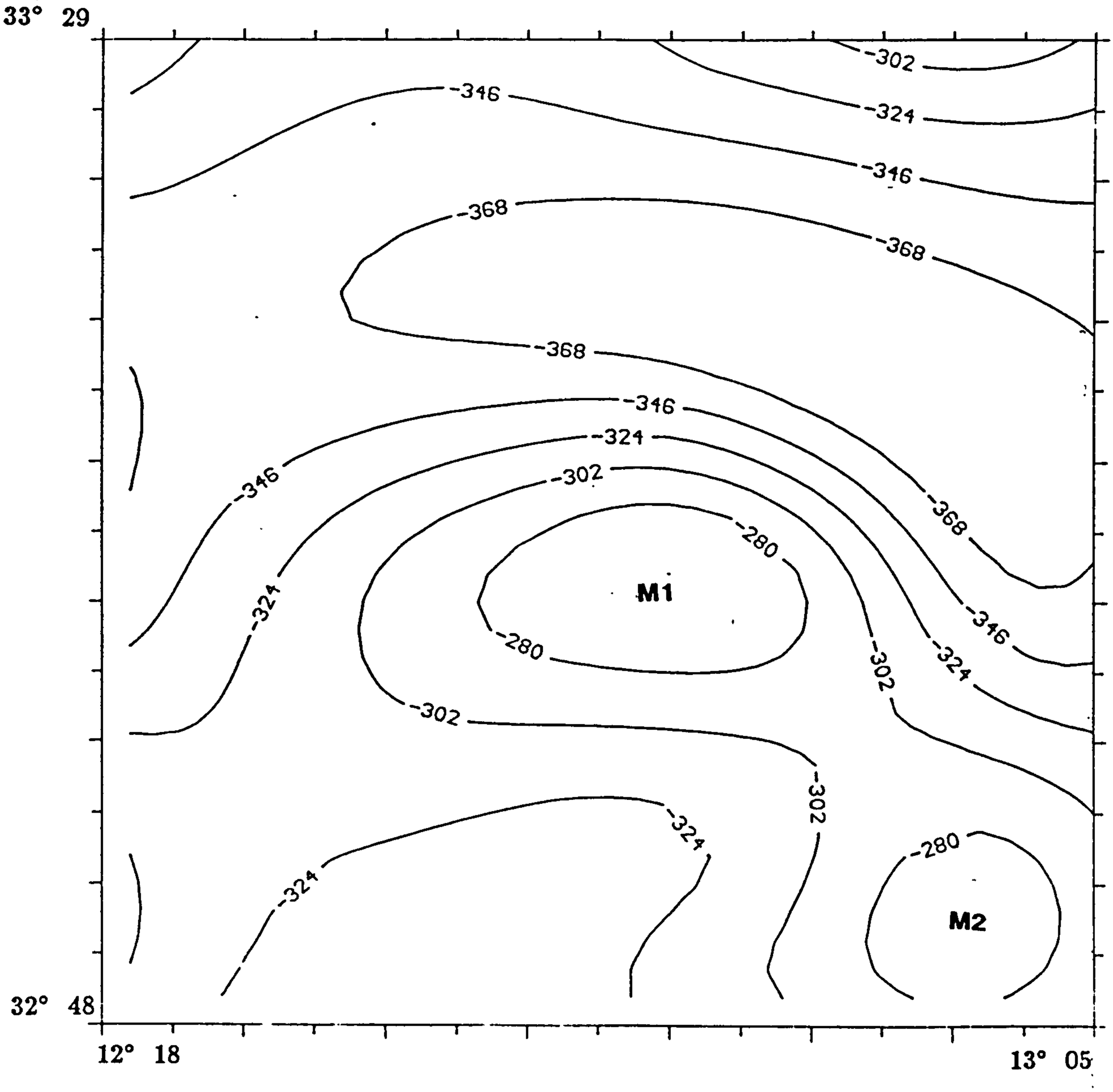

Figure 6.23: Magnetic map of the (55x55) dataset continued upwards by 6 km. Contour interval: 22 nT. Individual anomalies (M1 and M2) are identified.

(a)

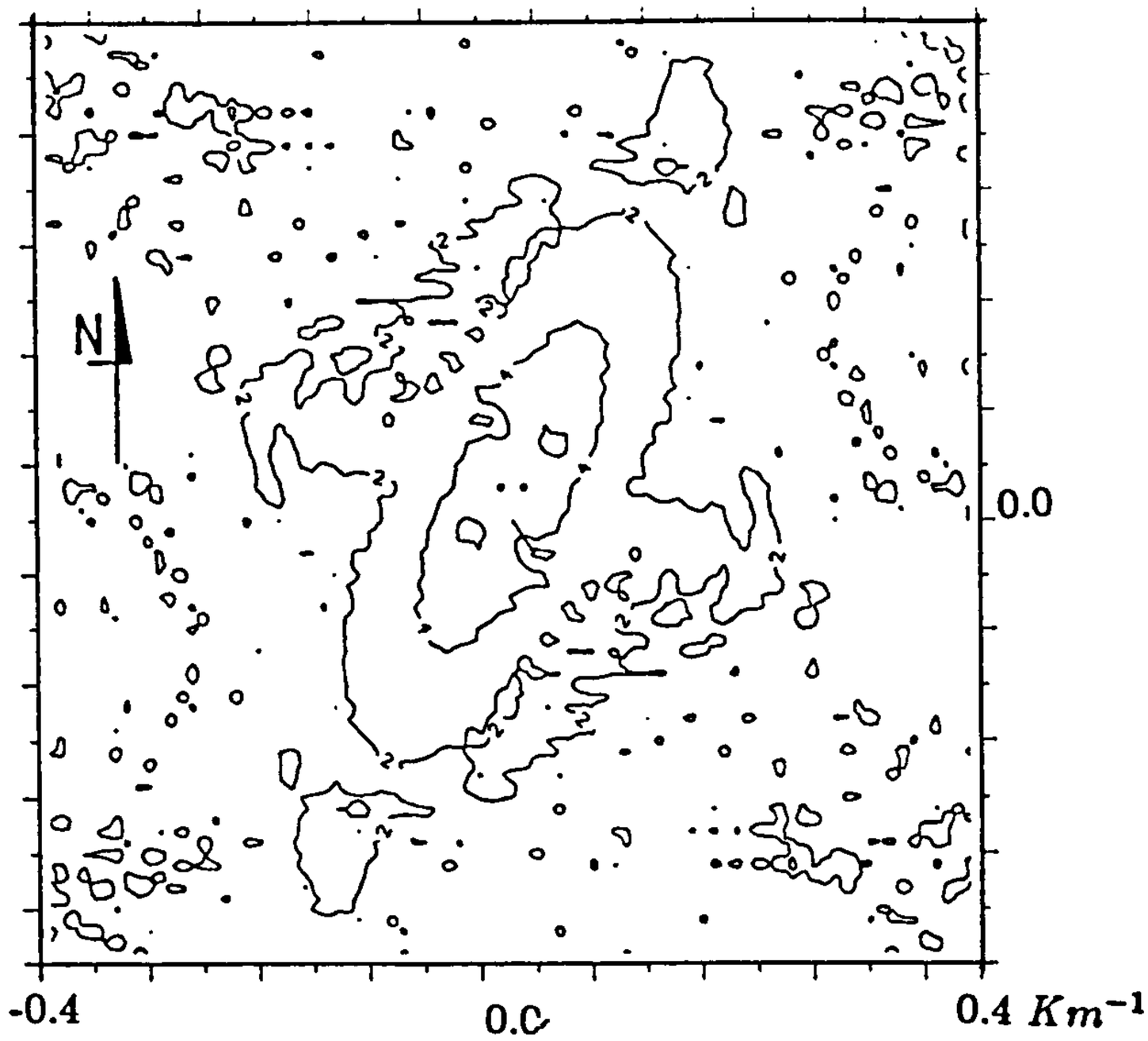

(b)

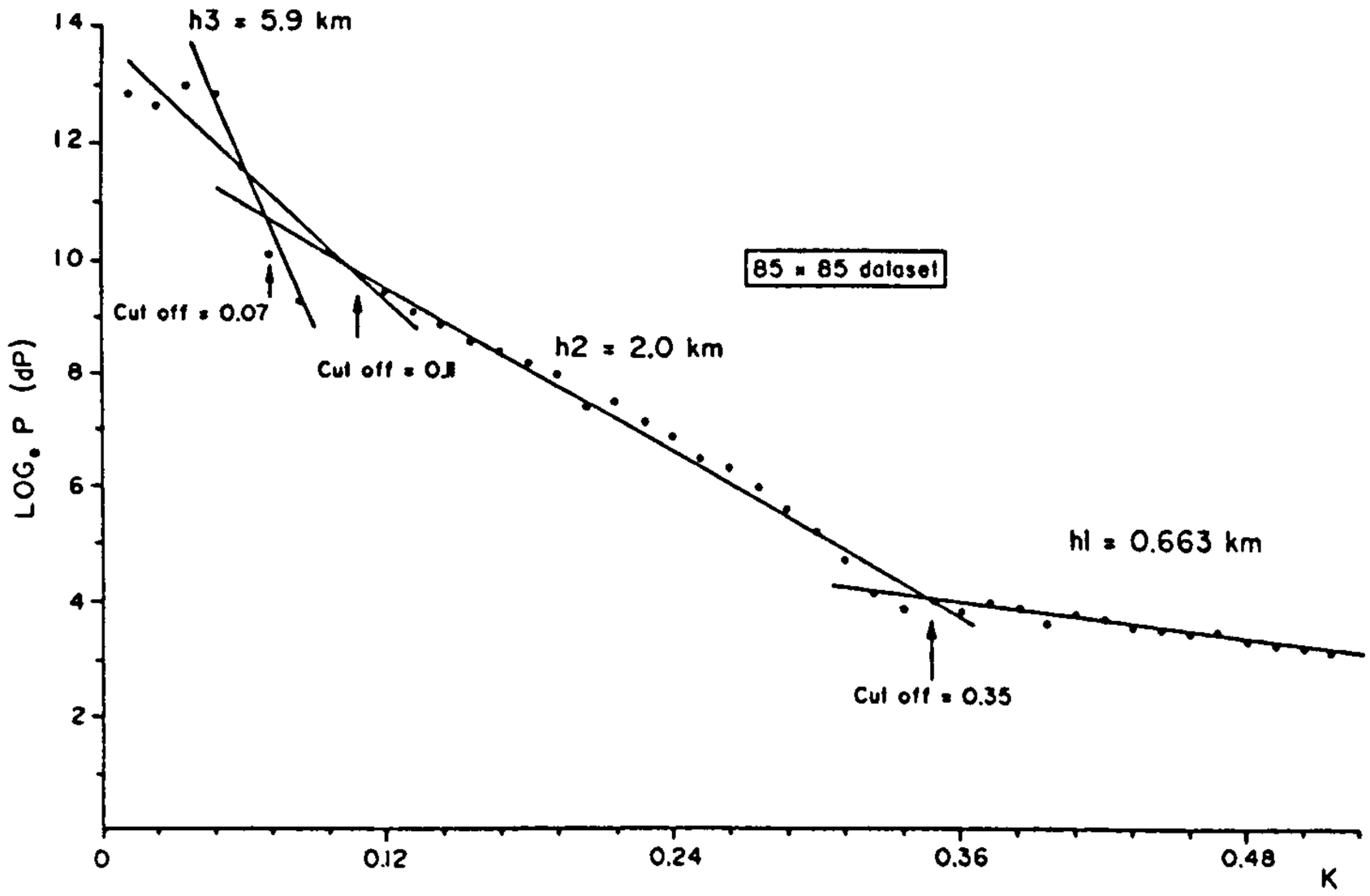

Figure 6.24: (a)-Log power spectrum. (b)-Radially-averaged log power spectrum versus wavenumber $K = \sqrt{u^2 + v^2}$ graph of the magnetic map of the (85x85) dataset. The units are based on a decibel scale.

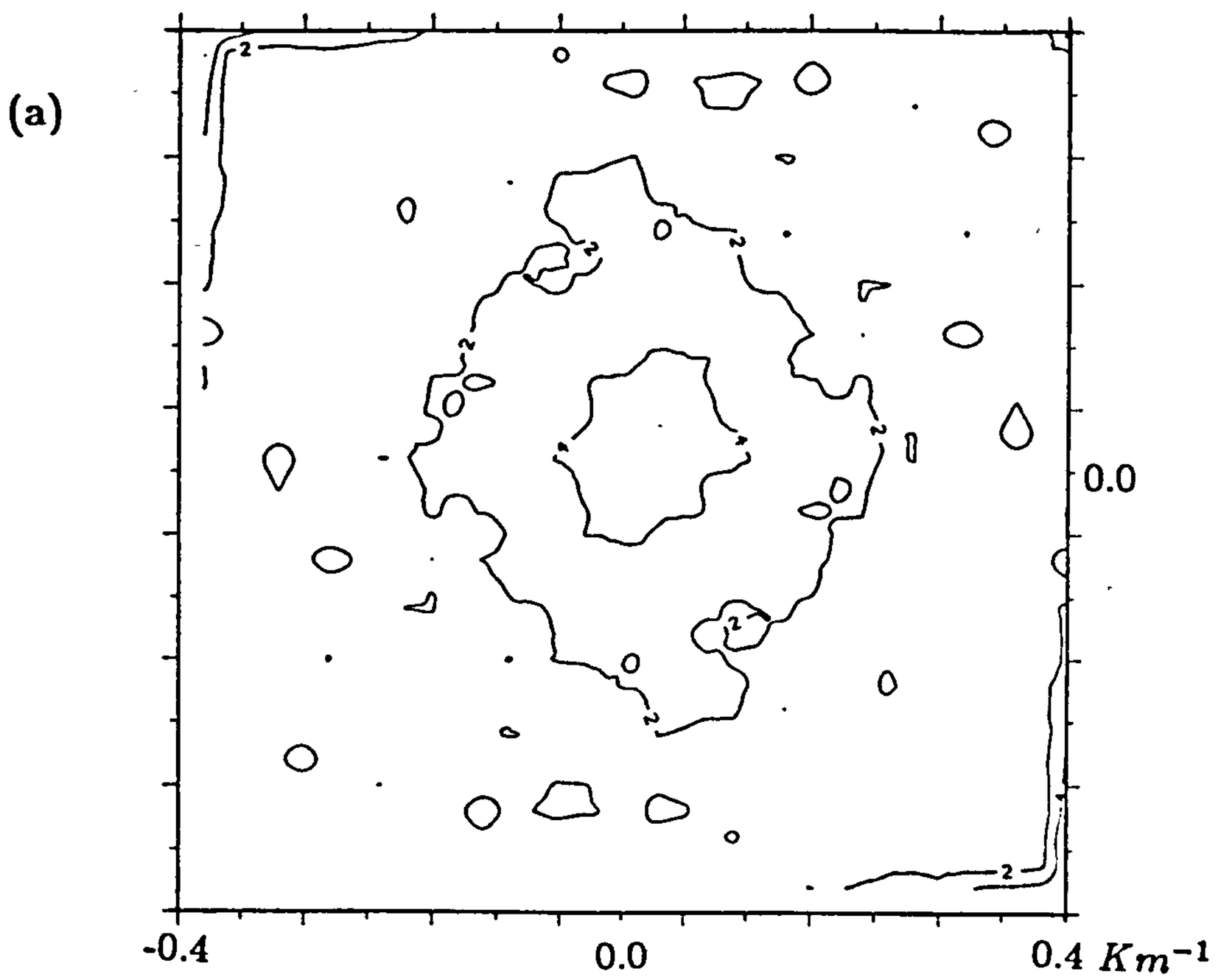

Figure 6.25: (a)-Log power spectrum. (b)-Radially-averaged log power spectrum versus wavenumber $K = \sqrt{u^2 + v^2}$ graph of the magnetic map of the (55x55) dataset. The units are based on a decibel scale.

The power spectrum analysis consequently reveals the presence of two groups of magnetic sources. The depth of the upper group (h2 and h3) is confirmed by seismic depth sections and borehole data. The depth distribution of the deeper group (h3) was not penetrated by any borehole. A possible interpretation of the source of this group is a thick volcanic unit. Therefore, the depth of 5.9 km represents a maximum depth estimate for these sources.

Radially-averaged log power spectrum provides the basis for a method of designing wavenumber filters which enhance the contribution to the anomalies of different groups of sources. The magnetic source comprises an ensemble of bodies, a model of the spectrum of the deep sources can be obtained by fitting a straight line to the low wavenumber portion of the spectrum and extrapolating to the higher wavenumbers. In Figure 6.24 (b) a low-pass (cutoff = 0.7, 0.11, and 0.35) filters have been designed to reduces the observed power at any wavenumber to that of the deep sources. In a similar fashion, a high-pass filter was obtained by extrapolating the high wavenumber segment of the spectrum to the low wavenumbers and reducing the observed power at any wavenumber to that of the shallower sources.

Low-pass and high-pass filtered maps have been produced for the (85x85) and (55x55) datasets (Figures 6.26, 6.27, 6.28 and 6.29, respectively). Figures 6.26 and 6.28 represent the magnetic anomaly arising from deep sources, and Figures 6.27 and 6.29 represents the anomaly from shallow sources.

Figure 6.26 represents the magnetic anomalies arising from deep sources with different wavenumber filters (cutoff values), and different depths, eg the low-pass filtered magnetic maps cutoff = 0.07 and 0.11, and 0.35 are represented the magnetic anomalies from the depths h3 and h2, respectively.

Figure 6.26 (b) is similar to the magnetic map of the (85x85) dataset continued upwards by 5 km (Figure 6.20).

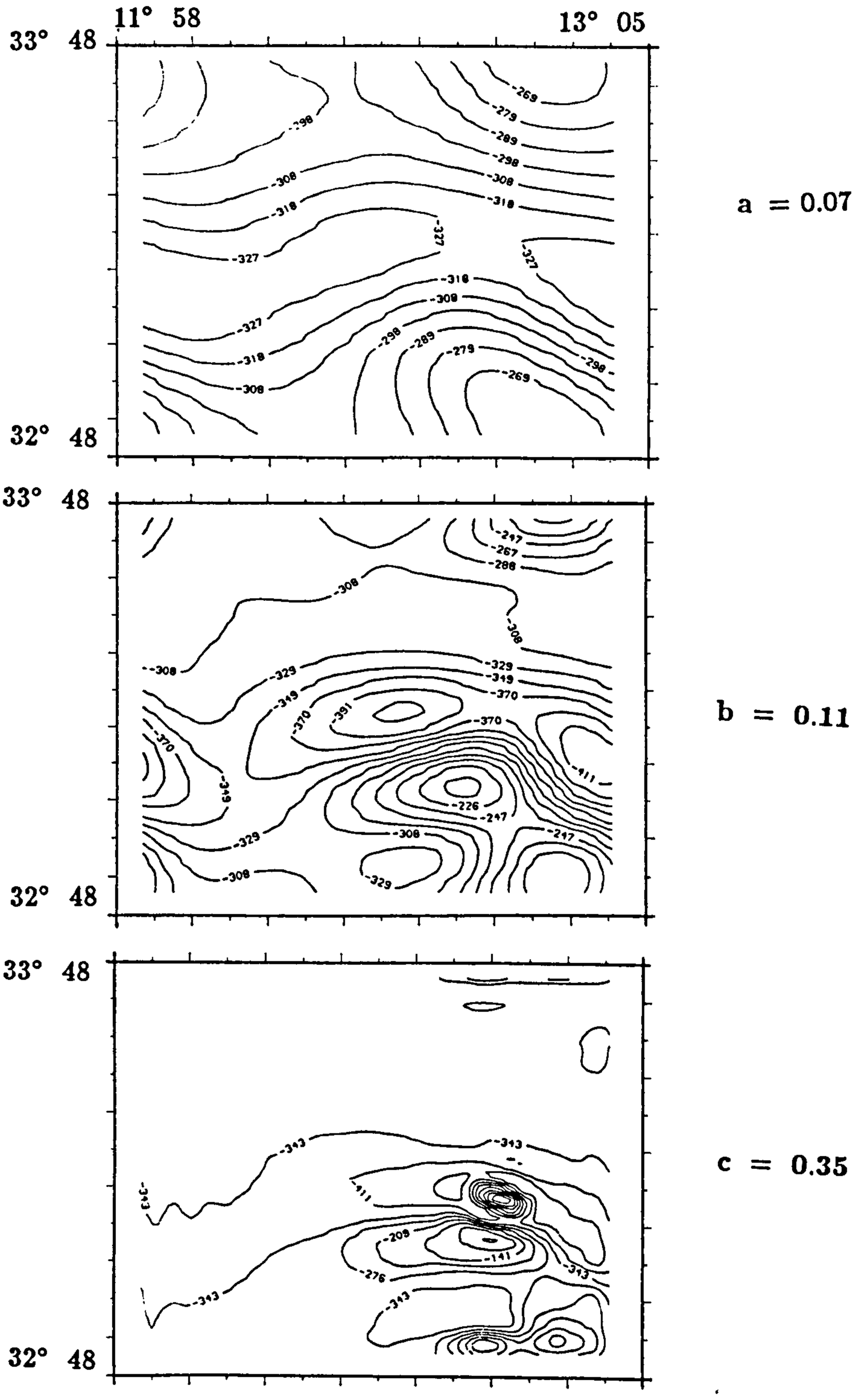

Figure 6.26: Low pass filtered magnetic field (85x85) dataset. Wavenumber filter cutoffs: $(a) = 0.07, (b) = 0.11, and (c) = 0.35$.

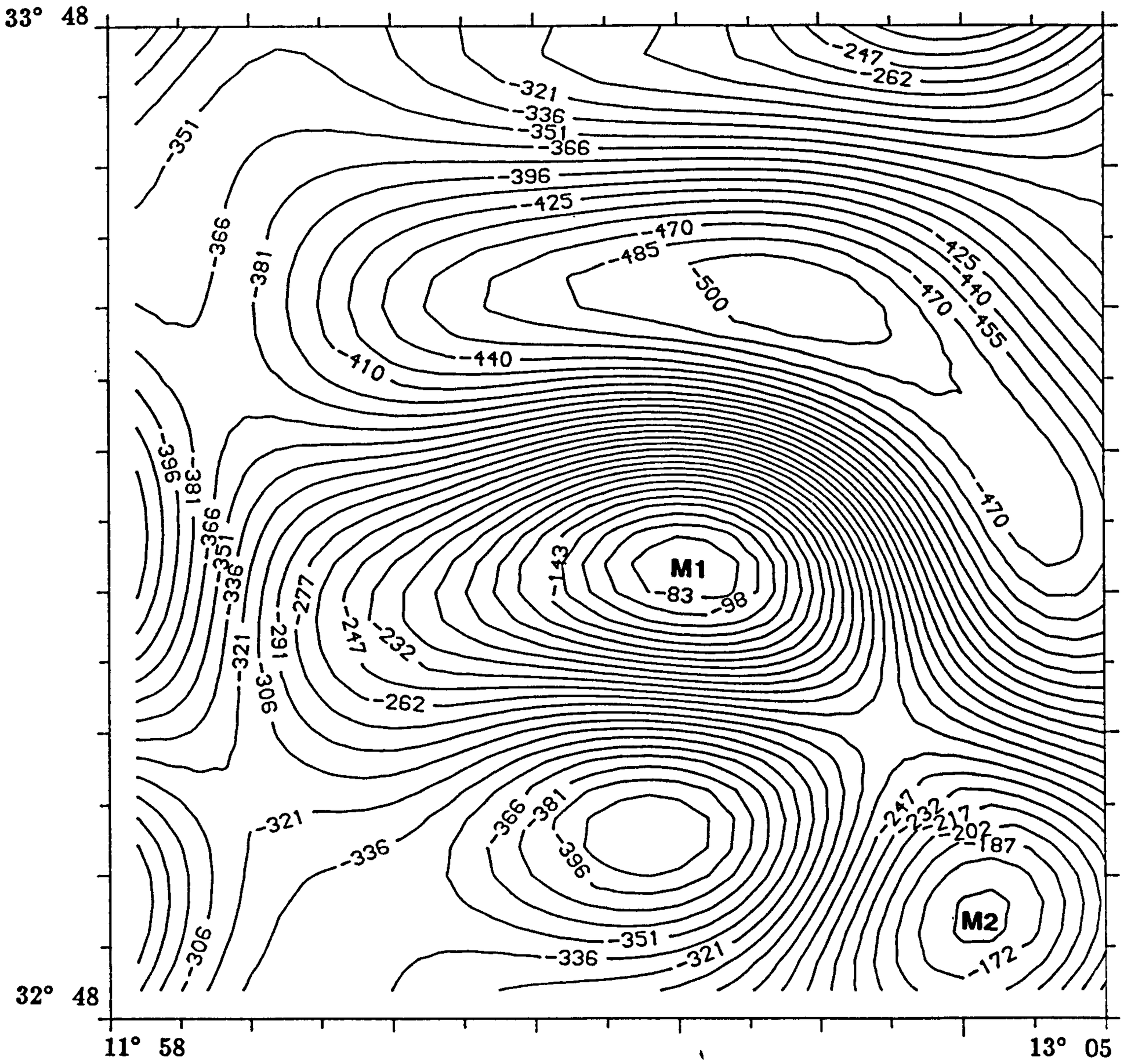

Figure 6.27: High pass filtered magnetic field (85x85) dataset. Wavenumber filter cutoff: 0.11. Contour interval= contour value x 10 mGal.

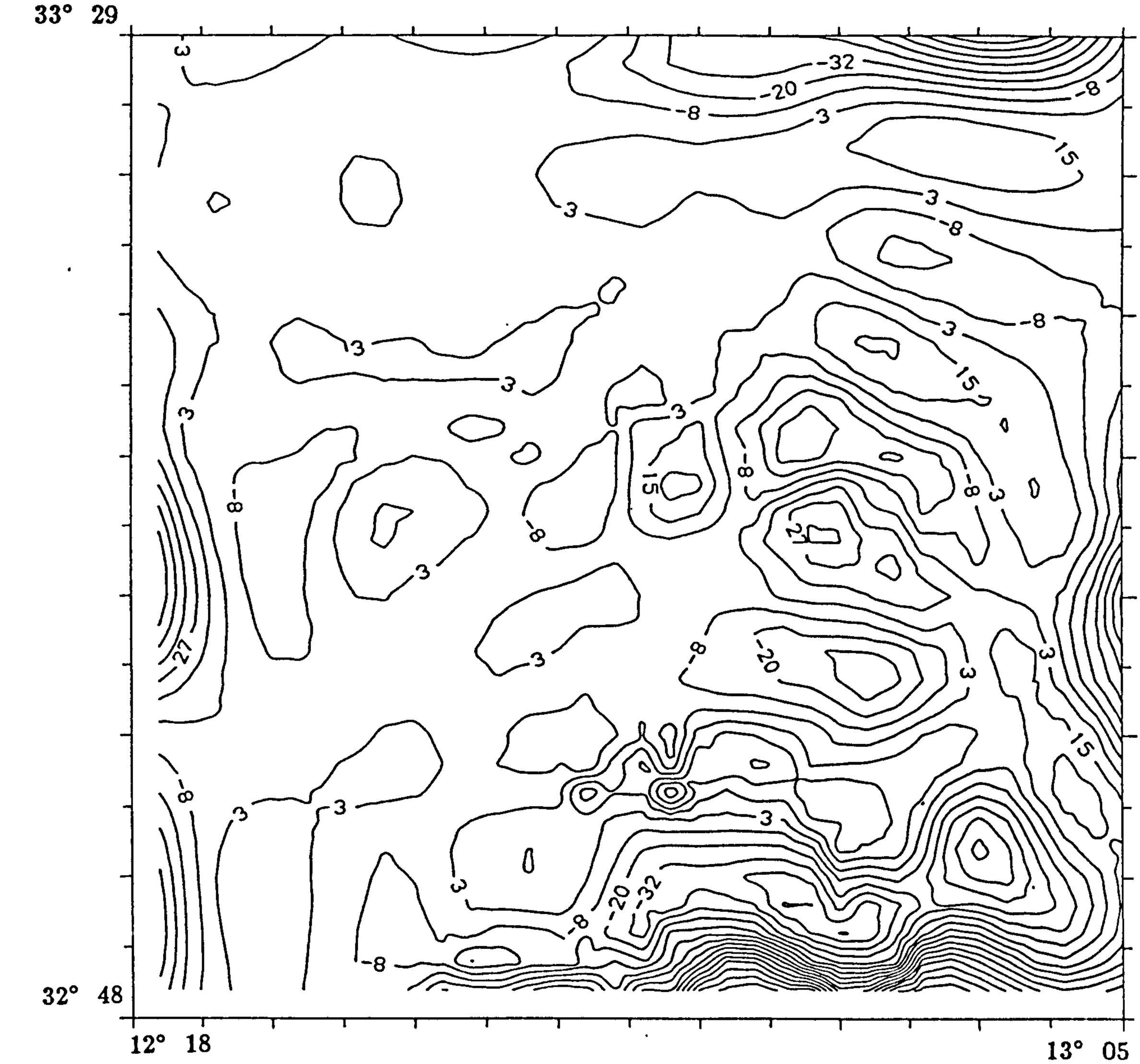

Figure 6.28: Low pass filtered magnetic field (55x55) dataset. Wavenumber filter cutoff: 0.2. Contour interval= contour value x˙10 mGal.

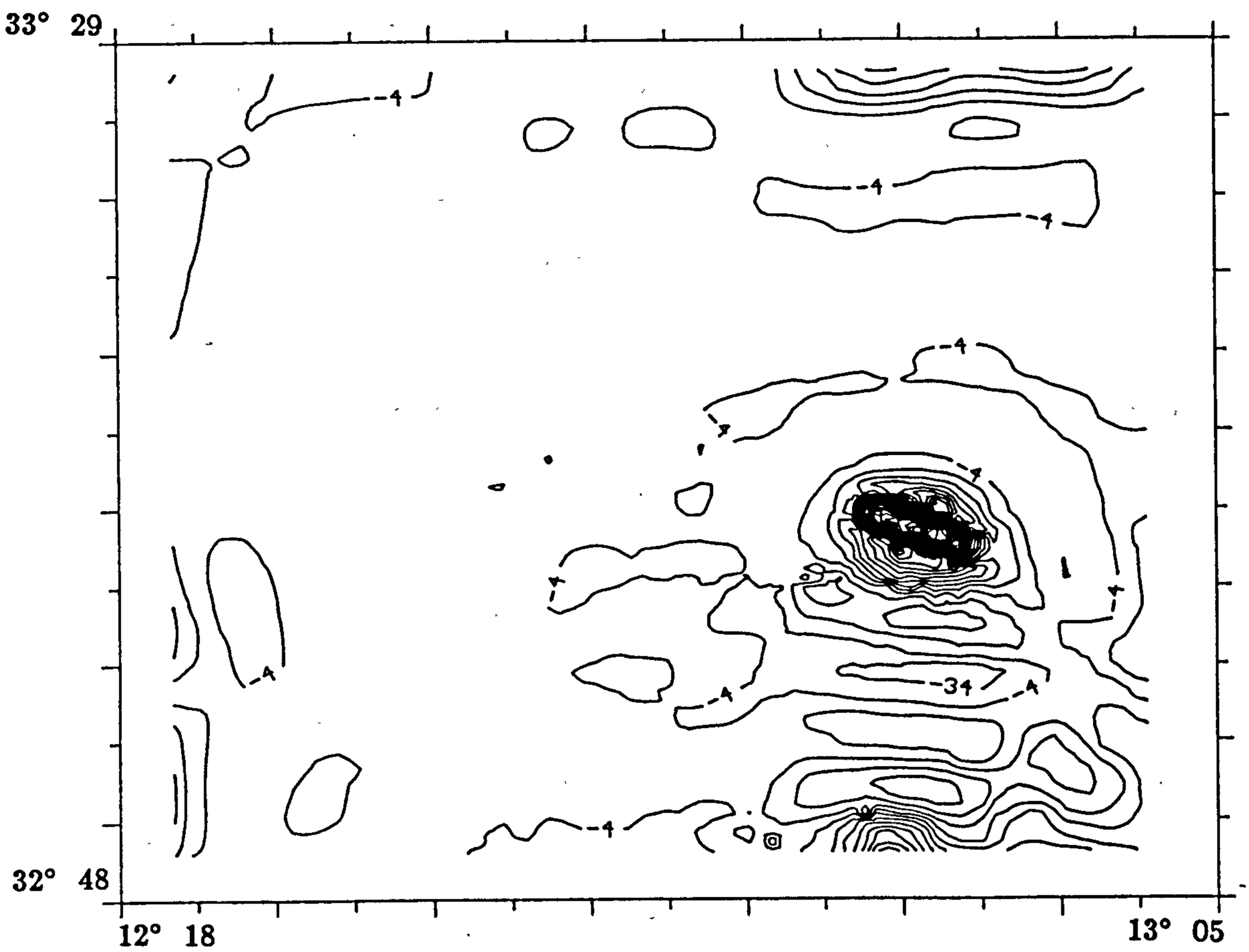

Figure 6.29: High pass filtered magnetic field (55x55) dataset. Wavenumber filter cutoff: 0.2. Contour interval= contour value x 10 mGal.

6.2.4.5 Reduced-to-the-pole magnetic anomaly

The reduced-to-the-pole magnetic map was shown in Figure 5.6. The magnetic highs are located over the bodies which cause them. In particular the large amplitude magnetic anomalies M1, M2, and M3 (100 nT). The low negative magnetic anomalies are associated with the Salt and Thick Sediment Domains areas (low magnetic susceptibility), giving value of about -350 nT. This map also shows the true magnetic intensity of the anomalies, which best represents the causative geological feature. Therefore such a map is ideally suited to the application of 2D anomaly modelling.

6.3 Modelling interpretation of gravity and magnetic anomalies

Detailed Bouguer gravity and total magnetic intensity (reduced to the pole) anomaly maps for the study area, given as Figures 5.1 and 5.6 (Chapter 5), form the basis for further quantitative interpretation. Originally, the Bouguer gravity map showed little useful information, due the smoothing by the gravity contouring, particularly, in the salt domain area, and no significant magnetic anomalies are indicated in the western and north-central parts of the study area. The 2D models developed in this section concentrate on the anomalies of interest only. These are the ones associated with the intrasedimentary volcanic units in the southern part of the study area (M1 and G8).

6.3.1 Physical property observations

Density

The density values for each geological formation were averaged from well log data, and have been presented in chapter 5 (Table 5.2). Representative densities are 2550 kg/m^3 and 2700 kg/m^3 for the V1 (Lower Eocene) and V2 (Cenomanian) units, respectively. The density contrast between the V1 unit and underlying Abiod Formation is $-50\ kg/m^3$, and

between the V2 unit and the underlying Lower Zebbag Formation is +125 km/m^3. The density information from well K1-137 is plotted in the form of density versus depth in Figure 6.30. The fitted smooth curve is shown to demonstrate the general pattern of density increase with depth.

Magnetic susceptibility

Magnetic susceptibility values for the small cutting samples are shown in Tables 5.5–5.8. Small cutting samples from intrasedimentary volcanic units V1 and V2 show a range of susceptibility from 144.466 X 10^{-3} SI to 1.872 X 10^{-3} SI.

General observations

The generally good quality of the seismic data for the sediment sequences overlying the Upper Zebbag Formation, allowed several significant reflections to be identified, but below the Upper Zebbag Formation it was not possible to resolve the depth and thickness of the intrasedimentary volcanic unit (V2) which is composite with the upper unit (V1). These are believed to be the major source of the potential field anomalies. As described in Chapter 4, these volcanic units (V1 and V2) were identified on several seismic lines and were clearly observed in some wells. The seismic line WT-24 (Figure 6.31) represents a good reference section for the geological considerations of 2-D gravity and magnetic modelling.

6.3.2 Two-dimensional modelling

Gravity modelling of intrasedimentary volcanic bodies:

A profile (line AB) was drawn in an approximately NE-SW direction across the main part of the positive gravity anomaly (G8) (Figure 5.1) which is associated with the intrasedimentary volcanic units (V1 and V2). The profile has a length of 30 km. 26 gravity contour

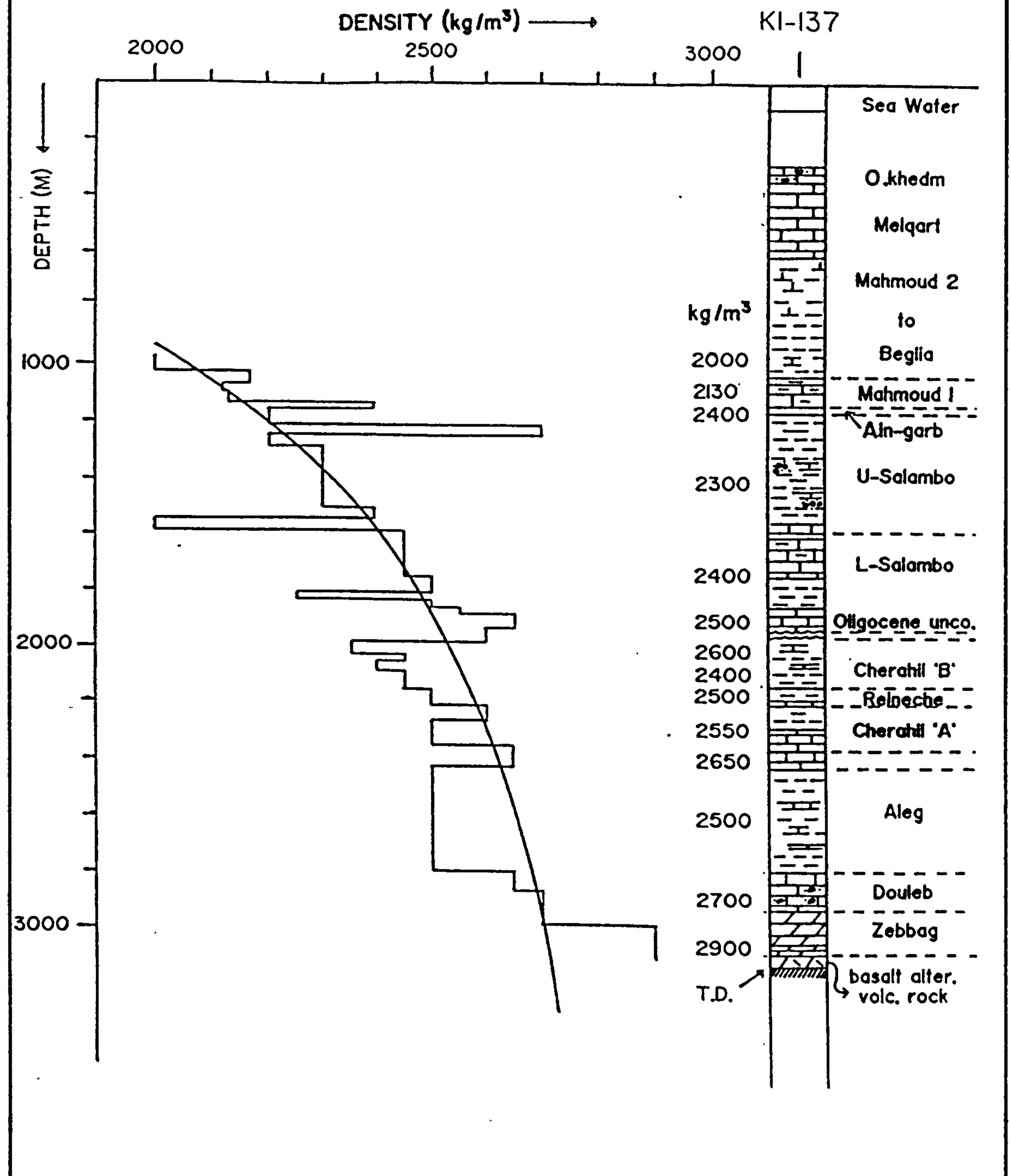

Figure 6.30: Formation density and lithologies encountered in the K1-137 well. The fitted smooth curve is shown to demonstrated the general pattern of density increase with depth.

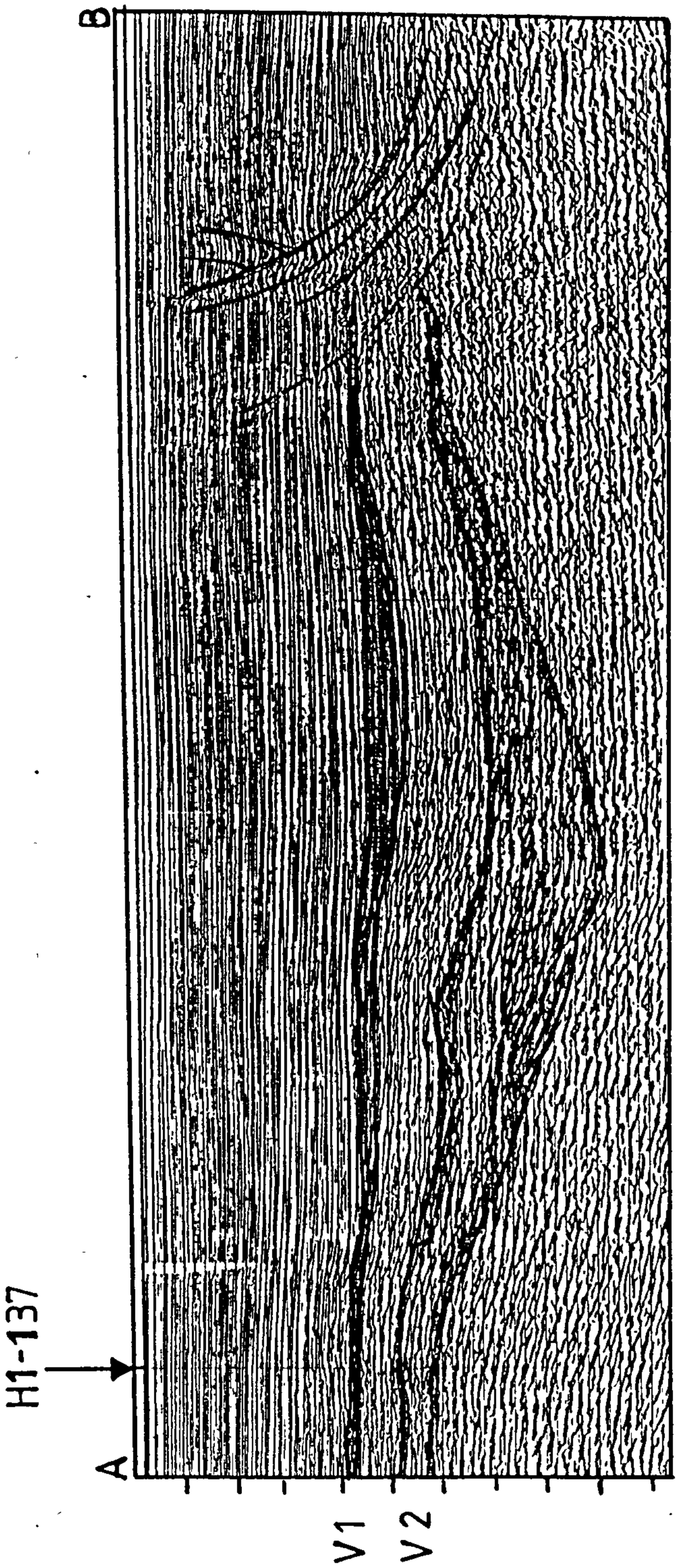

Figure 6.31: TWT seismic profile WT-24 associated with the magnetic and gravity anomalies. V1 and V2 are intrasedimentary volcanic units of L-Eocene and U-Cretaceous ages, respectively.

values were used for the construction of the profile. A borehole (H1-137) is located on this profile at a position use to its origin (SW end). This borehole penetrated the units V1 and V2, the origin and distribution of which were discussed in Chapter 4.

A 2-D gravity interpretation model was made by using the density contrasts of $-50\ kg/m^3$ and $125\ kg/m^3$ for the V1 and V2 bodies, respectively. Figure 6.32 demonstrates that the thicknesses deduced were 0.5 km and 1.1 km , and the depths 3.4 and 5.1 kms, for V1 and V2 respectively. The theoretical curve for the 2D model of gravity anomaly produces a good fit with the experimental curve, and provides the estimations of the thicknesses and depths which are in close agreement with existing borehole information, seismic data, and power spectrum graph (see Table 6.1). The basement depth at this position on the profile can be predicted as greater than 5.1 km (in the Continental Shelf Domain).

Magnetic modelling of intrasedimentary volcanic bodies:

The computer program MPL2A was used to compute the magnetic field over the intrasedimentary volcanic bodies anomaly. In order to interpret the magnetic anomaly M1 which is associated with these units, a profile (AB) has been drawn across the main part of the anomaly M1 (Figure 5.6). 47 magnetic contour values were used for the construction of this profile. The shape and depth of the intrasedimentary volcanic bodies have been estimated from the seismic reflection and well control data (Figure 6.31). The computed anomaly profile is than plotted together with an observed anomaly profile, and the parameters of the model structure can then be adjusted until a best-fit is obtained with the observed profile.

The input data to the programme was provided under three headings

1. Magnetic field data
2. Magnetization data
3. Body data

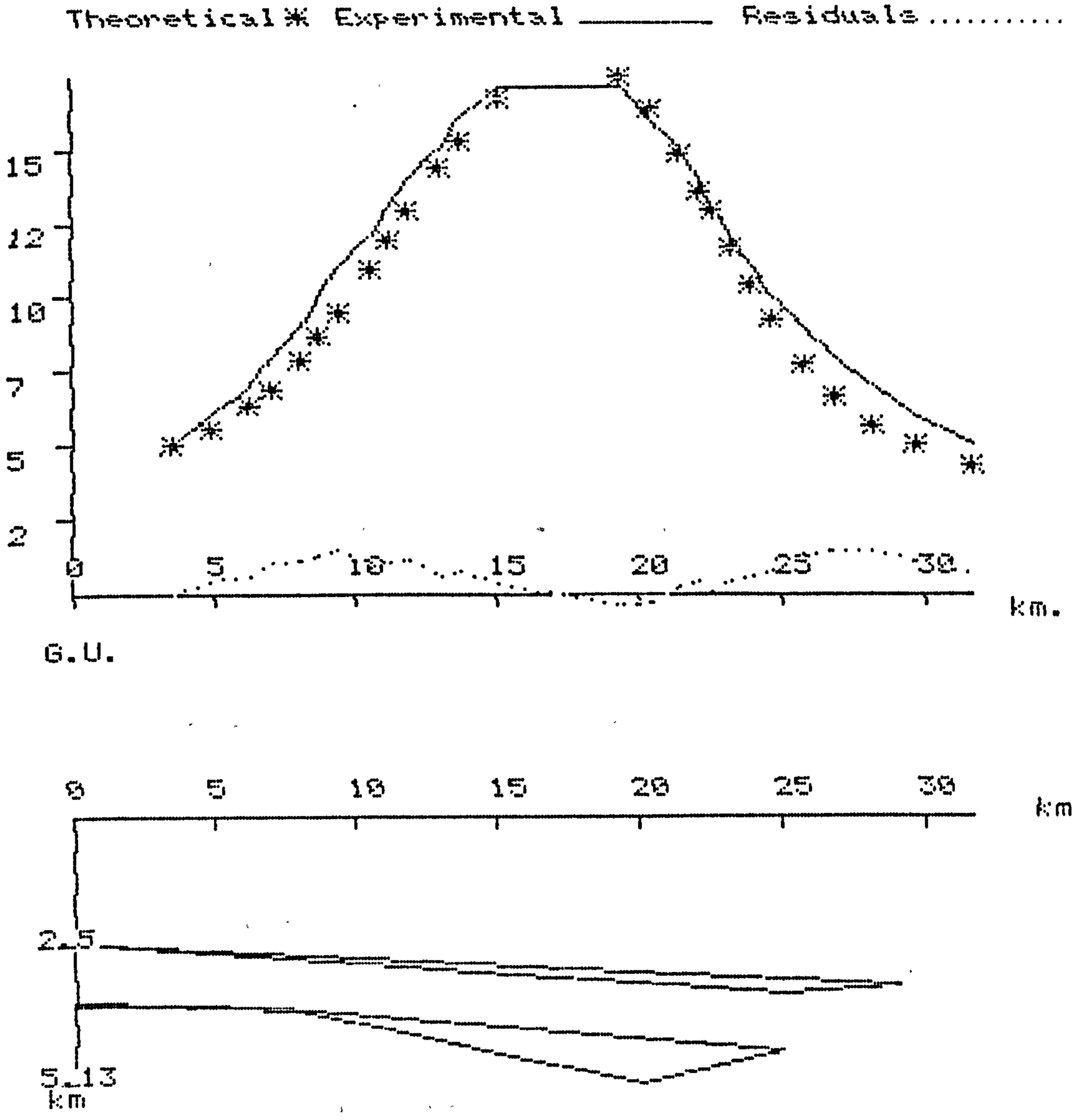

Figure 6.32: Two-dimensional model of the intrasedimentary volcanic bodies along the gravity profile AB. 30 *km* length. Effective Densities $V1 = -50$ *and* $V2 = 125\ kg/m^{-3}$, respectively.

1. **Magnetic field data**

   This specifies the intensity and direction of the ambient geomagnetic field at the magnetic survey site.

   - **The ambient field intensity is input in nanotesla (nT) units.**
   - **The local field inclination (dip) is specified as positive if downwards and negative if upwards.**
   - **The local field declination is specified in degree (clockwise) from geographic north.**

2. **Magnetization data**

   This specifies the intensity and direction of the total magnetism within the model body.

   - **The intensity of magnetization is input in SI units (nT).**
   - **The inclination and declination of the magnetism as in (1) above.**

3. **Body data**

   This specifies the geometry of the assumed model structure.

   - **The azimuth of the x-axis.**
   - **The number of body edges is equal to the number of vertices of the model structure.**
   - **The body coordinates are input as pairs, eg (x_i, z_i), in clockwise order around the body.**
   - **The magnetic anomalies are computed at station whose horizontal and height positions (x, z) are input from a data file.**
   - **The units of measurement are as follows:**

     Horizontal coordinates: Km

     Vertical coordinates: Km

     Magnetic field values: nanoTesla (nT) Magnetization intensity: nT

The geomagnetic field intensity in the region is 42350 nT (Geomagnetic Bulletin 10, 1978). The local field inclination (dip) is 53°. The local field declination from geographic north is 0°.

The model of Figure 6.33 was calculated on the basis of induced magnetization only, using a magnetic intensity of 6120 nT, an inclination of 53° and declination 0°, and a susceptibility value of $144.466\ X\ 10^{-3}$ SI. This value is the result of detailed susceptibility measurements on samples from three boreholes given earlier (see Chapter 5).

The model of Figure 6.34 was produced using the remanent magnetization only, with a magnetic intensity of 281 nT, an inclination of 31° and a declination of 0°, and a susceptibility value of $144.466\ X\ 10^{-3}$ SI. The theoretical curve for this model does not fit the experimental (observed). A possible explanation for this lack of fit relates to the weakness of the remanent magnetization in these volcanic rock units.

The model of Figure 6.35 was produced by a combination of induced and remanent magnetizations, using the total magnetization 6381 nT, an inclination 52°, declination 0°, and a susceptibility value of $144.466\ X\ 10^{-3}$ SI.

The theoretical curve for the combined model produces a good fit with the experimental curve, which indicates that the magnetic intensity of the M1 anomaly can be attributed to the total intensity magnetization of induced and remanent magnetization of the V1 and V2 bodies. This model predicts thicknesses of V1 = 0.7 and V2 = 4 kms, and width of 29 and 25 kms of V1 and V2 respectively (perpendicular to strike).

6.3.3 Comparison of the different techniques

The computed depth for the bodies by the 2-D gravity and magnetic modelling techniques can be compared with (i) that estimated in the borehole H1-137 positioned at the end of the profile AB, (ii) the depth indicated by seismic data, and (iii) the estimated depth which was computed from the power spectrum graphs of the gravity and magnetic maps (Figures 6.10, 6.24, and 6.25). The comparison of these results are shown in Table 6.1

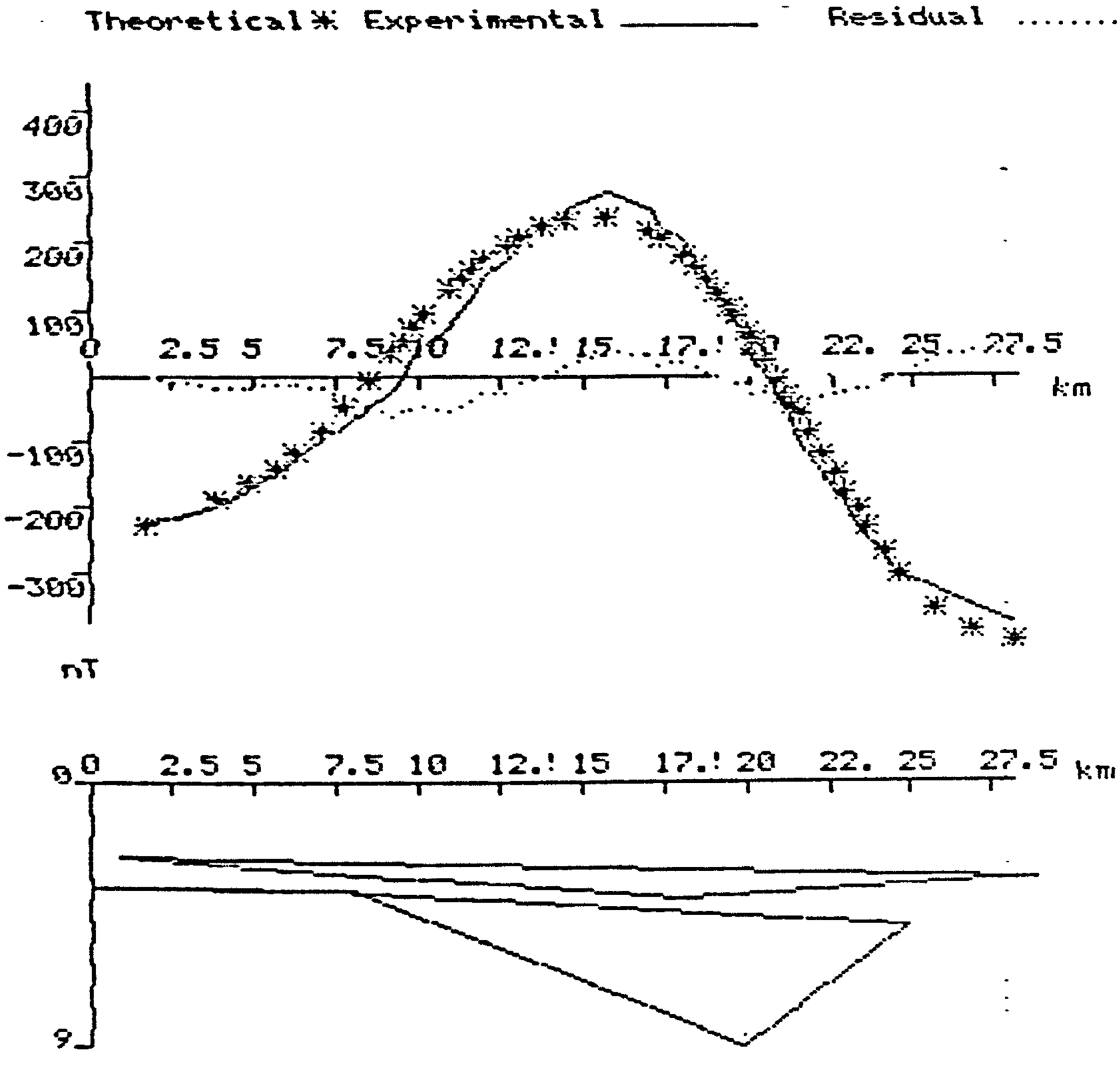

Figure 6.33: 2D model of the intrasedimentary volcanic bodies along the magnetic profile AB (30 *km* length). Produced on the induced magnetization only, using the susceptibility value of 144.466 X 10^{-3} SI.

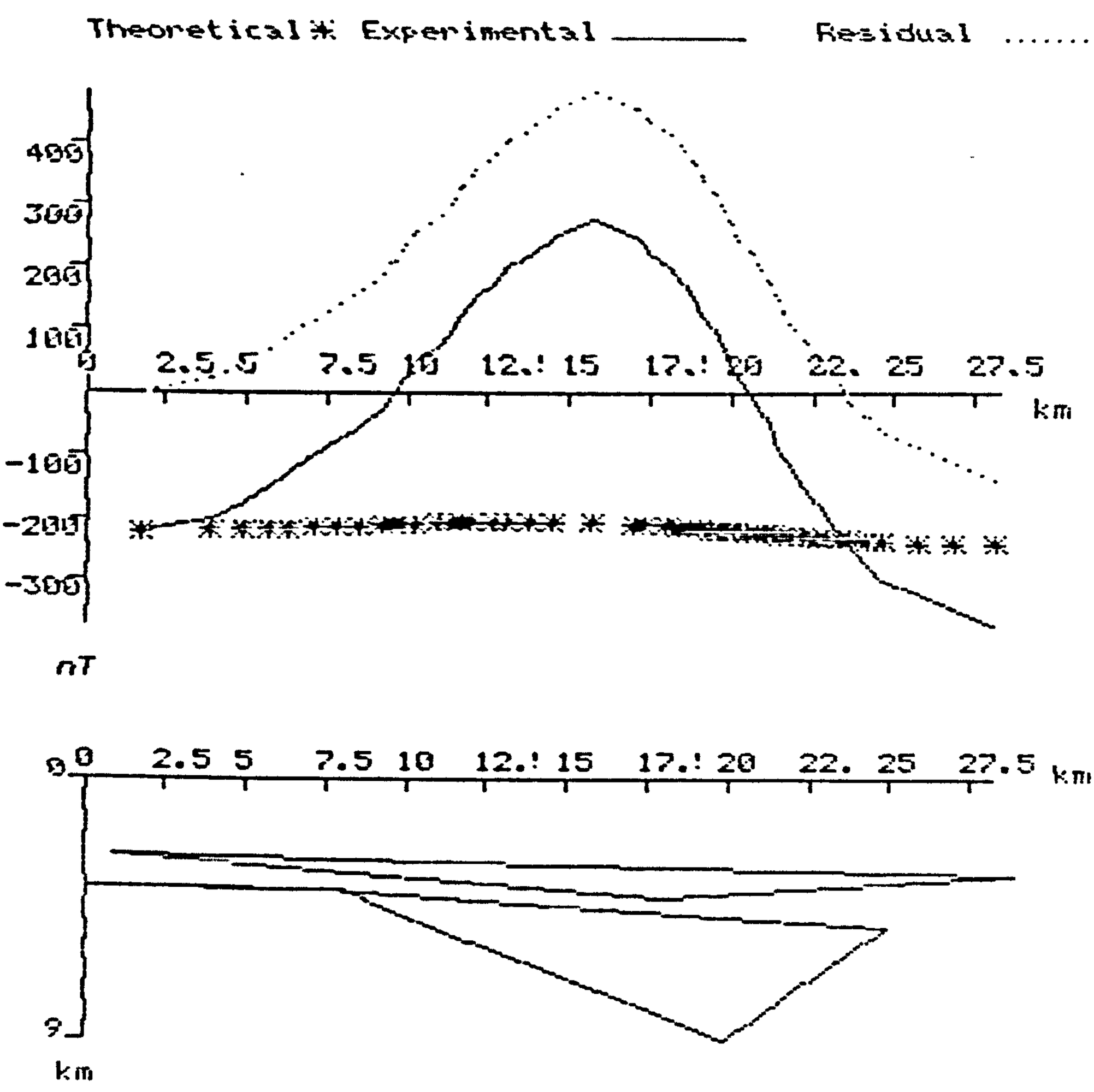

Figure 6.34: 2D model of the intrasedimentary volcanic bodies along the magnetic profile AB. Produced on the remanent magnetization only, using the magnetic intensity 281 mA/m, inclination 31°, declination 0°, and the susceptibility value of $144.466X10^{-3}$ SI.

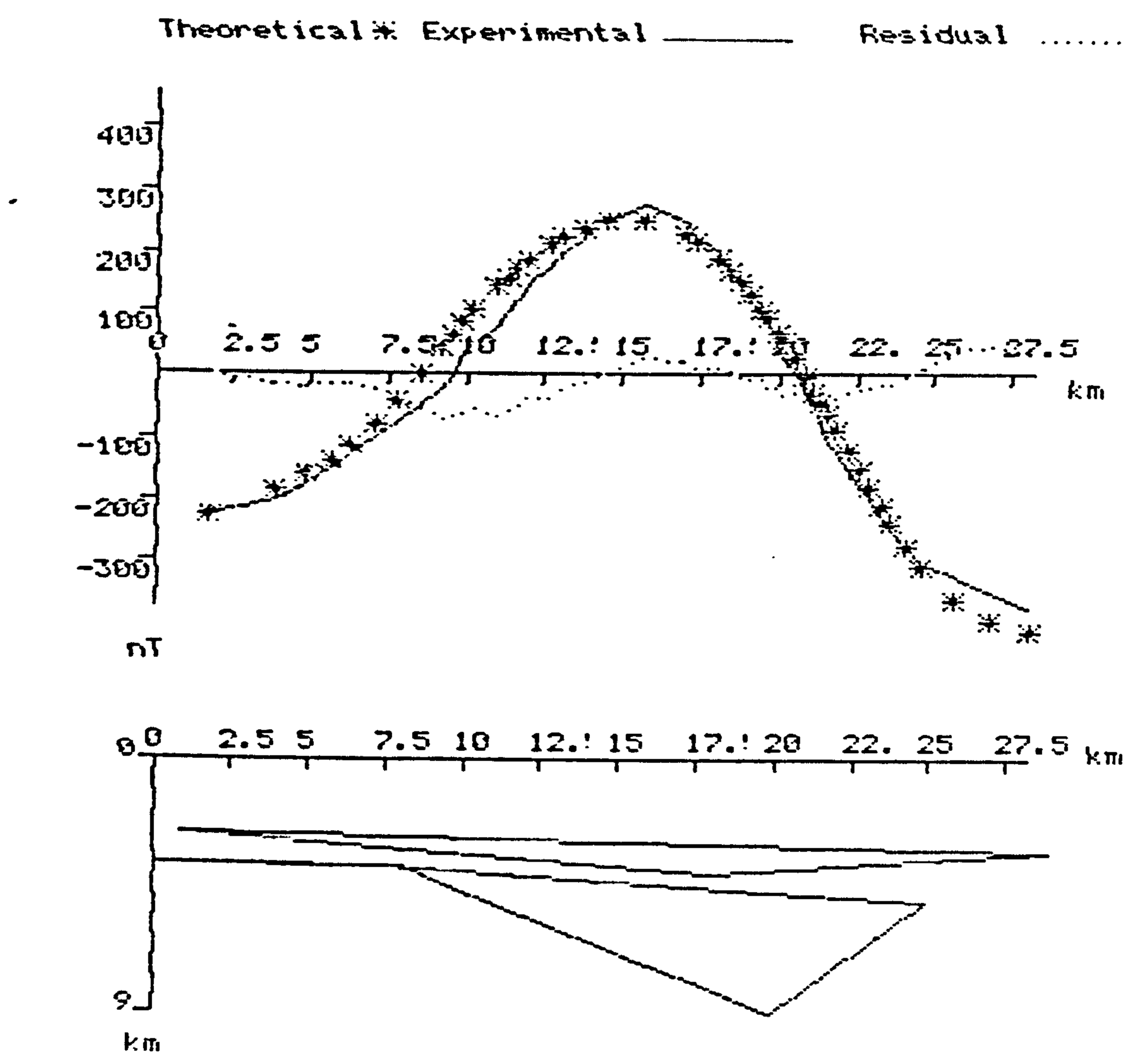

Figure 6.35: 2D model of the intrasedimentary volcanic bodies along the magnetic profile AB (30 *km* length). Produced on the combined of the induced and remanent magnetizations, using the total magnetization 6381 nT, inclination 52°, declination 0°, and the susceptibility value of 144.466 X 10^{-3} SI.

Technique	V1 depth	V2 depth	V1 thickness	V2 thickness
Borehole data (H1-137)	2.6 T–2.75 B	3.6 T–3.7 B	0.15	0.12
Seismic interpretation	2.6 T–2.75 B	3.6 T–5.0 B	0.15	?
Magnetic power spectra (85x85)	2.0	5 – 6	-	-
Magnetic power spectra (55x55)	2.6	3.3	-	-
Gravity power spectra (70x70)	2.7	4.7	-	-
2D gravity modelling	2.5 T–3.4 B	5.2	0.5	1.1
2D magnetic modelling	2.5 T–3.5 B	3.6 T–9 B	0.7	4 ?

Table 6.1: The comparison of the depths and thicknesses which have been estimated by different geophysical techniques in the study area. The depths and thicknesses are in Km. T = Top and B = Bottom of unit.

6.4 Summary

In summary, the application of analytical methods leads to a few additional insights into the geological cause of the gravity and magnetic anomalies. Specifically:

1. Analytical regionals defined by low-order polynomials (k,1 = 1,1 and 2,2) produce satisfactory regional gravity and magnetic maps.

2. The analytical methods confirm that the regional gravity and magnetic field anomaly is high in the southern part, associated with intrasedimentary volcanic units and the uplift structure.

3. The gravity and magnetic field continued upwards from 1 to 7 kms, indicates that the salt basin has limited gravity response. The lowest gravity values are in the

west-central, and the highest gravity values are in the south along the Tripoli Coast. The strong gravity and magnetic anomalies are associated with intrasedimentary volcanic units and probably a shallow basement uplift structure in the southern part. In comparing the gravity map with the magnetic map it can be seen that the positive gravity anomalies (G7, G8 and G9) correspond with the magnetic high (M1) where both anomalies are caused by the same intrasedimentary volcanic units. Many of the gravity anomalies do not have associated magnetic anomalies, (e.g G1, G2, G3, G4, G5, and G6).

Comparison of gravity and magnetic maps with the two-way time structural maps for the Base of the Oligocene and the top of the Zebbag Formations (Figures 4.3 and 4.4), show that the positive gravity anomalies (G7, G8 and G9) and the high magnetic anomaly (M1) corresponds with the seismic event representing intrasedimentary volcanic units and uplift structure in the south. The large negative gravity anomalies and the low magnetic anomalies in the western and central parts correspond to the Salt and Thick Sedimentary Domains. The WNW-ESE lineament trend identified from the seismic structural maps correlates with the lineaments on the gravity and magnetic maps.

4. The second derivative gravity and magnetic maps contain little useful geological information to delineate the anomalies produced by shallow gravity and magnetic sources.

5. Radially averaged power spectra contain linear segments indicating the average depth to source ensembles. The examination of the magnetic data provided an average depth of intrasedimentary volcanic units V1= 2.0 km and V2= 3.3 km, which are in close agreement with the borehole data (V1= 2.3 km and V2= 3.1 km). The basement depth estimations can be concluded as follows: In the Thick Sediment Domain area, the values are not defined by the potential field methods, but have been estimated to be greater than 9 km from the seismic data. In the Salt Domain area, as the basement rocks probably have low susceptibilities and are very deep, no depth estimates could be obtained.

6. **The 2D interpretation of gravity and magnetic results, clearly shows that there is a discrepancy between the depths predicted by the gravity and magnetic modelling interpretation. A close agreement exists between the predicted depth and thickness by 2D gravity interpretation and power spectra analysis. A good fit of the theoretical and experimental curve for combined (induced and remanent) intensity field, indicates that magnetic anomaly M1 can be attributed to the combined induced and remanent magnetization of bodies V1 and V2.**

7. **3D modelling would be a more appropriate method for interpreting these anomalies, since clearly they are not elongate or two dimensional in nature. However an operating 3D modelling computer program was not available, so, in order to achieve a first approximation to a solution the 2-D modelling method was used instead.**

Chapter 7

Synthesis and conclusions

7.1 Synthesis

The geological structure of the study area has been investigated and interpreted by three geophysical methods. Various stages of interpretation and methods of data analysis and modelling have been followed. Discussion of these results, is given in the following sections:

7.2 Seismic and borehole data interpretation

Two-way time structure contour maps have been produced, as a result of the seismic investigation and interpretation. According to these maps, the study area can be divided into three structural domains: *the Salt Domain*, *the Continental Shelf Domain*, and *the Thick Sediment Domain*. The *Salt Domain* represents the region of salt tectonic phenomena in the western and central part of the study area. Selected seismic profiles crossing the salt domain confirmed the distribution of salt structures and interpretations identify different stages of salt piercement. The salt configuration map for the study area has been used to classify the distribution of the salt structures into: *Salt walls*, *salt diapirs*, and *salt pillows*. Several salt structure examples have been used to demonstrate the salt type, shape, and

size.

Interpretation of the seismic reflection data, has shown that the diapiric phenomena, relates to halokinetic movement of the Upper Triassic/Lower Jurassic salt. The salt movements may have been initiated in more than one way and various processes could be responsible for the initiation. The salt movement was explained in terms of either *halotectonic* or *halokinetic processes*. These processes are closely associated in the Sabratah Basin, but the alignment of the salt structures with the principal tectonic features (the Jeffara and Coastal Fault system), suggests strongly that the initiation of salt movement and diapirism was halotectonic.

Evolution of the Sabratah Basin has been influenced by the Upper Cretaceous rifting and subsidence which ocurred in the adjacent Sirte Basin; this was probably synchronous with the initiation of the salt movements. The Sirte graben was formed as the result of east-west shearing movements. Initiation of movement of Triassic salt within the Sabratah Basin occurred in association with these tectonic events during Upper Cretaceous times (Cenomanian/Turonian).

The seismic interpretation indicates the development of a genetic connection between the salt diapir family in the Sabratah Basin, including the mother (salt wall), the daughter (salt diapir), and the grandchild (salt pillow). Timing of the salt mobilization is believed to be within the Upper Cretaceous.

The *Continental Shelf Domain* is located in the southern part of the study area, and comprise a part of the African continental margin which developed during Late Triassic or Early Jurassic times. This has been affected by extensional faults related to cratonic rifting and is characterized by considerable subsidence and volcanic activity (the intrasedimentary volcanic units). The episodes of magmatic activity (Late Cretaceous/Early Tertiary and Middle/Late Cretaceous age) have been investigated by utilizing both migrated seismic sections and well data.

The *Thick Sediment Domain* is located in the east-central part of the study area; the seismic reflection data for this area indicates a stratigraphically complete section of Upper

Cretaceous deposits and a thick Tertiary basin, which represents the ideal condition for source rock maturation. Hydrocarbon accumulation is believed to have commenced in the deepest part of the basin, and migrated to the northern part. The salt migration occurred from the eastern part to the western part of the study area, under the overburden of the thick sediment sequences in the eastern part and the thick volcanic unit in the continental shelf area.

The major tectonic elements identified are the Coastal Fault system and the sub-parallel salt trend. The general framework of the dominant tectonic trends of the Sabratah Basin, can be summarized as (i) a NW-SE (Sirtic) tectonic trend (north-eastern part of area). (ii) a W-E (Jeffara) tectonic trend (southern part) and (iii) a W-E (salt tectonic) trend (western and central parts).

7.3 Salt distribution and structures in the Sabratah Basin

7.3.1 The development of the salt structures in the study area.

Initiation of salt features

In general, geologists concerned with problems of the origin of diapiric salt structures agree on five hypotheses of initiation which can be summarized as follows:

1. Irregularities in the upper surface of the salt.

2. Variations in the density of the overburden.

3. Progressive plasticization of the salt by heat.

4. Initiation of one or more salt features by another *(salt structure families)*.

5. Tectonics.

Application of these hypotheses to the Sabratah basin

It is possible that the salt structures in the Sabratah basin have been initiated in more than one way, for when salt becomes ready to move it seem likely that various processes are responsible for the initiation of the salt movement. The first and second hypotheses unlikely to be of primary relevance in the Sabratah basin.

Progressive plasticization of the salt by heat:

As mentioned in Section 3.3, Chapter 3, it has been proposed by Gussow (1968) that salt does not diapir until it has reached depths of about 7600 m, and a temperature of about 300° C and becomes sufficiently plastic. This change in state is thought to occur abruptly and in a subsiding basin could be responsible for successive sets of diapirs, as subsidence progressively raises the temperature of the salt to the critical point of about 300° C. Ben Dhia (1987) studied the geothermal gradient of Central Tunisia and the eastern part of the Pelagian basin (close to the study area), and found that the temperature is in the linear function depth (a depth of 5500 m corresponding to 220° C).

This hypothesis does not seem applicable to the diapic structure area in the western part of Sabratah basin, because it can be shown that the salt was never buried below 7600 m during salt movement time.

Tectonics:

Most salt movement can be explained in terms of either *halotectonic* or *halokinetic processes* (these terms having been introduced by Trusheim (1960), as described above). In many areas, halotectonic and halokinetic processes are closely associated, where salt structures are elongated parallel to principal tectonic trends, as in the North Sea Basin and elsewhere.

In the Sabratah Basin, the alignments of the principal salt structures are parallel

with the tectonic features (the Jeffara and Coastal Faults system), which strongly suggests that the initiation of salt movement and diapirism was halotectonic. The Sabratah Basin has been influenced by the Upper Cretaceous rifting and subsidence in the Sirte Basin. The Sirte graben were formed as the result of east-west shearing movements. Probably the initiation of Triassic salt movements is related to these shear movements during the Upper Cretaceous time (Cenomanian/Turonian) .

Salt structure families.

The author believes that this idea has much applicability in the Sabratah Basin. Genetic connections between salt diapirs are recognizable. Thus the characteristic part of a salt-stock family is shown in the seismic section ZB-9 which indicates the development of the three generations of salt structures (Figure 4.15). The *mother* structure is represented by D3 *(salt wall)*, the *daughter* by D2 *(salt diapir)*, and the *grandchild* by D1 *(salt pillow)*. When D3 had almost completed development, the diapir stage which had begun in D2 and D1 at that time still was growing. The maximum thickness of the rim-syncline is developed in the location between D3 and D2, the thickness decreasing continuously toward the salt stock. The seismic profiles in the study area document the timing of salt mobilization in Upper Cretaceous times.

7.3.1.1 Age of salt movement

In the study area the first mobilization of the Upper Triassic-Lower Jurassic salt began in Cenomanian/Turonian times, which is the same age as that of Sirte Basin rifting. This halotectonic activity associated with tectonic movement seems likely to have enhanced the imbalance of the overburden resulting from such movements which was the prime cause for the onset of salt flowage.

A careful study of reflection seismic and well data indicates that halokinesis began in the Cenomanian/Turonian. Figure 7.1, shows the development history of the salt structure movement, which appears to have begun in the Early Cretaceous. The *Brown*

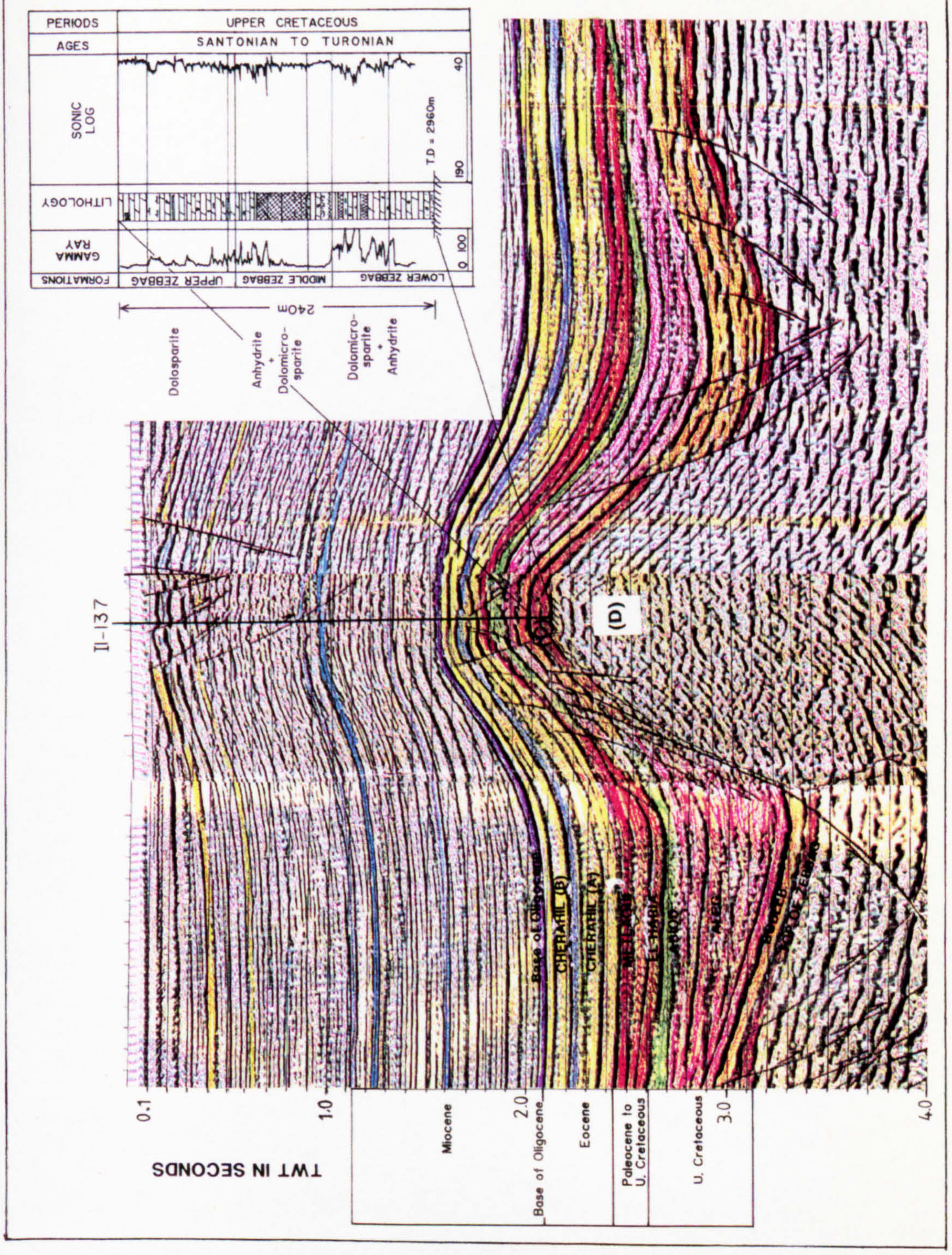

Figure 7.1: An example of a migrated seismic section, and the well data for the lower-part of I1-137, showing the age of the salt movement in the Upper Cretaceous (Cenomanian/Turonian age), represented by the Zebbag Formation (Brown reflector). This corresponds to a strong reflector for the cap rock (C) above the salt diapir. The cap rock is defined from the well data.

reflector **(Figure 7.1) Cenomanian/Turonian age, which represents the Zebbag Formation on the rim-syncline and above the crest of the salt structures, is a very strong reflection, which is interpreted as a cap rock (C). The well I1-137, which penetrated the cap rock formations, is shown on the top right of the same figure. Figure 4.9 shows that salt movements began in the individual structures at different times, and shows the different ages of neighbouring salt structures.**

7.3.1.2 Forms

In general the salt structures have many forms. There are plugs, teardrops, mushrooms, domes, pillows, and waves. The salt diapirs form in Sabratah basin, are characterized by elliptical shaped bodies to sub-circular structures. Salt walls in cross section are generally cylindrical, but downward enlargement is common. The top of the salt masses are slightly convex upwards. A mushroom-like development, or overhang, is not found in the basin. The most common type of salt feature in the basin is the salt pillow, which is a swell of non-diapiric salt. Salt pillows are present on many of the seismic sections. The salt walls are elongate salt diapirs (piercement salt), the only difference between the two seen in the seismic sections is that the salt wall reaches to the sea floor.

Normally, however, the salt diapir does not take a simple form, and the shape and size of the peripheral sinks (rim-synclines), also may be greatly varied. Each salt structure has its own history, and closely adjoining structures may have developed quite differently.

7.3.1.3 Cap rock

The term *cap rock*, in general refers to the uppermost unit in a dome-shaped stratigraphic sequence. Many salt diapirs have summits which consist of flat or domed shaped tops comprising apparently layered structures sometimes several hundred of meters thick. These are termed the cap rocks. The layering normally includes some or all of the following materials in varying proportions: anhydrite, gypsum, calcite and sulphur. The presence of cap rock is believed to be due to accumulation of insoluble residues of the salt rock at

the rising crest.

Figure 7.1 shows an example of a salt diapir in the Sabratah Basin, which provides a very strong acoustic impedance contrast with both overlying sediments and underlying salt. The strong reflection event at the diapir is related to a cap rock (C), some 240 m thick. The well I1-137 has a good tie with the seismic event, which indicates that the cap rock comprise the following units: Upper Zebbag, Middle Zebbag, and Lower Zebbag, consisting of anhydrite, dolomicrosparite and shale. In general cap rock development appears to be absent in the other parts of the study area.

7.3.1.4 Salt structure trends

The majority of salt structures in the Sabratah Basin have a distinct W-E or WNW-ESE trend, where alignments are approximately parallel to the fault trends at the southern edge of the basin (c.f Chapter 4).

7.3.1.5 Salt migration

Parker and McDowell (1955), have shown that the salt migration would have begun in the deepest part of the sedimentary basin. This is evident in the Sabratah Basin where salt migration began in the central-eastern part of the basin. The Upper Triassic-Lower Jurassic salt has travelled out from the eastern part of the study area and migrated into the western part. The regional behavior of salt migration in the Sabratah Basin has been discussed previously in Chapter 4.

7.3.1.6 Classifying salt structures

Halbouty (1967), classified the salt domes of the Gulf of Mexico by reference to:

1. Depth of burial of the salt mass below the surface.

2. Form or shape of the salt structures.

3. Genetic relationship of salt structures or group structures.

In this thesis, the salt structure (salt pillow, diapir and wall structures) classification is adapted for the Sabratah Basin according to the depth from the sea floor to the top of the cap rock or salt as follows:

1. Shallow domes (diapirs) range from the sea floor to a depth of 550 m: These are piercement or salt wall structures, located in the western part of the study area.

2. Intermediate domes range from 550 m to 1500 m below sea floor: These includes the salt diapirs which are concentrated in the central part of the study area.

3. Deep salt structures below 1500 m: These include structures where salt has not been reached by drilling *(salt pillows)*, which is the most common type in the study area.

The salt structures may also be classified according to age (Levorsen, 1967):

- *Young*: Characterized by anticlines and domes, with relatively little deformation.
- *Mature*: Cap rock has begun to accumulated on the salt core.
- *Old*: A thick cap rock has formed, commonly with an overhang. The adjacent sediments are much faulted and fractured, and well-defined rim syncline exists.

7.3.1.7 Comparison of the Salt Basins in the Mediterranean

Evaporite basins and diapirs occur in many parts in the world. The Mediterranean region lies in one of the salt plug provinces. A listing of the geographic locations/ages and the types of diapirs, and their distribution throughout the world, has been shown in Table 3.1 (Chapter 3).

Table 7.1, shows the different ages of the salt and diapirs in the Mediterranean region. These can be described as follows: Firstly, diapiric domal and anticlinal structures

Country	*Age of Salt*	*Age of Diapiric*	*Type of diapir*
Tunisia	Triassic	U-Cretaceous	Domal-Anticlinal
Algeria	Triassic	U-Cretaceous	Domal-Anticlinal
Morocco	Triassic	U-Cretaceous	Domal-Anticlinal
Egypt	Jurassic	Cretaceous	Anticlinal
Syria	Jurassic	Cretaceous	Anticlinal
Spain	Triassic	U-Cretaceous	Domal-Anticlinal
France	U-Miocene	Messinian	Domal-Anticlinal
Sicily	U-Miocene	Messinian	Domal-Anticlinal
East Mediterranean	U-Miocene	Messinian	Domal-Anticlinal
West Mediterranean	U-Miocene	Messinian	Domal-Anticlinal

Table 7.1: Distribution of diapiric structures and their ages in the Mediterranean region.

of Upper Triassic evaporite age and Upper Cretaceous time of movements in Morocco, Algeria, Tunisia and Spain. Secondly, anticlinal salt structures of Jurassic evaporite age, and Cretaceous time of movement in Egypt and Syria. Finally, diapiric domal and anticlinal structures of Upper Miocene evaporite age and Messinian time of movement in East and West Mediterranean Basins (including France and Sicily). More details of the comparison of these areas with the Sabratah basin, are given below:

Algeria

Upper Triassic salt domes are situated in the north-central part of Algeria. These salt domes exist in linear trends along the margins of the most central parts of the saucer-shaped basins , aligned with an Atlassic trend. The salt movement and diapirism has been characterized by halokinetic phenomena. Assaad (1983) explained the salt movement in terms of plate kinematics, which can briefly be described as follows:

(a) Triassic-Jurassic times: Extension ocurred between Europe and Africa; the

Tethys Ocean existed. Primary salt-dome structures may have been inaugurated in the Atlassic trend at the end of that period.

(b) Jurassic-Upper Cretaceous times: Africa moved left-laterally with respect to Europe from the Triassic to upper Cretaceous. Salt pillows continued to be formed as salt accumulations where the migration took place.

(c) Upper Cretaceous-present: The mass displacement of salt may have caused primary peripheral sinks. During this period the African plate ceased to move left-laterally and started a right-lateral movement of limited extent which continued until Ypresian times. Halotectonic diapiric emplacement took place directly due to the influence of plate tectonics movements.

Tunisia

Triassic evaporite diapirs are common in two parts of Tunisia: (i) In the northern part of (having the same trend as those of the Algerian salt structures) along the Atlas Mountains, which were controlled by the tectonic events associated with Alpine folding. (ii) In the Gabes Basin (Gabes-Sabratah Basin) in the western part of the study area, salt piercement domes and walls are present, which were controlled by tectonic events associated with African plate rotation, producing the same tectonic style for the salt structure in the Sabratah Basin.

Egypt and Syria

Diapiric structures have been recorded in Egypt (in the Abu Roash area west of Cairo) and Syria (in the Syrian arc system) in the mobile belt, south and east of the Mediterranean (Omara 1964). The area has been characterized by anticlinal evaporite structures of Jurassic age.

Western Mediterranean

The common feature through all the basins of the Mediterranean Sea is the widespread occurrence of evaporites in the Upper Miocene; halokinetic features are commonly seen in the Balearic Basin, Alboran Basin, and Gulf of Lion. The Upper Miocene salt basins of the Mediterranean were controlled by Alpine tectonics (Mulder 1973).

Central Mediterranean

Upper Miocene evaporites occur in the Tyrrhenian Sea and Calabrian Basin. No salt structures have been found in the Tyrrhenian Sea (Mulder 1973).

Eastern Mediterranean

The diapirs in the eastern Mediterranean Sea formed as a result of flowage of the Miocene Messinian evaporitic series (Levant Basin).

7.3.1.8 Salt tectonics and hydrocarbon traps

Salt structures are not purely of technical interest; they have considerable economic importance. Salt structures and the beds surrounding them, are major sources of oil and gas, sulphur, salt, and potash. Hydrocarbons in major quantities are found in association with salt domes of NW-offshore Libya.

There is an infinite number of possible hydrocarbon trap situations of structural, stratigraphic and combination type. Some of the simplest trap situations are associated with doming above salt pillows and thinning above their flanks due to syndepositional movement. Trap situations occur due to faulting, and also stratigraphic porosity traps are common in the sedimentary sequence. The principal types of trap created by the salt pillows, as described by Jenyon (1986) are shown in Figure 7.2. These include:

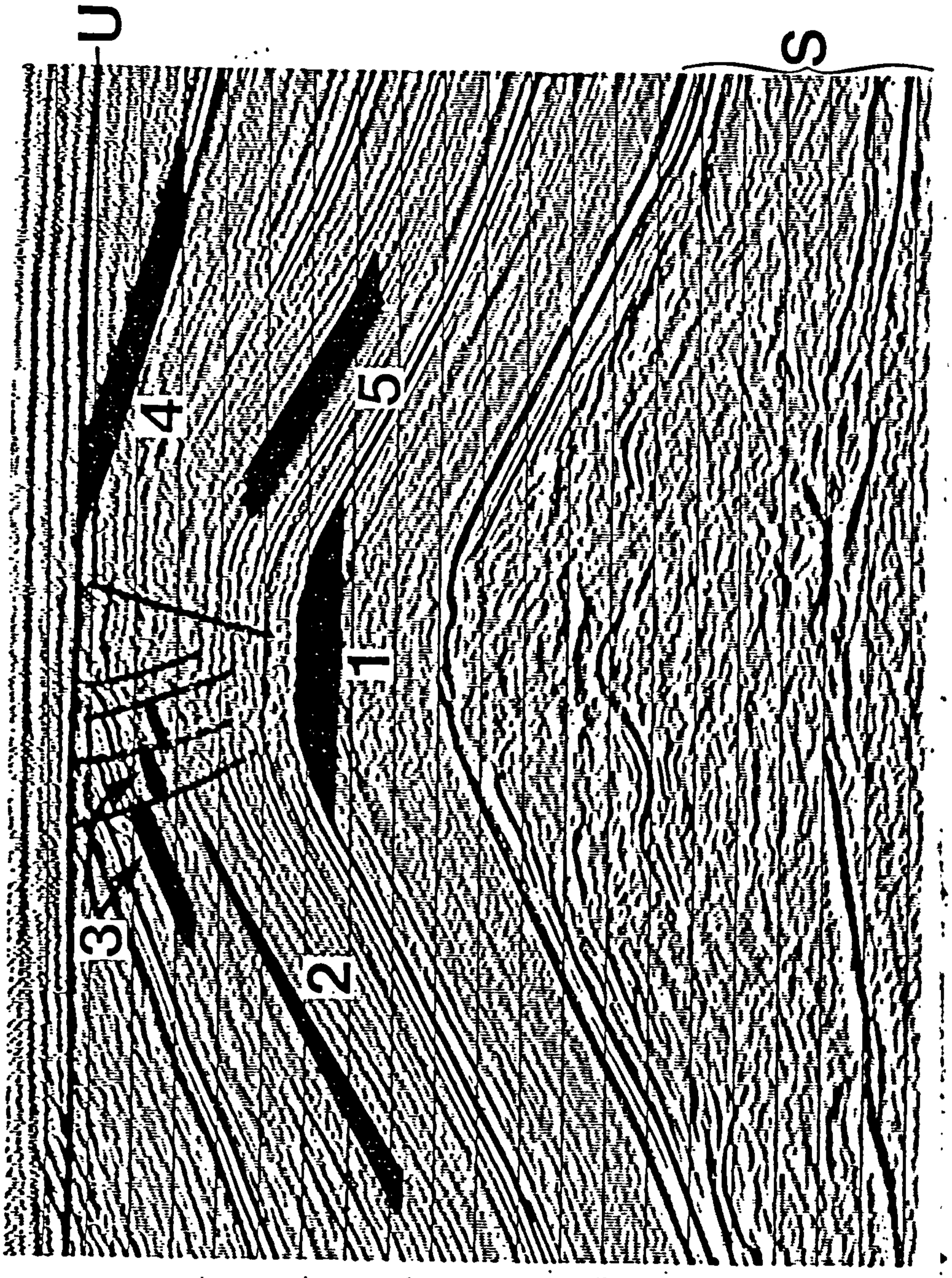

Figure 7.2: Classes of hydrocarbon trap which may associated with a salt pillow. Salt interval is bracketed as S; U is a shallow unconformity. (*From Jenyon 1986*).

1. The domal trap.

2. Pinchout trap.

3. Fault trap.

4. Unconformity traps.

5. Porosity traps.

The general types of trap which are associated with diapiric salt structures are described and modelled in a seismic section across a wall diapir in Figure 7.3, (from Jenyon (1986)).

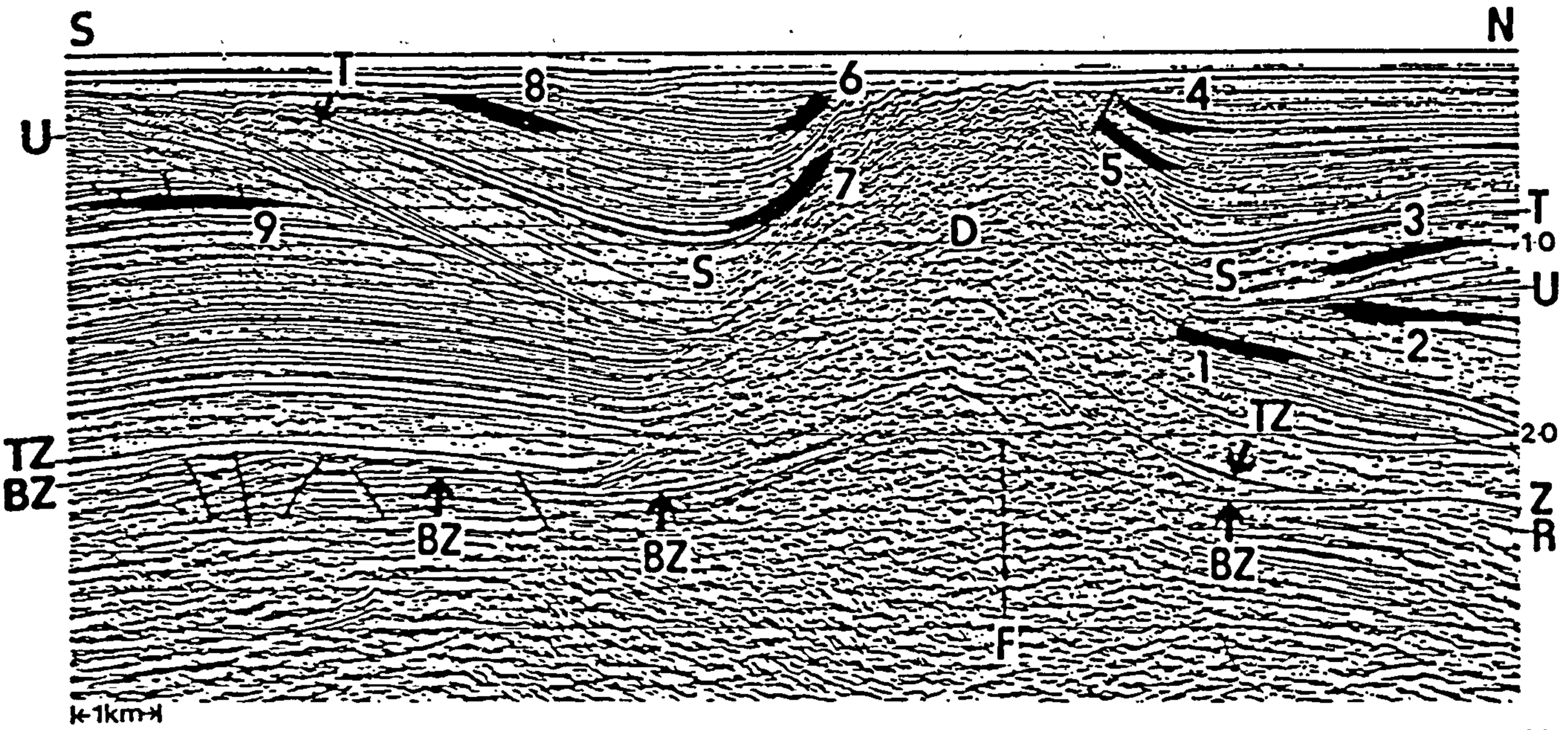

Figure 7.3: Classes of hydrocarbon trap which may be associated with a salt wall diapir (D), (*From Jenyon 1986*).

The trap types shown in Figure 7.3 are:

- (1) and (7) truncation traps against the diapir flanks.
- (3) Pinchout trap due to thinning of secondary rim syncline sediments away from the diapir.

- (4) pinchout trap related to uplift and thinning of sediments contemporaneously with the salt rise.
- (5) fault trap related to peripheral faulting near the diapir crest.
- (2) unconformity trap related to the major unconformity U.
- (8) unconformity traps related to a shallower unconformity.
- (9) turtle shaped trap in primary rim syncline sediments which are thinning towards the diapir.

Almost all the exploration wells in the study area have been drilled on the crest of salt structures (diapir or pillow). They are often dependent on such factors as the degree of disruption at the crest of the structure due to graben faulting of either structural or dissolution-collapse origin. Anticlines over these diapiric structures form a major exploration play, with several successful wells to date, including the giant Bouri field.

7.4 Gravity and magnetic data interpretation

The interpretation of gravity and magnetic data has involved various stages and methods of data analysis and modelling, such as second-derivative calculation, upward continuation, power spectral analysis, low-pass and high pass filtering and 2-D modelling. The gravity and magnetic anomaly sources identified range from the salt diapiric phenomena, the cap rocks above the crest of the salt structures (in the west), the large accumulation of sediments (in the central-east) and the intrasedimentary volcanic units and uplift structure (in the south). Consideration of the seismic data has helped to clarify these possible anomaly sources.

The Bouguer gravity map shows that the major negative gravity anomalies are associated with the salt structures, and a thick sedimentary basin. The major positive gravity anomaly is associated with the intrasedimentary volcanic units and uplift structure in the southern part of the study area.

The densities and density contrast values for the various formations have been obtained from Formation Density logs for a number of key boreholes. These were used in the 2D gravity anomaly modelling.

The total field magnetic intensity map shows the magnetic anomalies of the Sabratah Basin. The major anomaly (M1) is attributed to the occurrence of intrasedimentary volcanic rock units, and the uplift structure. The other large magnetic anomalies (M2 and M3) are associated with the igneous activity and shallow basement elevation development during the initial rifting and subsidence of the Sabratah Basin. There is a low amplitude anomaly field associated with the thick sedimentary basin and salt structures area.

Magnetic susceptibility and NRM intensity values from cuttings samples from boreholes have also been measured and the results utilized in the 2D magnetic anomaly interpretation.

Analytical regional fields defined by low-order polynomials produce satisfactory regional gravity and magnetic maps. The analytical methods confirm that the regional gravity and magnetic high in the southern part is associated with intrasedimentary volcanic units and uplift. The gravity and magnetic field continued upwards from 1 to 7 kms, indicates that the salt basin produce a limited gravity anomaly response, lowest gravity values occurring in the west-central part, and the highest gravity values in the south along the Tripolitanian Coast. The strong gravity and magnetic anomalies in the southern part are associated mainly with the intrasedimentary volcanic units and probably also the shallow basement uplift structure.

In comparing the gravity map with the magnetic map it can be seen that the positive gravity anomalies (G7, G8 and G9) correspond with the magnetic high (M1), both anomalies being caused by the same intrasedimentary volcanic units and uplift structure. Many of the gravity anomalies do not have associated magnetic anomalies (due to the low magnetic susceptibility of salt rock) e.g G1, G2, G3, G4, G5, and G6.

The second derivative gravity and magnetic maps contain little useful geological information to delineate the anomalies of shallow gravity and magnetic sources.

Radially-averaged power spectra contain linear segments indicating the average depth to source ensemble. The interpretation of the magnetic data provides an average depth of intrasedimentary volcanic units which is in close agreement with the borehole data. The basement depth estimations can be summarized as follows: In the Thick Sediment Domain, it has been estimated to be greater than 9 km (from seismic data). In the Salt Domain, as the basement rocks may have low susceptibilities and be very deep, no depth estimates could be obtained. In the Continental Shelf Domain, the basement depth is below 5.6 km.

7.5 Conclusions

The combination of several geophysical methods (*seismic, gravity, and magnetic*), have proved particularly useful in identifying the cause of various anomalies and delineating regional and local structures in the Sabratah Basin. It is clear that uncertainties in interpretation from any one method are reduced by this combined approach.

The gravity and magnetic maps exhibit a strong correlation between the potential field and the regional geological controls and seismic interpretation. The two-way time structural maps of the Base of the Oligocene and the top of the Zebbag Formations (Figures 4.3 and 4.4), show a pronounced seismic high which can be correlated with the strong positive gravity and magnetic anomalies (G7, G8 and G9 and M1) respectively. This feature is interpreted as due to an uplift structure and intrasedimentary volcanic units. The large negative gravity anomalies and low magnetic anomalies in the western and central parts correspond with salt structures and the thick sedimentary basin. The WNW-ESE lineament trend identified from seismic structural maps closely corresponds with the anomaly lineaments defined from the gravity and magnetic maps.

In comparing the Bouguer gravity map with TWT structure maps, several of the positive gravity anomalies correlate with seismic highs, while other anomalies do not, indicating that some of the gravity features may represent localized density changes only.

The gravity and magnetic maps support the indicate that the intrasedimentary volcanic units (south), and salt/thick sedimentary basin, are the main sources of the positive and negative potential field anomalies, respectively. There structures had been indicated previously by seismic interpretation. The available gravity data delineates only the general salt trend and salt basin boundaries, and provides little useful geological information to delineate the anomalies arising from the salt structures.

Depth estimates to statistically discrete sources, produced by power spectral analysis of gravity and magnetic maps, indicate the existence of two magnetic and gravity sources. Modelling of gravity and magnetic anomalies associated with major intrasedimentary volcanic units has produced estimates of the shape, thickness, and depth in each of them. The 2D interpretation of gravity and magnetic results shows that there is a discrepancy between the depths predicted by the 2D gravity and magnetic interpretations. Moreover, there is a closer agreement between the predicted depth and thickness by 2D gravity interpretation and power spectra analysis.

7.6 Future work

The limitations of seismic and potential field methods which have been outlined in the previous Chapters, can be summarized as follow:

1. The present seismic data do not reveal seismic events below the middle Cretaceous; it is not possible to deduce in full the history of salt structures and their stages of development prior to middle Cretaceous times.

2. The potential field maps in the salt area and the thick sedimentary basin, have poor resolution for locating the salt structures and estimating the basement depth. The salt basin has a limited gravity response.

3. 2D gravity and magnetic modelling solution is never unique.

Therefore, the study area requires future geophysical investigations, including:

1. **A deep reflection and refraction seismic survey, with the objectives to constrain the geological model of the Sabratah Basin evolution and to image the Lower Crust.**

2. **Detailed gravity work (including micro gravity observations) over the salt domain area, and to complete the missing data over the western part of the study area. Reprocessing the available gravity data over the salt structures domain is required.**

3. **Further work on accurate determination of depth to basement throughout the area incorporating more detailed magnetic field data and modelling.**

4. **A deep drilling project to penetrate the salt diapirs and the thick sediment flanks, to determine the salt thickness, and establish its movement history and the nature of halokinetic processes in the study area.**

References

Agarwal, B, N, P. and Lal, T., 1971, Application of rational approximation in computation of the second derivative of the gravity field: Geophysics, **36**, 571–581.

Agarwal, B, N, P. and Lal, T., 1972, A generalized method of computing second derivative of gravity field: Geophys. Prosp., **20**, 385–394.

Agocs, W. B., 1951, Least squares of residual anomaly determination: Geophysics, **16**, 686–696.

Assaad, F. A., 1983, An approach to Halokinematics and interplate tectonics (North-Central Algeria): J. Petrol. Geol., **6**, 83–88.

Assereto, A., and Benelli, F., 1971, Sedimentology of the Pre-Cenomanian Formations of the Jebel Gharyan, Libya: *in:* Symposium on the Geology of Libya, Triopoli 1969, (Ed.) Carlyle Gray, 522. Imprimerie Catholique, Beirut, Lebanon.

Baranov, V., and Naudy, H., 1964, Numerical calculation of the formula of reduction to the magnetic pole: Geophysics, **29**, 67–79.

Barton, D. C., 1926, Pine Prairie salt dome: Bull. Amer. Assoc. Petrol. Geol., **9**, 738–755.

Barton, D. C., 1933, Mechanics of formation of salt domes with special reference to Gulf Coast salt domes of Texas and Louisiana: Bull. Amer. Assoc. Petrol. Geol., **17**, 1025–1083.

Barton, P., and Wood, R., 1984, Tectonic evolution of the North Sea basin: crustal stretching and subsidence: Geophys. J. R. astr. Soc., **79**, 987–1022.

Ben Dhia, H., 1987, The geothermal gradient map of central Tunisia comparison with structural, gravimetric and petroleum data: Tectonophysics, **142**, 99–109.

Bellini, E., and Massa, D., 1980, A stratigraphic contribution to the Palaeozoic of the

Southern Basin of Libya: Second symposium on the Geology of Libya, Tripoli, 1978, Salem, J. M., and Busrewil, T. M., Eds, Academic Press London. I, 1–348.

Bhattacharyya, B. K., 1965, Two-Dimensional harmonic analysis as a tool for magnetic interpretation: Geophysics, **30**, 829–857.

Bhattacharyya, B. K., 1966, Continuous spectrum of the total magnetic field anomaly due to a rectangular prismatic body: Geophysics, **31**, 97–121.

Bhattacharyya, B. K. and Navclio , M. E., 1975, Digital convolution for computing gravity and magnetic anomalies due to arbitrary bodies: Geophysics, **40**, 981–992.

Biju-Duval, B., Letquzey, J., Montadert, L., Courrie, p., mugniot, J.F., and Sancho, J., 1974, Geology of the Mediterranean Sea Basin: *in:* Geology of Continental margin, Eds, Burke, C. A., and Darke, C. L., Springer Verlag, New York, Heidlberg, Berlin, 685–721.

Biju-Duval, B., and Montadert, L., 1977, Introduction to the structural history of the Mediterranean Basins: *in:* International symposium on the structural history of the Mediterranean Basins, SPLIT (Yugoslavia) 25-29 October 1976, Biju-Duval, B., and Montadert, L., Eds, Technip Paris, 1–22.

Biju-Duval, B., Dercourt, J., and Le Pichon, X., 1977, From the Tethys Ocean to the Mediterranean Seas : A plate tectonic model of the evolution of the western Alpine system: *in:* International symposium on the structural history of the Mediterranean Basins, SPLIT (Yugoslavia) 25–29 October 1976, Biju-Duval, B., and Montadert, L., Eds, Technip, Paris, 143–164.

Biot, A. M. and Ode, H., 1965, Theory of gravity instability with variable overburden and compaction: Geophysics, **30**, 213–227.

Bishop, W. F., 1975, Geology of Tunisia and adjacent parts of Algeria and Libya: Bull. Amer. Assoc. Petrol. Geol., **59**, 413–450.

Bishop, W. F., 1988, Petroleum geology of east-central Tunisia: Bull. Amer. Assoc.

Petrol. Geol., **72**, 9, 1033–1058.

Bishop, S. R., 1978, Mechanism for emplacement of piercement diapirs: Bull. Amer. Assoc. Petrol. Geol., **62**, 1561–1583.

Braunstein, J., and O'Brien, D., 1968, Diapirism and diapirs:*in:* A symposium 50th ann. Mtg., Amer. Assoc. Petrol. Geol., *in:* New Orleans, Louisiana, April 26–29, 1965, Bull. Amer. Assoc. Petrol. Geol., Tulsa, Oklahoma, USA, 444.

Burollet, P. G., 1965, Contribution a l'etude stratigraphique de la Tunisie central: Annales des Mines et de l'energie. Tunis. 1–16.

Burollet, P. F., 1969, Petroleum geology of the Western Mediterranean basin: Joint Conf. Inst. Bull. Amer. Petrol. Geol., Brighton, U.K.

Burollet, P. F., Mugniot, J. M., and Sweeney, P., 1978, The geology of the Pelagian block, the margins and basins off southern Tunisia and Tripolitania: *in:* Eds, Nairn, E. M. A., Kanes, W. H., and Stehli, F. G., The Ocean Basin and margins: The western Mediterranean: **4B**, Plenum press, New York and London, 331–359.

Byerly, P. E., 1965, Convolution filtering of gravity and magnetic maps: Geophysics, **30**, 281–283.

Cloos, E., 1955, Experimental analysis of fracture patterns: Bull. Amer. Soc. Geol., **66**, 241–256.

Cooly, J. W. and Tukey, J. W., 1965, An algorithm for machine calculation of complex Fourier series: Math. of computation, **19**, 297–301.

Darby, E. and Davies. E. B., 1967, The analysis and design of two-dimensional filters for two-dimensional data: Geop. Prosp., **15**, 383–406.

Dercourt, J., 1970, L 'expansion oc'eanique actuelle et fossile: ses implications geotectoniques: Bull. Soc. Geol. France, **12**, 261–317.

Dercourt, J., Zonenshain, L. P., Ricou, L. E., Kazmin, V. G., Le Pichon,

X., Knipper, A. L., Grandjacquet, C., Sbortshikov, I. M., Geyssant. J., Lepvrier, C., Pechersky, D. H., Boulin, J., Sibuet,J. C., Savostin, L. A., Sorokhtin, O., Westphal, M., Bazhenov, M. L., Lauer, J. P., and Biju-Duval, B., 1986, Geological evolution of the Tethys belt from the Atlantic to the Pamirs since thr Lias: Tectonophysics, **123**, 241-315.

Dean, W. C., 1958, Frequency analysis for gravity and magnetic interpretation: Geophysics, **23**, 97–127.

DeGolyer, E. , 1924, Origin of North American salt domes: Bull. Amer. Assoc. Petrol. Geol., **9**, 831–874.

Dewey, F. J., Pitman, C. W., Ryan, F. B. W., and Bonnin, J., 1973, Plate tectonics and the evolution of the Alpine system: Bull. Geol. Soc. Amer., **84** , 3137–3180.

Dewey, F. J., and Booth, J. , 1989, Rosa project offshore Libya: unpublished report, Sirte Oil Co.

Dobrin, M. B., 1941, Some quantitative experiments on a fluid salt-domes model and their geological implications: Tectonophysics, **22**, 528–542.

Dobrin, M. B., 1976, Introduction to geophysical prospecting:Third edition, publish by McGraw Hill, 630.

Ellis, P. F., and Kearey, P. , 1984, An investigation of the Reading-Newbury magnetic anomaly: J. Geol. Soc. London., **141**, 349–356.

Elkins, T. A., 1951, The second derivative of gravity interpretation: Geophysics, **16**, 29–50.

Exploration Department Staff of Aquitaine Libya Oil company., 1969 Main exploration results, Concession 137, NW-offshore Libya, unpublished report, R.G.n: 56, 23.

Exploration Department Staff of Agip Libya Oil Company., 1985, Main exploration results, Concession NC-41, NW-offshore Libya, unpublished report., 48.

Exploration Department Staff of Sirte Oil company., 1989 Rosa project, offshore Libya: unpublished report.

Finetti, I., 1982, Structure stratigraphy and evolution of the Central Mediterranean : Bollettino di Geofisica ed Applicata, **24**, 247–313.

Fuller, B. D., 1967. Two dimensional frequency analysis and design of grid operators: Soc. Exp. Geophys. Min. Geophys, **2**, 658–708.

Garfunkel, Z., and Almagor, G., 1987, Active salt dome development in the Levant basin, Southern Mediterranean: *in:* Dynamical geology of salt and related structures, Eds. Lerche, I., and O'Brien, J. J., 1987, Publish by: Academic press, Inc.,Orlando, Florida, 263–300.

Garland, G. D., 1977, The Earth' shape and gravity: *in* : Pergamon Press, Oxford, 183.

Gealey, K. W., 1988, Plate tectonic evaluation of the Mediterranean-Middle East region: tectonophysics, **155**, 285–306.

Grant, F. S., and West, G. F., 1957, A problem in the analysis of geophysical data: Geophysics, **22**, 309–344.

Grant, F. S., and West, G. F., 1965, Interpretation theory in applied geophysics: *in* McGraw Hill, 513.

Goudarzi, Gus. H., 1980, Structure of Libya: *in:* Second symposium on the Geology of Libya, held at Tripoli, 1978, Salem, J. M., and Busrewil, T. M., Eds, Academic Press London. **III**, 781–1155.

Gotze, J. H., and Lahmeyer, B., 1988, Application of three-dimensional interactive modeling in gravity and magnetics:Geophysics, **53**, 1096–1108.

Gussow, W. C., 1968, Salt diapirism: importance of temperature and energy source of

emplacement: Bull. Amer. Assoc. Petrol. Geol., Memoir 8, Diapir and diapirism, 16–52.

Hammuda, S. O., and Missallati, A. A., 1980, A study of the Libyan-Tunisian continental shelf, submitted by Socialist People's Libyan Arab Jamahiriya. *in*: International Court of Justice. Continental shelf. (Tunisia/Libyan Arab Jamahiriya). Annex, II, 1–24.

Hammuda, S. O., Sbeta, M. A., Mouzughi, J. A., and Eliagoubi, A. B., 1985, Stratigraphic nomenclature of north western offshore Libya, *in* : The Earth Sicences Society of Libya, Tripoli, Libya, Interprint Limited, Malta, 166.

Halbouty, M. T., 1967, Salt domes, Gulf region United States and Mexico: Houston, Tex., Gulf Publishing Co., 425.

Henderson, R. G., and Zietz, I., 1949, The upward continuation of anomalies in total magnetic intensity field: Geophysics, **14**, 517–534.

Henderson, R. G., and Zietz, I., 1949, The computation of second vertical derivatives of geomagnetic fields: Geophysics, **14**, 508–516.

Henderson, R. G., and Zietz, I., 1960, A comprehensive system of automatic computation in magnetic and gravity interpretation: Geophysics, **25**, 569–585.

Hsu, K. J., 1972, Origin of Saline giants: A critical review after the discovery of the Mediterranean evaporite: Earth-Sci. Rev., Elsevier Publishing company, **8**, 371–396.

Hubbert, M. K., Theory of scale models as applied to the study of geology structures: Bull. Amer. Soc. Geol., **48**, 1459–1520.

Illing, L., Wells, A. and Taylor, J., 1965, Penecontemporary dolomite in the Arabian Gulf: *In* Dolomitization and limestone diagenesis. Soc. Econ. Pal. Min., Sp. Publ. **13**. 89–111.

Jenyon, M. K., 1986, Salt tectonics. Elsevier applied science Publishers Ltd. 191.

Kearey, P., and Brooks, M., 1984, An introduction to geophysical exploration. Blackwell Scientific Publications.296.

Kendall, A. C., 1978a, Facies models 11. Continental and supratidel (Sabkha) evaporites: Geosci. Canada., 5, 66–78.

Kendall, A. C., 1978b, Facies models 12. Subaqueous evaporites: Geosci. Canada., 5, 124–139.

Keen, E. C., and Barrett, L. D., 1981, Thinned and subsided continental crust on the rifted margin of Eastern Canada: crustal structure, thermal evolution and subsidence history: Geophys. J. R. astr. Soc. 65. 443–465.

Keen, E. C., 1979, Thermal history and subsidence of rifted continental margins-evidence from wells on the Nova Scotian and Labrador Shelves: Canadian Jnl. Earth Sci., 6. 505–522.

Kogbe, A. C., 1980, The trans-Saharan Seaway during the Cretaceous:*in:* Second symposium on the Geology of Libya, Tripoli, 1978, Salem, J. M., and Busrewil, T. M., Eds, Academic Press London. I. 1–348.

Lerche, I., and O'Brien, J. J., 1987, Dynamical geology of salt and related structures, Publish by: Academic press, Inc. Orlando, Florida, 832.

Levorsen, A. I., 1976, Geology of petroleum : Second Edition, Freeman, W., and company, San Fransisco, 724.

Link. T. A., 1930, Experimental related to salt-dome structures: Bull. Amer. Assoc. Petrol. Geol., 14, 483–503.

Livermore R. A., and Smith, A. G., 1985, Some boundary condition for the evolution of the Mediterranean region: *in* : Geological evolution of the Mediterranean Basin, Stanley, J. D., and Wezel F. C., eds, New York, Springer Verlag, 83–98.

Logan. B., Davies, G. Read, J. and Cebulski, D., 1970, Carbonate sedimentation and environments, Shark Bay, Western Australia: Bull. Amer. Assoc. Petrol. Geol., Mem. **13**. 223.

Maltezou, F., 1986, Gravity and magnetic studies of the Rhodope region, NE Greece: Ph.D., thesis, Southampton University, 273.

McKenzie, D., 1972, Active tectonics of the Mediterranean region: Geophy. J. R. astr. Soc., **30**, 109-185.

McKenzie, D., 1978, Some remarks on the development of sedimentary basins: Eart Plant. Sci. Lett., **40**, 25–32.

Megerisi, M. F., and Mamgain, D., V., 1980, The Upper Cretaceous-Tertiary Formation of Northern Libya:*in:* Second symposium on the Geology of Libya, Tripoli, 1978, Salem, J. M., and Busrewil, T. M., Eds, Academic Press London. I. 1–348.

Mesc'o, A., 1965, Some notes concerning the frequency analysis for gravity interpretation: Geophys ., **36**, 835–855.

Morgan, W. J., 1981, Hotspot tracks and the opening of the Atlantic and Indian oceans: *in:* C. Emiliani Ed., The Sea. **7**. The Oceanic Lithosphere. Wiley, New York, N. Y. 443–487.

Morgan, J. W., 1983, Hotspot tracks and the early rifting of the Atlantic: Tectonophysics, **94**, 123–139.

Mufti, I.R., 1972, Design of small operation for the continuation of potential field data: Geophysics, **37**, 488–506.

Mulder, J. C., 1973, Tectonic framework and distribution of Miocene evaporites in the Mediterranean, *in :* Drooger W. C. Eds, Massinian evants in the Mediterranean, North Holland Publ. Co., Amsterdam. 44–59.

Murray, G. E., 1961, Geology of the Atlantic and Gulf Coastal Province of North Amer-

ica. Harper Bros. New York, 692.

Nettleton, L. L., 1934, Fluid mechanics of salt domes: Bull. Amer. Assoc. Petrol. Geol., 18, 1175–1204.

Nettleton, L. L., 1943, Recent experimental and geophysical evidence of mechanics of salt dome formation: Bull. Amer. Assoc. Petrol. Geol., 27, 51–63.

Nettleton, L. L., and Elkins, A. T., 1947, Geologic models made from granular materials: Amer. Geophys. Union. Trans., 28, 451–466.

Nettleton, L. L., 1954, Regional, residuals and structures: Geophysics, 19, 1–22.

Nettleton, L. L., 1955, History of concepts of Gulf Coast salt dome formation: Bull. Amer. Assoc. Petrol. Geol., 39, 2373–2383.

Nettleton, L. L., 1976, Gravity and magnetics in oil prospecting: Publish by: McGraw Hill, Inc., 464.

Oldham, C. H. G., 1967. The $\frac{\sin(x)}{X}.\frac{\sin(y)}{Y}$ method for continuation of potential fields: Soc. Exp. Geophys. Min. Geophys, 2, 591–605.

Omara, S., 1964, Diapiric structures in Egypt and Syria : Bull. Amer. Assoc. Petrol. Geol., 48, 1116–1125.

Parker, T. J., and McDowell, A. N., 1955, Model studies of Salt-domes tectonics: Bull. Amer. Assoc. Petrol. Geol., 39, 2384–2470.

Peters, L. J, 1949, The direct approach to magnetic interpretation and its practical application: Geophysics, 14, 290–320.

Pitman, W. C., and Talwani, M., 1972, Sea-Floor spreading in the North Atlantic: Bull. Amer. Assoc. Petrol. Geol., 83, 619–646.

Pitman W. C., Cochran, J. R., Ryan W. B. F., and Ladd, W. J., 1981, Evolution of Libyan margin : Lamont-Doherty geological observatory of Columbia University,

Annex. II-6, (Libyan National Oil Corporation documents), 1–12.

Rosenbach, O., 1953, A contribution to the computation of the second derivative from gravity data: Geophysics, 18, 894–912.

Royden, L., and Keen, E. C., 1980, Rifting process and thermal evolution of the continental margin of Eastern Canada determined from subsidence curves: Earth Plante Sci. Lett., 51, 343–631.

Ryan, W. F., Stanley, D. J., Hersey, J. B., Fahlquist, D. A., and Allan. T. D., 1969, The tectonics and geology of the Mediterranean Sea, *in :* The Sea. ed. Maxwell, A. E., Wilely- Interscience. 4, 387–492.

Ryan, W. B. F., 1971, Can an ocean dry up? Results of deep-sea drilling in Mediterranean: Bull. Amer. Assoc. Petrol. Geol., 55, 362.

Sannemann, D.,1965, Salt-stock families in northwestern Germany, *in :* Diapirism and diapirs: Amer. Assoc. Petrol. Geol., Memoir 8, 261–270.

Schmalz, R. F., 1969, Deep-water evaporite deposition: A genatic model: Bull. Amer. Assoc. Petrol. Geol., 53 798–823.

Seni, J. S., and Jackson, A. P. M., 1983, Evolution of Salt structures, East Texas Diapir Province, *part 1 :* Sedimentary record of Halokinsis: Amer. Assoc. Petrol. Geol., 67, 1219–1244.

Seni, J. S., and Jackson, A. P. M., 1983, Evolution of Salt structures, East Texas Diapir Province, *part 2 :* Pattern and rates of Halokinsis: Amer. Assoc. Petrol. Geol., 67, 1245–1274.

Smith, A. G., 1971, Alpine deformation and the Oceanic areas of the Tethys, Mediterranean, and Atlantic: Bull. Geol. Soc. Amer., 82, 2039–2070.

Smith, A. G., 1976, Plate tectonic and orogeny: A review: Tectonophsics, 33, 215–285.

Sonnenfeld, P., 1985, Models of Upper Miocene evaporite genesis in the Mediterranean

region: *in:* Geological evolution of the Mediterranean basin, Selli, R., (Ed.), Stanley, J. D., and Wezel F. C., New York, Springer Verlag, 323–346.

Spector, A. and Grant,S. F, 1970, Statistical models for interpreting aeromagnetic data: Geophysics, **35**, 293–302.

Talwani, M., and Ewing, M., 1960, Rapid computation of gravitational attraction of three-dimensional bodies of arbitrary shape: Geophysics, **25**, 203–225.

Talwani, M., 1965, Computation with the help of a digital computer of magnetic anomalies caused by bodies of arbitrary shape: Geophysics, **25**, 797–817.

Taylor, M. C. J., 1984, Late Permian Zechstein: *in:* Introduction to the petroleum geology of the North Sea, Chapter 4, 61–81.

Telford, W. M., Geldart, P. L., Sheriff, E. R., and Keys, A. D., 1976, Applied geophysics: Publish by: The syndics of the Cambridge University press, Cambridge, 843.

Torry, P. D., and Fralich, E. C., 1926, An experimental study of the origin of salt domes: Jour. Geol., **34**, 224–234.

Trusheim, F., 1960, Mechanism of the salt migration in North Germany: Bull. Amer. Assoc. Petrol. Geol., **44**, 1519–1540.

Van Houten, F. B., 1983, Sirte Basin, north-central Libya: Cretaceous rifting above a fixed mantle hotspot: Geology, **11**, 115–118.

APPENDIX 1

Computer program **UPDOWN** for upward continuation and second derivative calculations (see section 5.6.1.5).

```
C PROGRAM  <UPDOWN  > CALCULATES THE UPWARD OR DOWNWARD
C                     CONTINUATION AT ANY HEIGHT OR DEPTH OF
C                     THE GIVEN DATA AT A PARTICULAR LOCATION.
C                     IT ALSO OBTAINS 1ST, 2ND OR HIGHER SET
C                     OF DERIVATIVES (ID). OPTION FOR ANOMALY
C                     REDUCTION TO POLE.
C (ID=1,2,...)
C IF;
C IFLAG =1, SUPPLY ID AND Z IN SUBROUTINE <CONDER  >
C IFLAG =2, SUPPLY NRM VECTOR DIRECTION IN SUBROUTINE <REDMAG>
C Z**2;  UPWARD   (-VE) HEIGHT
C        DOWNWARD (+VE) HEIGHT
C ID     =0 NO DERIVATIVE
C ID     =1 FOR 1ST DERIVATIVE
C ID     =2 FOR 2ND DERIVATIVE
C ID     =N FOR NTH DERIVATIVE
C XI(I,J)=THE REAL INPUT MATRIX IN SPACE DOMAIN
C NX     =NUMBER OF X POINTS IN THE GRID
C NY     =NUMBER OF Y POINTS IN THE GRID
C NXY    =TOTAL NUMBER OF THE POINTS IN THE GRID
C DELT   =THE DEGITIZING INTERVAL IN KM.
C OOP    =THE SMOOTHING OPERATOR ACCORDING TO AGARWAL & LAL
C        (1972)
C PLANE TO+TI*(I-1)+TJ*(J-1) REMOVED FROM DATA PRIOR TO MULFFT1
C AND REPLACED IN O/P FOR RED. TO POLE AND CONTINUATIONS
C NORMALY SET TO -0.23.  IF NO SMOOTHING IS REQUIRED THEN
C SET OOP=0
C         MODIFIED BY <<<F. MALTEZOU (1985)>>>
C         MODIFIED BY <<<M. ABUHAJAR (1990)>>>
      PROGRAM  UPDOWN
      INTEGER  IA(19,19),IFMT(3)
      REAL     XI(19,19)
      REAL     X(36,36),Y(36,36)
      READ (05,    *) IFLAG
      NCR=1
      READ (NCR,    *) N1,N2
      READ (NCR,    *) DELT
      READ (NCR,    *) OOP
      DO 10 J=1,N2
      READ (NCR,    *) (XI(I,J),I=1,N1)
   10 CONTINUE
      CALL PLANE  (XI,N1,N2,TO,TI,TJ)
      CALL PLOT2D (XI,N1,N2,IA)
C     SET X AS SYMMETRICAL VECTOR OF SIZE (2N1-2)*(2N2-2)
      MN1=(2*N1)-2
      MN2=(2*N2)-2
      CALL EXPSYM (XI,X,N1,N2,MN1,MN2)
      NN=N1
      NNN=N2
      N1=2*N1-2
      N2=2*N2-2
      NOPTS=N1*N2
      CALL FLZERO (Y,N1,N2)
      CALL MULFFT (X,Y,N1*N2,N1,N1,1)
      CALL MULFFT (X,Y,N1*N2,N2,N1*N2,1)
      FN=1./(2.*DELT)
      FP=FN/(NOPTS)
      FNORM=1./(NOPTS)
      DO 20 J=1,N2
      DO 20 I=1,N1
      X(I,J)=X(I,J)*FNORM
      Y(I,J)=Y(I,J)*FNORM
   20 CONTINUE
      IF (IFLAG.EQ.0) GOTO 30
      IF (IFLAG.EQ.1) CALL CONDER (X,Y,N1,N2,DELT,ID,Z,OOP)
      IF (IFLAG.EQ.2) CALL REDMAG (X,Y,N1,N2)
      CALL MULFFT (X,Y,N1*N2,N2,N1*N2,-1)
   30 CONTINUE
      DO 40 I=1,NN
      DO 40 J=1,NNN
      XI(I,J)=X(I,J)
   40 CONTINUE
      IF(IFLAG.EQ.2 .OR. ID.EQ.0) CALL GPLANE (XI,NN,NNN,TO,TI,TJ)
      ZX=ABS(Z)
      IF (ABS(Z).LT.1) ZX=(ZX*10)+0.001
      IF (Z.EQ.0) NCW=20
      IF (Z.LT.0) NCW=20+ZX-10
      IF (Z.GT.0) NCW=20+ZX
      WRITE (NCW,   91) Z
      DO 50 J=1,NNN
      DO 50 I=1,NN
      RI=I
      RJ=J
      WRITE (NCW,   92) RI,RJ,XI(I,J)
   50 CONTINUE
   91 FORMAT (1X,F6.3)
   92 FORMAT (2(1X,F6.3),1X,E12.6)
```

```
      STOP
      END
      SUBROUTINE <EXPSYM  > EXPANDS A 2-DIMENSIONAL DATA ARRAY
                            STORED IN A(N1,N2) TO PRODUCE AN
                            ENLARGED ARRAY
                            B(MN1,MN2) WHICH HAS SYMMETRY ABOUT THE
                            FIRST AND LAST ROWS AND COLUMNS OF
                            A(N1,N2).0
      SUBROUTINE EXPSYM (A,B,N1,N2,MN1,MN2)
      REAL     A(N1,N2),B(MN1,MN2)
      MN1=2*N1-2
      MN2=2*N2-2
      DO 10 I=1,N1
      DO 10 J=1,N2
      B(I,J)=A(I,J)
   10 CONTINUE
      MAPS DATA INTO TOP R.H QUADRANT
      WRITE(6,*)'N1=',N1,'N2=',N2,'MN1=',MN1,'MN2=',MN2
      II=N1+1
      JJ=N2+1
      WRITE(6,*)'II=',II,'JJ=',JJ
      DO 20 I=1,N1
      DO 20 J=JJ,MN2
      ID=I
      JD=2*N2-J
      WRITE(6,*)'I=',I,'J=',J,'ID=',ID,'JD=',JD
      B(I,J)=A(ID,JD)
   20 CONTINUE
      MAPS DATA INTO BOTTOM L.H. QUADRANT
      DO 30 I=II,MN1
      DO 30 J=1,N2
      ID=2*N1-I
      JD=J
      B(I,J)=A(ID,JD)
   30 CONTINUE
      MAPS DATA INTO BOTTOM R.H. QUADRANT
      DO 40 I=II,MN1
      DO 40 J=JJ,MN2
      ID=2*N1-I
      JD=2*N2-J
      B(I,J)=A(ID,JD)
   40 CONTINUE
      RETURN
      END
```

```
SUBROUTINE <CONDER> CONTINUATION AND DERIVATIVE CALCULATIONS
Z     =9999 FOR DERIVATIVE CALCULATIONS ONLY
Z     =NEGATIVE FOR UPWARD CONTINUATION
SUBROUTINE CONDER (X,Y,N1,N2,DELT,ID,Z,OOP)
 REAL     X(N1,N2),Y(N1,N2)
 WRITE (06,    *) 'ID=?, DEGREE OF THE DERIVATIVE'
 READ (05,    *) ID
 WRITE (06,    *) 'Z=?, HEIGHT'
 READ (05,    *) Z
 WRITE (06,  991) ID,Z
 Z=-Z
TO MULTIPLY FREQUENCIES BY A FACTOR
EXP(I**2+J**2)*(2.0*PI*Z/(N1*DELT)))
FOR; I     =0,1,2,...,N1
     J     =0,1,2,...,N2
FN1=(0.5*N1)+1
FN2=(0.5*N2)+1
DO 100 I=1,N1
 IF (I.GT.FN1) GOTO 10
 AA=I-1
 GOTO 20
 10 CONTINUE
    AA=N1+1-I
 20 CONTINUE
    DO 100 J=1,N2
    IF (J.GT.FN2) GOTO 30
    B=J-1
    GOTO 40
 30 CONTINUE
    B=N2+1-J
 40 CONTINUE
    IF (Z.EQ.9999) GOTO 50
    CONT=EXP((SQRT((AA/N1)**2+(B/N2)**2)*2.0*3.14159*Z)/DELT)
    DIER1=(N1)*DELT
    DIER2=(N2)*DELT
    CONT=EXP((SQRT((AA/DIER1)**2+(B/DIER2)**2)*2.0*3.14159*Z))
    IF (ID.EQ.0) GOTO 60
 50 CONTINUE
    CONTD1=(SQRT((AA/N1)**2+(B/N2)**2)*(2*3.14159)/(DELT))**ID
    CONTD1=(SQRT((AA/DIER1)**2+(B/DIER2)**2)*2.0*3.14159)**ID
 60 CONTINUE
    IF (Z.EQ.9999) GOTO 70
    X(I,J)=X(I,J)*CONT
    Y(I,J)=Y(I,J)*CONT
```

```
      IF (ID.EQ.0) GOTO 100
   70 CONTINUE
      OP=EXP(OOP*CONTD1)
      X(I,J)=X(I,J)*CONTD1*OP
      Y(I,J)=Y(I,J)*CONTD1*OP
  100 CONTINUE
      J=0
  991 FORMAT (' DEGREE OF DERIVATIVE=',I1,'   HEIGHT=',F6.3)
      RETURN
      END
     SUBROUTINE <PLANE   > FITS A PLANE SURFACE TO A 2-DIMENSIONAL
                           DATA ARRAY F(N1,N2) BY LEAST SQUAR
                           EQUATION OF PLANE IS:
                           F(X,Y) = A0 + A1*X + A2*Y
                           REMOVES BEST FITTING PLANE FROM DATA,
                           THEN REMOVES MEAN.
                           DE-TRENDED DATA RETURNED AS F(N1,N2).
      SUBROUTINE PLANE  (F,N1,N2,A0,A1,A2)
      REAL     F(N1,N2),B(3,3),T(3),C(3,3)
      N=N1*N2
      SX=0
      SY=0
      SXX=0
      SYY=0
      SXY=0
      SF=0
      SXF=0
      SYF=0
          COMPUTES SUMS AND PRODUCTS OF DATA VALUES
      DO 10 I=1,N1
      FI=(I-1)
      DO 10 J=1,N2
      FJ=(J-1)
      SX=SX+FI
      SY=SY+FJ
      SXX=SXX+FI*FI
      SYY=SYY+FJ*FJ
      SXY=SXY+FI*FJ
      SF=SF+F(I,J)
      SXF=SXF+FI*F(I,J)
      SYF=SYF+FJ*F(I,J)
   10 CONTINUE
     SETS ELEMENTS OF MATRIX TO BE INVERTED,
     AND VECTOR ON R.H.S. OF EQUATION.
      B(1,1)=(N)
      B(1,2)=SX
      B(1,3)=SY
      B(2,1)=SX
      B(2,2)=SXX
      B(2,3)=SXY
      B(3,1)=SY
      B(3,2)=SXY
      B(3,3)=SYY
      T(1)=SF
      T(2)=SXF
      T(3)=SYF
     CALCULATES ADJOINT MATRIX OF B
     N.B. SINCE B IS SYMMETRIC, ADJ(B) = COFACTOR MATRIX OF B
      C(1,1)=B(2,2)*B(3,3)-B(2,3)*B(3,2)
      C(1,2)=B(2,3)*B(3,1)-B(2,1)*B(3,3)
      C(1,3)=B(2,1)*B(3,2)-B(2,2)*B(3,1)
      C(2,1)=B(1,3)*B(3,2)-B(1,2)*B(3,3)
      C(2,2)=B(1,1)*B(3,3)-B(1,3)*B(3,1)
      C(2,3)=B(1,2)*B(3,1)-B(1,1)*B(3,2)
      C(3,1)=B(1,2)*B(2,3)-B(1,3)*B(2,2)
      C(3,2)=B(1,3)*B(2,1)-B(1,1)*B(2,3)
      C(3,3)=B(1,1)*B(2,2)-B(1,2)*B(2,1)
     CALCULATES INVERSE MATRIX OF B
     DETB=B(1,1)*C(1,1)+B(1,2)*C(1,2)+B(1,3)*C(1,3)
      DO 20 I=1,3
      DO 20 J=1,3
      C(I,J)=C(I,J)/DETB
   20 CONTINUE
     MULTIPLIES VECTOR T BY MATRIX B**(-1) TO GIVE COEFFICIENTS
      A0=C(1,1)*T(1)+C(1,2)*T(2)+C(1,3)*T(3)
      A1=C(2,1)*T(1)+C(2,2)*T(2)+C(2,3)*T(3)
      A2=C(3,1)*T(1)+C(3,2)*T(2)+C(3,3)*T(3)
      REMOVES PLANE FROM OBSERVATIONS
      DO 30 I=1,N1
      FI=(I-1)
      DO 30 J=1,N2
      FJ=(J-1)
      F(I,J)=F(I,J)-(A0+A1*FI+A2*FJ)
   30 CONTINUE
      CALCULATES AND REMOVES MEAN
      FSUM=0.
      DO 40 I=1,N1
```

```
      DO 40 J=1,N2
      FSUM=FSUM+F(I,J)
   40 CONTINUE
      FM=FSUM/(N)
      DO 50 I=1,N1
      DO 50 J=1,N2
      F(I,J)=F(I,J)-FM
   50 CONTINUE
      RETURN
      END
            SUBROUTINE <DVCHCK> DIVIDES A(I,J) BY W(I,J)
                        CHECKING FOR W(I,J)=0.
      SUBROUTINE DVCHCK (A,W,N1,N2)
      REAL     A(N1,N2),W(N1,N2)
      DO 20 I=1,N1
      DO 20 J=1,N2
      IF (W(I,J).NE.0) GOTO 10
      A(I,J)=0
      GOTO 20
   10 CONTINUE
      A(I,J)=A(I,J)/W(I,J)
   20 CONTINUE
      RETURN
      END
     SUBROUTINE <PLOTTR> PRINTS OUT 2-DIMENSIONAL FOURIER
     TRANSFORM COEFFICIENTS IN CORRECT CONFIGURATION.
     SUBROUTINE PLOTTR(XI,N1,N2,IA)
     REAL     IA(84,84),XI(84,84)
      FN=(FLOAT(N2))/20.
      M=INT(FN)+1
      I1=N1/2+1
      I2=N1/2+2
      I3=N1+1
      J1=N2/2+1
      J2=N2/2-1
      DO 20 J=1,J1
      L=J2+J
      DO 10 I=1,I1
      K=I2-I
   10 CONTINUE
      IA(K,L)=INT(XI(I,J)+0.5)
   20 CONTINUE
      DO 40 J=1,J2
      L=J1+J
      DO 30 I=1,I1
      K=I2-I
   30 CONTINUE
      IA(K,J)=INT(XI(I,L)+0.5)
   40 CONTINUE
      DO 60 J=1,J1
      L=J2+J
      DO 50 I=I2,N1
      II=I-I1
      K=I3-II
   50 CONTINUE
      IA(K,L)=INT(XI(I,J)+0.5)
   60 CONTINUE
      DO 80 J=1,J2
      L=J1+J
      DO 70 I=I2,N1
      II=I-I1
      K=I3-II
   70 CONTINUE
      IA(I,J)=INT(XI(K,L)+0.5)
   80 CONTINUE
      DO 90 K=1,M
      JL=(K-1)*20+1
      JM=JL+19
      IF (K.EQ.M) JM=N2
      IF (JM.LT.JL) RETURN
      WRITE (06,   91) K
      DO 90 I=1,N1
      WRITE (06,   92) (IA(I,J),J=JL,JM)
   90 CONTINUE
   91 FORMAT ( 1X,'ARRAY COLUMN=',I3)
   92 FORMAT (20(1X,I5))
      RETURN
      END
    SUBROUTINE FLZERO (Y,N1,N2)
      REAL     Y(N1,N2)
      DO 10 J=1,N2
      DO 10 I=1,N1
      Y(I,J)=0.
   10 CONTINUE
      RETURN
      END
```

```
SUBROUTINE <MULFFT  > MULTIVARIATE COMPLEX FOURIER TRANSFORM,
                      COMPUTED IN PLACE USING MIXED-RADIX FAST
                      FOURIER TRANSFORM ALGORITHM.
                      ARRAYS A AND B ORIGINALLY HOLD THE REAL
                      AND IMAGINARY COMPONENTS OF THE DATA,
                      AND RETURN THE REAL AND IMAGINARY
                      COMPONENTS OF THE RESULTING FOURIER
                      COEFFICIENTS.
                      MULTIVARIATE DATA IS INDEXED ACCORDING TO
                      THE FORTRAN ARRAY ELEMENT SUCCESSOR
                      FUNCTION WITHOUT LIMIT ON THE NUMBER OF
                      IMPLIED  MULTIPLE SUBSCRIPTS.  THE
                      CALLS FOR A  MULTIVARIATE TRANSFORM MAY
                      BE IN ANY ORDER.
 NTOT   =THE TOTAL NUMBER OF COMPLEX DATA VALUES.
 N      =THE DIMENSION OF THE CURRENT VARIABLE.
 NSPAN/N=THE SPACING OF THE CONSECUTIVE DATA VALUES WHILE INDEX
        THE CURRENT VARIABLE.
 IERR   =AN ERROR RETURN INDICATOR.  IT IS NORMALY ZERO, BUT I
         SET TO 1, IF THE NUMBER OF TERMS CANNOT BE FACTORED
         IN THE SPACE AVAILABLE.  IF IT IS PERMISSIBLE, THE
         APPROPARIATE ACTION AT THIS STAGE IS TO ENTER
         <MULFFT  > AGAIN AFTER HAVING REDUCED THE LENGTH
         OF THE SERIES BY ONE TERM.
 ISN    =1, NORMALY.  ITS SIGN DETERMINES THE SIGN OF THE
        COMPLEX  EXPONENTIAL, AND THE MAGNITUDE OF ISN IS
        NORMALLY ONE.
 TRI-VARIATE TRANSFORM WITH A(N1,N2,N3), B(N1,N2,N3) IS
        COMPUTED BY
CALL MULFFT (A,B,N1*N2*N3,N1,N1,1)
CALL MULFFT (A,B,N1*N2*N3,N2,N1*N2,1)
CALL MULFFT (A,B,N1*N2*N3,N3,N1*N2*N3,1)
NTOT  =N
      =NSPAN
      =(NUMBER OF COMPLEX DATA VALUES), E.G. FOR A SINGLE
       VARIATE TRANSFORM.
CALL MULFFT (A,B,N,N,N,1)
WITH MOST FORTRAN COMPILERS THE DATA CAN ALTERNATIVELY BE
STORED IN A SINGLE COMPLEX ARRAY A, THEN THE MAGNITUDE OF
ISN IS CHANGED TO TWO, TO GIVE THE CORRECT INDEXING INCREMENT
AND A(2) USED TO PASS THE INITIAL ADDRESS FOR THE SEQUENCE OF
IMAGINARY VALUES.
```

```
CALL MULFFT (A,A(2),NTOT,N,NSPAN,2)
ARRAYS AT(MAXF), CK(MAXF), BT(MAXF), SK(MAXF), AND NP(MAXP)
ARE USED FOR TEMPORARY STORAGE. IF THE AVAILABLE STORAGE IS
INSUFFICIENT, THE PROGRAM IS TERMINATED BY THE ERROR RETURN
OPTION.
 MAXF   MUST BE .GE. THE MAXIMUM PRIME FACTOR OF N.
 MAXP   MUST BE .GT. THE NUMBER OF PRIME FACTORS OF N.
 IN ADDITION, IF THE SQUARE-FREE PORTION K OF N HAS TWO OR
 MORE PRIME FACTORS, THEN MAXP MUST BE .GE. K-1.
 WRITTEN BY: R.C.SINGLETON, STANFORD RESEARCH INSTITUTE, SEPT.
 1968.
SUBROUTINE MULFFT(A,B,NTOT,N,NSPAN,ISN)
REAL      A(NTOT),B(NTOT)
ARRAY STORAGE IN NFAC FOR A MAXIMUM OF 15 PRIME FACTORS OF N.
IF N HAS MORE THAN ONE SQUARE-FREE FACTOR, THE PRODUCT OF THE
SQUARE-FREE FACTORS MUST BE .LE. 210.
REAL      NFAC(4999),NP(5000)
ARRAY STORAGE FOR MAXIMUM PRIME FACTOR OF 23.
REAL      AT(4999),CK(4999),BT(4999),SK(4999)
EQUIVALENCE (I,II)
THE FOLLOWING TWO CONSTANTS SHOULD AGREE WITH THE ARRAY
DIMENSIONS.
MAXF=4999
MAXP=5000
IERR=0
IF (N.LT.2) RETURN
INC=ISN
C72=0.30901699
S72=0.95105652
S120=0.86602540
RAD=6.28318531
IF (ISN.GE.0) GOTO 10
S72=-S72
S120=-S120
RAD=-RAD
INC=-INC
10 CONTINUE
NT=INC*NTOT
KS=INC*NSPAN
KSPAN=KS
NN=NT-INC
JC=KS/N
RADF=RAD*(JC)*0.5
I=0
JF=0
```

```
      DETERMINE THE FACTORS OF N
      M=0
      K=N
      GOTO 120
  110 CONTINUE
      M=M+1
      NFAC(M)=4
      K=K/16
  120 CONTINUE
      IF (K-(K/16)*16.EQ.0) GOTO 110
      J=3
      JJ=9
      GOTO 140
  130 CONTINUE
      M=M+1
      NFAC(M)=J
      K=K/JJ
  140 CONTINUE
      IF (MOD(K,JJ).EQ.0) GOTO 130
      J=J+2
      JJ=J**2
      IF (JJ.LE.K) GOTO 140
      IF (K.GT.4) GOTO 150
      KT=M
      NFAC(M+1)=K
      IF (K.NE.1) M=M+1
      GOTO 190
  150 CONTINUE
      IF (K-(K/4)*4.NE.0) GOTO 160
      M=M+1
      NFAC(M)=2
      K=K/4
  160 CONTINUE
      KT=M
      J=2
  170 CONTINUE
      IF (MOD(K,J).NE.0) GOTO 180
      M=M+1
      NFAC(M)=J
      K=K/J
  180 CONTINUE
      J=((J+1)/2)*2+1
      IF (J.LE.K) GOTO 170
  190 CONTINUE
      IF (KT.EQ.0) GOTO 210
      J=KT
  200 CONTINUE
      M=M+1
      NFAC(M)=NFAC(J)
      J=J-1
      IF (J.NE.0) GOTO 200
      COMPUTES FOURIER TRANSFORM
  210 CONTINUE
      SD=RADF/(KSPAN)
      CD=2.0*SIN(SD)**2
      SD=SIN(SD+SD)
      KK=1
      I=I+1
      IF (NFAC(I).NE.2) GOTO 510
      TRANSFORM FOR FACTOR OF 2 (INCLUDING ROTATION FACTOR)
      KSPAN=KSPAN/2
      K1=KSPAN+2
  310 CONTINUE
      K2=KK+KSPAN
      AK=A(K2)
      BK=B(K2)
      A(K2)=A(KK)-AK
      B(K2)=B(KK)-BK
      A(KK)=A(KK)+AK
      B(KK)=B(KK)+BK
      KK=K2+KSPAN
      IF (KK.LE.NN) GOTO 310
      KK=KK-NN
      IF (KK.LE.JC) GOTO 310
      IF (KK.GT.KSPAN) GOTO 1010
  320 CONTINUE
      C1=1.0-CD
      S1=SD
  330 CONTINUE
      K2=KK+KSPAN
      AK=A(KK)-A(K2)
      BK=B(KK)-B(K2)
      A(KK)=A(KK)+A(K2)
      B(KK)=B(KK)+B(K2)
      A(K2)=C1*AK-S1*BK
      B(K2)=S1*AK+C1*BK
      KK=K2+KSPAN
```

```
      IF (KK.LT.NT) GOTO 330
      K2=KK-NT
      C1=-C1
      KK=K1-K2
      IF (KK.GT.K2) GOTO 330
      AK=CD*C1+SD*S1
      S1=(SD*C1-CD*S1)+S1
      C1=C1-AK
      KK=KK+JC
      IF (KK.LT.K2) GOTO 330
      K1=K1+INC+INC
      KK=(K1-KSPAN)/2+JC
      IF (KK.LE.JC+JC) GOTO 320
      GOTO 210
      TRANSFORM FOR FACTOR OF 3 (OPTIONAL CODE)
  410 CONTINUE
      K1=KK+KSPAN
      K2=K1+KSPAN
      AK=A(KK)
      BK=B(KK)
      AJ=A(K1)+A(K2)
      BJ=B(K1)+B(K2)
      A(KK)=AK+AJ
      B(KK)=BK+BJ
      AK=-0.5*AJ+AK
      BK=-0.5*BJ+BK
      AJ=(A(K1)-A(K2))*S120
      BJ=(B(K1)-B(K2))*S120
      A(K1)=AK-BJ
      B(K1)=BK+AJ
      A(K2)=AK+BJ
      B(K2)=BK-AJ
      KK=K2+KSPAN
      IF (KK.LT.NN) GOTO 410
      KK=KK-NN
      IF (KK.LE.KSPAN) GOTO 410
      GOTO 810
      TRANSFORM FOR FACTOR OF 4
  510 CONTINUE
      IF (NFAC(I).NE.4) GOTO 710
      KSPNN=KSPAN
      KSPAN=KSPAN/4
  520 CONTINUE
      C1=1.0
      S1=0.
  530 CONTINUE
      K1=KK+KSPAN
      K2=K1+KSPAN
      K3=K2+KSPAN
      AKP=A(KK)+A(K2)
      AKM=A(KK)-A(K2)
      AJP=A(K1)+A(K3)
      AJM=A(K1)-A(K3)
      A(KK)=AKP+AJP
      AJP=AKP-AJP
      BKP=B(KK)+B(K2)
      BKM=B(KK)-B(K2)
      BJP=B(K1)+B(K3)
      BJM=B(K1)-B(K3)
      B(KK)=BKP+BJP
      BJP=BKP-BJP
      IF (ISN.LT.0) GOTO 560
      AKP=AKM-BJM
      AKM=AKM+BJM
      BKP=BKM+AJM
      BKM=BKM-AJM
      IF (S1.EQ.0) GOTO 570
  540 CONTINUE
      A(K1)=AKP*C1-BKP*S1
      B(K1)=AKP*S1+BKP*C1
      A(K2)=AJP*C2-BJP*S2
      B(K2)=AJP*S2+BJP*C2
      A(K3)=AKM*C3-BKM*S3
      B(K3)=AKM*S3+BKM*C3
      KK=K3+KSPAN
      IF (KK.LE.NT) GOTO 530
  550 CONTINUE
      C2=CD*C1+SD*S1
      S1=(SD*C1-CD*S1)+S1
      C1=C1-C2
      C2=C1**2-S1**2
      S2=2.0*C1*S1
      C3=C2*C1-S2*S1
      S3=C2*S1+S2*C1
      KK=KK-NT+JC
      IF (KK.LE.KSPAN) GOTO 530
      KK=KK-KSPAN+INC
```

```
      IF (KK.LE.JC) GOTO 520
      IF (KSPAN.EQ.JC) GOTO 1010
      GOTO 210
  560 CONTINUE
      AKP=AKM+BJM
      AKM=AKM-BJM
      BKP=BKM-AJM
      BKM=BKM+AJM
      IF (S1.NE.0) GOTO 540
  570 CONTINUE
      A(K1)=AKP
      B(K1)=BKP
      A(K2)=AJP
      B(K2)=BJP
      A(K3)=AKM
      B(K3)=BKM
      KK=KJ+KSPAN
      IF (KK.LE.NT) GOTO 530
      GOTO 550
      TRANSFORM FOR FACTOR OF 5 (OPTIONAL CODE)
  610 CONTINUE
      C2=C72**2-S72**2
      S2=2.0*C72*S72
  620 CONTINUE
      K1=KK+KSPAN
      K2=K1+KSPAN
      K3=K2+KSPAN
      K4=K3+KSPAN
      AKP=A(K1)+A(K4)
      AKM=A(K1)-A(K4)
      BKP=B(K1)+B(K4)
      BKM=B(K1)-B(K4)
      AJP=A(K2)+A(K3)
      AJM=A(K2)-A(K3)
      BJP=B(K2)+B(K3)
      BJM=B(K2)-B(K3)
      AA=A(KK)
      BB=B(KK)
      A(KK)=AA+AKP+AJP
      B(KK)=BB+BKP+BJP
      AK=AKP*C72+AJP*C2+AA
      BK=BKP*C72+BJP*C2+BB
      AJ=AKM*S72+AJM*S2
      BJ=BKM*S72+BJM*S2
      A(K1)=AK-BJ
      A(K4)=AK+BJ
      B(K1)=BK+AJ
      B(K4)=BK-AJ
      AK=AKP*C2+AJP*C72+AA
      BK=BKP*C2+BJP*C72+BB
      AJ=AKM*S2-AJM*S72
      BJ=BKM*S2-BJM*S72
      A(K2)=AK-BJ
      A(K3)=AK+BJ
      B(K2)=BK+AJ
      B(K3)=BK-AJ
      KK=K4+KSPAN
      IF (KK.LT.NN) GOTO 620
      KK=KK-NN
      IF (KK.LE.KSPAN) GOTO 620
      GO TO 810
      TRANSFORM FOR ODD FACTORS
  710 CONTINUE
      K=NFAC(I)
      KSPNN=KSPAN
      KSPAN=KSPAN/K
      IF (K.EQ.3) GOTO 410
      IF (K.EQ.5) GOTO 610
      IF (K.EQ.JF) GOTO 730
      JF=K
      S1=RAD/(K)
      C1=COS(S1)
      S1=SIN(S1)
      IF (JF.GT.MAXF) GOTO 2000
      CK(JF)=1.0
      SK(JF)=0.0
      J=1
  720 CONTINUE
      CK(J)=CK(K)*C1+SK(K)*S1
      SK(J)=CK(K)*S1-SK(K)*C1
      K=K-1
      CK(K)=CK(J)
      SK(K)=-SK(J)
      J=J+1
      IF (J.LT.K) GOTO 720
  730 CONTINUE
      K1=KK
      K2=KK+KSPNN
```

```
      AA=A(KK)
      BB=B(KK)
      AK=AA
      BK=BB
      J=1
      K1=K1+KSPAN
  740 CONTINUE
      K2=K2-KSPAN
      J=J+1
      AT(J)=A(K1)+A(K2)
      AK=AT(J)+AK
      BT(J)=B(K1)+B(K2)
      BK=BT(J)+BK
      J=J+1
      AT(J)=A(K1)-A(K2)
      BT(J)=B(K1)-B(K2)
      K1=K1+KSPAN
      IF (K1.LT.K2) GOTO 740
      A(KK)=AK
      B(KK)=BK
      K1=KK
      K2=KK+KSPNN
      J=1
  750 CONTINUE
      K1=K1+KSPAN
      K2=K2-KSPAN
      JJ=J
      AK=AA
      BK=BB
      AJ=0
      BJ=0
      K=1
  760 CONTINUE
      K=K+1
      AK=AT(K)*CK(JJ)+AK
      BK=BT(K)*CK(JJ)+BK
      K=K+1
      AJ=AT(K)*SK(JJ)+AJ
      BJ=BT(K)*SK(JJ)+BJ
      JJ=JJ+J
      IF (JJ.GT.JF) JJ=JJ-JF
      IF (K.LT.JF) GOTO 760
      K=JF-J
      A(K1)=AK-BJ
      B(K1)=BK+AJ
      A(K2)=AK+BJ
      B(K2)=BK-AJ
      J=J+1
      IF (J.LT.K) GOTO 750
      KK=KK+KSPNN
      IF (KK.LE.NN) GOTO 730
      KK=KK-NN
      IF (KK.LE.KSPAN) GOTO 730
      MULTIPLY BY ROTATION FACTOR (EXCEPT FOR FACTORS OF 2 AND 4)
  810 CONTINUE
      IF (I.EQ.M) GOTO 1010
      KK=JC+1
  820 CONTINUE
      C2=1.0-CD
      S1=SD
  830 CONTINUE
      C1=C2
      S2=S1
      KK=KK+KSPAN
  840 CONTINUE
      AK=A(KK)
      A(KK)=C2*AK-S2*B(KK)
      B(KK)=S2*AK+C2*B(KK)
      KK=KK+KSPNN
      IF (KK.LE.NT) GOTO 840
      AK=S1*S2
      S2=S1*C2+C1*S2
      C2=C1*C2-AK
      KK=KK-NT+KSPAN
      IF (KK.LE.KSPNN) GOTO 840
      C2=C1-(CD*C1+SD*S1)
      S1=S1+(SD*C1-CD*S1)
      KK=KK-KSPNN+JC
      IF (KK.LE.KSPAN) GOTO 830
      KK=KK-KSPAN+JC+INC
      IF (KK.LE.JC+JC) GOTO 820
      GOTO 210
      PERMUTE THE RESULTS TO NORMAL ORDER---DONE IN TWO STAGES
      PERMUTATION FOR SQUARE FACTORS OF N
 1010 CONTINUE
      NP(1)=KS
      IF (KT.EQ.0) GOTO 1250
```

```
      K=KT+KT+1
      IF (M.LT.K) K=K-1
      J=1
      NP(K+1)=JC
 1020 CONTINUE
      NP(J+1)=NP(J)/NFAC(J)
      NP(K)=NP(K+1)*NFAC(J)
      J=J+1
      K=K-1
      IF (J.LT.K) GOTO 1020
      K3=NP(K+1)
      KSPAN=NP(2)
      KK=JC+1
      K2=KSPAN+1
      J=1
      IF (N.NE.NTOT) GO TO1210
      PERMUTATION FOR SINGLE VARIATE TRANSFORM (OPTIONAL CODE)
 1110 CONTINUE
      AK=A(KK)
      A(KK)=A(K2)
      A(K2)=AK
      BK=B(KK)
      B(KK)=B(K2)
      B(K2)=BK
      KK=KK+INC
      K2=KSPAN+K2
      IF (K2.LT.KS) GOTO 1110
 1120 CONTINUE
      K2=K2-NP(J)
      J=J+1
      K2=NP(J+1)+K2
      IF (K2.GT.NP(J)) GOTO 1120
      J=1
 1130 CONTINUE
      IF (KK.LT.K2) GOTO 1110
      KK=KK+INC
      K2=KSPAN+K2
      IF (K2.LT.KS) GOTO 1130
      IF (KK.LT.KS) GOTO 1120
      JC=K3
      GOTO 1250
      PERMUTATION FOR MULTIVARIATE TRANSFORM
 1210 CONTINUE
      K=KK+JC
 1220 CONTINUE
      AK=A(KK)
      A(KK)=A(K2)
      A(K2)=AK
      BK=B(KK)
      B(KK)=B(K2)
      B(K2)=BK
      KK=KK+INC
      K2=K2+INC
      IF (KK.LT.K) GOTO 1220
      KK=KK+KS-JC
      K2=K2+KS-JC
      IF (KK.LT.NT) GOTO 1210
      K2=K2-NT+KSPAN
      KK=KK-NT+JC
      IF (K2.LT.KS) GOTO 1210
 1230 CONTINUE
      K2=K2-NP(J)
      J=J+1
      K2=NP(J+1)+K2
      IF (K2.GT.NP(J)) GO TO1230
      J=1
 1240 CONTINUE
      IF (KK.LT.K2) GOTO 1210
      KK=KK+JC
      K2=KSPAN+K2
      IF (K2.LT.KS) GOTO 1240
      IF (KK.LT.KS) GOTO 1230
      JC=K3
 1250 CONTINUE
      IF (2*KT+1.GE.M) RETURN
      KSPNN=NP(KT+1)
      PERMUTATION FOR SQUARE-FREE FACTORS OF N
      J=M-KT
      NFAC(J+1)=1
 1310 CONTINUE
      NFAC(J)=NFAC(J)*NFAC(J+1)
      J=J-1
      IF (J.NE.KT) GOTO 1310
      KT=KT+1
      NN=NFAC(KT)-1
      IF (NN.GT.MAXP) GOTO 2000
      JJ=0
      J=0
```

```
      GOTO 1340
 1320 CONTINUE
      JJ=JJ-K2
      K2=KK
      K=K+1
      KK=NFAC(K)
 1330 CONTINUE
      JJ=KK+JJ
      IF (JJ.GE.K2) GOTO 1320
      NP(J)=JJ
 1340 CONTINUE
      K2=NFAC(KT)
      K=KT+1
      KK=NFAC(K)
      J=J+1
      IF (J.LE.NN) GOTO 1330
      DETERMINE THE PERMUTATION CYCLES OF LENGTH GREATER THAN 1
      J=0
      GOTO 1420
 1410 CONTINUE
      K=KK
      KK=NP(K)
      NP(K)=-KK
      IF (KK.NE.J) GOTO 1410
      K3=KK
 1420 CONTINUE
      J=J+1
      KK=NP(J)
      IF (KK.LT.0) GOTO 1420
      IF (KK.NE.J) GOTO 1410
      NP(J)=-J
      IF (J.NE.NN) GOTO 1420
      MAXF=INC*MAXF
      REORDER A AND B, FOLLOWING THE PERMUTATION CYCLES
      GOTO 1570
 1510 CONTINUE
      J=J-1
      IF (NP(J).LT.0) GOTO 1510
      JJ=JC
 1520 CONTINUE
      KSPAN=JJ
      IF (JJ.GT.MAXF) KSPAN=MAXF
      JJ=JJ-KSPAN
      K=NP(J)
      KK=JC*K+II+JJ
      K1=KK+KSPAN
      K2=0
 1530 CONTINUE
      K2=K2+1
      AT(K2)=A(K1)
      BT(K2)=B(K1)
      K1=K1-INC
      IF (K1.NE.KK) GOTO 1530
 1540 CONTINUE
      K1=KK+KSPAN
      K2=K1-JC*(K+NP(K))
      K=-NP(K)
 1550 CONTINUE
      A(K1)=A(K2)
      B(K1)=B(K2)
      K1=K1-INC
      K2=K2-INC
      IF (K1.NE.KK) GOTO 1550
      KK=K2
      IF (K.NE.J) GOTO 1540
      K1=KK+KSPAN
      K2=0
 1560 CONTINUE
      K2=K2+1
      A(K1)=AT(K2)
      B(K1)=BT(K2)
      K1=K1-INC
      IF (K1.NE.KK) GOTO 1560
      IF (JJ.NE.0) GOTO 1520
      IF (J.NE.1) GOTO 1510
 1570 CONTINUE
      J=K3+1
      NT=NT-KSPNN
      II=NT-INC+1
      IF (NT.GE.0) GOTO 1510
      RETURN
 2000 CONTINUE
      WRITE (06,   *) 'ARRAY BOUNDS EXCEEDED WITHIN SUBROUTINE
                      <MULFFT>'
      IERR=1
      RETURN
      END
```

```
  SUBROUTINE <GPLANE> ADDS A PLANE TO A 2-DIMENSIONAL DATA
  ARRAY  A(N1,N2)
        A(X,Y) = A(X,Y) + A0 + A1*X + A2*Y
  SUBROUTINE GPLANE (A,N1,N2,A0,A1,A2)
   REAL     A(N1,N2)
   DO 10 I=1,N1
   FI=(I-1)
   DO 10 J=1,N2
   FJ=(J-1)
   A(I,J)=A(I,J)+A0+A1*FI+A2*FJ
10 CONTINUE
   RETURN
   END
  SUBROUTINE <REDMAG> REDUCTION TO MAGNETIC POLE CACULATION
   INPUT MAGNETIZATION DIRECTIONS:
   AIO    =INCLINATION OF NRM VECTOR IN ROCKS
   AI     =INCLINATION OF EARTHS FIELD
   DO     =DECLINATION OF NRM VECTOR
   D      =DECLINATION OF EARTHS FIELD
   SUBROUTINE REDMAG (X,Y,N1,N2)
   REAL     X(N1,N2),Y(N1,N2)
   A=66.0
   D=-9.0
   WRITE (06,     *) 'INCLINATION OF NRM VECTOR IN ROCKS, <AIO=?>'
   READ (05,     *) AIO
   WRITE (06,     *) 'INCLINATION OF EARTHS FIELD, <AI =?>'
   READ (05,     *) AI
   WRITE (06,     *) 'DECLINATION OF NRM VECTOR IN ROCKS, <DO=?>'
   READ (05,     *) DO
   WRITE (06,     *) 'DECLINATION OF EARTHS FIELD, <D  =?>'
   READ (05,     *) D
   READ (05,     *) AIO,AI,DO,D
   CONVERSION FROM DEGREES TO RADIANS
   PIE=4.*ATAN(1.)
   CONST=PIE/180.
   DO=DO*CONST
   D=D*CONST
   AIO=(180-AIO)*CONST
   AI=(180-AI)*CONST
   COTR=COS(AIO)/SIN(AIO)
   COTE=COS(AI)/SIN(AI)
   COSDR=COS(DO)
   COSDE=COS(D)
   SINDR=SIN(DO)
   SINDE=SIN(D)
   SINIR=SIN(AIO)
   SINIE=SIN(AI)
   SIOSI=1./(SINIR*SINIE)
   TO MULTIPLY FREQUENCIES BY A FACTOR
   FN1=(0.5*N1)+1
   FN2=(0.5*N2)+1
   DO 50 I=1,N1
   IF (I.GT.FN1) GOTO 10
   AA=I-1
   GOTO 20
10 CONTINUE
   AA=N1+1-I
20 CONTINUE
   DO 50 J=1,N2
   IF (J.GT.FN2) GOTO 30
   B=J-1
   GOTO 40
30 CONTINUE
   B=N2+1-J
40 CONTINUE
   IF (AA.EQ.0 .AND. B.EQ.0) GOTO 50
   PMN=SQRT(AA**2+B**2)
   AKM=AA/PMN
   BKM=B/PMN
   SAI1=COTR*(AKM*COSDR+BKM*SINDR)
   SAI2=COTE*(AKM*COSDE+BKM*SINDE)
   XTEMP=X(I,J)
   YTEMP=Y(I,J)
   DEN=1./((1+SAI1**2)*(1+SAI2**2))
   FPART=DEN*(1-SAI1*SAI2)
   DA1=SAI1+SAI2
   SPART=DEN*DA1
   X(I,J)=FPART*XTEMP-SPART*YTEMP
   Y(I,J)=FPART*YTEMP+SPART*XTEMP
   MULTIPLY WITH THE INCLINATION FACTOR DUE TO THE ROCKS AND
   THE EARTH'S MAGNETIC FIELD
   X(I,J)=X(I,J)*SIOSI
   Y(I,J)=Y(I,J)*SIOSI
50 CONTINUE
   SET D.C. OF REAL PART TO ZERO
   X(1,1)=0
   J=0
91 FORMAT (' AIO=',F6.2,'  AI=',F6.2,'  DO=',F6.2,'  D=',F6.2)
```

```
      RETURN
      END
     SUBROUTINE <PLOT2D> PRINTS OUT DATA ARRAY A(N1,N2) IN INTEGER
                         FORMAT ON A 2D GRID 20 POINTS WIDE.
      SUBROUTINE PLOT2D (A,N1,N2,IA)
      REAL     IA(N1,N2),A(N1,N2)
      FN=((N2))/20.
      M=INT(FN)+1
      DO 10 I=1,N1
      DO 10 J=1,N2
      IA(I,J)=INT(A(I,J)+0.5)
   10 CONTINUE
      DO 20 K=1,M
      JL=(K-1)*20+1
      JM=JL+19
      IF (K.EQ.M) JM=N2
      IF (JM.LT.JL) RETURN
      WRITE (06,   91) K
      DO 20 I=1,N1
      WRITE (06,   92) (IA(I,J),J=JL,JM)
   20 CONTINUE
   91 FORMAT ( 1X,'ARRAY COLUMN=',I3)
   92 FORMAT (20(1X,I5))
      RETURN
      END
```

APPENDIX 2

Two-way time contour maps of the base of Oligocene (Salambo/Cherahil Formation interface) and the top of the Zebbag Formation. Scale of 1.250.000.

TWO-WAY TIME CONTOUR MAP OF THE BASE OF OLIGOCENE

(Salambo/Cherahil interface)

Figure 4.4: Two-way time structural map of the Salambo/Cherahil interface Formation.

KEY

- Major Fault
- Minor Fault
- Uncertain Major Fault
- Uncertain Minor Fault
- Uncertain Contour
- Salt Piercement
- Closed Low
- Closed High
- 1200 — Two-way time in milliseconds Contour intervals 100ms
- Study area boundaries

AUTHOR: M. ABUHAJAR

ZUWARAH

TRIPOLI

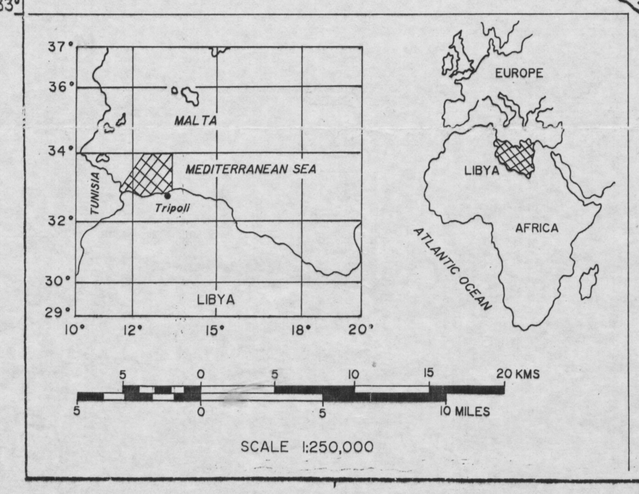

TWO-WAY TIME CONTOUR MAP OF THE TOP OF THE ZEBBAG FORMATION

Figure 4.5: Two-way time structural map of the top the Zebbag Formation.

KEY

- Major Fault
- Minor Fault
- Uncertain Fault
- Salt Piercement
- Closed High
- Closed Low
- Study area boundaries

contour interval 200m/sec

AUTHOR: M. ABUHAJAR

ZUWARAH

TRIPOLI